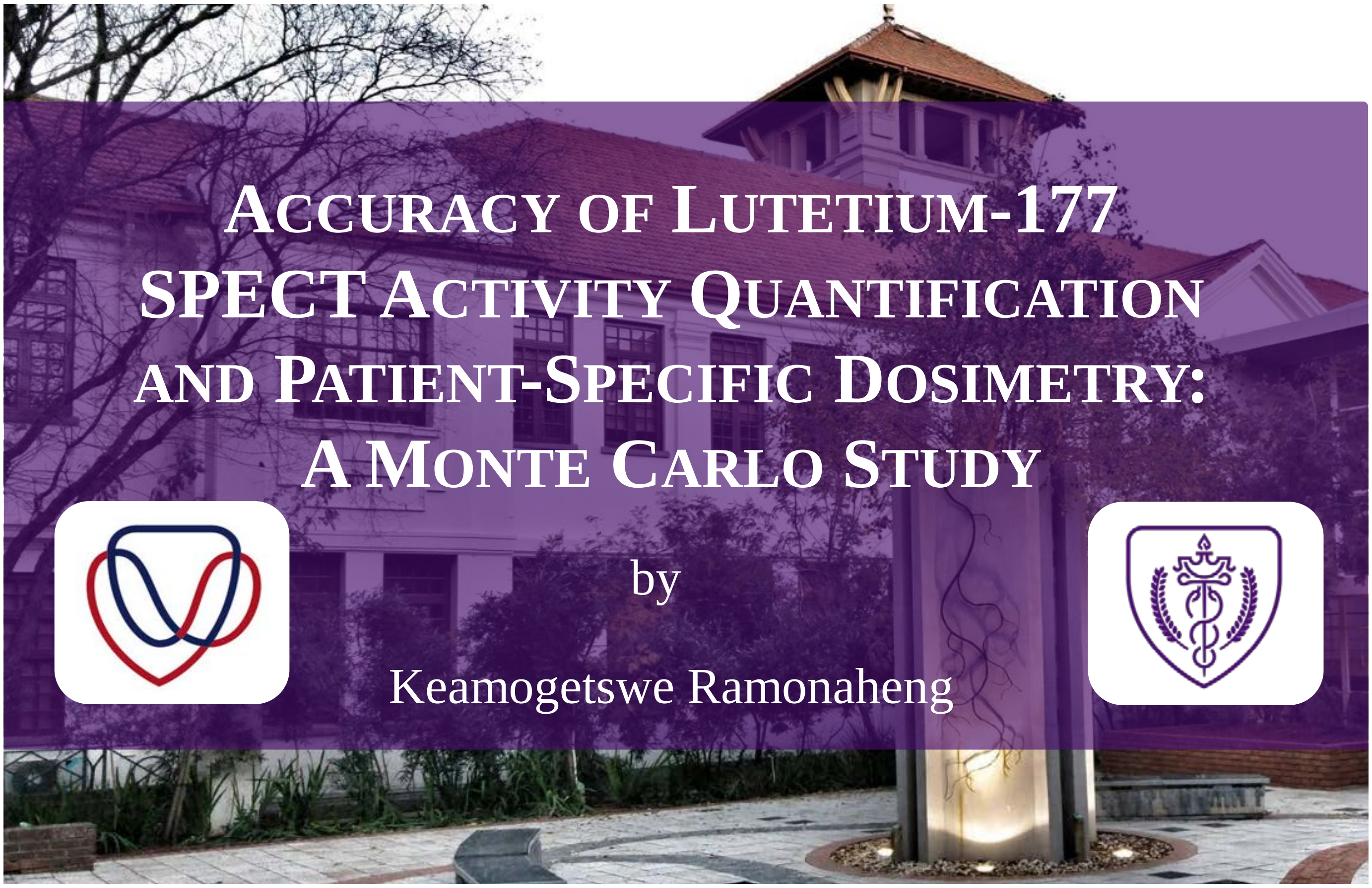

ACCURACY OF LUTETIUM-177 SPECT ACTIVITY QUANTIFICATION AND PATIENT-SPECIFIC DOSIMETRY: A MONTE CARLO STUDY

by

Keamogetswe Ramonaheng

Submitted in fulfilment of the requirements in respect of the

Doctoral Degree

Ph.D. (Medical Physics) in the Department of Medical Physics in the

Faculty of Health Sciences at the University of the Free State.

30 November 2021

Promoter:	Dr. Johannes A. van Staden
Co-promoter:	Dr. Hanlie du Raan

T: +27 51 405 3157 | E: BoomK@ufs.ac.za | www.ufs.ac.za
UFSUV | UFSweb | UFSweb | ufsuv

Inspiring excellence.
Transforming lives.

UNIVERSITY OF THE
FREE STATE
UNIVERSITEIT VAN DIE
VRYSTAAT
YUNIVESITHI YA
FREISTATA
UFS
HEALTH SCIENCES

DECLARATION

I, Keamogetswe Ramonaheng,
declare that the thesis that I herewith submit for the
Doctoral Degree Ph.D. (Medical Physics) at the University of the Free State, is
my independent work, and that I have not previously submitted it for a
qualification at another institution of higher education.

Bloemfontein

30 November 2021

Ramon

Keamogetswe Ramonaheng

DEDICATION

I dedicate this work to:

The loving memory of my mother,
Keitumetsi Harriet Malebye.
Thank you for the lessons.

And

My son and biggest motivator, Neo Ramonaheng, thank you for giving me purpose.
My husband and biggest supporter, Ts'epo Ramonaheng, thank you for the love and patience.

Evidence is not a substitute for faith.
Faith is the substance of things hoped for, the evidence of things not seen (Hebr. 11:1).
The will of God is not a matter of evidence or proof.
It's a matter of will.

All the glory goes to God. His grace and mercy sustain me.

ACKNOWLEDGEMENTS

Motho ke motho ka batho babang – Jeremy Cronin.

I am grateful to the Department of Nuclear Medicine at Universitas Academic Hospital for permission to use their equipment and friendly support. I thank the Free State Province Department of Health and the Faculty of Health Sciences at the University of the Free State for permission to conduct the study.

I want to express my profound gratitude to my study promotors, Dr. Johannes van Staden and Dr. Hanlie du Raan. I am grateful for their support, guidance, and patience. Thank you for always availing yourselves and sharing your knowledge selflessly. Thank you for the travel opportunities that allowed me to share this work with the world. Thank you for the laughter and for being human throughout the process. I cannot express my gratitude enough.

I had the honour of working with Professor Michael Ljungberg and Professor Katarina Sjögreen from the Department of Medical Radiation Physics at the University of Lund, Sweden, as collaborators in this work. A true privilege and a blessing! I want to express my ineffable gratitude to them. Thank you for sharing your software program and knowledge so generously. Thank you for your kind patience and understanding. Thank you for your continuous support and always making time in your busy schedules to troubleshoot problems pertaining to this study. I'm forever grateful and will carry your kindness in my heart.

To Michaella Morphis, thank you for being more than a colleague. I want to express my deepest gratitude for all your technical assistance, but most of all for your unwavering support and friendship. I am glad to have walked this journey with you. You have been a blessing.

ACKNOWLEDGEMENTS

To Milani Qebetu, thank you for all the technical assistance with the software. Thank you for always taking the time to troubleshoot problems I encountered during my investigations. I am grateful for all the support you have shown me throughout this work.

I want to extend my gratitude to Professor Charles Herbst for the software programs. Your friendly assistance and enthusiasm have made a significant contribution to this work. I want to thank Professor Andries van Aswegen and Professor William Rae for the language editing of the articles included in this work and Theanette Mulder for the technical and editorial preparation of the articles. I am grateful to Dr. Freek du Plessis for his motivating words.

I want to express my deepest gratitude to my home-carer, Irene Pau. Thank you for showing my family so much love and support. You genuinely are God-sent. I am eternally grateful and indebted to you.

To all my friends, Maleshwane Pule, Anita Conradie, Rose Molatedi, Dikeledi Maduma, Jay Jiyun Lee, thank you for your friendship and prayers. To my colleague, Modise Mongane, thank you for all your assistance with the clinic. To the late Mme Lucy Mositi, thank you for your love, support, and for making my life at Medical Physics memorable throughout the years.

TABLE OF CONTENTS

Chapters

Appendices

Abstract

The goal of radiopharmaceutical therapy (RPT) is to deliver the maximum dose to cancerous tumours while sparing healthy tissue. Ideally, the radiopharmaceutical should accumulate in the tumorous tissue and the radiation entirely absorbed for tissue destruction; however, this is not the case. Dosimetry strives to balance the efficacy of delivering the maximum dose to the tumour cells with minimal toxicity to the healthy tissue. Patient-specific dosimetry offers the potential for RPT to reach its full potential as a powerful precision-based treatment. Efforts for patient-specific dosimetry remain a challenge due to the steps involved in the clinical dosimetry workflow. SPECT/CT imaging allows the estimation of the bio-kinetic distribution of the radiopharmaceuticals with good precision, which is required for accurate dosimetry. Different dosimetry software is available (commercial and non-commercial), but these should be benchmarked before being used. Optimising the imaging process for activity quantification and dosimetry in the NM discipline is essential, and Monte Carlo (MC) techniques have been used successfully in this endeavour. Furthermore, full MC dosimetry gained wide acceptance as the gold standard and the most accurate means for patient-specific dosimetry. MC simulations offer the advantage of having a gold standard against which the dosimetry can be benchmarked, and the dosimetry accuracy evaluated.

Therefore this thesis aimed to assess the accuracy of ^{177}Lu SPECT activity quantification and patient-specific dosimetry using MC simulations. The focus was on the bio-distribution of ^{177}Lu-DOTATATE due to its clinical relevance in RPT of patients with metastasised neuroendocrine tumours. The kidneys are the dose-limiting organs for RPT with ^{177}Lu-DOTATATE. Studies have shown kidney doses to vary significantly between patients. Given the relation between tumour absorbed dose and tumour reduction, for a complete efficacy evaluation, absorbed doses should be determined not only for the kidneys but, where possible, extended to the tumours. This study incorporated voxel-based phantoms generated from phantom and patient CT data to perform virtual image-based activity quantification and dosimetry using MC simulations. The voxel-based phantoms were modified to include spherical structures mimicking tumours.

The first objective of this study was to validate a model of the Siemens Symbia T16 dual-head SPECT/CT gamma camera available in our clinic using the SIMIND MC program for ^{177}Lu imaging. The validation was achieved by comparing experimental and simulated gamma camera performance planar and SPECT criteria tests. The results were in good agreement and provided adequate confidence that SIMIND could emulate the Symbia T16 successfully and be used for further investigations of ^{177}Lu SPECT/CT image quantification.

The second objective investigated the effect of sphere and cylinder calibration factor (CF) geometries and their corresponding recovery coefficients (RCs) on the quantification accuracy of ^{177}Lu SPECT images using MC simulations. The investigations were performed using geometries of a cylindrical, an anthropomorphic torso, and patient-specific phantoms. The quantification accuracy was evaluated for tumours and the kidneys. The results demonstrated that ^{177}Lu SPECT quantification accuracies compared favourably for sphere-based and cylinder-based CF and RC combinations when all SPECT corrections were applied. The absolute quantification accuracy of $\leq 3.5\%$ compared well to literature findings and complied with the 5% requirements for accurate dosimetry.

The third objective of the thesis aimed to compare the accuracy of the absorbed doses computed with the software LundADose and OLINDA/EXM 1.0 using three patient-specific voxel-based phantoms. The dosimetry accuracy was assessed by comparing the computed doses to the “true” activity images combined with full MC dosimetry to define the gold standard. The accuracy between LundADose (6.6%) and OLINDA/EXM 1.0 (8.1%) was comparable. The $\leq 10\%$ dosimetry accuracy suggested that the software platforms approximated the true dose estimates and advocated for the dosimetry accuracy to be reliable.

Keywords: Monte Carlo, SIMIND, Lutetium-177, SPECT, Activity Quantification, Calibration Factor, Recovery Coefficient, Dosimetry Accuracy, Patient-specific Phantom, Voxel-based phantom.

Abbreviations

General abbreviations

BED	Biological effective dose
c.a	Carrier added
CDR	Collimator-detector response
CF	Calibration factor
CF_{cyl}	Cylinder calibration factor
$CF\text{-}RC_{sphere}$	Sphere calibration factor and sphere recovery coefficient
$CF\text{-}RC_{cyl}$	Cylinder calibration factor and cylinder recovery coefficient
CF_{sphere}	Sphere calibration factor
CT	Computed tomography
C_{SPECT}	SPECT estimated activity concentration
C_{true}	True activity concentration
DEW	Dual-energy window
DFs	Dose conversion factors
DNA	Deoxyribonucleic acid
DOTA	Dodecane tetraacetic acid
DOTANOC	[DOTA0-1-Nal3]-octreotide
DOTATATE	[DOTA0,Tyr3]-octreotate
DOTATOC	[DOTA0,Tyr3]-octreotide
DTPA	Diethylene-triamine-pentaacetate
DVH	Dose-volume histogram
DVK	Dose-voxel kernel
EBRT	External-beam radiation therapy
$e\text{-}D_{True}$	Absorbed dose computed in LundADose from local energy deposition of electrons using the true activity images
E_{max}	Maximum energy
ESSE	Effective source scatter estimation

FDA	Food and Drug Administration
FWHM	Full width at half maximum
FWTM	Full width at tenth the maximum
GATE	GEANT4 application for tomographic emission
Hybrid WB/SPECT	Hybrid planar whole-body SPECT/CT
IAEA	International Atomic Energy Agency
ICRP	International Commission on Radiological Protection
LED	Local energy deposition
LND-D_{SPECT}	Mean absorbed dose computed in LundADose using reconstructed SPECT images
MC	Monte Carlo
MC-D_{True}	Mean absorbed dose computed using true activity images with full Monte Carlo transport
MCMATV3D	Monte Carlo matrix vectorized 3D
ME	Medium energy
MIBG	Metaiodobenzylguanidine
MIRD	Medical Internal Radiation Dose
ML-EM	Maximum likelihood expectation maximization
MRI	Magnetic resonance imaging
NaI(Tl)	Sodium iodide (thallium-doped)
n.c.a	No-carrier added
NEMA	National Electrical Manufacturers Association
NETs	Neuroendocrine tumours
NM	Nuclear medicine
NMISA	National Metrology Institute of South Africa
NRF	National Research Foundation
OAR	Organs at risk
OLINDA	OLINDA/EXM version 1.0
OLINDA-D_{SPECT}	Mean absorbed dose computed in OLINDA/EXM 1.0 using reconstructed SPECT images
OLINDA/EXM	Organ level internal dose assessment/exponential modelling

OS-EM	Ordered subset expectation maximization
PET/CT	Positron emission tomography/computed tomography
PETSIM	Simulation of positron imaging system
PRRT	Peptide receptor radionuclide therapy
PSMA	Prostate-specific membrane antigen
PVCs	Partial volume corrections
PVEs	Partial volume effects
RC	Recovery coefficient
RC_{cyl}	Cylinder recovery coefficient
RC_{sphere}	Sphere recovery coefficient
RMS	Root mean square
RPT	Radiopharmaceutical therapy
RSD	Radiological support devices
SIMIND	Simulation of imaging nuclear detectors
SIMSET	Simulation system for emission tomography
SIMSPECT	System for SPECT simulation and modelling
SPECT/CT	Single-photon emission computed tomography/computed tomography
SPECT-TIA	Time-integrated activity calculated from reconstructed SPECT activity images
SSTR	Somatostatin receptor
STINT	Swedish Foundation for International Cooperation in Research and Higher Education
TAC	Time-activity curve
TEW	Triple-energy window
TIA	Time-integrated activity
True-TIA	Time-integrated activity calculated from true activity images
Tumour-LNG	Tumour placed between the lungs
Tumour-LV	Tumour placed adjacent to the liver
VOI	Volume of interest

Isotope and Chemical Name Abbreviations

^{255}Ac	Actinium-255
^{133}Ba	Barium-133
^{213}Bi	Bismuth-213
^{68}Ga	Gallium-68
^{177}Hf	Hafnium-177
^{123}I	Iodine-123
^{124}I	Iodine-124
^{131}I	Iodine-131
^{111}In	Indium-111
^{176}Lu	Lutetium-176
^{177}Lu	Lutetium-177
^{177m}Lu	Lutetium-177 metastable
Lu_2O_3	Lutetium oxide
$^{223}RaCl_2$	Radium-223 dichloride
^{99m}Tc	Technetium-99m
^{227}Th	Thorium-227
^{176}Yb	Ytterbium-176
^{177}Yb	Ytterbium-177
Yb_2O_3	Ytterbium oxide
^{86}Y	Yttrium-86
^{90}Y	Yttrium-90

1

Chapter 1: Introduction

TABLE OF CONTENTS

1.1 Background

1.1.1 Radiopharmaceutical Therapy

There is a strong driving force in the health community for personalised medicine. The recent advances in molecular medicine have resulted in the Nuclear Medicine (NM) community experiencing a proliferation in radiopharmaceutical therapy (RPT) development. These developments have offered scientific and clinical opportunities to introduce patient-specific dosimetry where RPT can tailor the therapy to the patient for the best response while ensuring a safety margin, resulting in better patient care. However, reliable dosimetry depends on the accuracy of quantifying the radiopharmaceutical distribution in each patient. Although the term RPT has been officially introduced fairly recently (1), the phenomenon has already been established using radioiodine to diagnose and treat different thyroid diseases. RPT has in the past decade also been described by terms such as theranostics, molecular radiotherapy, molecular-targeted radiopharmaceutical therapy, and targeted radiopharmaceutical therapy. However, the Society of Nuclear Medicine Molecular Imaging therapy task force survey suggested that the term RPT be used as a standard nomenclature to describe therapy using radiopharmaceuticals (1). This follows the need to distinguish between systemic radiation from external-beam radiation therapy (EBRT) and RPT.

Although the two therapy modalities have some similarities, there are also distinct differences between them. RPT is a form of targeted therapy as the radionuclide is directed towards its target by transport of the pharmaceutical, which exhibits specific binding to the target tissue. The phenomenon is characterised biochemically and physically by a metabolic process within the time interval of the decaying radionuclide. Patient bio-kinetic data, such as tissue cell uptake and release, non-homogeneous expression by the target, and metabolism, play an important role in determining the absorbed radiation dose. RPT employs a low and continuous decreasing radiation dose rate which requires a radiobiological approach (2,3). This results in a more complex temporal and spatial radiation dose distribution compared to EBRT. EBRT employs fractionated high dose rates aiming to cause lethal damage to the cancer cells coupled with non-treatment intervals for repair (2). Another distinct difference between the two modalities, shown in Figure 1-1, is that EBRT delivers the same absorbed dose per cell, regardless of the number of cells involved in the irradiation. In contrast, the absorbed dose per cell by internal emissions from surrounding cells in RPT depends on the particle emission ranges and the number of targeted cells (4).

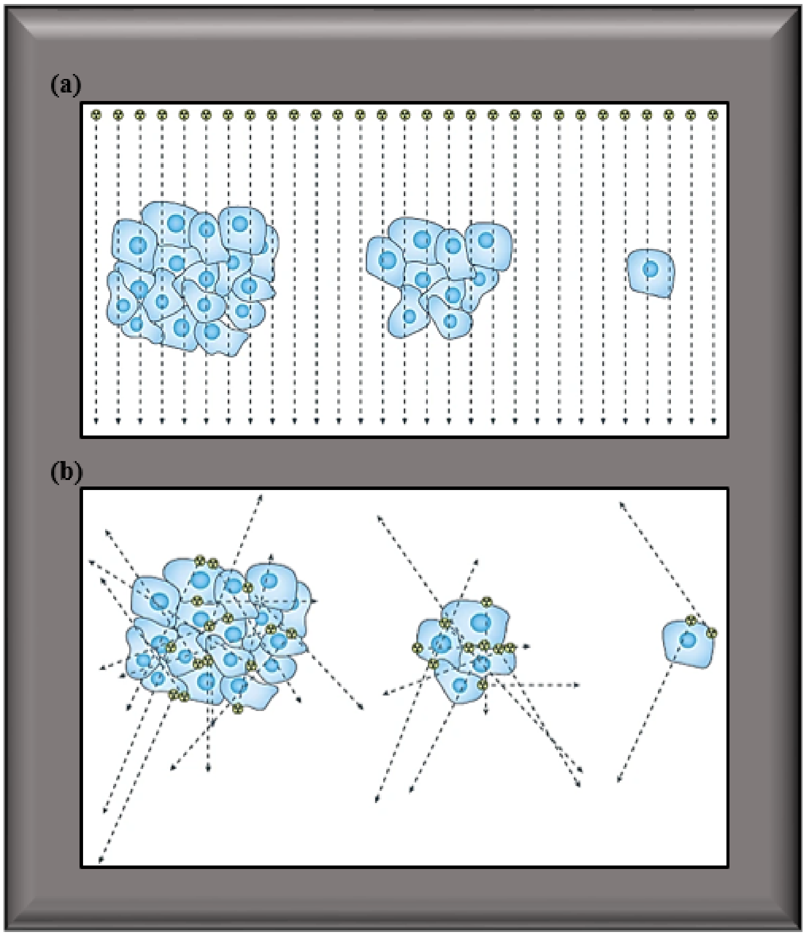

Figure 1-1: *An example illustrating tumour cell irradiation using **(a)** external beam radiation therapy versus **(b)** radiopharmaceutical therapy* (4).

The goal of RPT is to selectively deliver the highest possible absorbed dose to the tumours in a manner that will cause minimal toxicity to the organs at risk (OAR), which shall also be referred to as critical organs. This is achieved by ensuring that the absorbed doses to OAR are kept below their tolerance levels to minimize side effects (5). The success of this type of treatment relies on the selective concentration and prolonged retention of the radiopharmaceutical in the tumour cells and less so in the normal tissue. The ideal treatment scenario is when the tumour entirely absorbs the radiation dose, resulting in destructive tissue effects, which is not the case in clinical practice. The destruction of the cells is described by the absorbed radiation dose, which is the amount of energy transferred to the target by the radiopharmaceutical per unit mass. The dosimetry defines this energy deposition by the patient's body as the driving force expanding the NM field. Dosimetry in RPT is undergoing significant development attributed to the introduction of novel radiopharmaceuticals and new positron emission tomography (PET) agents. Dosimetry can balance the efficacy of delivering the maximum dose to the tumourous cells with minimal normal tissue toxicity.

Dosimetry-based patient-specific treatment can improve patient outcomes and survival (6). Added advantages include: (i) Establishing effective minimum and maximum absorbed dose tolerance levels. (ii) Obtaining dose-response between tumours and normal tissue based on pre-therapy dosimetry. (iii) Comparing dose-response between different radiopharmaceuticals and patients to provide RPT radiobiology information. Patient individualized therapy is standard in treatment planning with EBRT, aiming to achieve better tumour control and less normal tissue toxicity (2). The same principle should be adopted with RPT. Patient-specific dosimetry for RPT offers the potential to avoid under-/over dosing from fixed-dose regimes.

Generally, therapeutic radionuclides emit short-range charged particles such as beta and alpha particles or Auger electrons and have longer physical half-lives than diagnostic radionuclides. Alpha particles and Auger electrons have higher linear energy transfers and deposit their energy over shorter distances to induce more cell death with limited deoxyribonucleic acid (DNA) damage repair (7). Auger electrons and alpha particles are ideal for treating smaller tumours (8,9). Beta particles are also used to treat small tumours, and their effectiveness depends on their energy and range in tissue. The range of the emitted beta particle should be compatible with the volume of the tumour and, at the same time, be short enough to deliver a minimal dose to the surrounding normal tissue (10). Many radionuclides used in RPT emit short-range charged particles (non-penetrating radiation) and gamma rays (penetrating radiation), which enables therapy and subsequent imaging to allow for patient-specific dosimetry. A longer physical half-life is preferred for prolonged retention and thus cumulative tumour irradiation and a high penetrating to non-penetrating radiation ratio. The physical half-life of the radionuclide must be compatible with the biological half-life of the radiopharmaceutical for effective treatment.

1.1.1.1 Radiopharmaceutical Treatment using ^{177}Lu

Numerous radionuclides exhibit the above-mentioned therapeutic decay characteristics and are well described (7). ^{131}I continues to play a major role as a therapeutic radionuclide, involving ^{131}I-NaI for adult thyroid ablation (11). RPT has evolved in the last decade from the introduction of radiolabelled anti-bodies and molecules such as somatostatin analogues and ligands. There has been widespread use of ^{177}Lu-PSMA for the treatment of castrate-resistant prostate cancer (12) as well as $^{223}RaCl_2$ (13). ^{90}Y microspheres have been used for the treatment of primary or metastatic liver cancer. Due to the high biological effectiveness of alpha emitters, there has been growing interest in RPT employing ^{227}Th, ^{213}Bi, and ^{225}Ac (14). Recent RPT applications include routinely used ^{177}Lu-DOTATATE or, less common, ^{90}Y-DOTATOC for the treatment of late-stage neuroendocrine tumours (NETs) with widespread metastases (15–17). Due to its favourable decay characteristics and amenable chemistry to labelling with peptides, ^{177}Lu exhibits ideal properties and is widely adopted for this treatment.

i. Decay Characteristics of ^{177}Lu

^{177}Lu is a radionuclide of the 71st element in the periodic table, and its main decay pathway is shown in Figure 1-2. It is unstable and decays by beta emission to the stable ground state of ^{177}Hf with a physical half-life of 6.7 days and three excited levels above the ground state. The maximum energy (E_{max}) released by beta emission is 498.3 keV (79.3%) (18). The beta particles with E_{max} of 177.0 keV are encountered in 12.0% of the events and yield an excited state of ^{177}Hf at 321.3 keV above the ground state. Furthermore, beta particles with a E_{max} of 385.4 keV (9.1%) are encountered, leading to an excited state of ^{177}Hf at 249.7 keV above the ground state. Small amounts of x-rays and Auger electrons are produced during the decay process. ^{177}Hf de-excites to the ground state through low-energy gamma rays, the most abundant being energies 112.9 keV (6.2%) and 208.4 keV (10.4%).

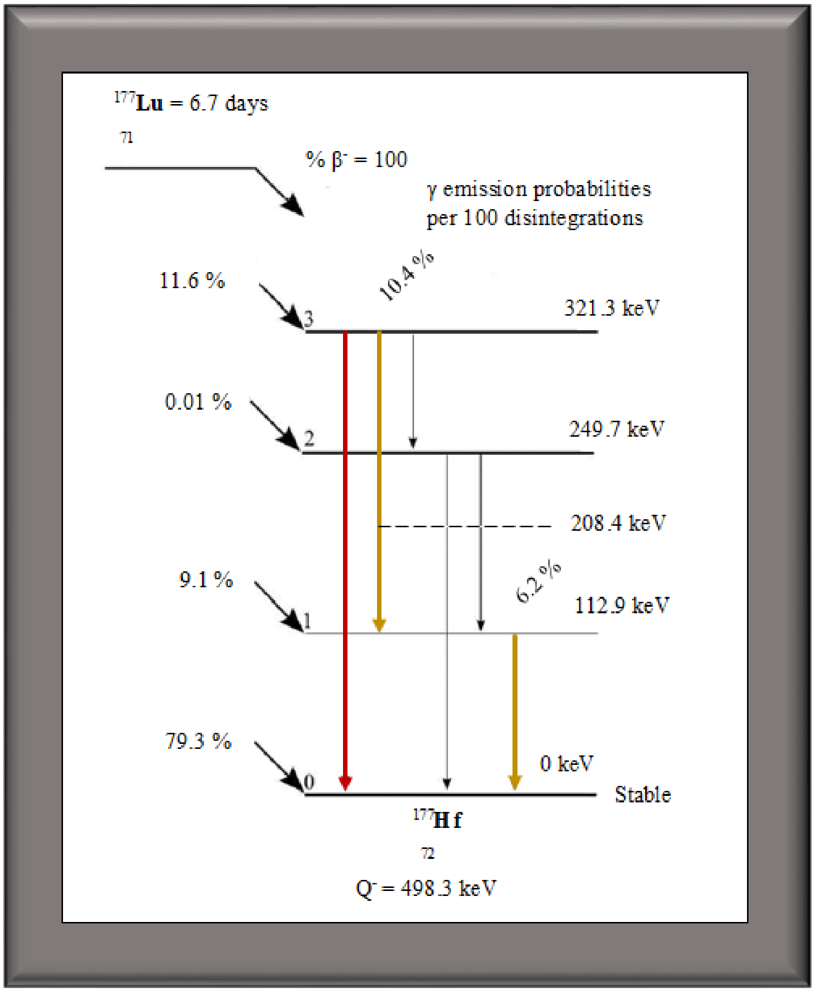

Figure 1-2: *A simplified beta decay scheme for* ^{177}*Lu* (18).

The two gamma rays mentioned above have been used successfully for imaging purposes (19) to enable dosimetry (20). This is because they are penetrative enough to be detected by the gamma camera. The beta particles (E_{max} of 498.3 keV) have a short mean soft tissue penetration depth of 0.7 mm (21), and are used successfully in RPT (22). The short-range of the beta particles makes them therapeutically effective in delivering energies high enough to result in homogeneous absorbed doses at a cellular level to respective small volumes while sparing the healthy surrounding tissue (23). Characteristic x-rays are obtained at energies of 54.6 keV (1.6%) and 55.8 keV (2.8%) (18). The bremsstrahlung yield, due to the interaction of the beta particles with tissue, has been observed to be very low (> 11%), with most (~ 85%) of the photons having energies below 50 keV (24).

ii. Production of ^{177}Lu

^{177}Lu is produced in a nuclear reactor by the (n, γ) reaction. Two distinct methods for ^{177}Lu production exists, namely, the direct and indirect methods. Both the direct and indirect reactor production routes can be followed to produce ^{177}Lu.

Direct method (carrier added – c.a): The direct pathway entails thermal neutron irradiation of enriched ^{176}Lu (Lu_2O_3) using the following reaction,

$[^{176}\text{Lu (n, }\gamma) \rightarrow {}^{177}\text{Lu}]$

This method of production may contain contaminants of lutetium (^{176}Lu, ^{177m}Lu) in the final product. The production of ^{177}Lu using the above reaction may be with a natural or an enriched lutetium oxide (Lu_2O_3) target. In both cases, the radionuclide purity has been reported to be 100%. The drawback is that 0.1% of ^{177m}Lu which has a half-life of 160.5 days, and beta E_{max} of 200 keV may be produced (10). This makes the waste management of the carrier added ^{177}Lu cumbersome. IDB (IsotopenDienst Benelux-Isotope Services Belgium, Netherlands, Luxembourg, LuMark®), is a leading manufacturer and distributor of ^{177}Lu c.a, to many countries, including South Africa. Their ^{177}Lu is produced directly from ^{176}Lu irradiated target material and distributed under the brand name LuMark® ^{177}Lu chloride with vial volumes ranging from 0.1 to 5mL and activity ranges of 8 GBq to 400 GBq.

Indirect method (no-carrier added – n.c.a): The indirect pathway involves the neutron irradiation of ^{176}Yb (Yb_2O_3) by the reaction,

$[^{176}\text{Yb (n, }\gamma)\ {}^{177}\text{Yb} \rightarrow {}^{177}\text{Lu}]$

This method produces the short-lived isotope ^{177}Yb, with a physical half-life of 1.9 h, which decays to ^{177}Lu. Chemical separation of the ^{177}Lu daughter product from the Yb target is required and easily achieved. The advantages of this method (n.c.a) in comparison to the direct method (c.a) are summarised in Table 1-1 (22). There is a clinical requirement of specific activity of 37 MBq to 74 MBq ^{177}Lu per µg, and only a few high neutron-flux reactors can produce up to 0.74 GBq/ug (25). The company itG, (itG, Isotope Technologies Garching GmbH, Germany) is a distributor to South Africa and affiliated with the Australian Nuclear Science and Technology Organisation (ANSTO, Australia) and NTP Radioisotopes SOC Ltd-South Africa. This company produces the itG ^{177}Lu n.c.a using the indirect method of highly enriched ^{176}Yb, in the FRM-2 reactor, with high radionuclide purity and specific activity (3800 GBq/mg). In collaboration with itG, NTP has commenced production of ^{177}Lu-n.c.a supplying activity dosages of up to 7.4 GBq to the South African market and other African countries.

Table 1-1: *Comparison of carrier added and non-carrier added ^{177}Lu for clinical applications.*

^{177}Lu n.c.a	**^{177}Lu c.a**
No long-lived ^{177m}Lu impurity	Production of ^{177m}Lu impurity with long-lived half-life (160.5 days)
High radiolabelling yield	Lower radiolabelling yield
Shorter shelf half-life	Longer shelf half-life
High specific activity (3,900 GBq/mg) at expiry date	Lower specific activity (500 GBq/mg) at calibration date
Lower molar ratio between ^{177}Lu and DOTATATE (1:4)	Higher molar ratio between ^{177}Lu and DOTATATE (1:10)
Specific activity does not decrease rapidly with time	Specific activity decreases more rapidly with time

It is essential to ascertain the binding efficiency of the ^{177}Lu metal with the tracers such as dodecane tetraacetic acid (DOTA) molecules to ensure a stable complex. Binding efficiency of 98% is required where the mass of the peptide should not exceed 250 µg (22). Quality assurance check of impurities such as metal ions that will lower the specific activity of the radiopeptide and hinder labelling should also be checked.

1.1.1.2 Treatment of Neuroendocrine Tumours with ^{177}Lu-DOTATATE

RPT of NETs commenced in the early 1990s using ^{111}In-octreotide as a therapeutic agent, through its emission of Auger and conversion electrons following the peptide receptor complex (22). ^{111}In-pentetreotide has been abandoned for more efficient beta-emitting radionuclides such as ^{90}Y and ^{177}Lu. ^{177}Lu has received much attention since its first diagnostic and therapeutic demonstrations in bone imaging and arthritis treatment in rabbits (26,27). It has been coupled to a few somatostatin analogues with DOTA as the binding molecule (chelator). Some of the DOTA peptide compounds

^{177}Lu has been coupled with inlcude: [DOTA0,Tyr3]-octreotide (DOTATOC), [DOTA0,Tyr3]-octreotate (DOTATATE) and [DOTA0-1-Nal3]octreotide (DOTANOC) (28–32). ^{177}Lu-DOTATATE treatment of patients with metastatic NETs has compared favourably with its alternatives, evidenced by well-known clinical trials like the NETTER trial (33). It has become the preferred peptide RPT choice due to its higher tumour uptake (16), longer tumour residence time (34), low whole-body retention with improved overall survival, quality of life (35,36) and, markedly longer progression-free survival (33). There is an increase in overall survival of up to several years for patients treated with ^{177}Lu-DOTATATE from the time of diagnosis (35). ^{177}Lu-DOTATATE RPT is not a cure for late-stage NETs, however, it improves the quality of life with limited side effects.

^{177}Lu-DOTATATE has been found favourable to ^{90}Y-DOTANOC for RPT of patients with NETs due to the difference in the decay properties between ^{90}Y and ^{177}Lu (16,17). These include the lower energy (498.3 keV) of the ^{177}Lu beta particle in comparison to that of ^{90}Y (2.2 MeV), which results in lower kidney and bone marrow absorbed doses (37). The difference in the half-life of ^{177}Lu (6.7 days) and ^{90}Y (2.7 days) implies a difference in radiobiological tumour response and tolerability between the two radionuclides, where better tumour response was observed with ^{177}Lu (15). ^{177}Lu has been demonstrated in animal models to provide better irradiation of small tumours than ^{90}Y, which has a longer beta range (38), making ^{177}Lu advantageous for the treatment of NETs with widespread metastases. Treatment of patients with NETs using ^{177}Lu-DOTATATE has also been found to be more effective when combined with radio sensitising chemotherapy agents (39) as well as EBRT (40).

Due to the high cost of RPT with^{177}Lu-DOTATATE, ^{131}I-MIBG (metaiodobenzylguanidine) continues to play a major role in the treatment of NETs in developing countries such as South Africa, as is still the case in our clinic. ^{131}I-MIBG is used in the treatment of NETs with chromaffin cell origin after prior MIBG imaging has shown sufficient tumour uptake of the tracer. ^{131}I-MIBG imaging has shown to have high specificity and sensitivity in identifying tumours such as: neuroblastoma, phaeochromocytoma and paraganglioma, both localized and metastatic for ^{131}I-MIBG therapy. The physical half-life of ^{131}I (8.0 days) is comparable to that of ^{177}Lu (6.7 days). However, ^{131}I emits gamma rays with high energies (722.9 keV at 1.7%, 636.9 keV at 7.1% and 364.5 keV at 83.0%), which can lead to septal penetration and poorer image quality, in comparison to the lower gamma energies encountered with ^{177}Lu (208.4 keV at 10.4% and 112.9 keV at 6.2%). The low gamma yield from ^{177}Lu compared to that of ^{131}I results in rather small count losses due to gamma camera dead-time even for high therapeutic activities. The high gamma yield of ^{131}I also results in higher radiation exposures to personnel handling the patients and higher cross-doses from source organs. In addition, the volatility of ^{131}I complicates the handling and disposal of radioactive waste. A study by de Araújo et al. (41) compared ^{177}Lu-DOTATATE and ^{131}I-DOTATATE, showing a higher renal and lower tumour uptake for ^{131}I-DOTATATE, which reduced the therapeutic potential of ^{131}I in comparison to ^{177}Lu. The study also demonstrated faster blood clearance and higher binding affinity for ^{177}Lu-DOTATATE compared to ^{131}I-DOTATATE. These are the drawbacks for the therapeutic use of ^{131}I, with DOTATATE as the binding molecule, and the preferred clinical use of ^{177}Lu. Furthermore, ^{177}Lu has been deemed the most viable radionuclide for therapy of small-sized non-thyroid tumours (10). Due to the widespread clinical use of ^{177}Lu-DOTATATE, it may well be the RPT first choice in patients with metastasized or inoperable NETs (35). ^{177}Lu-DOTATATE has become an important treatment option in the subgroup of patients who have grade III NETs with high somatostatin receptor (SSTR) type-2 expression (cellular proteins of subtype 2-SSTR2) (42).

i. Patient Selection for ^{177}Lu-DOTATATE Treatment

The primary treatment for patients with NETs is surgical removal before regional or distant metastases. However, the treatment options for patients with advanced NETs which are inoperable and have metastasized are limited. The treatment regime for these patients may include surgery, chemotherapy, immunotherapy, localized ablation therapy, EBRT and peptide RPT, and these treatment modalities are not mutually interchangeable (43). Well-differentiated NETs are heterogeneous and characterized by overexpression of somatostatin receptors, most expressing the SSTR type-2 in high amounts. In most cases, the patients remain asymptomatic until there is a significant tumour burden and most probably metastases to the liver (44). These patients present with advanced disease resulting in limited treatment options. For this reason, RPT has increasingly been utilised to treat patients with metastasized tumours of well-differentiated neuroendocrine origin for the past decade because of their overexpression of SSTRs (45).

According to the world health organisation classification, the selection criteria for treating patients with NETs using peptide RPT are adult patients with inoperable tumours with metastases of moderate or well-differentiated NETs of Grade 1 or 2 (46). Late-stage NETs have overexpression of 2-SSTR2 on their cell surface (47). These receptors offer the advantage of being targeted on a molecular level using peptides. The somatostatin analogue peptide, DOTATATE, is bound to ^{177}Lu, and used to target the tumour cells, resulting in the precision bombardment, with double- and single-stranded DNA breaks of the cancer cells. The expression of 2-SSTR2 in NETs is the reason for the wide use of ^{177}Lu-DOTATATE to treat these tumours (15). Part of the selection criteria to treat patients with late-stage NETs using ^{177}Lu-DOTATATE includes the high 2-SSTR2 expression, the existence of which should be proven by histopathology.

On the other hand, diagnostic scans involving ^{111}In-DTPA (diethylene-triamine-pentaacetate)-octreotide and ^{99m}Tc octreotide for single-photon emission computed tomography/computed tomography (SPECT/CT) imaging or ^{68}Ga-DOTATATE for positron emission tomography/computed tomography (PET/CT) imaging are used to verify whether the tumour expresses sufficient 2-SSTR2. It is to be noted that this type of treatment is not used in poorly differentiated tumours which are positive for a PET/CT scan with ^{18}F-FDG uptake but negative for ^{68}Ga-DOTATATE (22,35). The ^{68}Ga-DOTATATE PET/CT has superseded the ^{111}In-DTPA-octreotide SPECT/CT scan due to higher sensitivity, better spatial resolution, and increased accuracy to ensure the presence of 2-SSTR2 expression (15). The diagnostic ^{68}Ga-DOTATATE PET/CT scan is reported to improve patient management (48–50). Although PET/CT has been proven advantageous to SPECT/CT, it is costly and less readily available in many clinics, including our own. When available, PET/CT imaging is used as a diagnostic and staging tool, while SPECT/CT has gained popularity to determine the use of additional ^{177}Lu-DOTATATE cycles (47). This has made the collaboration of two modalities important for the treatment planning of ^{177}Lu-DOTATATE.

1.1.1.3 Theranostics Approach for Radiopharmaceutical Treatment

The concept of theranostics has long been used with the application of ^{131}I for therapy of well-differentiated thyroid cancer (51). However, due to the introduction of new radiopharmaceutical agents with RPT, the term “theranostics” has been heightened for the past decade (52). Theranostics employs the rationale that an agent (e.g. a peptide) is labelled with a diagnostic radionuclide to test if the molecular target intended for the treatment, is available. Since the diagnostic and therapeutic radionuclide will be labelled to the same radiopharmaceutical, it is assumed they will have the same bio-characteristics (53). The radiolabelled peptide is designed to target receptors overexpressed in tumours with high affinity and specificity (22). The approach facilitates RPT planning by diagnostically testing patients for the presence of the molecular target for which the radiopeptide or radiopharmaceutical is intended. This phenomenon is as described above using the ^{68}Ga-DOTATATE PET/CT scan. The objective of the treatment, as with any regime, is first to do no harm and, and thereafter do something good. The diagnostic selection is based on molecular disease features, prediction of critical organ involvement to estimate the likelihood of patient-specific adverse effects, and disease response monitoring (47). The effectiveness of the treatment is assessed using post-treatment ^{177}Lu-DOTATATE scans. The theranostics approach promises improved patient-specific treatment planning for RPT.

The theranostics dosimetry-based patient-specific treatment planning may be divided into direct or indirect methods. Indirect RPT planning examples include ^{123}I SPECT/CT (or planar) imaging and ^{124}I PET/CT imaging to predict treatment with ^{131}I, ^{86}Y PET/CT imaging to predict ^{90}Y treatment, ^{111}In SPECT/CT (or planar) imaging to predict ^{90}Y treatment and ^{68}Ga PET/CT imaging to predict ^{177}Lu treatment. In cases where the indirect method is not only used to test for the presence of a molecular target but also used for dosimetry purposes, it is crucial to consider that the physical half-lives of the therapeutic and diagnostic agents are different and may result in errors when predicting bio-kinetic models (54).

Direct methods, which include radionuclides such as ^{131}I and ^{177}Lu, are, for example, when the radiopharmaceutical emits both non-penetrating (e.g. alpha or beta) and penetrating (e.g. gamma) radiation and thus may be used for treatment and planning for the administration of additional cycles. An example of the theranostic direct approach is shown in Figure 1-3 using ^{177}Lu.

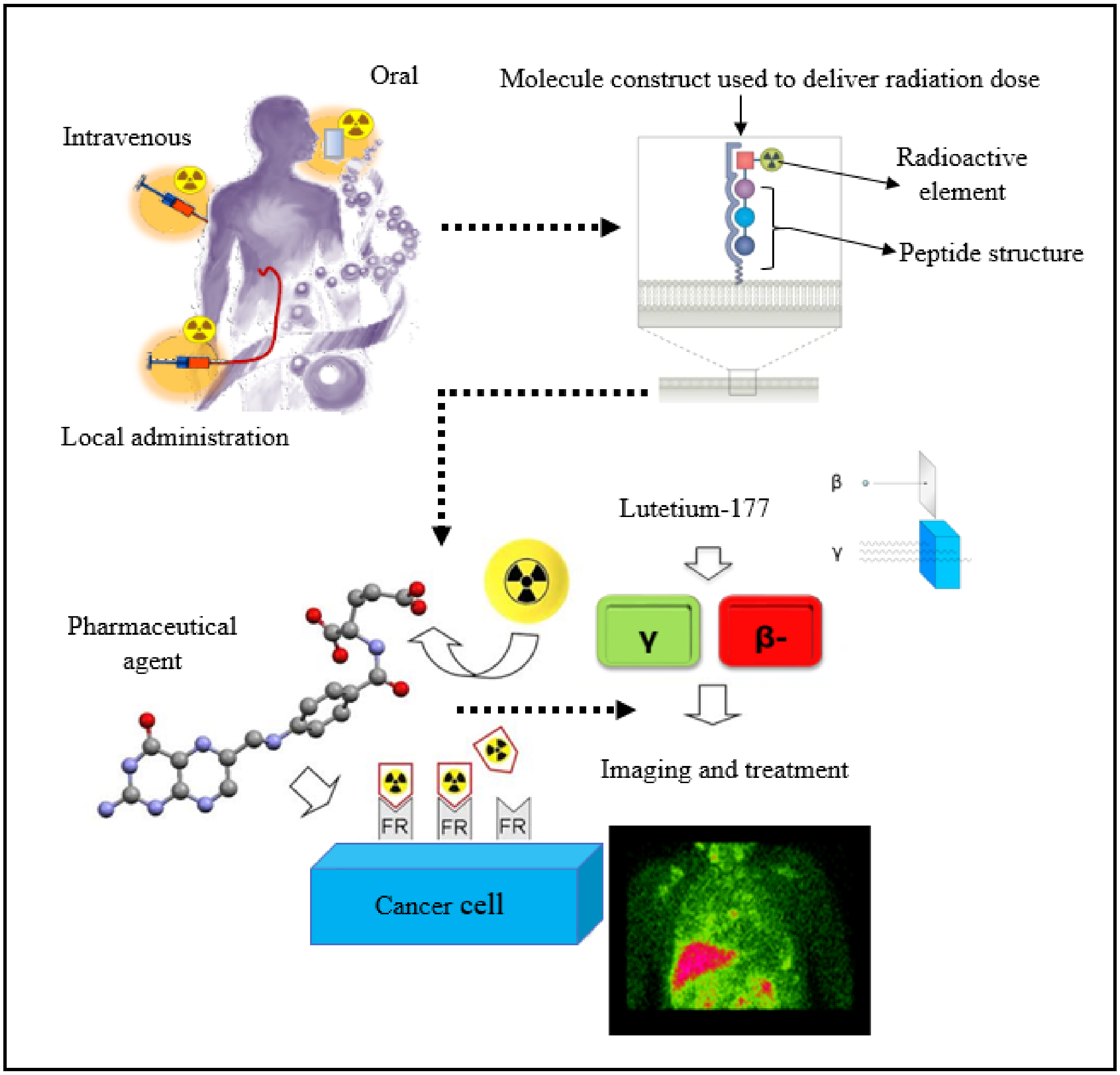

Figure 1-3: *Illustration of the theranostic direct approach using* ^{177}*Lu* (4).

The prediction of whether to administer additional treatment cycles using these radionuclides is determined from quantitative image information. Image-based RPT theranostics for patients with NETs entails the indirect use of ^{68}Ga-DOTATATE to diagnostically select patients positive for 2-SSTR2 and allegeable for ^{177}Lu-DOTATATE RPT. Following the initial ^{177}Lu-DOTATATE therapy, the direct approach predicts adverse effects and the feasibility of additional dose fractions using image-based dosimetry.

i. *Generic Dosing with* ^{177}*Lu-DOTATATE*

In general, the treatment regime for patients with NETs treated with ^{177}Lu-DOTATATE is 5.55 – 7.40 GBq/cycle with three to five cycles in intervals of 6 – 12 weeks (43). The widely adopted standard dose of 7.4 GBq requires patient isolation following the necessary radiation protection guidelines in a hospital ward. Patients may be confined for 1 – 3 days (15,55). The 7.4 GBq of ^{177}Lu labelled with peptides or antibodies has been reported to have an average radiation exposure rate of 4 – 11 μSv/h measured at a distance of 1m from the patient 24 hours post-administration (56) (LuMark® ^{177}Lu chloride product characteristics). This exposure rate was indicated to result in a dose (0.6 mSv) below the general public's tolerance (1mSv/year) for a person in the patient's vicinity, having continued exposure at 2m, assuming no excretion by the patient after discharge. Olmstead et al. (57) reported dose rates of 20.4, 14.0, and 6.6 μSv/hr 30 min, 4 and 20 hours post-administration, respectively. The cumulated dose from these dose rates was largely below the threshold of 0.03 mSv with a maximum value of 0.18 mSv. The reported exposure rates 1-day post-administration were below the tolerance of 25 μSv/h recommended for discharging patients (58) treated for NETs with ^{177}Lu-based RPT (59).

Treatment outcomes of patients administered with 7.4 GBq of ^{177}Lu vary, and the inconsistency in patient response has been attributed to the relatively low activity "one dose fits all" approach (60) (with "dose" referring to administered activity). The radiopeptide uptake in tumours and normal tissue varies vastly amongst patients, and in some cases, may result in under-treatment. From this, it follows that individualized patient treatment could improve RPT and should be attempted. RPT is on a crossroad between the fixed "one dose fits all" regime and patient-individualized treatment. For patient-individualized treatment to be optimally viable, factors such as dosimetry methodologies as well as tumour response and follow-up would have to be harmonised. Evidence-based trials would have to prove that patient-individualized RPT with ^{177}Lu-DOTATATE is better than the standard administration of 7.4 GBq over four cycles as indicated in the NETTER trial (33). Furthermore, randomized clinical trials would have to identify reliable and robust organ threshold tolerance values for toxicity to the dose-limiting organs applicable to RPT.

ii. *Dose Limiting Critical Organs*

The absorbed dose to the critical organs such as the kidney and bone marrow governs the administration of subsequent ^{177}Lu-DOTATATE cycles (61). If the additional cycles are predicted to exceed the tolerance levels of these critical organs, then subsequent cycles may not be administered. The kidney and bone marrow are the dose-limiting organs for RPT of patients with NETs using ^{177}Lu-DOTATATE. Acute haematological toxicity is not uncommon, and impoverished bone marrow must be considered with the potential use of additional cycles. The permissible maximum absorbed dose to the bone marrow is 2 Gy (35). Some authors have shown that bone marrow absorbed doses range from 0.02 – 0.08 mGy/MBq in patient studies (16,26,32,62). The calculated absorbed doses of 0.03 mGy/MBq may result in cumulative absorbed dose ranges of 0.5-1.3 Gy (15). Although bone marrow involvement is considered, it is not the main dose-limiting organ (63).

The kidneys are the most critical OAR for ^{177}Lu-DOTATATE RPT. This is owing to the proximal tubular reabsorption and retention of the radiopeptide in the interstitium and subsequently renal irradiation. Renal toxicity has been associated with RPT for several isotopes (53,64–70). It is important to follow up patient kidney doses and function as kidneys are late responding tissue, and the potential damage from deterministic effects may be seen after one or several years post-treatment. This finding has led to a kidney dosimetry research cascade in ^{177}Lu-DOTATATE RPT (71–74).

The maximum tolerance threshold of 23 Gy has been widely adopted for kidney doses obtained from RPT (75). It is based on the fractionated EBRT tolerance, which results in a 5% probability of developing late kidney damage in 5 years (76). Garkavij et al. (61) argued that the recommendation could be questioned because the absorbed dose rate between the two modalities differs significantly. For this reason, the application of dose-response data applied to RPT has been reviewed (77–79). In a study by Valkema et al. (80), the authors increased the tolerance to 27 Gy with the rationale that the dose rate given by EBRT is substantially higher than RPT. However, the maximum kidney dose upper limit permissible with RPT is still widely adopted as 23 Gy. The upper limit was reported to be reached at a cumulative administered activity of 33.3 GBq or more, established from kidney dosimetry of 177 patients (35). This indicates that the fixed maximal dose fraction may result in under-treatment. Kidney doses of 0.9 mGy/MBq have been reported for ^{177}Lu-DOTATATE treatment, resulting in absorbed doses of 6.7 Gy from the 7.4 GBq standard activity administration (32). The generic administration of 7.4 GBq has also been reported by Sandström et al. (81) to result in absorbed kidney doses of 5±2 Gy in a cohort of 24 patients.

Consistent with these findings were kidney doses reported by Guerriero et al. (82), which were 6±2 Gy for their cohort of 25 patients. Dose to the kidney may be reduced to a certain extent by positively charged amino acid infusion, which reduces the high kidney retention and thus limits the proximal re-absorption (83). Renal protection with amino acid infusion can result in significant kidney absorbed dose reductions of 9% to 65% (15). Patient factors such as diabetes and hypertension increase the risk of kidney disease in patients treated with peptide RPT, and thus the kidney dose may have to be reduced for these patients (80,84).

Clinical trials have been conducted whereby additional cycles are administered until the calculated biological effective dose (BED) of the kidneys has reached 27 Gy or 40 Gy, and the choice between the two levels is determined by the above-mentioned patient risk factors (85). BED models the concept that a relationship can be determined between kidney dose and toxicity, taking into consideration the administration protocols (dose rate, fractionation schedule, dose per fraction, and repair times), clearance kinetics, adjuvant therapy regimes, exposure to drugs, and critical organ involvement (86). Kidney dosimetry should be performed for high-risk patients prior to peptide RPT. It should be noted that BED dose limits are independent of the radionuclide used but rather depends on risk factors for renal radiation damage. Critical organs such as the liver and, to a lesser extent, the spleen are large, and therefore radioactivity from ^{177}Lu-DOTATATE is fairly uniformly distributed and is less of a concern than the kidney (86).

The assumption of a uniform activity distribution in the kidney has become the tradition in NM dosimetry that models kidney doses and only permits estimation of mean absorbed dose (87). This results in a misrepresentation of local, regional doses to specific kidney subunits such as the cortex, medulla, and papillae. There is heterogeneity in the absorbed dose to the kidney obtained with peptide RPT with an increased initial concentration in the renal cortex (80,86). PET images with ^{86}Y-Dota-Tyr-octreotide and SPECT images with ^{111}In-DTPA-octreotide and ^{177}Lu-DOTATATE have shown this phenomenon (88). The increased uptake in the cortex as seen with the PET and SPECT images was confirmed with ex-vivo radiography to a 1mm scale resolution portraying the distribution in detail. Even so, the ex-vivo radiography studies have confirmed that the gamma cameras' limited spatial resolution cannot differentiate between kidney sub-regions. Different methods exist for calculating kidney absorbed doses, and there is no consensus on which is the best. Kidney doses will vary depending on the method used for quantification and absorbed dose calculations (61). The kidneys may be the dose-limiting organs for ^{177}Lu-DOTATATE, however, the relation between the tumour-absorbed dose and tumour reduction is also important (89). Due to the wide variation between the tumour and kidney responses following peptide RPT (16,81), it is good practice to extend dosimetry-based individualised planning to the critical organs and tumours for a comprehensive understanding of the effects from peptide RPT.

1.1.1.4 Summary

The above discussion focused on treatment planning in RPT, RPT with ^{177}Lu, and its applications for ^{177}Lu-DOTATATE in patients with late-stage NETs. The kidneys are the critical organs, and there is a considerable variation between the kidney doses and tumour response amongst patients. Dosimetry-based treatment planning aids in correctly selecting eligible patients for ^{177}Lu-DOTATATE RPT and estimating absorbed dose to critical organs and tumour control. The “one dose fits all” may not be optimal and could result in under-/overestimating critical organ tolerances depending on the patient radiation risk factors. The lack of threshold values has made individualised dosing for peptide RPT labelled as a “quest to the holy gray” using maximum “tolerated-holy gray” values as a guide for dosimetry (2). Tremendous effort has been made in RPT dosimetry, yet the threshold ambiguity gives rise to questions such as “to what extent is dosimetry needed for RPT applications” (90)?

However, it remains up to the NM community to optimize and tailor patient treatment in this exciting era of novel RPT agents with the potential for precision irradiation. Paving the way for this effort would commence at harmonising the widely varying dosimetry methods. This means there would have to be an agreement on accepted standard methods and their validation for most centres. Furthermore, the documentation for dosimetry reporting also plays a vital role (91). Dosimetry is a physics-based endeavour that involves image quantification of activity distributions and absorbed dose modelling. The uniqueness of RPT, compared to other treatment modalities, lies in the fact that the radiopharmaceutical is distributed both temporally and spatially in the body. Thus fundamentally, dosimetry needs to determine the radiopharmaceutical bio-distribution and estimate the absorbed dose to the organs of interest from this distribution. The methods used to acquire the bio-distribution data involve many steps, and assumptions vary widely for different protocols, radiopharmaceuticals, and centres. The wide variation in the absorbed dose methodologies and the estimated “tolerated holy-gray” are some of the reasons for the clinicians' relatively poor acceptance of dosimetry. Understanding the value and limitation of each step in the clinical dosimetry chain allows for a starting point towards standardising the dosimetric methodologies.

1.1.2 Image-Based Activity Quantification for Dosimetry

Systemic administrations of radiopeptides such as ^{177}Lu-DOTATATE in patients are conventionally by intravenous infusion. The radiopeptide then distributes in a spatially variant manner throughout the body, based on normal physiological mechanisms and physical properties. Physiological mechanisms govern the temporal distribution pertaining to the uptake and retention, its biochemical and decay properties are unique for each patient, giving rise to patient-specific bio-kinetic data. As mentioned above, the decay process of ^{177}Lu includes the emission of beta particles and gamma radiation. Depending on their range, the beta particles deposit their energy near their point of decay while the gamma rays are penetrative and travel longer distances before they interact and allow for post-administration imaging. The spatial activity distribution after administration is determined from the radiopharmaceutical images (image activity quantification). The quantities that need to be determined for image-based dosimetry include:

- The number of decays in the organs of interest for the different times post-administration.
- The temporal pattern with which the decay particles impart their energy from the time-activity data.
- The calculation of the energy absorbed in the respective mass or volume of the organ or tissue of interest.

The image-based quantified activity is used directly to perform the absorbed dose calculations to the organs that have received radiation exposure. This makes image-based activity quantification a critical variable when determining absorbed dose calculations as it affects the dosimetry accuracy. It becomes evident from the quantities mentioned above that the absorbed dose calculations require a series of steps that form part of a chain shown in Figure 1-4. The chain commences with (i) acquiring images using a specific image acquisition protocol, and in the case of (ii) SPECT/CT acquisitions, image reconstruction and activity quantification, (iii) analysis of the time-activity curves (TACs) and integration, (iv) absorbed dose calculations, and (v) presenting the dosimetry results using a dosimetry software program. Each step contributes to the accuracy with which dosimetry is attained. It all begins with how faithfully the images represent the activity distribution and how accurately the activity is quantified.

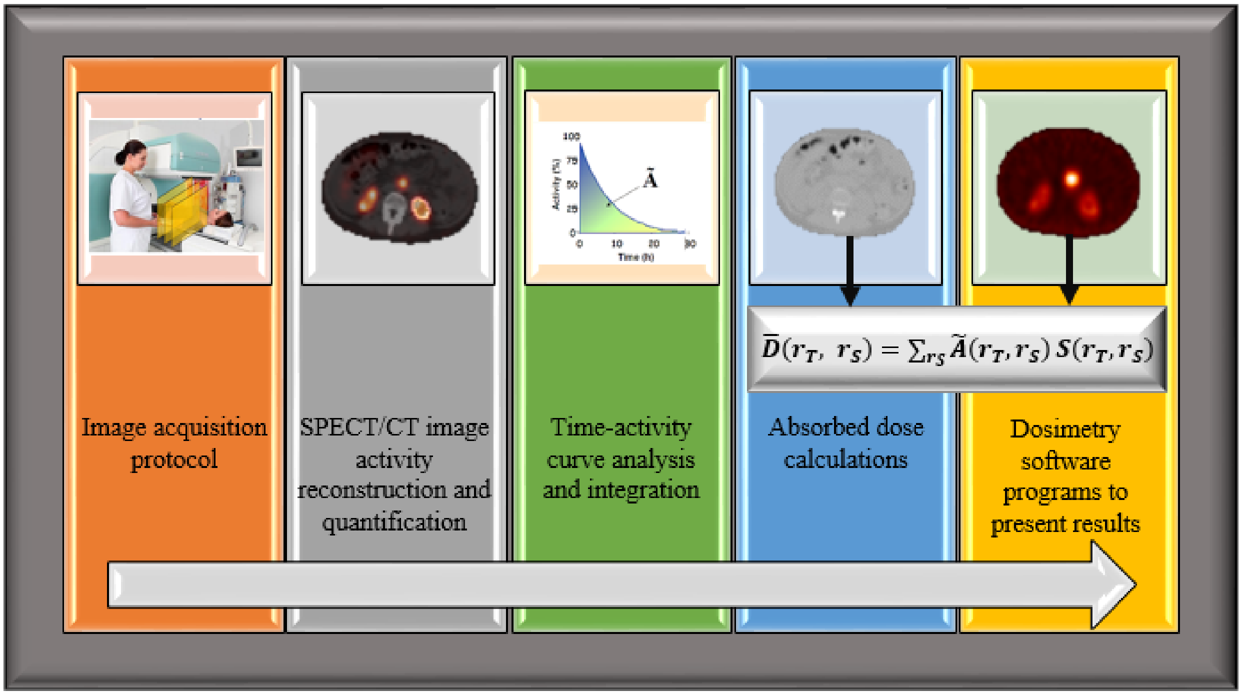

Figure 1-4: *Schematic illustrating the basic steps used in the image-based dosimetry workflow.*

1.1.2.1 Image Acquisition Protocol

The imaging and quantification process from which absorbed dose estimations are calculated is not perfect, and for this reason, it has been the subject of investigation for many years (92–99). The challenge is that patient dosimetry relies upon gamma camera images that have been compromised by inaccuracies involved in the imaging process and protocol followed. The accuracy with which activity quantification and image analysis is performed has been an ongoing improvement for many years (81,100–103).

Figure 1-5*:* *Siemens Symbia T-series hybrid SPECT/CT dual-head gamma camera* (104)*.*

An example of a clinical gamma camera is shown in Figure 1-5, which comprises of a NaI(Tl) crystal fitted with a selection of parallel-hole collimators chosen depending on the protocol used. The selection of the collimators is between low, medium, high-energy collimators depending on the energy of the imaged gamma ray as well as the trade-off between sensitivity and spatial resolution. The ideal choice of collimator, gamma ray energy to image and energy window settings for ^{177}Lu have been well investigated using Monte Carlo (MC) simulations (95). Literature findings advocate the use of the 208 keV photopeak with a medium energy (ME) collimator and a 20% energy window setting (19,61,95,105–108). This is due to the higher yield of the 208 keV gamma ray emission than the 113 keV, the avoidance of the 208 keV down scatter with the use of the 113 keV photopeak, and the complicated scatter correction with the use of both the 208 keV and 113 keV photopeak. The low gamma ray emission for ^{177}Lu has produced negligible dead-time and allows for immediate imaging after administration of therapeutic activity values (109).

Various image degrading physical factors are inherent in the imaging process that degrades the gamma camera images from an ideal representation of the object or patient, as shown in Figure 1-6. These factors include: photon attenuation and Compton scattering (further referred to as scatter), collimator-detector response (collimator blurring), partial volume effects (PVEs), and noise, which affect the accuracy of the quantified activity and propagate to absorbed dose calculations. The impact of these factors on patient dosimetry depends on the choice of the gamma camera imaging protocol, which includes the types of gamma camera images used for quantification and the corrections applied to compensate for the aforementioned degradation factors.

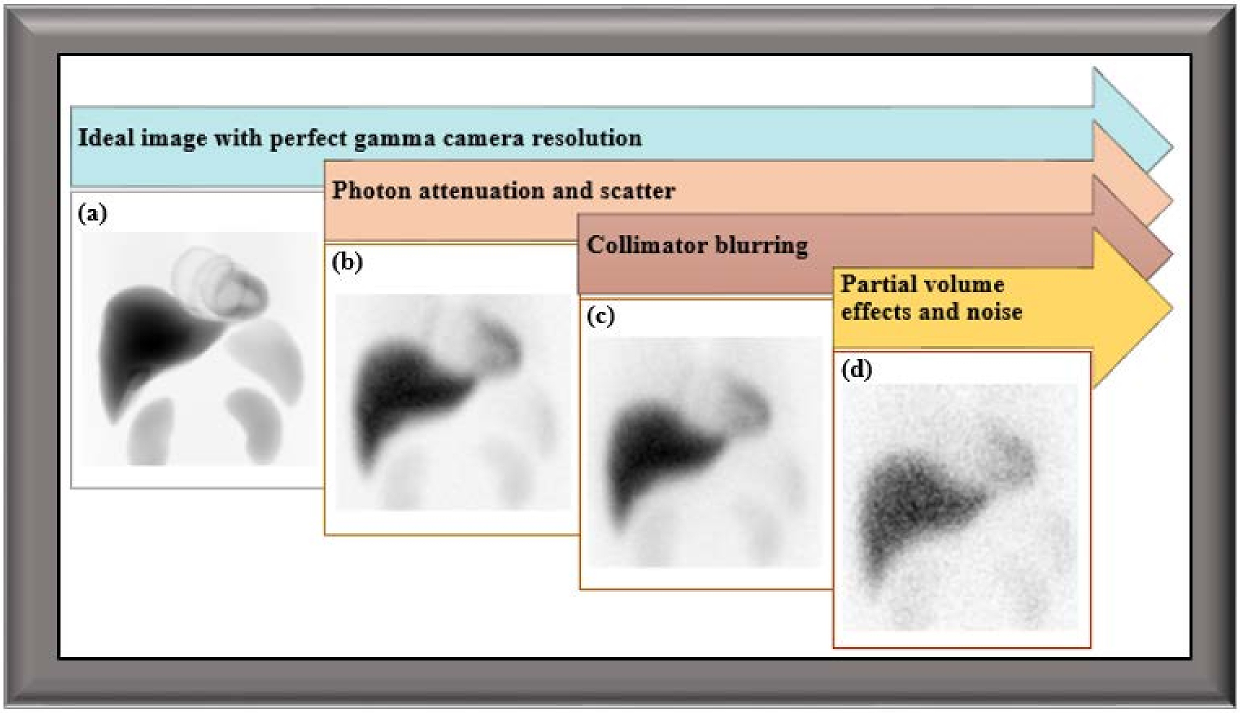

Figure 1-6: *Monte Carlo simulations corresponding to:* ***(a)*** *Image simulated with perfect gamma camera resolution.* ***(b)*** *Image including degradation from photon attenuation and scatter.* ***(c)*** *Image obtained in (b) including normal gamma camera resolution.* ***(d)*** *Image obtained in (c) including partial volume effects and clinically realistic noise levels* (95).

1.1.2.2 SPECT/CT Image Activity Quantification

Activity image quantification for dosimetry purposes has conventionally been performed using 2D planar anterior and posterior whole-body images (110–113). The motivation behind this is that, for dosimetry purposes, a series of whole-body images of the patient needs to be acquired over several days to determine the bio-kinetic data. Planar images provide a relatively fast and easy method to cover the whole-body of the patient. However, planar imaging has known limitations, including organ overlap, superimposed background activity, and the lack of organ volume information. These limitations are overcome in SPECT imaging, and corrections for absorption and scatter can be performed as part of the clinical workflow when state-of-the-art SPECT/CT modalities are used. In phantom and clinical studies, SPECT images have been proven to demonstrate superior image quality and better quantitative accuracy in comparison to planar images (114–116). It is not common for all centres to perform additional image processing to correct planar images for attenuation and scatter, which sometimes contributes to the reported poorer quantitative accuracy of planar images. For this reason, the International Atomic Energy Agency (IAEA) has endeavoured to compare different protocols for planar and SPECT quantitative data from multiple centres, using ^{133}Ba phantom sources (117). The objective of this undertaking was to identify the variability in the protocols used by the different centres and the accuracy achieved by the methods, in addition to proposing harmonised methodologies for obtaining planar and SPECT quantitative information. The trade-off between planar imaging advocated to speed up multiple image data acquisitions for dosimetry versus the improved accuracy by SPECT/CT images has been overcome by the hybrid planar whole-body SPECT/CT imaging methods (further referred to as hybrid WB/SPECT images) (118).

SPECT images are clinically acquired in typical projection matrices of 64 × 64 or 128 × 128 taking into account the balance between spatial resolution, image noise, and acquisition time (119). Step-and-shoot or continuous gantry rotation may be used to acquire the patient projection data. The auto-contour mode, where the gantry rotates following the patient body contour, is preferred in order to improve the image spatial resolution and therefore reduce the collimator blurring effect. SPECT reconstruction algorithms are used to reconstruct the projection data to obtain reconstructed slices of the acquired patient data. Even though SPECT has overcome some of the challenges obtained with planar imaging, it is complicated by the effects of the above-mentioned degradation factors and the integrity of the reconstruction algorithm. Attempts to compensate for these factors have to be made to improve the activity quantification accuracy. The steps taken to improve the quantitative accuracy are shown in Figure 1-7 and discussed in detail in the subsequent Sections 1.1.2.3 to 1.1.2.9.

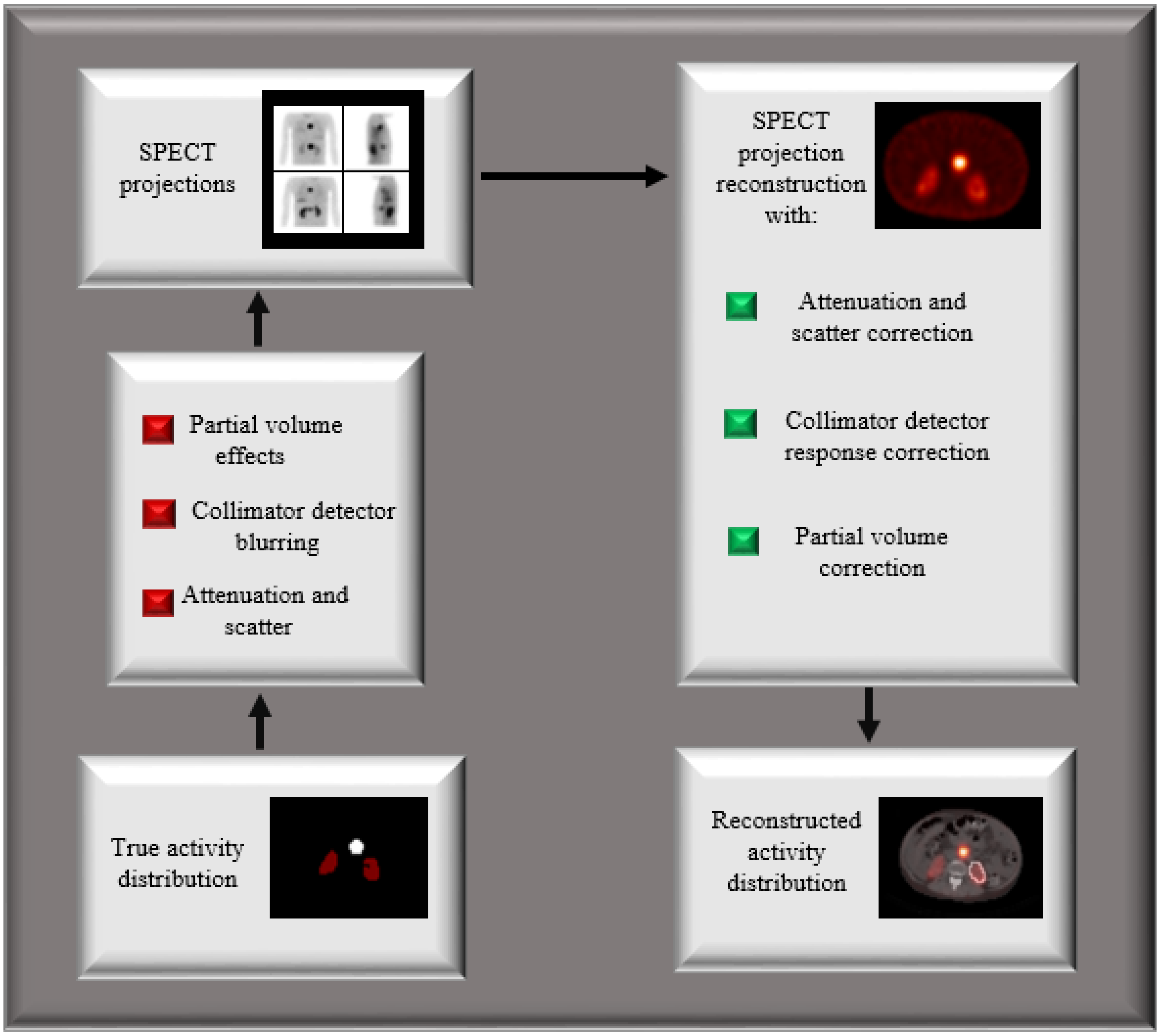

Figure 1-7: *Schematic illustrating the gamma camera imaging process, including image degradation factors in SPECT reconstruction and their compensations.*

1.1.2.3 SPECT Image Reconstruction

Iterative reconstruction algorithms such as the maximum likelihood expectation maximization (ML-EM) (120) and ordered subset expectation maximization (OS-EM) (121) are able to include modelling of the physical characteristics of the imaging process. These may comprise of compensation for collimator and object scatter, system geometry and finite detector resolution. These algorithms result in reconstructed images with better image quality and quantitative accuracy and are less prone to artefacts compared to analytical methods such as filtered back projection (122). The OS-EM algorithm, in particular, was developed to accelerate the iterative reconstruction process. With improved computing power, it has become a standard algorithm with most clinical SPECT processing units. It is highly recommended and commonly used to obtain improved quantitative SPECT data (119,123).

When using the OS-EM reconstruction algorithm, it is important to consider the optimum number of updates, defined as the product of the number of subsets and iterations which should be determined for a particular SPECT system's reconstruction algorithm of interest. This number is a trade-off between the quantitative activity accuracy, acceptable diagnostic image quality with a low image noise level, and the reconstruction speed for practical clinical applications. The trade-off is that an increased number of updates results in more accurate quantitative activity distributions from the reconstructed images while increasing image noise levels (119). The optimum number of updates is defined as the percentage of activity ratio recovered between the quantified activity distribution estimated from the reconstructed SPECT images to the true activity distribution, determined from phantom studies. For improved accuracy of quantitative data, the optimum number of OS-EM updates has been established at 90% recovery convergence. Reconstruction algorithms incorporating more corrections require a higher number of updates to reach convergence (95). The optimum OS-EM updates required for convergence are also a function of object size, where smaller objects are observed to converge slower than large objects (124). In the quest to improve image quality and activity quantification accuracy, the current 3D OS-EM reconstruction algorithms available with most SPECT systems include choices to correct for photon attenuation and scatter and collimator-detector response (CDR).

1.1.2.4 Attenuation Correction

Attenuated gamma rays are photons that are absorbed or scattered in the patient and subsequently undetected by the gamma camera. Attenuation, which in this context refers to absorption, leads to a reduction in the number of detected gamma rays relative to the ideal projection image. SPECT projections are acquired in multiple views around the patient, and photons emitted from deeper lying tissue undergo increased absorption and scattering compared to those emitted from superficial tissue. This results in fewer gamma rays detected, contributing to the quantified activity from the deeper lying tissues. Attenuation depends on the depth of the radionuclide source within the body, the tissue composition between the point of gamma ray emission and the surface of the patient, as well as the gamma ray energy. If not compensated for, attenuation is the most significant degradation factor of quantitative accuracy, especially in large patients or objects (125).

The advantage of hybrid imaging systems such as SPECT/CT is the availability of the integrated CT data acquired in quick succession with the SPECT data. In so doing, the two datasets are co-registered spatially and temporally in a fairly good manner (126). The co-registered SPECT/CT data have made attenuation compensation more practical and easy to implement routinely. Attenuation correction using CT data entails converting the CT images to appropriate attenuation maps containing linear attenuation coefficient data. This involves mapping of the effective CT energy to the primary emission energy of the radionuclide in use (Figure 1-8).

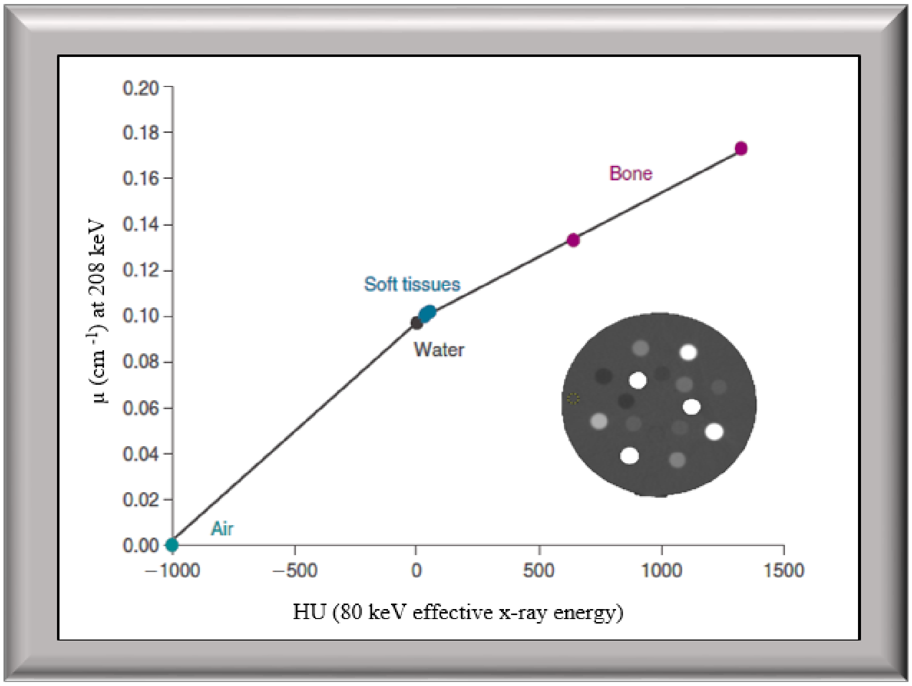

Figure 1-8: *An example of a bi-linear model used to map the effective CT energy to the imaging emission energy of the radionuclide of interest.*

The mapping is achieved using bi-linear models and is readily performed by the manufacturer (127). CT images of patients with metallic implants and those who have received contrast agents show increased CT numbers resulting in erroneous SPECT attenuation coefficients and attenuation correction maps. This may lead to overestimating the radionuclide uptake and producing false-positive results (100). Furthermore, because the CT data are of a higher spatial resolution and presented in a larger image matrix than the SPECT data, it is necessary to match the resolution of the two datasets, which is achieved by blurring the CT data to match the SPECT data. Overall the integrity of the attenuation correction using CT data depends on the precise registration of the SPECT and CT data (128).

1.1.2.5 Scatter Correction

Attenuation effects are more important than scatter on activity quantitative accuracy, particularly for large objects. However, gamma ray scatter still plays a significant part in the image quantification process. Emitted photons undergo scattering, which results in a reduced number of gamma rays detected from a specific source position. Gamma rays scattered via the Compton interaction will still be included in the final image if their energy falls within the defined energy window settings. This process results in an erroneous addition of gamma rays to the projections since these photons are not detected in the correct emission position. Therefore, scattered photons contain degraded information regarding the origin of the gamma ray emission in the patient and reduce image contrast. This degraded spatial information due to incorrect mispositioning of the scattered gamma rays will increase the number of detected events and induce quantitative accuracy errors. If the images are corrected for attenuation, and scatter effects are not accounted for, then the radioactivity uptake in the patient will be overestimated. The linear attenuation coefficients operate with the assumption that a photon is removed if it is fully absorbed or scattered (129). In emission imaging, there is a significant fraction of scattered photons that are detected by the gamma camera.

Scatter correction aims to remove these scattered photons that have occurred away from the emission site and improve the quantitative accuracy. The use of the photopeak window to distinguish between scattered and un-scattered gamma rays (primary photons), based on their energy difference, is not entirely effective due to the limited gamma camera energy resolution. Most gamma camera vendors use multiple window scatter compensation methods such as the dual-energy window (DEW) (130) and the triple-energy window (TEW) (131) to apply scatter correction for SPECT data due to their practical applications. These methods estimate the quantity of the scattered gamma rays in the main photopeak window, using additional sub-windows set on one side of the main photopeak window (DEW) or set on both sides (TEW). The DEW accounts for self-scatter from the source, while the TEW considers both self-scatter and down-scatter from higher energy gamma rays as the main gamma ray emission for which the imaging window has been set. The compensation is made by subtracting the estimated scatter projections on a pixel-by-pixel basis from the main photopeak projection image. The scattered gamma ray estimates of the two methods have some shortcomings. The subtraction method may result in noise amplification and sometimes negative counts (132). The spatial distribution of the scattered gamma rays recorded in the photopeak and the sub-windows are different. In addition, the scattering undergone by the gamma rays in the sub-windows does not match those in the photopeak windows. For ^{177}Lu quantification, Ljungberg et al. (95) found that the TEW scatter-estimate images for the 208 keV and 113 keV photopeaks were less sharp than the true scatter estimate images from MC simulation studies, with differences smaller than 10%.

Besides the energy window-based scatter estimations, scatter may be modelled in the reconstruction process with the effective source scatter estimation (ESSE) method (133,134). The ESSE uses MC-based pre-calculated scatter kernels of a point source in a uniform water-filled slab phantom at a set of distances from the collimator face to estimate the scatter contribution in the photopeak. The ESSE scatter kernels may be incorporated in the 3D OS-EM iterative reconstruction algorithm to correct for scatter. The ESSE has been reported to result in better quantification accuracies than the TEW, and the DEW scatter correction techniques (106).

1.1.2.6 Collimator-Detector Response

The CDR is an additional source of image degradation. CDR is the principal factor determining spatial image resolution of SPECT studies and is a function of source-to-detector distance (119). The image resolution of SPECT studies is derived from the spread functions of a point source, demonstrating the amount of blurring encountered at each step of the imaging process. The CDR is determined from these spread functions and results from three components affecting gamma rays as they pass through and interact with the gamma camera's collimator and detector (135). The first component is the collimator resolution which degrades linearly with the source-to-collimator distance and is determined by the geometrical acceptance angle of the collimator holes (129). The second component is the intrinsic function which refers to the intrinsic resolution of the detector. This component is limited by the uncertainty encountered in the crystal and gamma camera positioning electronics to accurately determine gamma ray interaction positions. The third component is the probability that the gamma rays will pass through the septa with or without an interaction. Septal scatter occurs when gamma rays scatter in the collimator septa and are detected in the main energy window. All these components propagate the image blurring process and degrade the spatial resolution. The effects of scatter and septal penetration are more pronounced for medium- and high-energy gamma rays. SPECT imaging results in a spatial variance in the CDR, depending on the components mentioned above and the gamma camera's rotational orbit. These factors affect the resolution of SPECT reconstructed images, degrading the quantitative accuracy of individual pixels of a source and the ability to detect microscopic diseased tissue such as metastasis.

CDR correction may be integrated into the 3D OS-EM iterative reconstruction algorithm. Most commercial systems readily compensate for the geometric response (consisting of the first two components discussed above) as part of the CDR during the iterative reconstruction process, and the manufacturer determines the details of the modelling. MC modelling scatter compensation methods such as the convolution-based forced detection scatter correction, which includes collimator and detector modelling, have improved quantification accuracies for ^{177}Lu of spheres placed in a phantom (94). The ESSE correction technique mentioned above incorporates CDR compensation, including geometric response, septal penetration, and septal scatter as part of the 3D OS-EM iterative reconstruction. CDR compensation reduces spill-out of activity to a certain extent by decreasing the poor resolution effects resulting in PVEs. A consequence of applying CDR, which should be considered, is that it may induce Gibbs ringing artefacts in the vicinity of sharp boundaries of activity distributions (136). Although CDR compensation is beneficial in reducing PVEs, it is still essential to apply partial volume corrections (PVCs) to the reconstructed images to improve the accuracy of activity quantification.

1.1.2.7 Partial Volume Correction

PVE refers to the phenomenon whereby image counts are not only contained in the corresponding voxel but smeared out into the neighbouring voxels. PVEs are attributed to the gamma camera's limited spatial resolution and image sampling in an image matrix. The PVE, shown in Figure 1-9, is due to the spill-out of counts from a radioactive object into surrounding objects typically seen in tumour imaging and reported to underestimate the quantified activity distribution (137). Conversely, spill-in of counts from surrounding radioactive objects is observed, resulting in overestimating the quantified activity. The total activity (counts) may be preserved by the sum of all voxels attributable to the object, however, the individual voxels do not represent the actual activity in the corresponding position in the object but are observed to have lower activity. The activity within the object will also be detected outside the area representing the object.

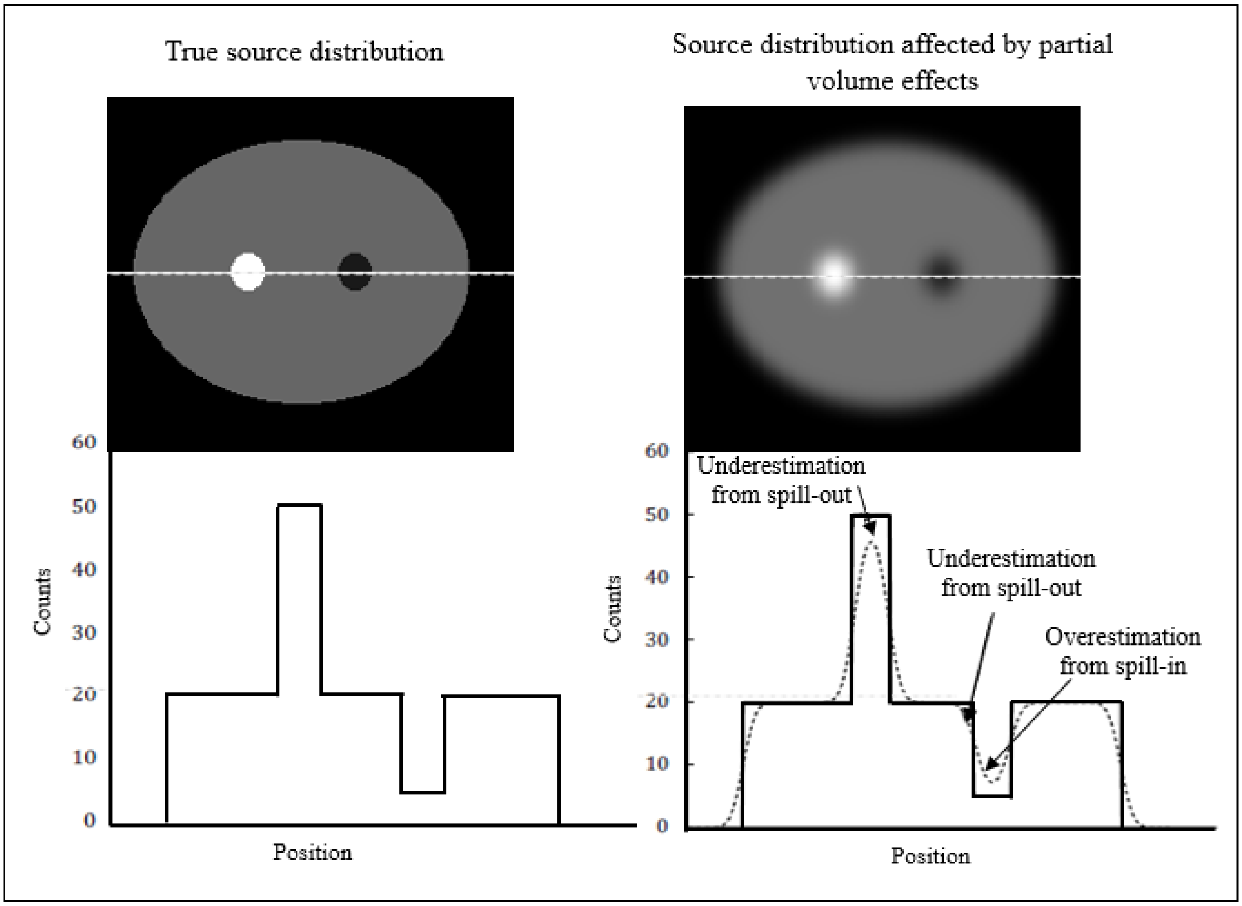

Figure 1-9: *The effects of partial volume due to spill-out of counts from a radioactive object and spill-in of counts from a surrounding radioactive object* (138).

It becomes evident that a voxel may contain a mixture of activity distributions (counts) from the object of interest and neighbouring objects, thereby blurring regions of interest. The fact that the actual contours of the object are not perfectly represented in the image matrix results in uncertainty of the quantified activity. PVE has a larger impact on smaller objects (< 3 × full width at half maximum (FWHM)) of the gamma camera (139). To avoid biased quantification results, especially in small objects, PVEs should be compensated for (100). This effect is aggravated by inadequate sampling, where larger pixels result in increased uncertainty in the border representation of the object by the image.

One of the methods for PVC is the use of a recovery coefficient (RC). This coefficient describes the ratio between the measured and true activity concentration. An RC curve can be generated as a function of object size for well-defined shapes, usually spheres. From this, characterization of the gamma camera's PVEs for specific shapes may be generated easily in phantom studies where the true activity and object size can be measured. However, this compensation method may be problematic in clinical studies where organ and tumour sizes are unknown with irregular geometries. Higher-resolution modalities such as CT or magnetic resonance imaging (MRI) studies may be used to determine the size of the tumours and organs. Still, it would be cumbersome to model partial volume from irregular geometries, as each clinical investigation would be unique.

On the other hand, due to the above described spill-out effects, a larger volume of interest (VOI) definition can be used to recover the activity distributed to neighbouring pixels. This method can be easily implemented in routine clinical studies. Its use is limited due to spill-in of activity distribution from adjacent organs. Different methods for PVC were investigated for ^{177}Lu quantification for a 3D printed kidney phantom with a medulla and cortical compartments (140). The phantoms used to generate RCs included a sphere, an ellipsoid, and the kidney phantom's medullary compartment. RC curves were calculated using different object size definitions such as filling size volume, CT volume, enlarged VOI and a fixed threshold. Optimum activity quantification of the kidney was found for an RC based on CT VOI definition. The authors advocated for a geometry-specific RC rather than a sphere RC for quantifying organs such as the kidney. Various software-based PVCs have been suggested (119), however, their complex nature has limited their clinical implementation. It is for this reason that RCs for PVC are still widely adopted, especially for tumour quantification.

1.1.2.8 Calibration Factor

3D OS-EM algorithms used in SPECT systems incorporate compensations for the above-mentioned factors, yet unlike PET images, SPECT images are still traditionally regarded as non-quantitative. This is because image voxels from reconstructed images of most commercial systems are expressed in units of image counts. With current SPECT/CT systems, it is only recently that image voxels from reconstructed SPECT images are obtained in units of radioactive concentration. Some of these systems, such as the Siemens Symbia Intevo$^{\text{TM}}$ scanner (Siemens Healthineers), incorporate a source with traceability to a secondary standard laboratory to convert the reconstructed SPECT images to images of activity concentration. Image quantification and dosimetry require SPECT images to be obtained in units of activity concentration (kBq/cm^3). Thus a calibration factor (CF) should be applied to the reconstructed image, implying that the activity used for this purpose is well-known with high accuracy. Different geometries have been reported to obtain CFs (105). The system sensitivity, determined from a planar image of a Petri dish in air with known activity (141), is often used as a CF in SPECT images to obtain quantitative data in units of activity concentration (142). However, due to the image degradation factors, the general rule is that a CF source should be subjected to the same effects as the quantified data. The CF source should incorporate photon attenuation and scatter properties, and for SPECT purposes, reconstruction and compensation methods, similar to that of the quantified geometry. This reduces the effects of imperfect scatter and attenuation corrections and improves quantitative accuracy (119). The CF measurement is source-geometry dependent and depends on how the volume used to obtain the counts for the CF is defined and incorporated with the RCs (143). The procedure to obtain the CF should approximate the method used in the quantified clinical studies.

1.1.2.9 Volume of Interest Definition

Another essential factor to consider in obtaining accurate activity quantification is the VOI definition which isolates the activity distribution to a particular organ (or object). Methods for VOI definition may include manual delineation or automated and semi-automated edge detection algorithms. These applications are available with clinical gamma camera software packages as well as software programs available to the public domain (144,145). There is no universally accepted method for VOI definition in NM images. Apart from the degrading factors mentioned above, object detection is affected by the shape, the object's proximity to adjacent organs, image noise, and the object-to-background ratio. The availability of the anatomical CT data with SPECT has provided a standard method for VOI definitions and has been widely adopted in clinical and phantom investigations (96,103,116,140,146). Caution should be exercised because SPECT quantification accuracy is affected by errors such as misdefinition (variability in organ delineation) and misregistration (between emission and transmission data) errors (He and Frey, 2010), where one voxel misdefinition can result in a quantification error of up to 8%. The errors increase in small organs with low activity uptake. Image sampling affects the variability in the VOI definition, and the precision of the quantification accuracy may be reduced by using smaller pixels (147).

All the factors mentioned above (Section 1.1.2.3 to 1.1.2.9) affect the accuracy of activity quantification. Improved activity quantification is obtained by compensating for these factors. There are various compensation methods available, and the choice depends on the radionuclide of interest, the availability of the compensation methods, and the clinical investigation at hand. The methods adopted for SPECT/CT activity quantification in the current study will be described in the subsequent chapters. The accuracy with which activity quantification is obtained directly impacts how accurate absorbed dose calculations can be achieved. The activity quantification accuracy is measured as the percentage difference between the true activity distribution and the quantified activity distribution obtained from the acquired images. One approach of validating the accuracy for image-based quantification is using MC simulations, which have the advantage of having reference values that may serve as the "truth" or "gold standards" against which the accuracy is benchmarked. Due to the complex nature of image-based activity quantification and the above-mentioned variables that affect it, MC simulations offer the advantage of investigating these phenomena in a manner that may not be possible clinically or in practice.

1.1.3 Monte Carlo Simulations

MC methods have been employed in several modalities to create models that mimic physical systems, phenomena, or quantities based on statistical probabilities and random samplings. The objective is to create a model that resembles the real physical system as close as possible using a statistical process. For applications in NM, it would be to model a gamma camera system that resembles the physical system used in the clinic. The statistical model would include interactions within the gamma camera based on known probability of occurrences using random sampling and probability density functions. The statistical uncertainty will decrease as the quality of the reported average of the model improves. This is achieved when a large number of events, termed histories, is simulated. Studies have proven MC simulations to involve radioactive decay, the mechanism of gamma ray and particle emission, interaction, and detection of these particles in various materials. MC methods are an essential tool and can assist in developing and designing new equipment. These methods allow for a detailed investigation of radiation transport and the effects of the degrading factors, as shown in Figure 1-6. Most MC applications have gained favour for optimizing imaging protocols involving developing and assessing SPECT reconstruction algorithms, evaluating corrections needed to improve NM images, and improving image quality for quantification purposes (148). Figure 1-10 illustrates these additional applications of MC simulations for ^{177}Lu-DOTATATE distribution investigating improved image quality for activity quantification. Figure 1-10 (a) represents the idealised imaging conditions without degradation factors and perfect gamma camera spatial resolution. Figure 1-10 (b) was simulated for a 20% energy window over the ^{177}Lu 113 keV photopeak and evidently had a lower contrast than Figure 1-10 (a) attributed to the increased background from scattered photons. While Figure 1-10 (c) simulated with a 20% energy window over the ^{177}Lu 208 keV photopeak displayed improved contrast compared to Figure 1-10 (b). MC applications in NM, particularly for SPECT imaging and successively in dosimetry, shall be discussed.

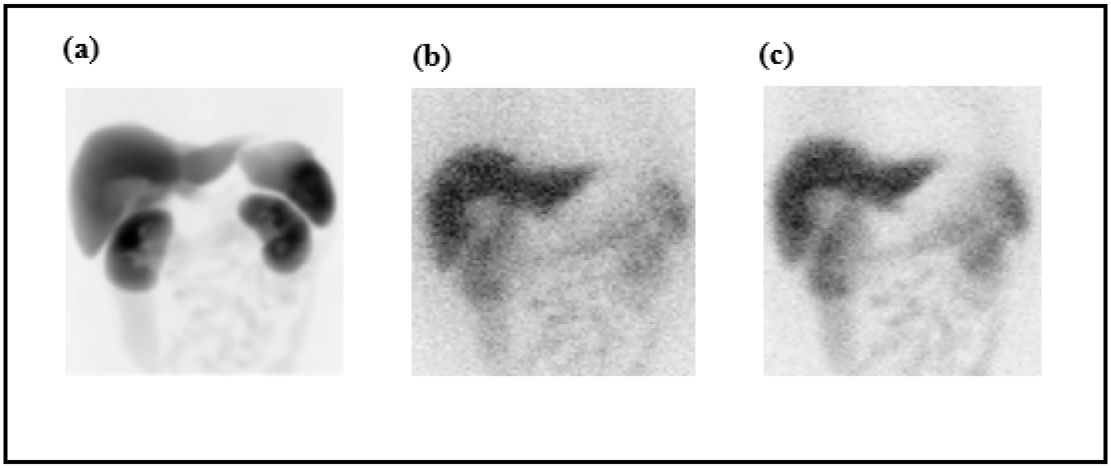

Figure 1-10: *Monte Carlo Simulation of the XCAT phantom anterior projection images corresponding to ^{177}Lu-DOTATATE distribution.* ***(a)*** *Image simulated by assuming a perfect gamma camera without image degrading factors such as imperfect gamma camera resolution photon attenuation and scatter.* ***(b)*** *Image simulated with photon attenuation and scatter as well as clinically realistic noise with a 20% energy window over the ^{177}Lu 113 keV photopeak with the gamma camera fitted with a medium energy collimator.* ***(c)*** *Same image as for (b) simulated with a 20% energy window over the ^{177}Lu 208 keV photopeak* (95).

1.1.3.1 Monte Carlo Programs for Emission Tomography

The evolution of MC simulations for emission tomography commenced in 1995 (149). Since then, several MC programs have been used in NM imaging, some of which are available to the public domain. There is no standard MC program used for SPECT and PET. Popular general purpose and dedicated MC simulation programs which are widely used have been described (150). Some dedicated programs, such as simulation system for emission tomography (SimSET) include simulations for SPECT and PET detectors, where the latter is based on the simulation of positron imaging system (PETSIM) code (151). System for SPECT simulation and modelling (SimSPECT) is suitable for investigating various SPECT collimator designs for collimator geometric response and SPECT detection for positron emitters as well as the effect of higher energy photons on images (152). The geometric response is also investigated for cone-beam collimation. The MC matrix vectorized 3D (MCMATV3D) (153) is used for phantom simulations to investigate transport in non-homogeneous media as well as attenuation and scatter compensation methods in SPECT. GEANT4 application for tomographic emission (GATE) is an open-source, general-purpose, user-friendly MC code enabling SPECT and PET simulations (148). It models a variety of detector designs, including prototypes and time-dependant processes such as source and detector movement and the decay kinetics of the source (154). Buvat and Castiglioni, (151) have presented a comprehensive guideline regarding the choice of MC codes for SPECT and PET to standardise the codes' description and facilitate a fair comparison between them. The guideline includes advantages and disadvantages of the different MC codes, appropriateness for given purposes, common features of the codes, simulation set-up, validation, and optimisation speed.

1.1.3.2 SIMIND Monte Carlo Program

A user-friendly, public-domain MC program is the simulation of nuclear imaging detectors (SIMIND) (155) MC program and will be used in the current study. The SIMIND version 6.1.2 MC program is written in FORTRAN-90. It is well established for the simulation of planar and SPECT images. SIMIND has been validated and used widely in optimising and modelling radionuclides such as ^{99m}Tc, ^{131}I, ^{111}In and ^{177}Lu (95,146,155–157). In particular, guidelines for quantitative ^{177}Lu SPECT imaging for dosimetry purposes have been well described from literature and investigations conducted using SIMIND (95,155). Apart from its applications in evaluating different scatter correction techniques, detector response to high count rates, reconstruction techniques, down-scatter, and collimator properties, including septal penetration and collimator scatter, it can also simulate transmission sources. SIMIND consists of two main programs, namely CHANGE and SIMIND. The CHANGE program is an interface that allows the user to define the physical characteristics of the modelled gamma camera as well as the simulation setup and geometry. In so doing, the simulation system is defined, and the details can be written to external record data files. SIMIND can be used to simulate gamma camera radionuclide imaging from analytical, voxel-based phantoms with the typical phantom cross-section being water and the 4D XCAT phantom population models (158,159). The 4D XCAT phantom provides a population of virtual patients for medical imaging applications in PET/CT and SPECT/CT. However, this population of phantoms represents a patient population of the 50th percentile in terms of height, weight, and organ volumes and thus still lacks patient-specific realism (Figure 1-11).

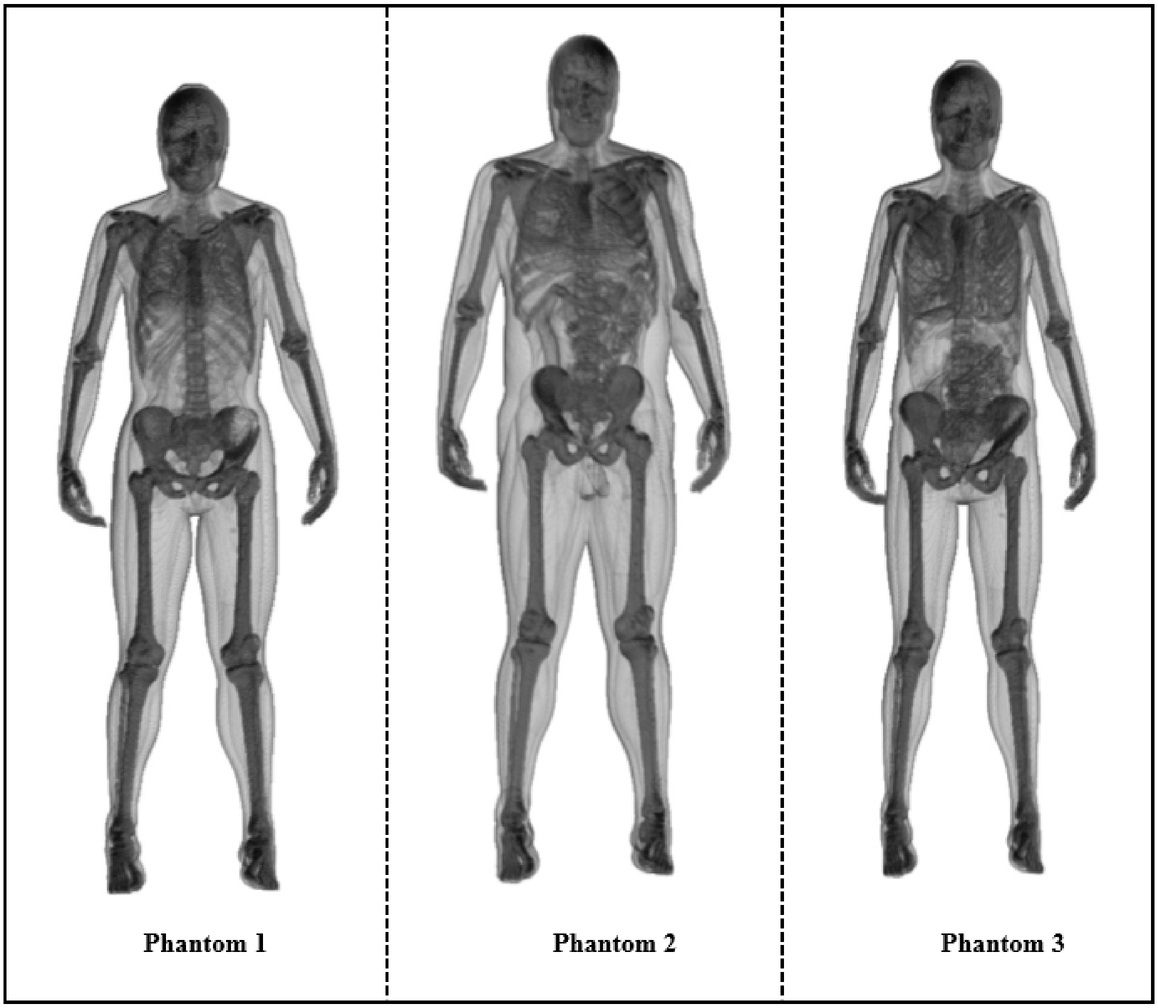

Figure 1-11*: XCAT digital phantoms modified for volume renderings of mass density distribution illustrating different body sizes and anatomical features* (160).

Voxel-based phantoms provide the user with the versatility to create phantoms using actual patients' CT data acquired with a clinical SPECT/CT system. These high-resolution CT datasets are segmented to assign values to specific voxels based on their density values, meaning that similar densities representing a specific organ would be assigned the same value. Although all digital voxel-based phantoms provide a known geometry and thus controlled results, the added advantage of creating phantoms from clinical CT data is that they present a more clinically realistic geometry of the patient cohort, as shown in Figure 1-12. The CHANGE program defines the input parameters in terms of the simulation protocol with the phantom description. SIMIND then reads the input files created by CHANGE and performs the MC transport calculations. The results obtained from SIMIND consist of simulated images and a result file describing the simulation protocol. SIMIND MC simulations from clinically realistic voxel-based phantoms have the potential to provide a better patient-specific geometry for RPT dose calculations.

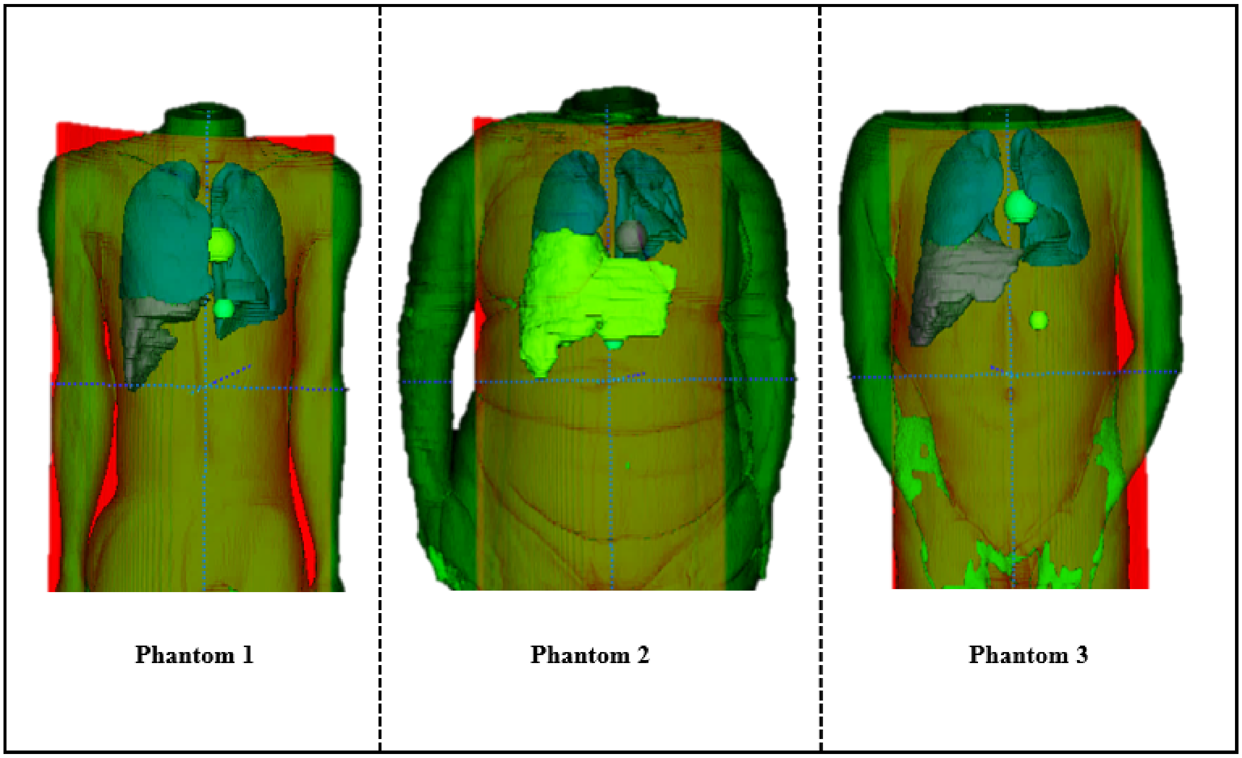

Phantom 1 **Phantom 2** **Phantom 3**

Figure 1-12: *Examples of 3D patient-specific voxel-based phantoms generated using CT data.*

1.1.4 Fundamentals of Internal Dosimetry

The accuracy of the absorbed dose estimates is important as it governs the upper limit of the activity administered to the patient for RPT. This is the case with ^{177}Lu-DOTATATE, which employs post-therapy imaging from the initial dose fractions. A radiation risk analysis is made from the images to assess the benefit of successive administrations versus the risk of exceeding the tolerance levels to the critical organs. As with any treatment regime, the benefit of the treatment must outweigh the risk, and the key element to justifying the treatment lies with the estimation of the absorbed dose (internal dosimetry) to the critical organs.

In general, the absorbed dose is defined as the energy imparted in a volume with a specific mass (161). The definition entails summing all the energy absorbed by a specific organ and dividing it by its mass. The energy of the radiation particle will be emitted at a rate depending on the amount of injected activity (energy per decay) and the decay properties of the radionuclide. The subsequent discussions will include the last steps of the clinical dosimetry chain i.e., the multiple-image acquisitions for the collection of the bio-kinetic data, the fits for TACs, and the absorbed dose estimates (Figure 1-4).

The absorbed dose, D is the physical quantity used to quantify the effects of ionization radiation in tissue. The international system unit used to express absorbed dose is Gray (J/kg). From this, it follows that the mean absorbed dose $\overline{D}$ is defined as shown in Equation 1-1.

$$\overline{D} = \frac{d\bar{e}}{dm} \tag{1-1}$$

Where $d\bar{e}$ is the mean energy imparted, and dm is the mass of a specific tissue volume. Equation 1-1 is extended to account for the different source-target relationships and the radionuclide decay characteristics and expressed as Equation 1-2.

$$\overline{D}(r_T, r_S) = \sum_{r_S} \tilde{A}(r_T, r_S) \sum_i \frac{n_i E_i \emptyset_i\,(r_T,\ r_S)}{m_T} \tag{1-2}$$

Where $\overline{D}(r_T, r_S)$ is the mean absorbed dose delivered to the target organ r_T due to activity contained in the source organ r_S over a defined dose-integration time. $\tilde{A}(r_T, r_S)$ is the total number of radiation decays in the source volume over a specific integration time and $\sum_{r_S}$ expresses the contributions of several source organs. Furthermore, n_i and E_i are the frequency and energy of each radiation type i, $\emptyset_i(r_T, r_S)$ represents absorbed energy fraction emitted from the source to the target for each radiation type while m_T is the mass of the target organ. Equation 1-2 indicates the fundamental basis for internal dose calculations, which essentially consists of two terms.

The first term $\tilde{A}(r_T, r_S)$ is known as the time-integrated activity (TIA), which depends on the bio-kinetics of the activity distribution and the term, $\sum_i \frac{n_{iE_i \emptyset_i}(r_T, r_S)}{m_T}$ simply known as the S value depends on decay characteristics of the radionuclide and the geometric properties of the tissue medium. The equation is simplified to a two-term equation (Equation 1-3), representing the fundamental basis on which absorbed dose calculations were developed and first laid out in the 1960s by the Medical Internal Radiation Dose (MIRD) Committee the Society of Nuclear Medicine as the MIRD formalism.

$$\bar{D}(r_T, r_S) = \sum_{r_S} \tilde{A}(r_T, r_S)\, S(r_T, r_S) \tag{1-3}$$

$S(r_T, r_S)$ is the mean absorbed dose deposited in the target organ per TIA unit present in the source organ. The MIRD formalism gained wide acceptance as the standard method for absorbed dose calculations (162). The absorbed dose calculation essentially becomes the product of two quantities, the TIA (cumulative activity) and the imparted energy summations over all emission types (S values), which shall be discussed below.

1.1.4.1 Time-Integrated Activity

The first quantity needed to calculate the absorbed dose is the TAC for a given organ or tissue of interest. The TAC provides temporal information regarding the radiopharmaceutical uptake, retention, and excretion, which varies amongst patients. This information is obtained from the quantified activity and directly impacts estimating the absorbed doses and, as a result, may have significant errors if not determined optimally. In the quest for patient-specific dosimetry, the TAC needs to be determined for every patient. The TACs are obtained through successive quantitative images over a number of imaging time-points post radiopharmaceutical administration. TACs are obtained for the different source organs, and integration of these curves yields the TIA. Apart from the activity quantification accuracy, the accuracy of the TAC depends on the image sampling schedule post-administration, which includes: the number of imaging time-points and their frequency, the appropriate imaging span period post-administration (integration period), and for the TIA purposes, the integration of these time periods and the model used to fit the TAC before integration (163–165). The integration time should match the biological endpoint of the study and for reliable results, a minimum of three data points should be collected over a duration of two-to-three effective half-lives (161). However, Gleisner et al. (166) noticed a measurable amount of ^{177}Lu-DOTATATE five to seven weeks post-administration due to tumour retention. Therefore, tumour dosimetry at a later stage than the standard seven-day post-administration time may be of merit.

Section 1.1.2.2 included the advantages of quantitative SPECT/CT images for dosimetry and their built-in compensation methods as part of the clinical workflow. SPECT/CT images have been reported to better estimate activity distributions and are used in most dosimetry studies (167). Therefore the focus shall be on the TAC obtained using SPECT/CT data with appropriate compensation methods for improved activity quantitative accuracy. The TAC calculation is performed from registered multiple quantitative SPECT/CT images, and CT data may be used for VOI definition (Section 1.1.2.9) provided that the SPECT and CT data are correctly co-registered. Most commercial software programs perform image registration reliably. However, it should be verified since misregistration can propagate errors in the dosimetry calculations (168). CT data permits slice-by-slice manual segmentation, which relies on accurate image registration. Manual segmentation is user-dependent as variations may be induced on a slice-by-slice basis. Therefore the segmentation process may also need to be validated and ideally performed by the same operator for the consecutive imaging time-points. Ideally, the VOI segmentation should be performed on the first SPECT/CT image and then copied to the respective time-points. This would require that the images be registered for the different time-points i.e., successive alignment of the imaging time-points. Otherwise, the VOI would fit incorrectly on the remaining time-points, inducing errors. In this case, individual VOIs would be defined for each time-point.

Multiple SPECT/CT acquisitions for dosimetry may be timely burdensome to the clinic and affect patient throughput. Even so, care should be taken as non-optimal image sampling schedules may result in large over-or underestimations of absorbed dose estimates to organs such as the kidneys. Optimal scheduling for the sampling of hybrid WB/SPECT images for kidney dosimetry has shown that the variability of determining TIA depends on the number of activity measurements post-administration, especially in low schedules such as two time-points (169). Apart from the hybrid WB/SPECT images method being incorporated to reduce imaging time for dosimetry, single time-point imaging for exponential clearance has been explored, particularly for ^{177}Lu-DOTATATE kidney dosimetry (170). In such cases, prior knowledge regarding population averages for bio-kinetic data has to be available, and the approach may not be suitable if the patients do not follow the population average for toxicity detection.

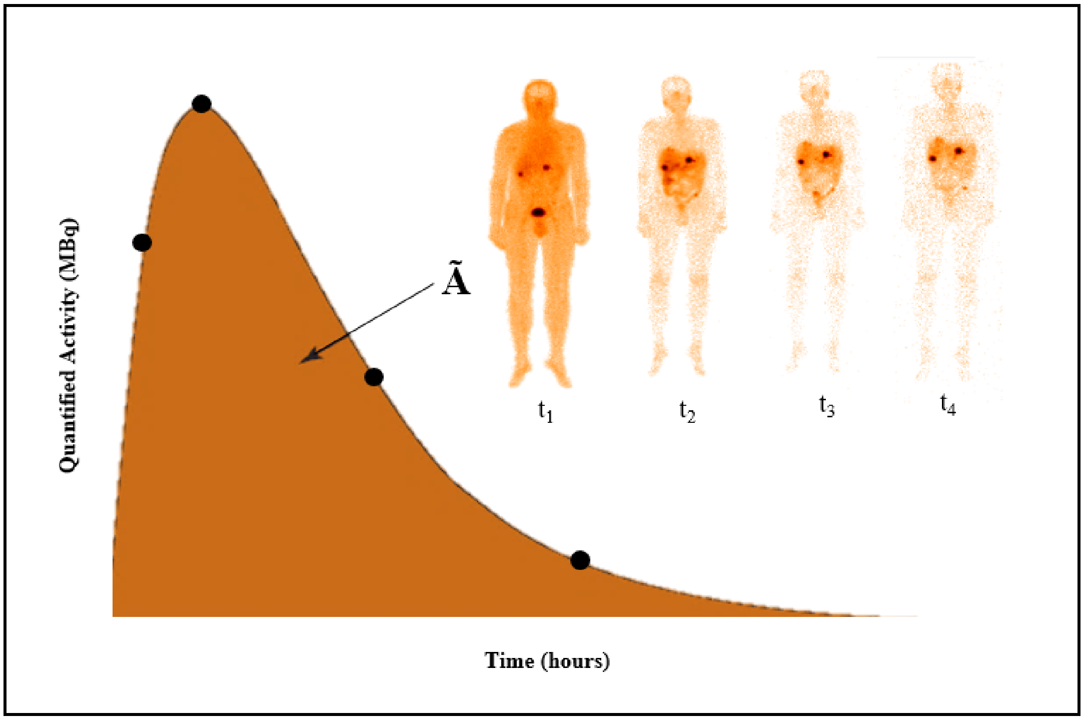

Figure 1-13: *An example of a time-activity curve used to calculate the time-integrated activity by fitting the quantified activity at each time-point for a specific organ of interest using an analytical fit and integrating the fit over time.*

The TIA is calculated as the area under the TAC obtained from successive imaging time-points, as shown in Figure 1-13. The TACs can be fitted with multi-exponential functions that are integrated analytically. Uncertainties in the TAC fitting models have been reported by (171). The constants determined from the exponential functions describe the bio-kinetic data in the organ of interest. Statistical investigations to choose the optimal fitting functions have been performed to optimize the TIA (163). Once i) the quantified activity has been determined accurately, ii) the optimum image sampling schedule obtained, and the iii) optimum fitting model to compute the TIA established, it follows that the total number of decays (S value) obtained within a specific volume has to be obtained to calculate the absorbed dose.

1.1.4.2 Absorbed Dose Calculations (S values).

Because activity concentrates in more than one organ, the multiple emissions from various source-target regions as shown in Figure 1-14, are required and simplified into the S values. The S value accounts for the mean energy emitted per decay of the radionuclide, the mass of the target organ, and the absorbed fraction of the energy emitted from the source organ. In turn, the absorbed fraction depends on the type and energy of the emitted radiation, the size, shape, and composition of the source and target regions, and the distance and type of material separating the source-target regions.

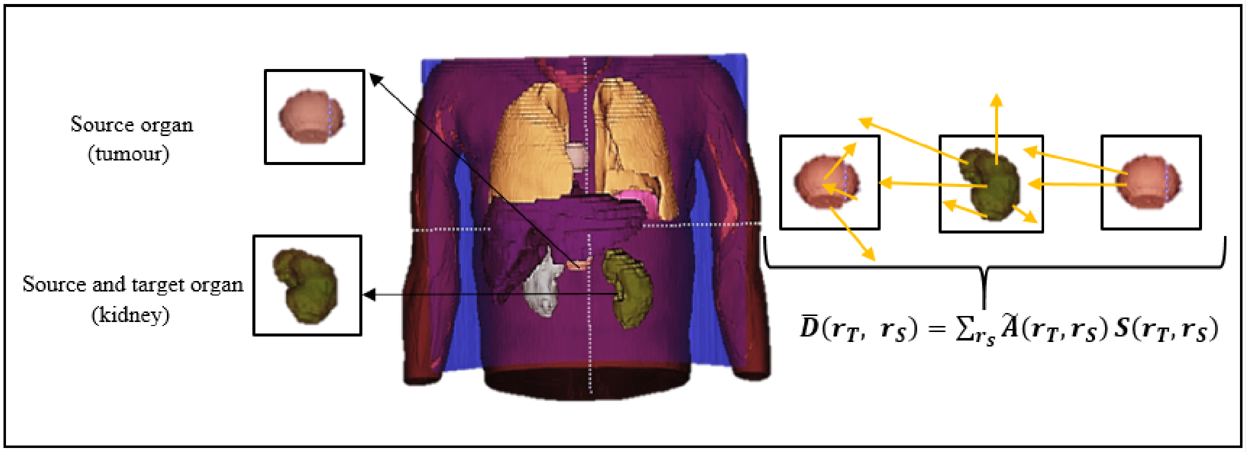

Figure 1-14: *Absorbed dose delivered to a target organ from one or more source organs containing radioactivity.*

S values have been calculated for multiple source-target organ combinations and stored as lookup tables for a wide range of radionuclides (172). Essentially three algorithms are available to generate the S values, namely, local energy deposition (LED), convolution with dose-voxel kernels (DVK), and full MC transport (explained below). Figure 1-15 illustrates the selection criteria that may be used as a guideline for choosing an appropriate algorithm for absorbed dose calculations. If the radiation considered is non-penetrating, then LED may be considered. However, the other two algorithms should be considered for penetrating radiation emitted with high yield where the energy deposition from the radiation outside the source volume may have a significant cross-dose contribution. If the propagation in tissue is homogeneous, then the LED is only governed by the emission point distance (173). If the propagation medium is homogeneous, but the radiation particles penetrate, then convolution with DVK may be used. Full MC methods should be considered if the radiation considered for dose deposition is penetrating in a non-homogeneous medium.

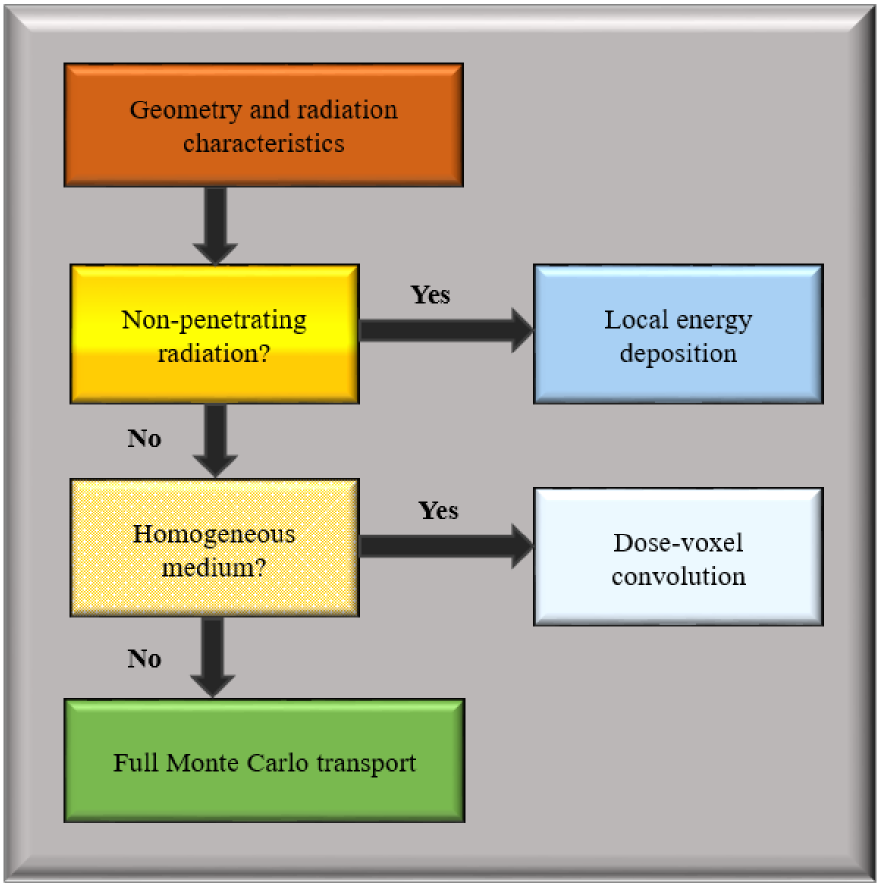

Figure 1-15: *A selection criteria for choosing an appropriate dosimetry algorithm* (174).

i. Local Energy Deposition

The simplest method for performing the dose calculation is to assume that all the emitted energy is deposited in the voxel of origin, LED, which only considers voxel self-dose. This entails setting the absorbed fractions to one (175). Since the largest energy deposition contribution is from the charged particles such as alpha's, beta's, and Auger electrons (176), the validity of this assumption depends on the range of the charged particles emitted during radioactive decay. This assumption is valid for most radionuclides used in RPT, where the projected path length of the charged particles in tissue does not exceed the voxel dimensions (96). The assumption is appropriate for ^{177}Lu as the charged particles' range is less than the typical voxel dimensions used for clinical SPECT images (118). Even for radionuclides with more extensive particle ranges such as ^{90}Y, most of the emitted charged particles do not exceed the 5mm projected path length which is comparable to SPECT voxel dimensions.

The assumption of LED applies to charged particles due to their limited range but is less valid to gamma rays, and the extent of the invalidity depends on the gamma ray yield. The method is found to be fairly accurate for the analysis of ^{177}Lu toxicity studies (177–179) because the ^{177}Lu 208.4 keV gamma ray has a low yield of 10.4%, meaning that the probability for cross-dose contribution from target organs' gamma rays is low. In the event of radionuclides with a higher gamma yield, such as ^{131}I there is a higher probability of cross-dose from the target organ, thus, other methods such as convolution with DVK (180,181) and full MC transport calculations are considered (96,182–185).

ii. Convolution with Dose-Voxel Kernels

Convolution with DVK is considered when photons have a path length that is longer than the spatial resolution of the reconstructed SPECT image. A source distribution can be modelled as a collection of radiation point sources. A dose point kernel then describes the deposited energy as a function of distance from the radiation emission site in a homogenous medium. The energy deposition variation is derived for a point source at various depths in a homogenous medium to compute dose point kernel functions using MC simulations. The TIA image is convolved with these functions to estimate the deposited energy distribution, thereby deriving the absorbed dose (186). Instead of calculating a continuous dose point kernel, a discrete DVK is often determined. The TIA image is then convolved with tissue-specific DVKs (187).

Deriving dose point kernels commenced in the 1960s by Berger, (188) and as mentioned above the methods initially employed simulations in homogeneous phantoms (189,190), with complete decay data for mono-energetic charged particles and photons. The methods were less accurate in applications to non-homogeneous media and have since been extended to density scaling for non-homogeneous tissue (180,181,191). ^{177}Lu DVKs have been adopted for inhomogeneities and compared to the full MC gold standard (187). The adapted DVK underestimated the mean absorbed dose from the MC method by 5% to 8%, partially attributed to the insufficient kernel size applied in DVK dosimetry. Dosimetry using DVKs has been applied to neural networks to predict absorbed dose calculations in critical organs such as the kidney (192). The application of deep learning has also been presented in a method developed for whole-body organ level dosimetry for tissue inhomogeneity and patient-specific anatomy using MC simulations. In this novel method deep learning was used to predict the energy deposition using the patient-specific anatomy and the

S value kernel, which compared well with the full MC dosimetry (193). The methods were also promoted to overcome the computational burden limitation of MC dosimetry. Although deep learning-assisted dosimetry is a very promising evolution to estimating absorbed doses, the results depend on the number of training kernels that need to be compiled for a very large number of voxels, all tissue combinations of interest, and a large patient cohort to reduce the inter-patient variability. It is due to the tissue heterogeneity of the human anatomy and the complex nature in which this affects energy propagation and deposition, that the above methods are based on some or other simplified calculation to estimate the absorbed doses

iii. Full Monte Carlo Transport for Dosimetry

It is evident from the assumptions in the methods mentioned above that full MC dosimetry constitutes the most accurate means of computing patient-specific absorbed dose calculations. Full MC-based dosimetry represents the complete meaning of patient-specific dosimetry because the pre-calculated S values are omitted and ideally calculated for each patient. Hence it has been adopted as the gold standard for patient-specific dosimetry Bardiès et. al (194). Full MC dosimetry involves calculating the S values for different source-target combinations following the anatomy geometry for each patient. Although full MC-based dosimetry calculations are deemed the most accurate means of calculating patient-specific dosimetry (96,101), they are still computationally burdensome for routine clinical use. Therefore, they have not been adopted as the gold standard for clinical dosimetry, however, the fast-growing computing power gives hope to such an idea.

Apart from calculating patient-specific S values, MC absorbed dose calculations can handle non-uniform absorbed dose calculations at a voxel level, overcoming assumptions included in the methods mentioned above. The MC techniques simulate the creation and transport of photons and charged particles through various structures in the body using predetermined patient atomic composition and density information. The quantified SPECT and CT-derived density images are used as input to model the radiation transport. The SPECT images simulate the radiation decay characteristics, while the density images simulate the particle transport. Therefore the source-target combinations can be defined from the specific geometry of the patient instead of reference phantom models. The S values have to be computed from each radiation source to the target, and the range of the radiation with each source-to-target geometry should be considered (173). Not only does MC dosimetry consider tissue heterogeneity and secondary particle emissions (photons) it also accounts for transitions between tissue types and tumour geometries (181,195). The complexity of the process and the long computational times needed to do the calculations are evident, providing an understanding of the limited adoption of full MC patient-specific dosimetry.

The quantified SPECT images used to sample decay locations assume that each voxel reflects activity from the corresponding volume element in the patient. This is part of the reason why quantified activity should be as accurate as possible. The photon and charged particle transport are simulated in the density image volumes. Absorbed dose rate images are computed by scoring the energy deposition at each interaction site in an image matrix with identical voxel dimensions as the reconstructed SPECT image (96). Therefore, a dosimetry program should ideally encompass all the steps needed in the clinical dosimetry workflow ranging from imaging (with conversions from counts to activity) up to and including the dose calculations steps (Figure 1-4). This facilitates a modular approach to the dosimetry chain. The workflow becomes more user-friendly, with incentives to complete all steps required to obtain accurate dosimetry in a clinical setting.

1.1.4.3 Dosimetry Software Programs

Currently, not all commercial dosimetry programs encompass all the steps in the dosimetry workflow (Figure 1-4). The error at each step should be minimised through optimisation to reduce the uncertainty in the dose estimates (171). It is for this reason that many clinics have developed institution-specific dosimetry programs such as MADOSE II (196), Voxeldose (197), JADA (198), NUKDOS (164), BIGDOSE (199) and LundADose (113) using their available resources with methodologies applicable to the needs of their clinics. Unfortunately, the use of these programs for clinical trials is restricted by the legislation of medical devices, which requires that a software package have the CE mark for routine clinical use. Due to the difficulty of obtaining the CE mark, which is often beyond the institutions' capabilities, many clinics are acquiring commercial software programs for dosimetry. Santoro et al. (200) has tabulated a list of commercial software with CE marking, including manufacturer, image format for input, VOI definitions, and the algorithm used in the dose calculation step. Even so, the organ level internal dose assessment/exponential modelling (OLINDA/EXM) remains the most widely adopted dosimetry program.

i. OLINDA/EXM

In conjunction with developing the MIRD formalism for dosimetry, S values were generated using geometric models and made available to the NM community through OLINDA/EXM version 1.0, which shall further be referred to as OLINDA (201). OLINDA is the first dosimetry program to receive Food and Drug Administration (FDA) clearance in 2004. It was available through Vanderbilt University (Nashville, TN, USA), and many institutions have adopted it to perform dosimetric calculations. OLINDA provides pre-calculated S values for more than 800 radionuclides for adults, children of different ages, and pregnant females. The program is designed for model-based dosimetry using these predefined patient models. However, it can be tailored for a more patient-specific approach to dosimetry by multiplying the S values with the patient-specific TIA data in the source organs to compute the mean absorbed doses for the organs of interest. More accurate patient-specific dosimetry can be achieved if the S values are scaled by the mass of the organ. S values for spheres, mimicking tumours, are included for self-absorbed tumour dose calculations without accounting for absorbed tumour cross doses i.e., from tumour to normal tissue and vice versa (172). The dosimetric models used to calculate the S values have evolved from geometrical shapes (87,202) to more realistic voxel-based phantom series of NURBS models, shown in Figure 1-16, based on standardized published masses (203,204). The expansion of these models and the included source-target organs have been documented (205). This led to the release of OLINDA/EXM version 2, available through HERMES medical solutions (Stockholm, Sweden), with these new NURBS models implemented.

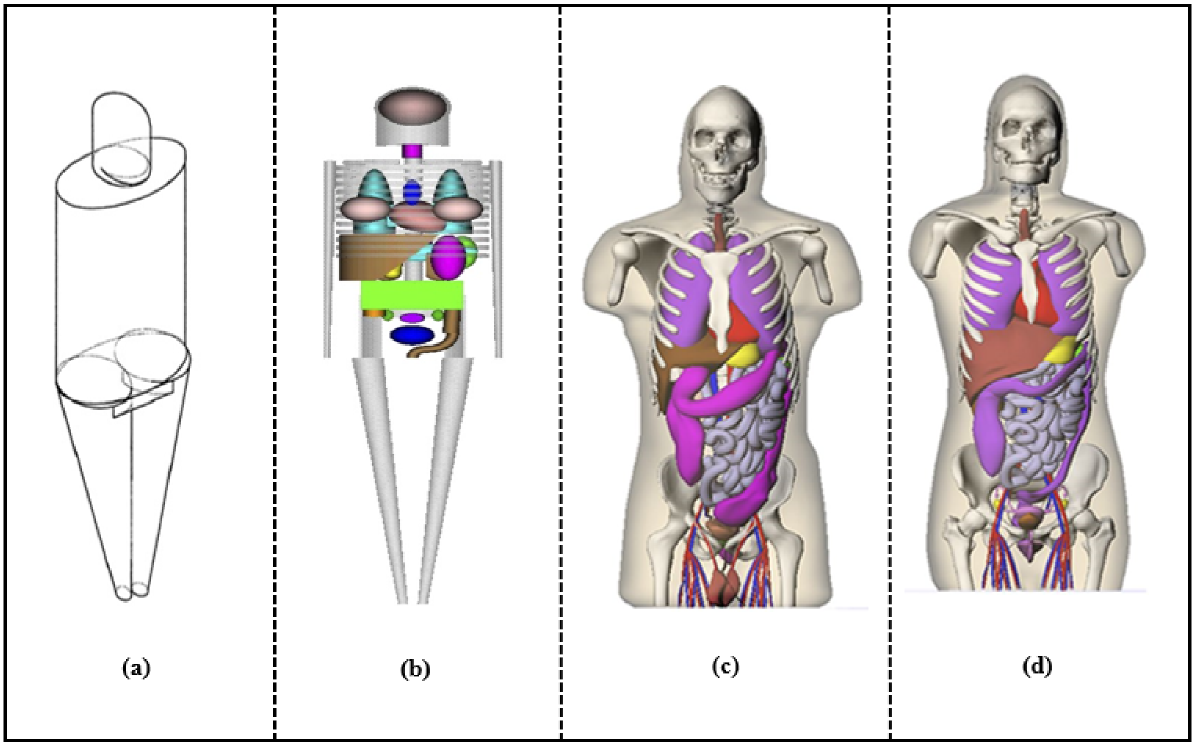

Figure 1-16: *Original stylized adult male model of* (202)*:* ***(a)*** *Exterior view,* ***(b)*** *skeleton and internal organs. Anterior views of the Segars NURBS models* (206) ***(c)*** *adult male and* ***(d)*** *adult female.*

Application of OLINDA for dosimetry should be made with the understanding that the S values are based on standard healthy patient models assuming uniform activity distributions within the organs and dose gradient near interfaces are not accounted for (201). The energy absorbed in each voxel is calculated from the radionuclide decay table using radiation energy transport models and the voxel activity. OLINDA is routinely used considering self-dose by LED of electrons in the calculation of absorbed doses. The CT data is used to derive a density map using a mass-density calibration from which the particle tracking and energy deposition are derived. Apart from the fact that the calculations are based on reference patient models, only one model is available for each category, resulting in uncertainties and inaccuracies when applied to patients. The well-established OLINDA program lacks the full MC tailored approach to dosimetry when calculating the S values and, in some instances, has been reported to have limited accuracy (207). This could explain why physicians are hesitant to use this program for individualised patient dosimetry (208). However, OLINDA is still the most commonly used dosimetry program and teaching tool due to its lower cost and FDA clearance. It is available at our institution and shall be used for subsequent investigations conducted in this work.

ii. LundADose

A program that includes all steps of the dosimetry workflow is the institution-specific program LundADose developed by the Department of Medical Radiation Physics, University of Lund, Sweden (101,209). The program is made available to our intuition through a research collaboration, funded by the Science and Technology Research Collaboration between the National Research Foundation (NRF) of South Africa, and the Swedish Foundation for International Cooperation in Research and Higher Education (STINT), and shall be used in this work. The LundADose interface is written in Interactive Data Language and has applications that calculate image-based absorbed doses using either planar, whole-body, hybrid WB/SPECT images or SPECT/CT images. It incorporates methods for SPECT reconstruction with complete corrections including image registration, activity quantification with the following corrections: CT-attenuation, ESSE-scatter, and CDR (geometric response, collimator resolution, collimator septal penetration and scatter) as part of the 3D OS-EM iterative reconstruction as shown in Figure 1-17. The method used in this program has been successfully validated in clinical studies (210,211). The program follows the photons by full MC transport in the dose calculations step to include the cross-doses between organs.

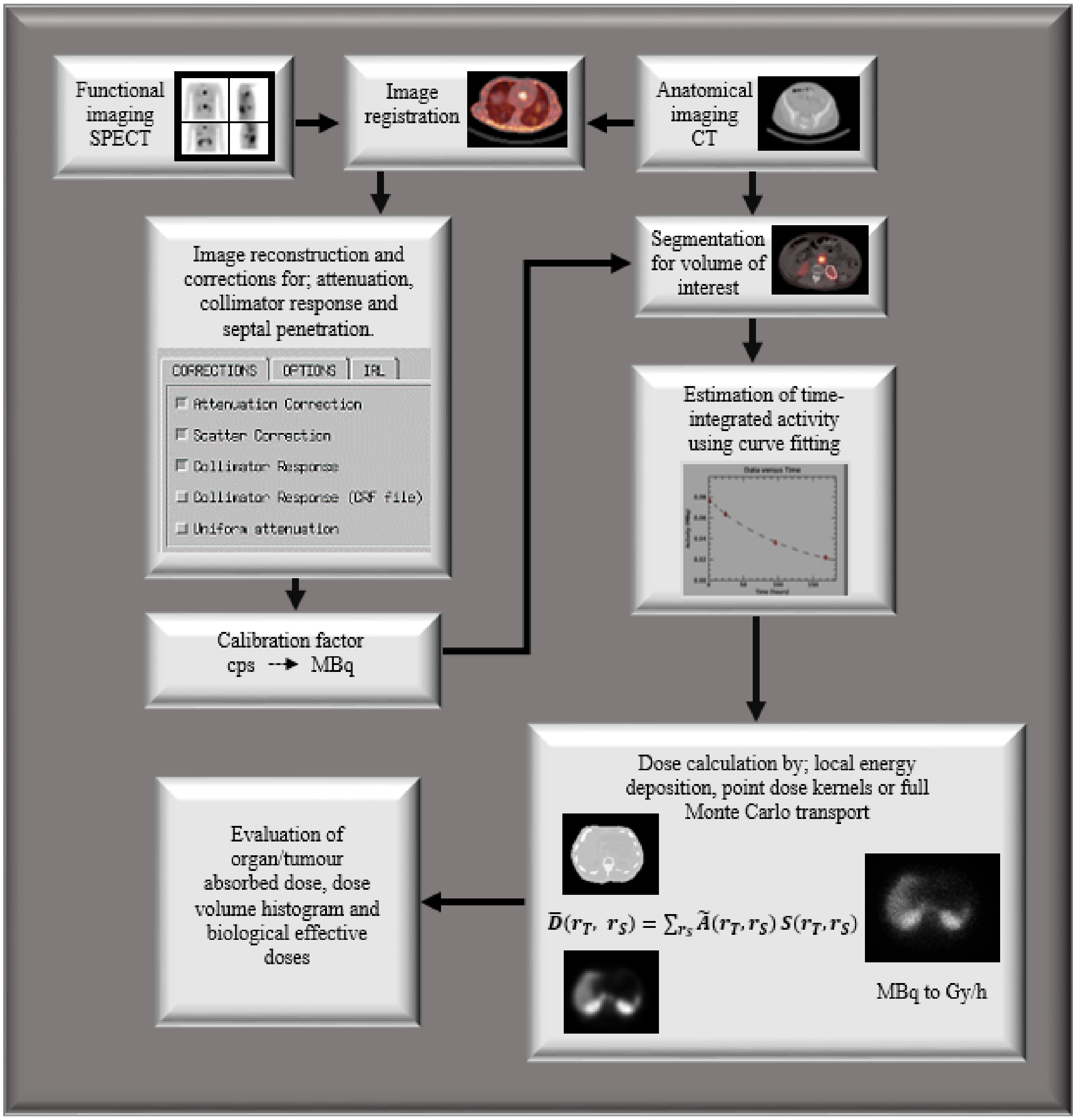

☑ Attenuation Correction
☑ Scatter Correction
☑ Collimator Response
☐ Collimator Response (CRF file)
☐ Uniform attenuation

Figure 1-17: *Illustration of the dosimetry workflow used in LundADose program* (96).

LundADose is written using the EGS4 MC code (212) to simulate radiation transport. Mortran, an extension of the Fortran programming language, is used to execute the simulations by the EGS4 MC code to perform the radiation transport. The program computes absorbed doses for voxel dimensions applicable to the clinic. It uses quantitative SPECT and registered CT-based density images to model the radiation transport and generate patient-specific S values derived from SPECT/CT patient data. The program follows the full MC transport of photons and assumes LED from the charged particles. As previously mentioned, this assumption follows that the input SPECT data has a poor spatial resolution (4 mm – 10 mm) comparable or larger than the range of the charged particles (101). Therefore the kinetic energy of the dose depositing charged particle would be absorbed within the same voxel from which it was emitted. The program can also follow all particles for full MC transport, including photons, electrons, and betas with dose gradients at lung, tissue, and bone interfaces. Options for the cut-off energy of the photons and electrons and the number of histories are available. Further details regarding dosimetry using LundADose is discussed in detail in Chapter 4.

LundADose generates patient-specific dose-volume histograms (DVHs) and BEDs to represent the tissue non-homogeneities. DVHs demonstrate the relationship between a volume (%) that has received a specific absorbed dose as a function of the absorbed dose (161). DVHs are commonly used in EBRT to describe dose distributions of tumours and critical organs. The best way to introduce DVHs as a reporting concept to the NM community has not been established (213). Due to their primary application to EBRT and the low spatial resolution of SPECT/CT images that do not support fine sub-region uptake (88), the applications of DVH and BEDs are still under development for applications in NM. They have not been fully validated clinically, therefore their use in the NM clinics has been limited.

1.2 Summary

RPT lies between EBRT and brachytherapy as a treatment modality. It has the advantage of following a bio-chemical pathway to deliver radiation to tumourous cells while sparing normal healthy tissue, constituting precision bombardment. There has been a tremendous acceleration in developing novel targeting agents such as peptide molecules, and their application in RPT has evoked the evolution of patient-specific dosimetry. Growing evidence has shown that the variability obtained between patients and the demand for optimizing tumour control while minimising critical organ toxicity has to be met. Even so, a fixed-dose regime is followed due to the uncertainty with which the dosimetry is calculated. This is attributed to obstacles such as: the lack of standardised methods in the clinical dosimetry workflow steps necessary to avoid non-optimised practices, the arduous effort for successive imaging examinations, and the lack of documentation to correlate patient outcomes administered activity.

The efforts for patient-specific dosimetry are challenging due to all the critical steps involved in the clinical dosimetry workflow. The attempt should follow a multidisciplinary collaboration between medical physicists, physicians, and technologists within the NM community. Since the dosimetry is computed from the quantified activity images, great effort should be made to improve their accuracy by incorporating all the corrections for the image degrading factors. The availability of reconstructed co-registered SPECT/CT data with build-in corrections makes this effort more manageable. To reduce imperfections in the reconstruction process, the CFs used to convert image counts into activity units should resemble scatter and attenuation properties and be processed similar to the quantitative SPECT/CT data. Patient-specific bio-kinetic data should be mandatory. Sequential patient-specific images used to determine TIA should be acquired for at least three time-points with the last time-point sufficient to fit the TAC tail. Appropriate multi-exponential fitting models for ^{177}Lu-DOTATATE are well established to determine TIA from TAC data. The choice of the best algorithm to compute absorbed dose calculations depends on the application. Full MC dosimetry is the gold standard for obtaining accurate patient-specific dosimetry. The method represents a complete patient-specific approach rather than estimations from standard geometries. However, the adoption of full MC dosimetry for clinical purposes has been limited due to long computational times.

The argument for tailoring RPT becomes that even though personalised dosimetry has an important role in safety, its use is not evidence-based and the “tolerated holy-gray” of the maximum threshold values exacerbate this notion. Thus the well-established empirical dosage is often followed instead of the standard-lacking, complex, time-consuming approach of patient-specific dosing for RPT (214). Conversely, the administered activity should be as high as achievable for optimum RPT efficacy. Hence, the European council directive 2013/59/Euratom statement that RPT should be individually planned and verified (215). Patient-specific dosimetry is the conveyance to evidence-based data needed for tailored RPT. This makes the efforts still very important as they can make RPT reach its full potential as a powerful precision-based cancer treatment modality.

1.3 Purpose of the Study

The present study entitled “Accuracy of ^{177}Lutetium SPECT Activity Quantification and Patient-Specific Dosimetry: A Monte Carlo Study” forms part of the endeavour to grow RPT dosimetry, striving towards optimal cancer treatment. ^{177}Lu was the radionuclide of choice to conduct investigations in this work. This is owing to its favourable beta-decay properties for RPT and low yield gamma ray emission for imaging. In addition, it has reliable bio-chemistry for peptide molecular labelling, making it an excellent agent for RPT. This research study will focus on ^{177}Lu-DOTATATE activity distribution due to its clinical relevance in treating patients with late-stage metastatic NETs. Due to its high cost, ^{177}Lu-DOTATATE RPT for NETs has not yet been adopted in our clinic, at the Department of Nuclear Medicine in Universitas Hospital, Bloemfontein, South Africa. However, its success in treating NETs has gained a compelling interest for its implementation in our clinic, and we hope to incorporate it as a treatment modality in the near future. For this reason, this study intends to familiarize and investigate the accuracy of ^{177}Lu SPECT/CT activity quantification and patient-specific dosimetry using voxel-based phantoms and MC simulations with the dosimetry software programs available in our institution and clinic.

The use of phantoms in activity quantification and absorbed dose distributions aids in fully understanding factors affecting the accuracy achieved with the chosen methods. Phantoms offer the advantage that the geometry and activity distribution is known and serve as a form of "truth" to which the quantified activity and dose distributions can be compared. This is unlike clinical patient data where the estimates are calculated from images that have been tainted by the imaging process already serving as an unknown. Digital voxel-based phantoms are created from CT data of physical phantoms and patients. Even though the imaging process has blurred the clinical patient images, the patient data represent the realism of clinical practice and are the best means of patient-specific quantification and dosimetry.

For this reason, and unique to this study, is the creation of patient-specific voxel-based phantom models from our clinic's patient CT data readily available from the hybrid SPECT/CT systems. These images are segmented to create patient-specific phantoms and converted from CT Hounsfield units to density maps to perform MC simulation of photon transport for SPECT/CT imaging and dosimetry. The advantage of such patient models is that they represent the patient's clinically realistic geometry with known volumes and true activity distributions that the imaging process has not degraded. The use of patient-specific phantom models in this way reduces errors that may be encountered clinically in the dosimetry steps, such as misregistrations in multiple SPECT/CT time-points and volume definitions. Virtual dosimetry performed using these voxel-based phantoms and MC simulations will provide the accuracy of the SPECT/CT activity quantification and the patient-specific MC dosimetry. Both the activity quantification and dosimetry will have known true values, which will serve as input into the virtual imaging and dosimetry clinical workflow chain. The results obtained after the virtual imaging dosimetry computations can be compared to the true values and provide the activity quantification and dosimetry accuracy, and thus the aim of this study.

1.4 Aim and Objectives

This study aimed *to determine the accuracy of ^{177}Lu SPECT activity quantification and patient-specific dosimetry using Monte Carlo simulations.* The study incorporated voxel-based phantoms obtained from CT data to perform virtual image activity quantification and dosimetry focussing on the bio-distribution of ^{177}Lu-DOTATATE in patients with metastasized NETs. The study was designed in three parts (Objective I – III) to cover the main steps of image-based activity quantification and dosimetry to fulfill a doctoral thesis using the article-based method.

The study included the following objectives, which were presented as three research articles, designed to:

Objective I	Validate a model of the Siemens Symbia dual-head gamma camera using the SIMIND MC program for ^{177}Lu imaging.
Objective II	Investigate the effect of two CF geometries and their corresponding RCs on the quantification accuracy of ^{177}Lu SPECT images using MC simulations.
Objective III	Evaluate SPECT/CT dosimetry accuracy of LundADose and OLINDA for ^{177}Lu RPT using voxel-based patient-specific phantoms.

1.5 Summary of Articles

This section summarises the work presented in objectives I to III, presented as articles I to III, respectively. The content of the sections follows the same logical progression as the original articles presented in Chapters 2 to 4.

Article I: *Validation of a Monte Carlo modelled gamma camera for Lutetium-177 imaging.*
Publication Status: Published in the Journal of Applied Radiation and Isotopes.
DOI: https://doi.org/10.1016/j.apradiso.2020.109200 (Appendix A-1)

MC techniques have gained wide favour in the NM field, particularly for optimising SPECT imaging with the gamma camera. However, gamma cameras are subject to detector and electronic changes. Thus it is essential to validate the capability of MC programs to model clinical gamma cameras. Therefore, the purpose of this article was to validate a model of the Siemens Symbia dual-head gamma camera using the SIMIND MC program for ^{177}Lu imaging. This was achieved by comparing the simulated results obtained with the modelled gamma camera to the experimental results of the clinical gamma camera. The results from the simulation data and those of the experiments compared well. The validation provided the confidence to use SIMIND for further investigations of ^{177}Lu SPECT/CT quantification.

Article II: *The effect of calibration factors and recovery coefficients on ^{177}Lu SPECT activity quantification accuracy: a Monte Carlo study.*
Publication Status: Published in the European Journal of Nuclear Medicine and Molecular Imaging.
DOI: https://doi.org/10.1186/s40658-021-00365-8 (Appendix B)

The study investigated the effect of sphere and cylinder CF geometries and their corresponding RCs on the quantification accuracy of ^{177}Lu SPECT images using MC simulations. The CFs were obtained from: (i) a radioactive sphere surrounded by non-radioactive water (sphere CF), and (ii) a cylindrical phantom uniformly filled with radioactive water (cylinder-CF). Two RC curves were generated for PVC using the sphere-CF to generate the sphere-RC and the cylinder-CF to generate the cylinder-RC. The effects of the sphere-CF-RC and cylinder-CF-RC combinations on the quantification accuracy of ^{177}Lu activity derived from SPECT images were evaluated using three voxel-based phantom geometries: a cylindrical, torso, and patient-specific phantom. The quantification accuracy was evaluated for spherical structures mimicking tumours and the kidneys. The results demonstrated that ^{177}Lu SPECT quantification accuracies compared favourably upon careful selection of sphere-based (≤ 3.47%) and cylinder-based (≤ 3.53%) CF and RCs combinations when all SPECT corrections were applied. Our absolute quantification accuracy of less than 5% compared well to literature findings and complied with requirements for accurate dosimetry.

Article III:	*Accuracy of two dosimetry software programs for ^{177}Lu radiopharmaceutical therapy using voxel-based patient-specific phantoms.*
Publication Status:	Under review at Heliyon.
DOI:	http://dx.doi.org/10.2139/ssrn.3958626 (Appendix C)

There has been extensive work on ^{177}Lu-DOTATATE dosimetry, and reports demonstrate variations in absorbed doses. This variation is caused by the different methodologies used in the clinics. As a result, dosimetry with ^{177}Lu-DOTATATE remains an ongoing investigation with scope for optimising the steps and methods in the clinical dosimetry workflow. Due to these reported variations, an investigation into the dosimetry accuracy becomes an important factor to consider. Therefore, this work presented a comparative study on the accuracy of two dosimetry software platforms: LundADose and OLINDA, using voxel-based patient-specific phantoms. The study was based on SPECT imaging of three phantoms with ^{177}Lu-DOTATATE distribution using MC simulations. The use of virtual dosimetry and MC simulations offered the advantage of having a gold standard against which the dosimetry accuracy of the software platforms could be evaluated. The gold standard was established from true TIA determined from the pre-defined activity images that had not undergone image degradation and applied full MC dosimetry. The accuracy between LundADose (6.59%) and OLINDA/EXM 1.0 (8.11%) was comparable. Overall, the less than 10% dosimetry accuracy suggested that the software platforms approximate the true doses.

1.6 References

1. Wahl RL, Ahuja S, Clarke B. Current Landscape of Radiopharmaceutical Therapies: SNMMI Therapy Task Force Survey. J Nucl Med Off Publ Soc Nucl Med. 2021 May 10;62(5):11N-16N.

2. Brans B, Bodei L, Giammarile F, Linden O, Luster M, Oyen WJG, et al. Clinical radionuclide therapy dosimetry: the quest for the ‘Holy Gray’. Eur J Nucl Med Mol Imaging. 2007 May;34(5):772–86. https://doi: 10.1007/s00259-006-0338-5

3. Dale R, Carabe-Fernandez A. The radiobiology of conventional radiotherapy and its application to radionuclide therapy. Cancer Biother Radiopharm. 2005 Feb;20(1):47–51. https://doi.org/10.1089/cbr.2005.20.47

4. Sgouros G, Bodei L, McDevitt MR, Nedrow JR. Radiopharmaceutical therapy in cancer: clinical advances and challenges. Nat Rev Drug Discov. 2020 Sep;19(9):589–608. https://doi.org/10.1038/s41573-020-0073-9

5. Sgouros G, Chiu S, Pentlow KS, Brewster LJ, Kalaigian H, Baldwin B, et al. Three-Dimensional Dosimetry for Radioimmunotherapy Treatment Planning. J Nucl Med. 1993 Sep 1;34(9):1595–601.

6. Strigari L, Konijnenberg M, Chiesa C, Bardies M, Du Y, Gleisner KS, et al. The evidence base for the use of internal dosimetry in the clinical practice of molecular radiotherapy. Eur J Nucl Med Mol Imaging. 2014 Oct;41(10):1976–88. https://doi: 10.1007/s00259-014-2824-5

7. Volkert WA, Goeckeler WF, Ehrhardt GJ, Ketring AR. Therapeutic radionuclides: production and decay property considerations. J Nucl Med Off Publ Soc Nucl Med. 1991 Jan;32(1):174–85.

8. Ersahin D, Doddamane I, Cheng D. Targeted Radionuclide Therapy. Cancers. 2011 Oct 11;3(4):3838–55. https://doi.org/10.3390/cancers3043838

9. Institute of Medicine (US) and National Research Council (US). Advancing Nuclear Medicine Through Innovation. Washington (DC): The National Academies Press (US); 2007. https://doi.org/10.17226/11985

10. Pillai MRA, Chakraborty S, Das T, Venkatesh M, Ramamoorthy N. Production logistics of ^{177}Lu for radionuclide therapy. Appl Radiat Isot Data Instrum Methods Use Agric Ind Med. 2003 Sep;59(2–3):109–18. https://doi:10.1016/s0969-8043(03)00158-1

11. Sjögreen Gleisner K, Spezi E, Solny P, Gabina PM, Cicone F, Stokke C, et al. Variations in the practice of molecular radiotherapy and implementation of dosimetry: results from a European survey. EJNMMI Phys. 2017 Dec 4;4(1):28. https://doi.org/10.1186/s40658-017-0193-4

12. Fendler WP, Rahbar K, Herrmann K, Kratochwil C, Eiber M. ^{177}Lu-PSMA Radioligand Therapy for Prostate Cancer. J Nucl Med. 2017 Aug 1;58(8):1196–200. https://doi: 10.2967/jnumed.117.191023

13. Stokke C, Gabiña PM, Solný P, Cicone F, Sandström M, Gleisner KS, et al. Dosimetry-based treatment planning for molecular radiotherapy: a summary of the 2017 report from the Internal Dosimetry Task Force. EJNMMI Phys. 2017 Nov 21;4(1):27. https://doi.org/10.1186/s40658-017-0194-3

14. Nelson BJB, Andersson JD, Wuest F. Targeted Alpha Therapy: Progress in Radionuclide Production, Radiochemistry, and Applications. Pharmaceutics. 2020 Dec 31;13(1):49. https://doi:10.3390/pharmaceutics13010049

15. Bodei L, Cremonesi M, Grana CM, Fazio N, Iodice S, Baio SM, et al. Peptide receptor radionuclide therapy with ^{177}Lu-DOTATATE: the IEO phase I-II study. Eur J Nucl Med Mol Imaging. 2011 Dec;38(12):2125–35. https://doi.org/10.1007/s00259-011-1902-1

16. Kwekkeboom DJ, Bakker WH, Kooij PP, Konijnenberg MW, Srinivasan A, Erion JL, et al. [^{177}Lu-DOTAOTyr3]octreotate: comparison with [^{111}In-DTPAo]octreotide in patients. Eur J Nucl Med. 2001 Sep;28(9):1319–25.

17. Pauwels S, Barone R, Walrand S, Borson-Chazot F, Valkema R, Kvols LK, et al. Practical dosimetry of peptide receptor radionuclide therapy with ^{90}Y-labeled somatostatin analogs. J Nucl Med Off Publ Soc Nucl Med. 2005 Jan;46 Suppl 1:92S-8S.

18. Laboratoire National Henri Becquerel (LNHB). Nuclear data: Table of Radionuclides; 2008. (http://www.lnhb.fr/nuclear-data/nuclear-data-table). [Accessed 2021 Nov 04]

19. Beauregard J-M, Hofman MS, Pereira JM, Eu P, Hicks RJ. Quantitative ^{177}Lu SPECT (QSPECT) imaging using a commercially available SPECT/CT system. Cancer Imaging Off Publ Int Cancer Imaging Soc. 2011 Jun 15;11:56–66. https://doi:10.1102/1470-7330.2011.0012

20. Sandström M, Garske-Román U, Johansson S, Granberg D, Sundin A, Freedman N. Kidney dosimetry during ^{177}Lu-DOTATATE therapy in patients with neuroendocrine tumors: aspects on calculation and tolerance. Acta Oncol. 2018 Apr 3;57(4):516–21. https://doi.org/10.1080/0284186X.2017.1378431

21. Dash A, Pillai MRA, Knapp FF. Production of ^{177}Lu for Targeted Radionuclide Therapy: Available Options. Nucl Med Mol Imaging. 2015 Jun;49(2):85–107. https://doi.org/10.1007/s13139-014-0315-z

22. Zaknun JJ, Bodei L, Mueller-Brand J, Pavel ME, Baum RP, Hörsch D, et al. The joint IAEA, EANM, and SNMMI practical guidance on peptide receptor radionuclide therapy (PRRNT) in neuroendocrine tumours. Eur J Nucl Med Mol Imaging. 2013;40(5):800–16. https://doi.org/10.1007/s00259-012-2330-6

23. Reijonen V, Kanninen LK, Hippeläinen E, Lou Y-R, Salli E, Sofiev A, et al. Multicellular dosimetric chain for molecular radiotherapy exemplified with dose simulations on 3D cell spheroids. Phys Medica PM Int J Devoted Appl Phys Med Biol Off J Ital Assoc Biomed Phys AIFB. 2017 Aug;40:72–8. https://doi.org/10.1016/j.ejmp.2017.07.012

24. Uribe CF, Esquinas PL, Gonzalez M, Celler A. Characteristics of Bremsstrahlung emissions of ^{177}Lu, ^{188}Re, and ^{90}Y for SPECT/CT quantification in radionuclide therapy. Phys Medica PM Int J Devoted Appl Phys Med Biol Off J Ital Assoc Biomed Phys AIFB. 2016 May;32(5):691–700. https://doi.org/10.1016/j.ejmp.2016.04.014

25. Breeman WAP, De Jong M, Visser TJ, Erion JL, Krenning EP. Optimising conditions for radiolabelling of DOTA-peptides with ^{90}Y, ^{111}In and ^{177}Lu at high specific activities. Eur J Nucl Med Mol Imaging. 2003 Jun;30(6):917–20. https://doi.org/10.1007/s00259-003-1142-0

26. Bard DR, Knight CG, Page-Thomas DP. Effect of the intra-articular injection of lutetium-177 in chelator liposomes on the progress of an experimental arthritis in rabbits. Clin Exp Rheumatol. 1985 Sep;3(3):237–42.

27. O’Mara RE, McAfee JG, Subramanian G. Rare earth nuclides as potential agents for skeletal imaging. J Nucl Med Off Publ Soc Nucl Med. 1969 Jan;10(1):49–51.

28. Frilling A, Weber F, Saner F, Bockisch A, Hofmann M, Mueller-Brand J, et al. Treatment with ^{90}Y- and ^{177}Lu-DOTATOC in patients with metastatic neuroendocrine tumors. Surgery. 2006 Dec;140(6):968–76; discussion 976-977. https://doi.org/10.1016/j.surg.2006.07.030

29. Kwekkeboom DJ, de Herder WW, Kam BL, van Eijck CH, van Essen M, Kooij PP, et al. Treatment with the radiolabeled somatostatin analog [^{177} Lu-DOTA 0,Tyr3]octreotate: toxicity, efficacy, and survival. J Clin Oncol Off J Am Soc Clin Oncol. 2008 May 1;26(13):2124–30. https://doi.org/10.1200/JCO.2007.15.2553

30. Maecke HR, Reubi JC. Somatostatin receptors as targets for nuclear medicine imaging and radionuclide treatment. J Nucl Med Off Publ Soc Nucl Med. 2011 Jun;52(6):841–4. https://doi.org/10.2967/jnumed.110.084236

31. Swärd C, Bernhardt P, Johanson V, Schmitt A, Ahlman H, Stridsberg M, et al. Comparison of [^{177}Lu-DOTA0,Tyr3]-octreotate and [^{177}Lu-DOTA0,Tyr3]-octreotide for receptor-mediated radiation therapy of the xenografted human midgut carcinoid tumor GOT1. Cancer Biother Radiopharm. 2008 Feb;23(1):114–20. https://doi: 10.1089/cbr.2007.0421

32. Wehrmann C, Senftleben S, Zachert C, Müller D, Baum RP. Results of individual patient dosimetry in peptide receptor radionuclide therapy with ^{177}Lu DOTA-TATE and ^{177}Lu DOTA-NOC. Cancer Biother Radiopharm. 2007 Jun;22(3):406–16. https://doi.org/10.1089/cbr.2006.325

33. Strosberg J, El-Haddad G, Wolin E, Hendifar A, Yao J, Chasen B, et al. Phase 3 Trial of ^{177}Lu-Dotatate for Midgut Neuroendocrine Tumors. N Engl J Med. 2017 12;376(2):125–35. https://doi.org/10.1056/NEJMoa1607427

34. Esser JP, Krenning EP, Teunissen JJM, Kooij PPM, van Gameren ALH, Bakker WH, et al. Comparison of [^{177}Lu-DOTA(0),Tyr(3)]octreotate and [^{177}Lu-DOTA(0),Tyr(3)]octreotide: which peptide is preferable for PRRT? Eur J Nucl Med Mol Imaging. 2006 Nov;33(11):1346–51. https://doi.org/10.1007/s00259-006-0172-9

35. Kam BLR, Teunissen JJM, Krenning EP, de Herder WW, Khan S, van Vliet EI, et al. Lutetium-labelled peptides for therapy of neuroendocrine tumours. Eur J Nucl Med Mol Imaging. 2012 Feb;39(Suppl 1):103–12. https://doi.org/10.1007/s00259-011-2039-y

36. Khan S, Krenning EP, van Essen M, Kam BL, Teunissen JJ, Kwekkeboom DJ. Quality of life in 265 patients with gastroenteropancreatic or bronchial neuroendocrine tumors treated with [^{177}Lu-DOTA0,Tyr3]octreotate. J Nucl Med Off Publ Soc Nucl Med. 2011 Sep;52(9):1361–8. https://doi.org/10.2967/jnumed.111.087932

37. Cremonesi M, Botta F, Di Dia A, Ferrari M, Bodei L, De Cicco C, et al. Dosimetry for treatment with radiolabelled somatostatin analogues. A review. Q J Nucl Med Mol Imaging Off Publ Ital Assoc Nucl Med AIMN Int Assoc Radiopharmacol IAR Sect Soc Of. 2010 Feb;54(1):37–51.

38. de Jong M, Breeman WAP, Valkema R, Bernard BF, Krenning EP. Combination radionuclide therapy using ^{177}Lu- and ^{90}Y-labeled somatostatin analogs. J Nucl Med Off Publ Soc Nucl Med. 2005 Jan;46 Suppl 1:13S-7S.

39. Wong JYC, Shibata S, Williams LE, Kwok CS, Liu A, Chu DZ, et al. A Phase I trial of ^{90}Y-anti-carcinoembryonic antigen chimeric T84.66 radioimmunotherapy with 5-fluorouracil in patients with metastatic colorectal cancer. Clin Cancer Res Off J Am Assoc Cancer Res. 2003 Dec 1;9(16 Pt 1):5842–52.

40. Rich TA, Shepard RC, Mosley ST. Four decades of continuing innovation with fluorouracil: current and future approaches to fluorouracil chemoradiation therapy. J Clin Oncol Off J Am Soc Clin Oncol. 2004 Jun 1;22(11):2214–32. https://doi.org/10.1200/JCO.2004.08.009

41. de Araújo EB, Caldeira Filho JS, Nagamati LT, Muramoto E, Colturato MT, Couto RM, et al. A comparative study of ^{131}I and ^{177}Lu labeled somatostatin analogues for therapy of neuroendocrine tumours. Appl Radiat Isot Data Instrum Methods Use Agric Ind Med. 2009 Feb;67(2):227–33. https://doi.org/10.1016/j.apradiso.2008.09.009

42. Demirci E, Kabasakal L, Toklu T, Ocak M, Şahin OE, Alan-Selcuk N, et al. ^{177}Lu-DOTATATE therapy in patients with neuroendocrine tumours including high-grade (WHO G3) neuroendocrine tumours: response to treatment and long-term survival update. Nucl Med Commun. 2018 Aug;39(8):789–96. https://doi.org/10.1097/MNM.0000000000000874

43. Bodei L, Mueller-Brand J, Baum RP, Pavel ME, Hörsch D, O'Dorisio MS, et al. The joint IAEA, EANM, and SNMMI practical guidance on peptide receptor radionuclide therapy (PRRNT) in neuroendocrine tumours. Eur J Nucl Med Mol Imaging. 2013 May;40(5):800–16. https://doi.org/10.1007/s00259-012-2330-6

44. Essen MV, Krenning EP, Jong MD, Valkema R, Kwekkeboom DJ. Peptide Receptor Radionuclide Therapy with radiolabelled somatostatin analogues in patients with somatostatin receptor positive tumours. Acta Oncol. 2007 Jan 1;46(6):723–34. https://doi.org/10.1080/02841860701441848

45. Vliet EI van, Teunissen JJM, Kam BLR, Jong M de, Krenning EP, Kwekkeboom DJ. Treatment of Gastroenteropancreatic Neuroendocrine Tumors with Peptide Receptor Radionuclide Therapy. Neuroendocrinology. 2013;97(1):74–85. https://doi.org/10.1159/000335018

46. Rindi G. The ENETS guidelines: the new TNM classification system. Tumori. 2010 Oct;96(5):806–9. https://doi.org/10.1177/030089161009600532

47. Sathekge M. Targeted radionuclide therapy. Contin Med Educ. 2013 Aug 3;31(8):289–94.

48. Ambrosini V, Campana D, Bodei L, Nanni C, Castellucci P, Allegri V, et al. ^{68}Ga-DOTANOC PET/CT clinical impact in patients with neuroendocrine tumors. J Nucl Med Off Publ Soc Nucl Med. 2010 May;51(5):669–73. https://doi.org/10.2967/jnumed.109.071712

49. Gabriel M, Decristoforo C, Kendler D, Dobrozemsky G, Heute D, Uprimny C, et al. ^{68}Ga-DOTA-Tyr3-octreotide PET in neuroendocrine tumors: comparison with somatostatin receptor scintigraphy and CT. J Nucl Med Off Publ Soc Nucl Med. 2007 Apr;48(4):508–18. https://doi: 10.2967/jnumed.106.035667

50. Virgolini I, Ambrosini V, Bomanji JB, Baum RP, Fanti S, Gabriel M, et al. Procedure guidelines for PET/CT tumour imaging with ^{68}Ga-DOTA-conjugated peptides: ^{68}Ga-DOTA-TOC, ^{68}Ga-DOTA-NOC, ^{68}Ga-DOTA-TATE. Eur J Nucl Med Mol Imaging. 2010 Oct;37(10):2004–10. https://doi.org/10.1007/s00259-010-1512-3

51. Seidlin SM, Marinelli LD, Oshry E. Radioactive iodine therapy: Effect on Functioning Metastases of Adenocarcinoma of the Thyroid. J Am Med Assoc. 1946 Dec 7;132(14):838–47. https://doi.org/10.1001/jama.1946.02870490016004

52. Funkhouser J. Reinventing pharma: The theranostic revolution. Curr Drug Discov. 2002 Aug 1;17–9.

53. DeNardo GL, O'Donnell RT, Shen S, Kroger LA, Yuan A, Meares CF, et al. Radiation dosimetry for ^{90}Y-2IT-BAD-Lym-1 extrapolated from pharmacokinetics using ^{111}In-2IT-BAD-Lym-1 in patients with non-Hodgkin's lymphoma. J Nucl Med Off Publ Soc Nucl Med. 2000 May;41(5):952–8.

54. Loke KSH, Padhy AK, Ng DCE, Goh ASW, Divgi C. Dosimetric Considerations in Radioimmunotherapy and Systemic Radionuclide Therapies: A Review. World J Nucl Med. 2011;10(2):122–38. https://doi.org/10.4103/1450-1147.89780

55. Bakker WH, Breeman W a. P, Kwekkeboom DJ, De Jong LC, Krenning EP. Practical aspects of peptide receptor radionuclide therapy with [^{177}Lu][DOTA0, Tyr3]octreotate. Q J Nucl Med Mol Imaging Off Publ Ital Assoc Nucl Med AIMN Int Assoc Radiopharmacol IAR Sect Soc Of. 2006 Dec;50(4):265–71.

56. European Medicines Agency. Lumark: Summary of product characteristics - Lu (^{177}Lu) chloride. Amsterdam, Netherlands; 2018. (https://www.ema.europa.eu/en/medicines/human/EPAR/lumark#product-information-section). [Accessed 2018 Jun 26]

57. Olmstead C, Cruz K, Stodilka R, Zabel P, Wolfson R. Quantifying public radiation exposure related to lutetium-177 octreotate therapy for the development of a safe outpatient treatment protocol. Nucl Med Commun. 2015 Feb;36(2):129–34. https://doi.org/10.1097/MNM.0000000000000232

58. ARPANSA Radiation protection series 4. Recommendations: Discharge of Patients Undergoing Treatment with Radioactive Substances; 2002. (https://www.arpansa.gov.au/sites/default/files/legacy/pubs/rps/rps4.pdf). [Accessed 2020 Jun 26]

59. Calais PJ, Turner JH. Radiation safety of outpatient ^{177}Lu-octreotate radiopeptide therapy of neuroendocrine tumors. Ann Nucl Med. 2014 Jul;28(6):531–9. https://doi.org/10.1007/s12149-014-0843-8

60. Radojewski P, Dumont R, Marincek N, Brunner P, Mäcke HR, Müller-Brand J, et al. Towards tailored radiopeptide therapy. Eur J Nucl Med Mol Imaging. 2015 Jul;42(8):1231–7. https://doi.org/10.1007/s00259-015-3030-9

61. Garkavij M, Nickel M, Sjögreen-Gleisner K, Ljungberg M, Ohlsson T, Wingårdh K, et al. ^{177}Lu-[DOTA0,Tyr3] octreotate therapy in patients with disseminated neuroendocrine tumors: Analysis of dosimetry with impact on future therapeutic strategy. Cancer. 2010 Feb 15;116(4 Suppl):1084–92. https://doi.org/10.1002/cncr.24796

62. Krenning EP, Bakker WH, Breeman WA, Koper JW, Kooij PP, Ausema L, et al. Localisation of endocrine-related tumours with radioiodinated analogue of somatostatin. Lancet Lond Engl. 1989 Feb 4;1(8632):242–4. https://doi: 10.1016/s0140-6736(89)91258-0

63. Oyen WJG, Bodei L, Giammarile F, Maecke HR, Tennvall J, Luster M, et al. Targeted therapy in nuclear medicine—current status and future prospects. Ann Oncol. 2007 Nov 1;18(11):1782–92. https://doi: 10.1093/annonc/mdm111

64. Behr TM, Sharkey RM, Sgouros G, Blumenthal RD, Dunn RM, Kolbert K, et al. Overcoming the nephrotoxicity of radiometal-labeled immunoconjugates: improved

cancer therapy administered to a nude mouse model in relation to the internal radiation dosimetry. Cancer. 1997 Dec 15;80(12 Suppl):2591–610.

65. Boerman OC, Oyen WJ, Corstens FH. Between the Scylla and Charybdis of peptide radionuclide therapy: hitting the tumor and saving the kidney. Eur J Nucl Med. 2001 Oct;28(10):1447–9. https://doi: 10.1007/s002590100597

66. Breitz HB, Fisher DR, Goris ML, Knox S, Ratliff B, Murtha AD, et al. Radiation absorbed dose estimation for ^{90}Y-DOTA-biotin with pretargeted NR-LU-10/streptavidin. Cancer Biother Radiopharm. 1999 Oct;14(5):381–95. https://doi.org/10.1089/cbr.1999.14.381

67. Casey JL, Pedley RB, King DJ, Green AJ, Yarranton GT, Begent RH. Dosimetric evaluation and radioimmunotherapy of anti-tumour multivalent Fab' fragments. Br J Cancer. 1999 Nov;81(6):972–80. https://doi.org/10.1038/sj.bjc.6690795

68. Cohen EP, Moulder JE, Robbins ME. Radiation nephropathy caused by yttrium 90. Lancet Lond Engl. 2001 Sep 29;358(9287):1102–3. https://doi.org/10.1016/S0140-6736(01)06220-1

69. Flynn AA, Pedley RB, Green AJ, Dearling JL, El-Emir E, Boxer GM, et al. The nonuniformity of antibody distribution in the kidney and its influence on dosimetry. Radiat Res. 2003 Feb;159(2):182–9.

70. Moll S, Nickeleit V, Mueller-Brand J, Brunner FP, Maecke HR, Mihatsch MJ. A new cause of renal thrombotic microangiopathy: yttrium 90-DOTATOC internal radiotherapy. Am J Kidney Dis Off J Natl Kidney Found. 2001 Apr;37(4):847–51. https://doi:10.1016/S0272-6386(01)80135-9

71. Dewaraja Y, Wilderman S, Niedbala J, Frey K, Wong KK. Multi SPECT/CT-based patient specific lesion and kidney dosimetry for verification of simpler approaches for treatment planning in Lu-177 DOTATATE PRRT. J Nucl Med. 2019 May 1;60(supplement 1):1626–1626.

72. Sandström M, Freedman N, Fröss-Baron K, Kahn T, Sundin A. Kidney dosimetry in 777 patients during ^{177}Lu-DOTATATE therapy: aspects on extrapolations and measurement time points. EJNMMI Phys. 2020 Dec 9;7(1):73. https://doi.org/10.1186/s40658-020-00339-2

73. Sundlöv A, Sjögreen-Gleisner K, Svensson J, Ljungberg M, Olsson T, Bernhardt P, et al. Individualised ^{177}Lu-DOTATATE treatment of neuroendocrine tumours based on kidney dosimetry. Eur J Nucl Med Mol Imaging. 2017 Aug;44(9):1480–9. https://doi.org/10.1007/s00259-017-3678-4

74. Willowson KP, Eslick E, Ryu H, Poon A, Bernard EJ, Bailey DL. Feasibility and accuracy of single time point imaging for renal dosimetry following ^{177}Lu-DOTATATE ('Lutate') therapy. EJNMMI Phys. 2018 Dec 20;5(1):33. https://doi:10.1186/s40658-018-0232-9

75. Emami B, Lyman J, Brown A, Coia L, Goitein M, Munzenrider JE, et al. Tolerance of normal tissue to therapeutic irradiation. Int J Radiat Oncol Biol Phys. 1991 May 15;21(1):109–22. https://doi: 10.1016/0360-3016(91)90171-y

76. Cassady JR. Clinical radiation nephropathy. Int J Radiat Oncol Biol Phys. 1995 Mar 30;31(5):1249–56. https://doi.org/10.1016/0360-3016(94)00428-N

77. Fowler JF. Radiobiological aspects of low dose rates in radioimmunotherapy. Int J Radiat Oncol Biol Phys. 1990 May;18(5):1261–9. http://doi: 10.1016/0360-3016(90)90467-x

78. International Commission on Radiation Units. ICRU Report 67: Absorbed-Dose Specification in Nuclear Medicine. International C, editor. J ICRU. 2002 Jan 1;2(1):5–105.

79. Langmuir VK, Fowler JF, Knox SJ, Wessels BW, Sutherland RM, Wong JY. Radiobiology of radiolabeled antibody therapy as applied to tumor dosimetry. Med Phys. 1993 Apr;20(2 Pt 2):601–10. https://doi.org/10.1118/1.597055

80. Valkema R, Pauwels SA, Kvols LK, Kwekkeboom DJ, Jamar F, de Jong M, et al. Long-term follow-up of renal function after peptide receptor radiation therapy with ^{90}Y-DOTA(0),Tyr(3)-octreotide and ^{177}Lu-DOTA(0), Tyr(3)-octreotate. J Nucl Med Off Publ Soc Nucl Med. 2005 Jan;46 Suppl 1:83S-91S.

81. Sandström M, Garske U, Granberg D, Sundin A, Lundqvist H. Individualized dosimetry in patients undergoing therapy with ^{177}Lu-DOTA-D-Phe (1)-Tyr (3)-octreotate. Eur J Nucl Med Mol Imaging. 2010 Feb;37(2):212–25. https://doi.org/10.1007/s00259-009-1216-8

82. Guerriero F, Ferrari ME, Botta F, Fioroni F, Grassi E, Versari A, et al. Kidney Dosimetry in ^{177}Lu and ^{90}Y Peptide Receptor Radionuclide Therapy: Influence of Image Timing, Time-Activity Integration Method, and Risk Factors. BioMed Research International. 2013. https://doi.org/10.1155/2013/935351

83. Kwekkeboom DJ, Teunissen JJ, Bakker WH, Kooij PP, de Herder WW, Feelders RA, et al. Radiolabeled somatostatin analog [^{177}Lu-DOTA0,Tyr3]octreotate in patients with endocrine gastroenteropancreatic tumors. J Clin Oncol Off J Am Soc Clin Oncol. 2005 Apr 20;23(12):2754–62. https://doi.org/10.1200/JCO.2005.08.066

84. Bodei L, Cremonesi M, Zoboli S, Grana C, Bartolomei M, Rocca P, et al. Receptor-mediated radionuclide therapy with ^{90}Y-DOTATOC in association with amino acid infusion: a phase I study. Eur J Nucl Med Mol Imaging. 2003 Feb;30(2):207–16. https://doi.org/10.1007/s00259-002-1023-y

85. Bodei L, Cremonesi M, Ferrari M, Pacifici M, Grana CM, Bartolomei M, et al. Long-term evaluation of renal toxicity after peptide receptor radionuclide therapy with ^{90}Y-DOTATOC and ^{177}Lu-DOTATATE: the role of associated risk factors. Eur J Nucl Med Mol Imaging. 2008 Oct;35(10):1847–56. https://doi.org/10.1007/s00259-008-0778-1

86. Bouchet LG, Bolch WE, Blanco HP, Wessels BW, Siegel JA, Rajon DA, et al. MIRD Pamphlet No 19: absorbed fractions and radionuclide S values for six age-dependent multiregion models of the kidney. J Nucl Med Off Publ Soc Nucl Med. 2003 Jul;44(7):1113–47.

87. Cristy M, Eckerman KF. Specific absorbed fractions of energy at various ages from internal photon sources: 7, Adult male. Oak Ridge National Lab.; 1987. Report No.: ORNL/TM--8381/V7.

88. Helisch A, Förster GJ, Reber H, Buchholz H-G, Arnold R, Göke B, et al. Pre-therapeutic dosimetry and biodistribution of ^{86}Y-DOTA-Phe1-Tyr3-octreotide versus ^{111}In-pentetreotide in patients with advanced neuroendocrine tumours. Eur J Nucl Med Mol Imaging. 2004 Oct;31(10):1386–92. https://doi.org/10.1007/s00259-004-1561-6

89. Ilan E, Sandström M, Wassberg C, Sundin A, Garske-Román U, Eriksson B, et al. Dose response of pancreatic neuroendocrine tumors treated with peptide receptor radionuclide therapy using ^{177}Lu-DOTATATE. J Nucl Med Off Publ Soc Nucl Med. 2015 Feb;56(2):177–82. https://doi.org/10.2967/jnumed.114.148437

90. Valkema R, Konijnenberg M, Pauwels S, Kvols L, Krenning E. How much dosimetry is needed for therapeutic applications? University Medical Center Rotterdam; 2010. (https://www.osti.gov/etdeweb/servlets/purl/21433208). [Accessed 2021 Jul 03]

91. Lassmann M, Chiesa C, Flux G, Bardiès M. EANM Dosimetry Committee guidance document: good practice of clinical dosimetry reporting. Eur J Nucl Med Mol Imaging. 2011 Jan;38(1):192–200. https://doi.org/10.1007/s00259-010-1549-3

92. Bailey DL, Hennessy TM, Willowson KP, Henry EC, Chan DLH, Aslani A, et al. In vivo quantification of ^{177}Lu with planar whole-body and SPECT/CT gamma camera imaging. EJNMMI Phys. 2015 Sep 17;2. https://doi.org/10.1186/s40658-015-0123-2

93. Bailey DL, Willowson KP. Quantitative SPECT/CT: SPECT joins PET as a quantitative imaging modality. Eur J Nucl Med Mol Imaging. 2014 May;41 Suppl 1:S17-25. https://doi.org/10.1007/s00259-013-2542-4

94. Hippeläinen E, Tenhunen M, Mäenpää H, Sohlberg A. Quantitative accuracy of ^{177}Lu SPECT reconstruction using different compensation methods: phantom and patient studies. EJNMMI Res. 2016 Feb 18;6. https://doi.org/10.1186/s13550-016-0172-0

95. Ljungberg M, Celler A, Konijnenberg MW, Eckerman KF, Dewaraja YK, Sjögreen-Gleisner K, et al. MIRD Pamphlet No. 26: Joint EANM/MIRD Guidelines for Quantitative ^{177}Lu SPECT Applied for Dosimetry of Radiopharmaceutical Therapy. J Nucl Med Off Publ Soc Nucl Med. 2016 Jan;57(1):151–62. https://doi.org/10.2967/jnumed.115.159012

96. Ljungberg M, Sjögreen Gleisner K. Personalized Dosimetry for Radionuclide Therapy Using Molecular Imaging Tools. Biomedicines. 2016 Nov 15;4(4). https://doi.org/10.3390/biomedicines4040025

97. Peters SMB, Meyer Viol SL, van der Werf NR, de Jong N, van Velden FHP, Meeuwis A, et al. Variability in lutetium-177 SPECT quantification between different state-of-the-art SPECT/CT systems. EJNMMI Phys. 2020 Feb 11;7(1):9. https://doi.org/10.1186/s40658-020-0278-3

98. International Atomic Energy Agency (IAEA). Chapter 5 - Quantitative SPECT OR SPECT/CT imaging. In: Quantitative nuclear medicine imaging: concepts, requirements and methods. IAEA Human Health Report No.9. Vienna, Austria: IAEA; 2014. p. 27–36.

99. Wevrett J, Fenwick A, Scuffham J, Johansson L, Gear J, Schlögl S, et al. Inter-comparison of quantitative imaging of lutetium-177 (^{177}Lu) in European hospitals. EJNMMI Phys. 2018 Aug 2;5(1):17. https://doi.org/10.1186/s40658-018-0213-z

100. Frey EC, Humm JL, Ljungberg M. Accuracy and precision of radioactivity quantification in nuclear medicine images. Semin Nucl Med. 2012 May;42(3):208–18. https://doi.org/10.1053/j.semnuclmed.2011.11.003

101. Ljungberg M, Sjögreen-Gleisner K. The accuracy of absorbed dose estimates in tumours determined by Quantitative SPECT: A Monte Carlo study. Acta Oncol. 2011 Aug 1;50(6):981–9. https://doi.org/10.3109/0284186X.2011.584559

102. Marin G, Vanderlinden B, Karfis I, Guiot T, Wimana Z, Flamen P, et al. Accuracy and precision assessment for activity quantification in individualized dosimetry of ^{177}Lu-DOTATATE therapy. EJNMMI Phys. 2017 Jan 26;4. https://doi.org/10.1186/s40658-017-0174-7

103. Uribe CF, Esquinas PL, Tanguay J, Gonzalez M, Gaudin E, Beauregard J-M, et al. Accuracy of ^{177}Lu activity quantification in SPECT imaging: a phantom study. EJNMMI Phys. 2017 Jan 7;4. https://doi.org/10.1186/s40658-016-0170-3

104. Siemens Healthineers. Symbia T Series SPECT/CT. (https://www.siemens-healthineers.com/en-us/molecular-imaging/spect-and-spect-ct/symbia-t) [Accessed 2019 Nov 7]

105. D'Arienzo M, Cazzato M, Cozzella ML, Cox M, D'Andrea M, Fazio A, et al. Gamma camera calibration and validation for quantitative SPECT imaging with ^{177}Lu. Appl Radiat Isot Data Instrum Methods Use Agric Ind Med. 2016;112:156–64. https://doi.org/10.1016/j.apradiso.2016.03.007

106. de Nijs R, Lagerburg V, Klausen TL, Holm S. Improving quantitative dosimetry in ^{177}Lu-DOTATATE SPECT by energy window-based scatter corrections. Nucl Med Commun. 2014 May;35(5):522–33. https://doi.org/10.1097/MNM.0000000000000079

107. He B, Nikolopoulou A, Osborne J, Vallabhajosula S, Goldsmith S. Quantitative SPECT imaging with Lu-177: A physical phantom evaluation. J Nucl Med. 2012 May 1;53(supplement 1):2407–2407.

108. Shcherbinin S, Piwowarska-Bilska H, Celler A, Birkenfeld B. Quantitative SPECT/CT reconstruction for ^{177} Lu and ^{177}Lu/^{90} Y targeted radionuclide therapies. Phys Med Biol. 2012;57(18):5733. https://doi.org/10.1088/0031-9155/57/18/5733

109. Delker A. Investigation of models with temporal and spatial interference in image based dosimetry of ^{177}Lu- labelled radioligand therapies. https://doi.org/10.5282/edoc.19714

110. Miller C, Filipow L, Jackson S. A Review of Activity Quantification by Planar Imaging Methods. J Nucl Med Technol. 1995;23(1):7..

111. Minarik D, Sjögreen K, Ljungberg M. A New Method to Obtain Transmission Images for Planar Whole-Body Activity Quantification. Cancer Biother Radiopharm. 2005 Feb 1;20(1):72–6. https://doi.org/10.1089/cbr.2005.20.72

112. Pereira JM, Stabin MG, Lima FRA, Guimarães MICC, Forrester JW. Image quantification for radiation dose calculations--limitations and uncertainties. Health Phys. 2010 Nov;99(5):688–701. https://doi.org/10.1097/HP.0b013e3181e28cdb

113. Sjögreen K, Ljungberg M, Wingårdh K, Minarik D, Strand S-E. The LundADose method for planar image activity quantification and absorbed-dose assessment in radionuclide therapy. Cancer Biother Radiopharm. 2005 Feb;20(1):92–7. https://doi.org/10.1089/cbr.2005.20.92

114. Cachovan M, Vija AH, Hornegger J, Kuwert T. Quantification of ^{99m}Tc-DPD concentration in the lumbar spine with SPECT/CT. EJNMMI Res. 2013 Jun 5;3:45. https://doi.org/10.1186/2191-219X-3-45

115. Gnesin S, Leite Ferreira P, Malterre J, Laub P, Prior JO, Verdun FR. Phantom Validation of Tc-99m Absolute Quantification in a SPECT/CT Commercial Device. Comput Math Methods Med. 2016;2016. https://doi.org/10.1155/2016/4360371

116. Willowson K, Bailey DL, Baldock C. Quantitative SPECT reconstruction using CT-derived corrections. Phys Med Biol. 2008 Jun 21;53(12):3099–112. https://doi.org/10.1088/0031-9155/53/12/002

117. Zimmerman BE, Grošev D, Buvat I, Coca Pérez MA, Frey EC, Green A, et al. Multi-centre evaluation of accuracy and reproducibility of planar and SPECT image quantification: An IAEA phantom study. Z Med Phys. 2017 Jun;27(2):98–112. https://doi.org/10.1016/j.zemedi.2016.03.008

118. Ljungberg M, Sjögreen Gleisner K. Hybrid Imaging for Patient-Specific Dosimetry in Radionuclide Therapy. Diagnostics. 2015 Jul 10;5(3):296–317. https://doi.org/10.3390/diagnostics5030296

119. Dewaraja YK, Frey EC, Sgouros G, Brill AB, Roberson P, Zanzonico PB, et al. MIRD pamphlet No. 23: quantitative SPECT for patient-specific 3-dimensional dosimetry in internal radionuclide therapy. J Nucl Med Off Publ Soc Nucl Med. 2012 Aug;53(8):1310–25. https://doi.org/10.2967/jnumed.111.100123

120. Shepp LA, Vardi Y. Maximum Likelihood Reconstruction for Emission Tomography. IEEE Trans Med Imaging. 1982 Oct;1(2):113–22. https://doi.org/10.1109/TMI.1982.4307558

121. Hudson HM, Larkin RS. Accelerated image reconstruction using ordered subsets of projection data. IEEE Trans Med Imaging. 1994;13(4):601–9. https://doi.org/10.1109/42.363108

122. Cherry SR, Sorenson JA, Phelps ME. Chapter 16 - Tomographic Reconstruction in Nuclear Medicine. In: Physics in Nuclear Medicine (Fourth Edition). Philadelphia: W.B. Saunders; 2012. p. 253–77. https://doi.org/10.1016/B978-1-4160-5198-5.00016-2

123. Kemin H. Impact of different reconstruction algorithms and OSEM reconstruction parameters on quantitative results in SPECT/CT. J Nucl Med. 2018 May 1;59(supplement 1):1800–1800. https://doi.org/10.13929/j.1003-3289.201704112

124. Dewaraja YK, Wilderman SJ, Ljungberg M, Koral KF, Zasadny K, Kaminiski MS. Accurate dosimetry in ^{131}I radionuclide therapy using patient-specific, 3-dimensional methods for SPECT reconstruction and absorbed dose calculation. J Nucl Med Off Publ Soc Nucl Med. 2005 May;46(5):840–9.

125. Patton JA, Turkington TG. SPECT/CT Physical Principles and Attenuation Correction. J Nucl Med Technol. 2008 Mar 1;36(1):1–10. https://doi.org/10.2967/jnmt.107.046839

126. Cherry SR, Sorenson JA, Phelps ME. Chapter 19 - Hybrid Imaging: SPECT/CT and PET/CT. In: Physics in Nuclear Medicine (Fourth Edition). Philadelphia: W.B. Saunders; 2012. p. 345–61. https://doi.org/10.1016/B978-1-4160-5198-5.00019-8

127. Ritt P, Vija H, Hornegger J, Kuwert T. Absolute quantification in SPECT. Eur J Nucl Med Mol Imaging. 2011 May;38 Suppl 1:S69-77. https://doi.org/10.1007/s00259-011-1770-8

128. Takahashi Y, Murase K, Higashino H, Mochizuki T, Motomura N. Attenuation correction of myocardial SPECT images with X-ray CT: effects of registration errors between X-ray CT and SPECT. Ann Nucl Med. 2002 Sep;16(6):431–5. https://doi.org/10.1007/BF02990083

129. Grimes J. Patient-specific internal dose calculation techniques for clinical use in targeted radionuclide therapy. Thesis: University of British Columbia; 2013. https://doi.org/10.14288/1.0073590

130. Jaszczak RJ, Greer KL, Floyd CE, Harris CC, Coleman RE. Improved SPECT quantification using compensation for scattered photons. J Nucl Med Off Publ Soc Nucl Med. 1984 Aug;25(8):893–900.

131. Ogawa K, Harata Y, Ichihara T, Kubo A, Hashimoto S. A practical method for position-dependent Compton-scatter correction in single photon emission CT. IEEE Trans Med Imaging. 1991;10(3):408–12. https://doi.org/10.1109/42.97591

132. Hutton BF, Buvat I, Beekman FJ. Review and current status of SPECT scatter correction. Phys Med Biol. 2011 Jul 21;56(14):R85-112. https://doi.org/10.1088/0031-9155/56/14/R01

133. Frey EC, Tsui BMW. New method for modeling the spatially-variant, object-dependent scatter response function in SPECT. In: IEEE Nuclear Science Symposium & Medical Imaging Conference. IEEE; 1996. https://doi.org/10.1109/NSSMIC.1996.591559

134. Frey EC, Ju Z-W, Tsui BMW. A fast projector-backprojector pair modeling the asymmetric, spatially varying scatter response function for scatter compensation in SPECT imaging. IEEE Trans Nucl Sci. 1993 Aug;40(4):1192–7. https://doi.org/10.1109/23.256735

135. Zaidi H. Chapter 5 - Collimator-detector response. In: Quantitative Analysis in Nuclear Medicine Imaging. Springer US; 2006.

136. Dewaraja YK, Koral KF, Fessler JA. Regularized reconstruction in quantitative SPECT using CT side information from hybrid imaging. Phys Med Biol. 2010 May 7;55(9):2523–39. https://doi.org/10.1088/0031-9155/55/9/007

137. Erlandsson K, Thomas B, Dickson J, Hutton BF. Partial volume correction in SPECT reconstruction with OSEM. Nucl Instrum Methods Phys Res Sect Accel Spectrometers Detect Assoc Equip. 2011 Aug 21;648:S85–8. https://doi.org/10.1016/j.nima.2010.12.106

138. Bettinardi V, Castiglioni I, De Bernardi E, Gilardi MC. PET quantification: strategies for partial volume correction. Clin Transl Imaging. 2014 Jun 1;2(3):199–218. https://doi.org/10.1007/s40336-014-0066-y

139. International Atomic Energy Agency (IAEA). Chapter 2 - Quantitative tasks. In: Quantitative nuclear medicine imaging: concepts, requirements and methods. IAEA Human Health Report No.9. Vienna, Austria: IAEA; 2014. p. 2–18.

140. Tran-Gia J, Lassmann M. Optimizing Image Quantification for Lu-177 SPECT/CT Based on a 3D Printed 2-Compartment Kidney Phantom. J Nucl Med. 2017 Nov 2;jnumed.117.200170. https://doi.org/10.2967/jnumed.117.200170

141. National Electrical Manufacturers Association. NEMA NU 1. Performance measurements of gamma cameras. Rosslyn, Virginia, USA: National Electrical Manufacturers Association; 2012. p. 2012.

142. Shcherbinin S, Celler A, Belhocine T, Vanderwerf R, Driedger A. Accuracy of quantitative reconstructions in SPECT/CT imaging. Phys Med Biol. 2008 Sep 7;53(17):4595–604. https://doi.org/10.1088/0031-9155/53/17/009

143. Ramonaheng K, van Staden JA, du Raan H. The effect of calibration factors and recovery coefficients on ^{177}Lu SPECT activity quantification accuracy: a Monte Carlo study. EJNMMI Phys. 2021 Mar 18;8(1):27. https://doi: 10.1186/s40658-021-00365-8.

144. Loening AM, Gambhir SS. AMIDE: A Free Software Tool for Multimodality Medical Image Analysis. Mol Imaging. 2003 Jul 1;2(3):15353500200303132. hhttps://doi.org/10.1162/15353500200303133

145. Schindelin J, Arganda-Carreras I, Frise E, Kaynig V, Longair M, Pietzsch T, et al. Fiji: an open-source platform for biological-image analysis. Nat Methods. 2012 Jun 28;9(7):676–82. https://doi.org/10.1038/nmeth.2019

146. Sjögreen K, Ljungberg M, Strand S-E. An activity quantification method based on registration of CT and whole-body scintillation camera images, with application to ^{131}I. J Nucl Med Off Publ Soc Nucl Med. 2002 Jul;43(7):972–82.

147. Adams MC, Turkington TG, Wilson JM, Wong TZ. A systematic review of the factors affecting accuracy of SUV measurements. AJR Am J Roentgenol. 2010 Aug;195(2):310–20. https://doi.org/10.2214/AJR.10.4923

148. Staelens S, Strul D, Santin G, Vandenberghe S, Koole M, D'Asseler Y, et al. Monte Carlo simulations of a scintillation camera using GATE: validation and application modelling. Phys Med Biol. 2003;48(18):3021. https://doi.org/10.1088/0031-9155/48/18/305

149. Buvat I, Lazaro D. Monte Carlo simulations in emission tomography and GATE: An overview. Nucl Instrum Methods Phys Res Sect Accel Spectrometers Detect Assoc Equip. 2006 Dec 1;569:323–9. https://doi.org/10.1016/j.nima.2006.08.039

150. Zaidi H. Relevance of accurate Monte Carlo modeling in nuclear medical imaging. Med Phys. 1999 Apr;26(4):574–608. https://doi.org/10.1118/1.598559

151. Buvat I, Castiglioni I. Monte Carlo simulations in SPET and PET. Q J Nucl Med Off Publ Ital Assoc Nucl Med AIMN Int Assoc Radiopharmacol IAR. 2002 Mar;46(1):48–61

152. Giannone CA. Monte Carlo Calculations in Nuclear Medicine: Applications in Diagnostic Imaging. Physiol Meas. 1999 Feb;20(1). Available from: https://doi.org/10.1088/0967-3334/20/1/010

153. Smith MF. Modelling photon transport in non-uniform media for SPECT with a vectorized Monte Carlo code. Phys Med Biol. 1993 Oct;38(10):1459–74. https://doi.org/10.1088/0031-9155/38/10/007

154. Jan S, Santin G, Strul D, Staelens S, Assié K, Autret D, et al. GATE: a simulation toolkit for PET and SPECT. Phys Med Biol. 2004 Oct 7;49(19):4543–61. https://doi.org/10.1088/0031-9155/49/19/007

155. Ljungberg M, Strand S-E. A Monte Carlo program for the simulation of scintillation camera characteristics. Comput Methods Programs Biomed. 1989 Aug 1;29(4):257–72. https://doi.org/10.1016/0169-2607(89)90111-9

156. He B, Du Y, Song X, Segars WP, Frey EC. A Monte Carlo and physical phantom evaluation of quantitative In-111 SPECT. Phys Med Biol. 2005 Sep 7;50(17):4169–85. https://doi.org/10.1088/0031-9155/50/17/018

157. Islamian JP, Bahreyni Toossi MT, Momennezhad M, Naseri S, Ljungberg M. Simulation of a quality control Jaszczak phantom with SIMIND Monte Carlo and adding the phantom as an accessory to the program. Iran. J. Med. Phys. 2012: https://doi.org/10.22038/IJMP.2012.319

158. Segars WP, Bond J, Frush J, Hon S, Eckersley C, Williams CH, et al. Population of anatomically variable 4D XCAT adult phantoms for imaging research and optimization. Med Phys. 2013 Apr;40(4). https://doi.org/10.1118/1.4794178

159. Segars WP, Sturgeon G, Mendonca S, Grimes J, Tsui BMW. 4D XCAT phantom for multimodality imaging research. Med Phys. 2010 Sep;37(9):4902–15. https://doi.org/10.1118/1.3480985

160. Brolin G, Gustafsson J, Ljungberg M, Gleisner KS. Pharmacokinetic digital phantoms for accuracy assessment of image-based dosimetry in^{177}Lu-DOTATATE peptide receptor radionuclide therapy. Phys Med Biol. 2015 Jul;60(15):6131–49. https://doi.org/10.1088/0031-9155/60/15/6131

161. Hindorf, C. Chapter 18 - Internal Dosimetry. In Nuclear Medicine Physics: A handbook for teachers and students. Vienna, Austria: International Atomic Energy Agency (IAEA); 2014.

162. Loevinger R, Budinger TF, Watson EE. Mird Primer for Absorbed Dose Calculations. Revised, Subsequent edition. New York, NY: Society of Nuclear Medicine; 1991.

163. Glatting G, Kletting P, Reske SN, Hohl K, Ring C. Choosing the optimal fit function: comparison of the Akaike information criterion and the F-test. Med Phys. 2007 Nov;34(11):4285–92. https://doi.org/10.1118/1.2794176

164. Kletting P, Schimmel S, Hänscheid H, Luster M, Fernández M, Nosske D, et al. The NUKDOS software for treatment planning in molecular radiotherapy. Z Med Phys. 2015 Sep;25(3):264–74. https://doi.org/10.1016/j.zemedi.2015.01.001.

165. Kletting P, Kull T, Reske SN, Glatting G. Comparing time activity curves using the Akaike information criterion. Phys Med Biol. 2009 Nov 7;54(21):N501-507. https://doi.org/10.1088/0031-9155/54/21/N01

166. Gleisner KS, Brolin G, Sundlöv A, Mjekiqi E, Östlund K, Tennvall J, et al. Long-Term Retention of ^{177}Lu/^{177m}Lu-DOTATATE in Patients Investigated by γ-Spectrometry and γ-Camera Imaging. J Nucl Med Off Publ Soc Nucl Med. 2015 Jul;56(7):976–84. https://doi.org/10.2967/jnumed.115.155390

167. Ljungberg M, Sjogreen Gleisner K. Three-dimensional image-based dosimetry in radionuclide therapy. IEEE Trans Radiat Plasma Med Sci. 2018 Jul 26;PP:1–1. https://doi.org/10.1109/TRPMS.2018.2860563

168. Isambert A, Bonniaud G, Lavielle F, Malandain G, Lefkopoulos D. A phantom study of the accuracy of CT, MR and PET image registrations with a block matching-based algorithm. Cancer Radiother J Soc Francaise Radiother Oncol. 2008 Dec;12(8):800–8. https://doi.org/10.1016/j.canrad.2008.04.009

169. Rinscheid A, Allmann A, Allmann J, Eberhardt N, Eiber M, Kletting P, et al. Optimal sampling schedules for kidney dosimetry for ^{177}Lu-PSMA therapy. J Nucl Med. 2019 May 1;60(supplement 1):266–266. https://doi.org/10.1002/mp.13846

170. Madsen MT, Menda Y, O'Dorisio TM, O'Dorisio MS. Technical Note: Single time point dose estimate for exponential clearance. Med Phys. 2018 May;45(5):2318–24. https://doi.org/10.1002/mp.12886

171. Gear J, Cox M, Gustafsson J, Sjogreen Gleisner K, Murray I, Glatting G, et al. EANM practical guidance on uncertainty analysis for molecular radiotherapy absorbed dose calculations. Eur J Nucl Med Mol Imaging. 2018 Dec 1;45. https://doi.org/10.1007/s00259-018-4136-7

172. Stabin MG, Siegel JA. Physical models and dose factors for use in internal dose assessment. Health Phys. 2003 Sep;85(3):294–310. https://doi: 10.1097/00004032-200309000-00006

173. Bardiès M, Gear JI. Scientific Developments in Imaging and Dosimetry for Molecular Radiotherapy. Clin Oncol R Coll Radiol G B. 2021 Feb;33(2):117–24. https://doi.org/10.1016/j.clon.2020.11.005

174. Bardies and Vergara Gil. Dosimetry algorithm selection from absorbed dose calculation in Dosimetry for Radiopharmaceutical Therapy (IAEA tech Series, in press).

175. van den Hoven AF, Rosenbaum CENM, Elias SG, de Jong HWAM, Koopman M, Verkooijen HM, et al. Insights into the Dose-Response Relationship of Radioembolization with Resin ^{90}Y-Microspheres: A Prospective Cohort Study in Patients with Colorectal Cancer Liver Metastases. J Nucl Med Off Publ Soc Nucl Med. 2016 Jul;57(7):1014–9. https://doi.org/10.2967/jnumed.115.166942

176. Huizing DMV, de Wit-van der Veen BJ, Verheij M, Stokkel MPM. Dosimetry methods and clinical applications in peptide receptor radionuclide therapy for neuroendocrine tumours: a literature review. EJNMMI Res. 2018 Aug 29;8:89. https://doi.org/10.1186/s13550-018-0443-z

177. Gustafsson J, Brolin G, Cox M, Ljungberg M, Johansson L, Gleisner KS. Uncertainty propagation for SPECT/CT-based renal dosimetry in 177Lu peptide receptor radionuclide therapy. Phys Med Biol. 2015 Oct 12;60(21):8329. https://doi.org/10.1088/0031-9155/60/21/8329

178. Hippeläinen E, Tenhunen M, Sohlberg A. Fast voxel-level dosimetry for ^{177}Lu labelled peptide treatments. Phys Med Biol. 2015 Sep 7;60(17):6685–700. https://doi.org/10.1088/0031-9155/60/17/6685

179. Svensson J, Berg G, Wängberg B, Larsson M, Forssell-Aronsson E, Bernhardt P. Renal function affects absorbed dose to the kidneys and haematological toxicity during ^{177}Lu-DOTATATE treatment. Eur J Nucl Med Mol Imaging. 2015;42(6):947–55. https://doi.org/10.1007/s00259-015-3001-1

180. Dieudonné A, Hobbs RF, Lebtahi R, Maurel F, Baechler S, Wahl RL, et al. Study of the impact of tissue density heterogeneities on 3-dimensional abdominal dosimetry: comparison between dose kernel convolution and direct Monte Carlo methods. J Nucl Med Off Publ Soc Nucl Med. 2013 Feb;54(2):236–43. https://doi.org/10.2967/jnumed.112.105825

181. Dieudonné A, Hobbs RF, Bolch WE, Sgouros G, Gardin I. Fine-resolution voxel S values for constructing absorbed dose distributions at variable voxel size. J Nucl Med Off Publ Soc Nucl Med. 2010 Oct;51(10):1600–7. https://doi.org/10.2967/jnumed.110.077149

182. Agostinelli S, Allison J, Amako K, Apostolakis J, Araujo H, Arce P, et al. Geant4—a simulation toolkit. Nucl Instrum Methods Phys Res Sect Accel Spectrometers Detect Assoc Equip. 2003 Jul 1;506(3):250–303. https://doi.org/10.1016/S0168-9002(03)01368-8

183. Kawrakow I, Mainegra-Hing E, Tessier F. The EGSnrc Code System: Monte Carlo Simulation of Electron and Photon Transport. 2016.

184. Larsson E, Ljungberg M, Strand S-E, Jönsson B-A. Monte Carlo calculations of absorbed doses in tumours using a modified MOBY mouse phantom for pre-clinical dosimetry studies. Acta Oncol Stockh Swed. 2011 Aug;50(6):973–80. https://doi.org/10.3109/0284186X.2011.582517

185. Waters L, Mckinney G, Durkee J, Fensin M, Hendricks J, James M, et al. The MCNPX Monte Carlo radiation transport code. AIP Conf Proc. 2007 Mar 19;896:81–90. https://doi.org/10.1063/1.2720459

186. Giap HB, Macey DJ, Podoloff DA. Development of a SPECT-based three-dimensional treatment planning system for radioimmunotherapy. J Nucl Med Off Publ Soc Nucl Med. 1995 Oct;36(10):1885–94.

187. Götz T, Schmidkonz C, Lang EW, Maier A, Kuwert T, Ritt P. A comparison of methods for adapting ^{177}Lu dose-voxel-kernels to tissue inhomogeneities. Phys Med Biol. 2019 Dec 19;64(24):245011. https://doi.org/10.1088/1361-6560/ab5b81

188. Berger MJ. Energy deposition in water by photons from point isotropic sources. J Nucl Med Off Publ Soc Nucl Med. 1968 Feb;Suppl 1:17-25

189. Berger MJ. Distribution of absorbed dose around point sources of electrons and beta particles in water and other media. J Nucl Med Off Publ Soc Nucl Med. 1971 Mar;Suppl 5:5-23.

190. Pacilio M, Amato E, Lanconelli N, Basile C, Torres LA, Botta F, et al. Differences in 3D dose distributions due to calculation method of voxel S-values and the influence of image blurring in SPECT. Phys Med Biol. 2015 Mar 7;60(5):1945–64.

191. Sanchez-Garcia M, Gardin I, Lebtahi R, Dieudonné A. Implementation and validation of collapsed cone superposition for radiopharmaceutical dosimetry of photon emitters. Phys Med Biol. 2015 Oct 21;60(20):7861–76. https://doi.org/10.1088/0031-9155/60/20/7861

192. Götz T, Lang E, Schmidkonz C, Kuwert T, Ludwig B. Dose voxel kernel prediction with neural networks for radiation dose estimation. Z Für Med Phys. 2020 Oct 1;31. https://doi.org/10.1016/j.zemedi.2020.09.005

193. Akhavanallaf A, Shiri I, Arabi H, Zaidi H. Deep Learning-Assisted Whole-Body Voxel-Based Internal Dosimetry. In: 2020 IEEE Nuclear Science Symposium and Medical Imaging Conference (NSS/MIC). Boston, MA, USA: IEEE; 2020. p. 1–3. https://doi.org/10.1109/NSS/MIC42677.2020.9507983

194. Bardies M, Ljungberg M. Monte-Carlo codes in radionuclide dosimetry. In: Nicol A, editor. Dosimetry for radionuclide therapy. York, UK: Institute of Physics and Engineering in Medicine; 2011.

195. Lanconelli N, Pacilio M, Lo Meo S, Botta F, Di Dia A, Aroche AT, et al. A free database of radionuclide voxel S values for the dosimetry of nonuniform activity distributions. Phys Med Biol. 2012 Jan 21;57(2):517–33. https://doi.org/10.1088/0031-9155/57/2/517

196. Johnson TK, McClure D, McCourt S. MABDOSE. II: Validation of a general purpose dose estimation code. Med Phys. 1999 Jul;26(7):1396–403. https://doi.org/10.1118/1.598637

197. Gardin I, Bouchet LG, Assié K, Caron J, Lisbona A, Ferrer L, et al. Voxeldoes: a computer program for 3-D dose calculation in therapeutic nuclear medicine. Cancer Biother Radiopharm. 2003 Feb;18(1):109–15. https://doi.org/10.1089/108497803321269386

198. Grimes J, Uribe C, Celler A. JADA: a graphical user interface for comprehensive internal dose assessment in nuclear medicine. Med Phys. 2013 Jul;40(7):072501. https://doi.org/10.1118/1.4810963.

199. Li T, Zhu L, Lu Z, Song N, Lin K-H, Mok GSP. BIGDOSE: software for 3D personalized targeted radionuclide therapy dosimetry. Quant Imaging Med Surg. 2020 Jan;10(1):160–70. https://doi.org/10.21037/qims.2019.10.09

200. Santoro L, Pitalot L, Trauchessec D, Mora-Ramirez E, Kotzki PO, Bardiès M, et al. Clinical implementation of PLANET® Dose for dosimetric assessment after [^{177}Lu]Lu-

DOTA-TATE: comparison with Dosimetry Toolkit® and OLINDA/EXM® V1.0. EJNMMI Res. 2021 Jan 4;11(1):1. https://doi.org/10.1186/s13550-020-00737-8

201. Stabin MG, Sparks RB, Crowe E. OLINDA/EXM: The Second-Generation Personal Computer Software for Internal Dose Assessment in Nuclear Medicine. J Nucl Med. 2005 Jun 1;46(6):1023–7.

202. Snyder WS. Mird Pamphlet No 5. Revised edition. Matthew Medical Books; 1978.

203. Stabin M, Brill A, Segars W, Emmons M, Gesner J, Milam R. Realistic phantom series for OLINDA/EXM 2.0. J Nucl Med. 2006 May 1;47(suppl 1):156P-156P.

204. Stabin M, Emmons MA, Segars WP, Fernald M, Brill AB. ICRP-89 based adult and pediatric phantom series. J Nucl Med. 2008 May 1;49(supplement 1):14P-14P.

205. Menzel H-G, Clement C, DeLuca P. ICRP Publication 110. Realistic reference phantoms: an ICRP/ICRU joint effort. A report of adult reference computational phantoms. Ann ICRP. 2009;39(2):1–164. https://doi.org/10.1016/j.icrp.2009.09.00

206. Segars W, Tsui B, Lalush D, Frey E, King M, Manocha D. Development and application of the new dynamic Nurbs-based Cardiac-Torso (NCAT) phantom. J Nucl Med. 2001 May 1;42:23.

207. Ljungberg M, Frey E, Sjögreen K, Liu X, Dewaraja Y, Strand S-E. 3D Absorbed Dose Calculations Based on SPECT: Evaluation for ^{111}In/^{90}Y Therapy using Monte Carlo Simulations. Cancer Biother Radiopharm. 2003 Feb 1;18(1):99–107. https://doi.org/10.1089/108497803321269377

208. Stabin M. Nuclear medicine dosimetry. Phys Med Biol. 2006;51(13):R187. https://doi.org/10.1088/0031-9155/51/13/R12

209. Ljungberg M, Sjögreen K, Liu X, Frey E, Dewaraja Y, Strand S-E. A 3-Dimensional Absorbed Dose Calculation Method Based on Quantitative SPECT for Radionuclide Therapy: Evaluation for ^{131}I Using Monte Carlo Simulation. J Nucl Med Off Publ Soc Nucl Med. 2002 Aug;43(8):1101–9.

210. Chiesa C, Mira M, Maccauro M, Spreafico C, Romito R, Morosi C, et al. Radioembolization of hepatocarcinoma with ^{90}Y glass microspheres: development of an individualized treatment planning strategy based on dosimetry and radiobiology. Eur J Nucl Med Mol Imaging. 2015 Oct;42(11):1718–38. https://doi.org/10.1007/s00259-015-3068-8

211. Knoll P, Kotalova D, Köchle G, Kuzelka I, Minear G, Mirzaei S, et al. Comparison of advanced iterative reconstruction methods for SPECT/CT. Z Med Phys. 2012 Feb;22(1):58–69. https://doi.org/10.1016/j.zemedi.2011.04.007

212. Nelson WR, Hirayama H, Rogers DWO. EGS4 code system. Stanford Linear Accelerator Center, Menlo Park, CA (USA); 1985 Dec. Report No: SLAC-265.

213. Xiao Y, Roncali E, Hobbs R, James SS, Bednarz B, Benedict S, et al. Toward Individualized Voxel-Level Dosimetry for Radiopharmaceutical Therapy. Int J Radiat Oncol. 2021 Mar;109(4):902–4. https://doi.org/10.1016/j.ijrobp.2020.08.026

214. Giammarile F, Muylle K, Delgado Bolton R, Kunikowska J, Haberkorn U, Oyen W. Dosimetry in clinical radionuclide therapy: the devil is in the detail. Eur J Nucl Med Mol Imaging. 2017 Nov;44(12):2137–9. https://doi.org/10.1007/s00259-017-3820-3.

215. Summary of the European Directive 2013/59/Euratom: essentials for health professionals in radiology. Insights Imaging. 2015 May 27;6(4):411–7. https://doi.org/10.1007/s13244-015-0410-4

2

Chapter 2:

Article I

Validation of a Monte Carlo modelled gamma camera for Lutetium-177 imaging.

This chapter includes the original work that has been published in the Journal of Applied Radiation and Isotopes.

The front page of the published article is shown in Appendix A

DOI: https://doi.org/10.1016/j.apradiso.2020.109200

TABLE OF CONTENTS

2.1 Abstract

This study validated a model of the Siemens Symbia T16 dual-head SPECT/CT gamma camera created using the Monte Carlo program SIMIND for ^{177}Lu. The validation was done by comparing experimental and simulated gamma camera performance criteria tests for the ^{177}Lu 208.4 keV photopeak with a medium-energy collimator. Results showed good agreement between the experimental and simulated values. These results illustrated that SIMIND could emulate the Symbia T16 successfully and therefore, can be used with confidence to model ^{177}Lu images.

Keywords: Validation, Modelling, ^{177}Lu, Monte Carlo, SIMIND, Simulations, Experiments, Planar, SPECT.

2.2 Introduction

Gamma camera imaging with ^{99m}Tc using a low-energy high-resolution (LEHR) collimator has fulfilled the role of ideal imaging in nuclear medicine for both planar and single-photon emission computed tomography (SPECT) images. SPECT imaging has been proven, in phantom and clinical studies, to demonstrate superior images and better quantitative accuracy in comparison to planar images (1–3). This is attributed to the fact that problems such as organ overlap and superimposed background activity are overcome in SPECT imaging. However, factors complicating quantitative SPECT imaging are photon attenuation, photon scatter, collimator detector response and partial volume effect. Furthermore, it is necessary to establish a calibration factor to convert image counts into absolute units of activity (4).

^{131}I has been used as a common therapeutic isotope for decades. Its imaging and quantification capabilities with a high-energy collimator have been investigated extensively in the literature (5,6). However, with the development of new peptides, ^{177}Lu has gained popularity as one of the isotopes of choice for peptide receptor radionuclide therapy (PRRNT) using the theranostic approach. This is owing to its favourable physical characteristics that make it an ideal imaging and therapeutic radionuclide(7–9). It has also been proven to reduce patient bone marrow toxicity in comparison to ^{131}I (10). ^{177}Lu has a physical half-life of 6.7 days and emits gamma rays, beta particles, characteristic x-rays and bremsstrahlung radiation (11). Of these gamma rays, two with an energy of 112.9 keV (6.2%) and 208.4 keV (10.4%) have been used successfully for imaging purposes

(12). The beta particles have a maximum and mean kinetic energy of 498.3 keV (79.3%) and 134 keV, respectively, and are used in radionuclide therapy. Characteristic x-rays from ^{177}Lu are prominent at energies of 54.6 keV (1.6%) and 55.8 keV (2.8%) (11). The bremsstrahlung yield, due to the interaction of the beta particles with tissue, has been observed to be very low (< 0.2%), with most (~ 85%) of the created photons having energies below 50 keV (13).

The ideal choice of which collimator, gamma ray imaging energy and energy window settings for ^{177}Lu are needed, have been well investigated using Monte Carlo (MC) simulations (8). Literature suggests the use of the 208.4 keV photopeak with a medium-energy (ME) collimator and a 20% energy window setting (7,8,12,14–17). This is owing to the higher yield of the 208.4 keV gamma ray emission compared to the 112.9 keV photon, the avoidance of down scatter using the 208.4 keV photopeak, and the complicated scatter correction when incorporating both the 208.4 keV and 112.9 keV photopeaks.

Studies have proven MC simulations to be a useful tool in the field of nuclear medicine research (18). This is due to the statistical nature of radioactive decay, the mechanism of gamma ray and particle emission, and the interaction and detection of these particles in various materials. Monte Carlo offers the advantage of evaluating phenomena involved in nuclear medicine imaging, which may be cumbersome or impossible to measure physically. For this reason, MC techniques have gained favour for optimising SPECT reconstruction algorithms, improving image quality for quantification purposes as well as dose planning for therapeutic purposes (19).

The MC program SIMIND has been implemented extensively to model gamma cameras for radionuclides such as ^{99m}Tc, ^{131}I, ^{111}In and ^{177}Lu (6,8,20–22). The guidelines for quantitative ^{177}Lu SPECT imaging for dosimetry purposes have been well established using the SIMIND MC program (8,22). As gamma cameras are subject to a variety of detector and electronic challenges, it is useful to validate the capability of MC programs to model clinical gamma cameras. SIMIND was implemented for this purpose using performance criteria tests, which included energy resolution, system spatial resolution and system sensitivity for ^{99m}Tc and ^{131}I (5,21,23,24).

To our knowledge, modelling of the Siemens Symbia T16 SPECT/CT gamma camera with ^{177}Lu, using the SIMIND MC program has not been reported, therefore, there is a need to validate the aforementioned modelled gamma camera with ^{177}Lu.

Thus, the aim of this study was to model the Siemens Symbia dual-head gamma camera using the SIMIND MC program for ^{177}Lu. This was achieved by comparing the simulated results obtained with the modelled gamma camera to the experimental results of the clinical gamma camera. Furthermore, such validation could lead to evaluating ^{177}Lu SPECT activity quantification accuracy using MC simulations.

2.3 Materials and Methods

In this study, a model of the Siemens Symbia T16 hybrid SPECT/CT (Symbia T16) (Siemens Medical Solutions, Inc. Hoffman Estates, IL., USA) dual-head gamma camera available in our clinic was created using the SIMIND MC program, version 6.1.2 (22). The modelled gamma camera was then used to simulate certain gamma camera performance criteria tests using $^{177}LuCl_3$ which involved four planar and two SPECT tests. Experimental measurements of these tests were performed on the clinical Symbia T16. The same tests were simulated using the SIMIND MC program to generate the corresponding simulated data. The experimental data were repeated three times and the average experimental values were compared to the simulated values by calculating the percentage and absolute differences using Equations 2-1 and 2-2, respectively. Where appropriate, simulated spectra distributions and images were compared.

$$\%\,Difference = \frac{Average\ Experimental\ - Simulated}{Average\ Experimental} \times 100 \qquad (2\text{-}1)$$

$$Absolute\ Difference = |Average\ Experimental\ - Simulated| \qquad (2\text{-}2)$$

2.3.1 Experimental Tests

The “no-carrier added” (n.c.a) $^{177}LuCl_3$ used in this study was produced in a FRM-2 nuclear reactor using the reaction [^{176}Yb (n, γ) $^{177}Yb \rightarrow ^{177}Lu$]. This is an indirect pathway for the production of ^{177}Lu, which involves the irradiation of Ytterbium-176 (^{176}Yb)-Yb_2O_3 to produce the short-lived ^{177}Yb, with a physical half-life of 1.9 h, which decays to ^{177}Lu. The Yb target can be chemically separated from the ^{177}Lu daughter product. This method of production allows for a higher specific activity, significantly longer shelf-life, and the highest achievable radionuclide purity (itG, Isotope Technologies Garching GmbH, Germany), as confirmed by Dash et al. (25). The indirect method of production omits the production of contaminants, i.e., long-lived lutetium products such as ^{177m}Lu, with a physical half-life of 160.5 days, as obtained in the alternative direct production method [^{176}Lu (n, y) $\rightarrow$ ^{177}Lu] of ^{177}Lu (10). The $^{177}LuCl_3$ activity concentration for the experimental data was measured using a Biodex Atomlab 500 dose calibrator (Biodex Medical Systems, New York, NY, USA). The accuracy of the dose calibrator for ^{177}Lu was traceable to a secondary standard (NAC 03540) through the National Metrology Institute of South Africa (NMISA) in Cape Town, South Africa (Appendix A-2).

One detector of the dual-head gamma camera was used for data acquisition as acceptance tests, and quality assurance showed small differences between the two detectors. The gamma camera detector was equipped with a ME collimator and the data was acquired using a 20% energy window centred over the 208.4 keV photopeak (187.2 – 228.8 keV) (7,8,12,14–17). Different matrix sizes were used appropriately for the different tests. The activity used for the respective tests was a compromise between the availability of the costly $^{177}LuCl_3$, which has a low gamma yield, and acquisitions at a low count rate with negligible count losses. The maximum observed count rate used during experimental studies was less than 9.0 kcps, where expected count losses were less than 1% as determined from the acceptance test data of the gamma camera. Dead time did not pose a problem for the acquired data, and thus no dead time corrections were applied.

2.3.1.1 Planar Validation Tests

The planar validation tests were performed using National Electrical Manufacturers Association (NEMA) recommendations stipulated for gamma camera performance criteria (26). The specific tests were chosen in accordance with literature reports for MC gamma camera validation (23,24,27). The tests included intrinsic and extrinsic energy resolution, system spatial resolution as well as system sensitivity. Detector one was peaked over the 208.4 keV photopeak and used for all the tests.

i. Energy Resolution

The detector intrinsic and extrinsic energy spectra were acquired in air without and with a ME collimator using 1.0±0.2 MBq and 769.6±23.2 MBq of $^{177}LuCl_3$ in two separate syringes, respectively. The individual syringes were placed in the centre of the field of view supported by a Styrofoam block with a source-detector distance of 40±0.5 cm. Intrinsic and extrinsic energy spectra within the available energy range (19.8 – 721 keV), were acquired using the software provided by the manufacturer (Siemens Syngo MI Applications version 7.5, Siemens Medical Solutions, Germany). The energy spectra included at least 10 000 counts in the peak channel.

Gaussian functions were fitted to the 208.4 keV and 112.9 keV photopeaks for the respective intrinsic and extrinsic energy spectra using the public domain software ImageJ (Fiji) (28). The full width at half maximum (FWHM) was determined from the Gaussian function, and the energy resolution value (%) was calculated using Equation 2-3 for each of the spectra.

$$Energy\ Resolution\ (\%) = \frac{FWHM\ (keV)}{Energy\ (keV)} \times 100 \tag{2-3}$$

Although 208.4 keV was the photopeak of interest for this study, in order to illustrate the gamma camera energy response, the intrinsic and extrinsic energy resolution of the respective energy spectra were reported for both the 208.4 keV and 112.9 keV photopeaks. The subsequent tests will only report results obtained over the 208.4 keV photopeak.

ii. System Spatial Resolution

The system spatial resolution was measured using two capillary tubes (inner diameter 1 mm), each uniformly filled with 23.5±2.2 MBq of $^{177}LuCl_3$. The capillary tubes were placed on a Styrofoam block and positioned on the patient bed 10 cm apart at a 10±0.5 cm distance from the gamma camera detector. Static images of the capillary tubes were acquired in a 512 × 512 matrix with a pixel size of 1.2 × 1.2 mm. Acquisitions included 10 000 counts in the peak channel of each line spread function. Line profiles were drawn at three different positions across the acquired static images of the capillary tubes and a Gaussian function was fitted to the profiles. The spatial resolution was reported in units of mm as the average FWHM of the Gaussian functions. The full width at tenth maximum (FWTM) was also reported.

iii. System Sensitivity

System sensitivity measurements were performed with an 87 mm diameter petri dish uniformly filled with 769.6±23.2 MBq of $^{177}LuCl_3$ to a depth of 2 mm. The uncertainty of the activity used in the petri dish was obtained from repeated measurements. The accuracy of the activity used to obtain the system sensitivity plays a vital role. Therefore, the uncertainty in the accuracy of the Biodex Atomlab 500 dose calibrator for ^{177}Lu was reduced through traceability to NMISA. The petri dish was placed in the centre of the field of view, 10±0.5 cm from the detector of the gamma camera. Static images were acquired for 4 000 000 counts using a 256 × 256 matrix with a pixel size of 2.4 × 2.4 mm. The system sensitivity was calculated using the decay corrected count rate, obtained from the summed counts over the entire image for the respective acquisition time, per activity as measured in the dose calibrator, indicated in Equation 2-4.

$$System\ Sensitivity\ (cps/MBq) = \frac{Count\ Rate\ (cps)}{Activity\ (MBq)} \times 100 \tag{2-4}$$

2.3.1.2 SPECT Validation Tests

The above-mentioned planar system sensitivity is commonly used to convert quantitative planar and SPECT data into units of activity (3,20,29,30). Using planar images to convert quantified SPECT data into units of activity is not ideal. The use of planar data would entail that accurate scatter and attenuation corrections are incorporated in the image reconstruction algorithms of the quantified SPECT images. It is generally believed that if the gamma camera system sensitivity or calibration factor is performed with a source geometry mimicking scatter and attenuation properties, the effects of imperfect scatter and attenuation corrections may be partly reduced (31). Different geometries to those stipulated by NEMA for sensitivity have been reported to generate calibration factors to successfully convert SPECT quantitative data into units of activity (14). Taking this into consideration, part of the validation included calibration factors, which provided simple scatter and attenuation environments in a SPECT setting. Therefore, we aimed to validate MC SPECT simulations using a calibration factor for two simple geometries. The objective was to provide a simple SPECT geometry to compare the experimental and simulation setup. The geometries included in air (air calibration factor) and water (water calibration factor) SPECT/CT acquisitions of a 4 cm diameter (34 ml) sphere. The water calibration factor was introduced to mimic attenuation and scatter properties in a simple SPECT acquisition setup, for the potential purpose of quantifying SPECT data. In doing so, the same acquisition and reconstruction techniques as those applied for the SPECT quantitative data may be used. The air calibration factor offered an additional simpler geometry (limited scatter and attenuation) to validate the SPECT setup. The choice of the sphere size was larger than three times the system spatial resolution (3× FWHM) to limit partial volume due to spill-out (32).

SPECT acquisitions were performed using the triple energy window (TEW) scatter correction method with a 20% window centred at the 208.4 keV photopeak (187.2 – 228.8 keV) and two adjacent scatter windows of 10% above (228.8 – 249.6 keV) and below (166.4 – 187.2 keV) the 208.4 keV photopeak (12,15,33). The SPECT acquisitions were performed according to clinical imaging protocols for ^{177}Lu. A non-circular step-and-shoot acquisition orbit was used with both detectors fitted with ME collimators. The images were acquired in a 128 × 128 matrix with a pixel size of 4.8 × 4.8 mm using 128 projections of 25 seconds per projection. The SPECT acquisition was followed by a CT scan for attenuation correction using the CareDose 4D protocol (CareDose, Siemens Medical Solutions, Germany) with a CT tube voltage of 130 kV and an effective tube current of 15 mAs.

i. Air Calibration Factor

To obtain an air calibration factor, the 4 cm diameter sphere was filled with a uniform concentration of $^{177}LuCl_3$ (2.3 MBq/ml). The sphere was placed on the patient bed and suspended in the air using a Styrofoam block. SPECT/CT acquisitions were performed using the above-mentioned acquisition protocol to obtain an air calibration factor.

ii. Water Calibration Factor

Similarly, for the water calibration factor, the sphere was filled with a uniform concentration of 2.5 MBq/ml $^{177}LuCl_3$. For this acquisition, the sphere was placed in a water-filled cylindrical phantom with an interior diameter of 21.6 cm and height of 18.6 cm.

iii. Reconstruction

The acquired SPECT projection images of the air and water calibration factor were reconstructed using the Syngo MI Application software FLASH 3D, which is based on the ordered subsets expectation maximization (OS-EM) iterative reconstruction algorithm (Hudson and Larkin, 1994) with four iterations and eight subsets, as recommended by the manufacturer (FLASH 3D, Siemens Medical Solutions, Germany). FLASH 3D incorporated a CT-based attenuation correction, TEW scatter correction and collimator depth-dependent 3D resolution recovery. The SPECT projection images were reconstructed in a 128 × 128 matrix with 128 slices and a 4.8 × 4.8 × 4.8 mm voxel size. The CT images were reconstructed in a 512 × 512 matrix with a pixel size of 1.27 × 1.27 mm and a slice thickness of 5 mm with a filtered back projection algorithm. The CT data reconstructed with a smooth kernel (B08s) were used for attenuation correction. The reconstructed SPECT images were analysed using the public domain software Amide by drawing spherical volumes corresponding to the physical size of the spheres (34). The total counts in each volume were used to determine the respective count rates, as shown in Equation 2-4. The SPECT calibration factors were incorporated in this study to compare the experimental and simulation setup (described in the subsequent Section 1.3.2), therefore, the SPECT calibration factors were not compared to the planar system sensitivity.

2.3.2 SIMIND Monte Carlo Simulations

The SIMIND version 6.1.2 MC program is written in FORTRAN-90 (Ljungberg and Strand, 1989). It is well established for simulation of planar and SPECT images, and its application to obtain optimal imaging parameters for ^{177}Lu data is well documented (9). SIMIND was incorporated to model the above-mentioned planar performance criteria and the SPECT calibration factor experiments. SIMIND consists of two main programs namely CHANGE and SIMIND. The CHANGE program is an interface that allows the user to define the physical characteristics of the gamma camera to be modelled as input parameters, and saves the data to external files. The physical parameters of the detector system were defined in the CHANGE program according to manufacturer specifications and acceptance test results (Siemens Symbia T series system specification sheet, Siemens Medical Solutions, USA, 2013). Table 2-1 shows general SIMIND parameters defined in the CHANGE program. SIMIND reads the external input files created by CHANGE and uses MC simulations to create various results as output files. This allows the user to prepare several input files to be loaded into a command file for submission to a batch queue.

Table 2-1: *General SIMIND gamma camera parameters used as input into the CHANGE program.*

Parameters	Model	Physical characteristics	
1. Collimator	Medium-energy (Siemens SIMIND model)	Number of holes	14 000
		Collimator thickness	4.064 cm
		Septal thickness	0.114 cm
		Hole diameter	0.294 cm
2. Crystal	Sodium iodide	Half length	29.55 cm
		Half width	22.25 cm
		Thickness	0.952 cm
3. Backscatter material	Water	Thickness	40 cm
4. Cover material	Aluminium	Thickness	0.10 cm

The energy response for the SIMIND gamma camera can be modelled according to an energy-dependent Gaussian function, or it can be expressed as a constant value. The former option convolves the imparted energy for each photon history with the Gaussian function, which varies with $\frac{1}{\sqrt{\text{Energy}}}$, whereby the reference energy resolution is defined for ^{99m}Tc (140.5 keV) (9). However, the measured energy resolution does not necessarily follow the simplified $\frac{1}{\sqrt{\text{Energy}}}$ function described by Cherry et al. (35), as shown by Rault et al. (36). For this reason, the option for the constant energy response was used in this study. This was achieved by including the experimental intrinsic energy resolution value for ^{177}Lu obtained at the 208.4 keV photopeak into the CHANGE program. Therefore allowing the modelled gamma camera energy resolution at the 208.4 keV photopeak to conform better to the clinical gamma camera energy resolution. Using the constant energy response option entailed that the lower energies were assigned a better energy resolution for the simulated spectrum.

Apart from defining the gamma camera physical parameters as input, the CHANGE program allows for input of phantoms with non-homogeneous densities and their corresponding source distributions. This feature was used to mimic the setup of the experimental tests. For this purpose, three input files were required. These were a source and a density map of the phantom as well as a text file defining the activity concentrations in the source map.

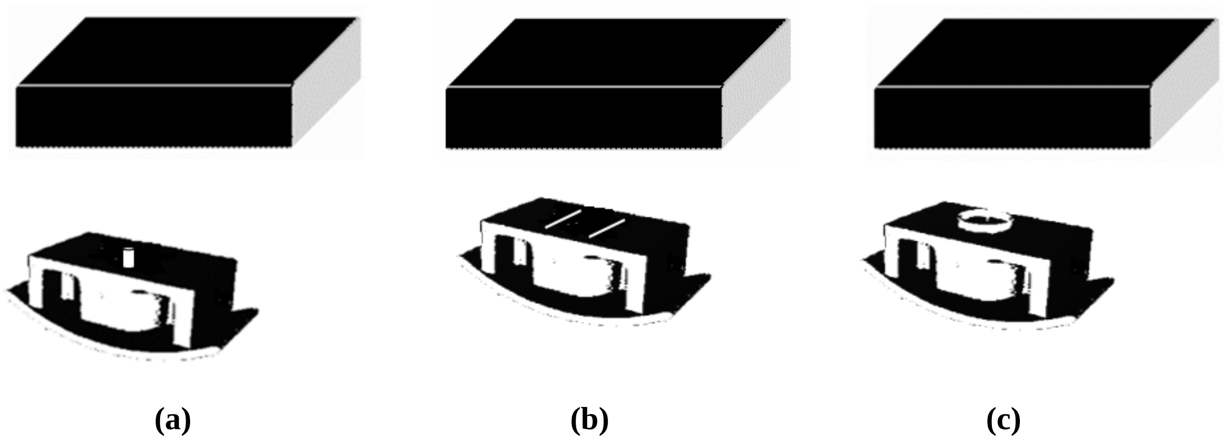
(a) (b) (c)

Figure 2-1: *Segmented CT images of the experimental setup used to create source and density maps that served as input to the CHANGE program to mimic the experimental setup during the simulations. The anterior detector of the gamma camera with the* ***(a)*** *syringe* ***(b)*** *capillary tubes and* ***(c)*** *petri dish supported with a Styrofoam base on the gamma camera patient pallet.*

To generate these files, CT images of the experimental setups were obtained for the planar and the SPECT validation tests using the previously mentioned CareDose 4D CT protocol. The public domain segmentation software ITK-snap version 3.2.0 was used to segment the reconstructed CT images as shown in Figure 2-1 (37). Each segmented region was assigned a unique label value, thereby generating a source map consisting of different label values. The label values from the source map were used to create a text file containing indexes for the radioactive concentrations assigned to these segmented regions. An in-house developed software program, referred to by Ejeh et al. (24), was used to create a density map by converting the CT Hounsfield units to density values for each experimental setup, thereby creating a density map. The source map, text file and density map of each experiment were used as the phantom design input for the CHANGE program. For the simulation of the validation studies, the energy window settings were as defined in the experimental setup. Similarly, acquisition parameters such as matrix size, pixel size, as well as the activity and acquisition time combination were used appropriately for each test, as defined in

Section 1.3.1. Interactions in the crystal, phantom and collimator were modelled. After the input parameters had been defined in the CHANGE program, the SIMIND program reads the input data and performs the MC simulations. The count statistics for the simulated energy spectra, respective images and SPECT projections were similar to those of the experimental set-up. The SPECT projections were reconstructed, as described in Section 1.3.1.2. The results obtained from SIMIND consisted of simulated images and a result file describing the simulation protocol. Similar to the experimental data, the simulated data were analysed using ImageJ and Amide for the planar images and reconstructed SPECT images, respectively.

2.4 Results

i. Energy Resolution

Figure 2-2 compares the experimental and simulated intrinsic and extrinsic energy spectra of $^{177}LuCl_3$ for the Symbia T16 normalised to the maximum value obtained at 208.4 keV. At energies below 20 keV, the experimental spectrum displays a cut-off energy. The iodine escape peak was visible at 27 – 30 keV and the lead x-ray peak at 83 – 84 keV.

The energy spectra show photopeaks at 55.8 keV, 112.9 keV and 208.4 keV. It should be noted that the 55.8 keV photopeak is a combination of the characteristic x-rays of 54.6 keV and 55.8 keV, which could not be resolved due to the limited energy resolution. There is a distinct difference in amplitude (peak height) between the experimental and the simulated energy spectrum, where the amplitude of the simulated spectrum overestimates that of the experiment at lower energies ($\leq$ 55.8 keV).

From Figure 2-2, the widths of the experimental and the simulated intrinsic energy spectra for the 208.4 keV photopeak compared favourably. The amplitudes and positions of the experimental and simulated 208.4 keV photopeaks compared well with a small positional difference of 0.3% observed between the maximum peak values. A slight spectral positional shift was observed between the 112.9 keV photopeaks, where the photopeak values differed by 0.7%. In addition, the experimental photopeak presented a slightly wider photopeak in comparison to the simulated photopeak. The observed spectral shift was most prominent for the 55.8 keV photopeak with a positional difference of 3.6% found between the experimental and simulated photopeak values.

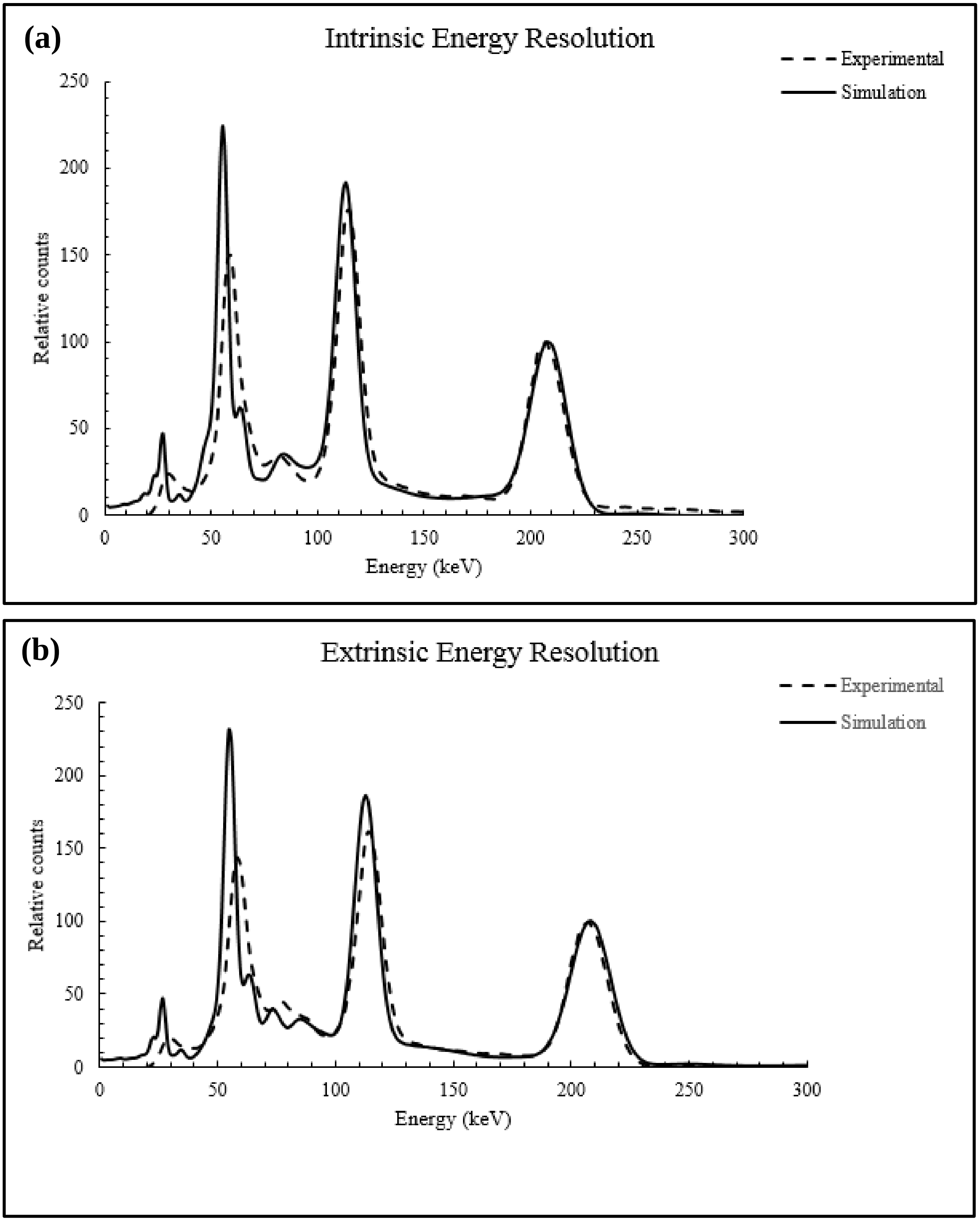

Figure 2-2: *Experimental and simulated* ***(a)*** *intrinsic and* ***(b)*** *extrinsic energy spectra for a* $^{177}LuCl_3$ *source in air acquired with a medium-energy collimator.*

The energy resolution of the 208.4 keV and 112.9 keV photopeaks for the experimental and simulated data were calculated from the respective spectra (Figure 2-2). Table 2-2 shows that the intrinsic energy resolution values for the ^{177}Lu 208.4 keV photopeak were 9.6±0.06% and 9.9% for the experimental and simulated energy resolution, respectively. The absolute difference of 0.3% and percentage difference of -3.1% indicated good agreement between the experimental and simulated data. Similarly, the intrinsic energy resolution for the 112.9 keV photopeak was 11.7±0.19% and 10.9% for the experimental and simulated energy resolutions, respectively. The absolute difference of 0.8% and percentage difference of 6.8% indicated that the values were comparable. The energy resolution for the 208.4 keV photopeak was better than that of the 112.9 keV photopeak for both the experimental and simulated energy resolution values.

The extrinsic energy resolution for the 208.4 keV photopeak values was 9.4±0.09% and 9.9% for the experimental and simulated energy resolution, respectively, with an absolute difference of 0.5% and a percentage difference of -5.3%. The 112.9 keV photopeak energy resolution was 11.4±0.18% and 10.5% for the experimental and simulated data, respectively, with an absolute difference of 0.9% and a percentage difference of 7.9%. Both cases indicated an acceptable difference between the experimental and simulated values.

Table 2-2: *Intrinsic and extrinsic energy resolution calculated from the full width at half maximum (FWHM) of the $^{177}LuCl_3$ 208.4 keV and 112.9 keV photopeaks.*

	Energy Resolution (%)			
	Experimental	**Simulated**	**Absolute Difference (%)**	**% Difference**
208.4 keV				
Intrinsic	9.6±0.06	9.9	0.3	-3.1
Extrinsic	9.4±0.09	9.9	0.5	-5.3
112.9 keV				
Intrinsic	11.7±0.19	10.9	0.8	6.8
Extrinsic	11.4±0.18	10.5	0.9	7.9

ii. System Spatial Resolution

Table 2-3 shows the results obtained from the Gaussian functions used to calculate the system spatial resolution. The calculated FWHM values were 11.5±0.35 mm and 11.0±0.03 mm for the experimental and simulated line spread functions, respectively. These results indicated good agreement with an absolute difference of 0.5 mm and a percentage difference of 4.3%. The experimental and simulated FWTM values of 20.8±0.82 mm and 20.1±0.06 mm, respectively, also showed good agreement with an absolute difference of 0.7 mm and a percentage difference of 3.4%.

Table 2-3: *Experimental and simulated planar system spatial resolution values obtained from capillary tubes uniformly filled with $^{177}LuCl_3$ placed in air at 10 cm from the detector acquired using the 208.4 keV photopeak for the detector equipped with a medium-energy collimator.*

	System Spatial Resolution (mm)			
	Experimental	**Simulated**	**Absolute Difference (mm)**	**% Difference**
FWHM[*]	11.5±0.35	11.0±0.03	0.5	4.3
FWTM[**]	20.8±0.82	20.1±0.06	0.7	3.4

[*] *FWHM*, full width at half the maximum; [**] *FWTM*, full width at a tenth maximum

iii. System Sensitivity

The Biodex Atomlab 500 dose calibrator used to measure the activity dispensed in the petri dish, underestimated the ^{177}Lu activity determined by NMISA with 6.75±1.8%. This underestimation was incorporated into the system sensitivity value. Table 2-4 indicates that the system sensitivity values for the experimental and simulated data were 10.0±0.03 cps/MBq and 10.3 cps/MBq, respectively. The small absolute (0.3 cps/MBq) and percentage (3.0%) differences showed good agreement between the simulation and the experimental values.

Table 2-4: *Experimental and simulated planar system sensitivity values for images of the petri dish uniformly filled with* $^{177}LuCl_3$ *acquired in a 20% window centred at the 208.4 keV photopeak for the detector equipped with a medium-energy collimator.*

System Sensitivity (cps/MBq)			
Experimental	**Simulated**	**Absolute Difference (cps/MBq)**	**% Difference**
10.0±0.03	10.3	0.3	-3.0

iv. SPECT Calibration Factors

Transverse slices of the reconstructed SPECT images obtained for the sphere in air are shown in Figure 2-3. The Gibbs artefact, which is a result of incomplete sampling of high-frequency information, is visible as an increased intensity around the edges of the images. This phenomenon was reported by Kangasmaa et al. (38). The experimental image displayed a non-uniform intensity around the edges as indicated by the intensity difference displayed between arrow 1 and 2, compared to the relatively uniform intensity indicated between arrow 3 and 4. Similar to the calculation of the system sensitivity values, the inaccuracy of the dose calibrator was incorporated in the SPECT calibration factor calculations.

(a) Experimental **(b) Simulated**

Figure: 2-3. *SPECT reconstructed transverse slices of a 4 cm diameter sphere uniformly filled with* $^{177}LuCl_3$ *measured in air displaying the Gibbs artefact for the* ***(a)*** *experimental* ***(b)*** *simulated images.*

The results for the SPECT air and water calibration factors are shown in Table 2-5. For the air calibration factor, the experimental and simulated calibration factor values compared well with an absolute and percentage difference of 0.1 cps/MBq and 1.2%, respectively. Slightly higher differences were observed for the water calibration factor with absolute and percentage differences of 1.6 cps/MBq and 7.7%.

Table 2-5: *^{177}LuCl$_3$ SPECT calibration factors obtained for a 4 cm diameter sphere suspended in air and placed in a water-filled cylindrical phantom.*

	SPECT Calibration Factors (cps/MBq)			
	Experimental	**Simulated**	**Absolute Difference (cps/MBq)**	**% Difference**
Air	8.4±1.04	8.3	0.1	1.2
Water	7.8±0.94	7.2	0.6	7.7

2.5 Discussion

In general, literature validation studies for MC modelling of gamma cameras compare simulation result values with values specified by the manufacturer and accept differences between the simulation and experimental data within manufacturer specifications (24,27). To our knowledge, there are no specification test reports available for the Symbia T series for ^{177}Lu.

i. Energy Resolution

In Section 1.4, we presented the comparison of intrinsic and extrinsic experimental and simulated energy spectra acquired in air. The general shape and alignment of the spectra (Figure 2-2(a)) indicated that the camera response was well modelled and the scatter processes in the detector were accurately simulated. Additionally, all prominent features in the measurement spectrum such as the iodine escape peak and the lead x-ray peak were appropriately simulated. Figure 2-2(b) shows similar agreement for the energy resolution if a scattering and attenuating medium, such as the collimator, is present. The difference between the experimental and the simulated energy spectra (Figure 2-2) observed below 20 keV can be attributed to the fact that physical gamma cameras have a cut-off energy below which the electronic signal is set to zero. This attempts to eliminate electronic noise and corresponds to an energy cut-off value of 20 keV for the Siemens

Symbia T series. These findings are corroborated by Uribe et al. (13) who investigated the reproducibility of experimental and simulated spectra for a range of isotopes, including ^{177}Lu. The prominence of the spectral shift with decreasing energy was attributed to the non-linear energy response of the gamma camera detector system (39).

The peak observed at 27 – 30 keV for both intrinsic and extrinsic spectra can be attributed to the escape of the characteristic iodine K-shell x-rays from the crystal. This escape peak showed a higher amplitude (peak height) for the simulated spectrum than for the experimental energy spectrum. This was attributed to the improved energy resolution allocated to the simulated spectrum. The lead x-ray peak observed at 83 – 84 keV, resulting from the photoelectric interaction of the gamma rays with the lead shielding of the detector and collimator, is evident in both the experimental and simulated spectra.

The overestimation of the peak values for the simulation spectrum observed at lower energies (27 keV and 55 keV) could be attributed to the constant energy response of the simulated energy spectrum, which deviates from the measured energy response at lower energies as described in Section 1.3.2. This resulted in a narrower photopeak with an increased amplitude for the simulated energy spectrum at lower energies, in comparison to the experimental, which presented a broader photopeak with decreased amplitude.

There was good agreement between the experimental and simulated energy spectra, more so for the 208.4 keV photopeak, with a minor shift (0.3%) compared to the 112.9 keV (0.7%) and the 55.8 keV (3.6%) photopeak. These observations occurred for both the intrinsic and extrinsic energy spectra. A slightly improved intrinsic energy resolution value was obtained for the experimental 208.4 keV photopeak (9.6±0.06%) compared to the simulated energy resolution (9.9%) (Table 2-2). However, the simulated 11.9 keV photopeak (10.9%) yielded better values compared to the experimental value (11.7±0.19%). This trend could also be due to allocating a constant energy response for the simulated gamma camera. The 208.4 keV photopeak provided a better energy resolution value than the 112.9 keV photopeak for both the experimental and simulated energy spectra. As a general rule, energy resolution improves with higher energies (35). The absolute and percentage differences of 0.3% and 3.1%, respectively, indicated that the experimental and simulated intrinsic energy resolution values compared well for the 208.4 keV photopeak. Similar results were found for the extrinsic values with the best agreement for the 208.4 keV photopeak with absolute and percentage differences of 0.5% and 5.3%, respectively. Comparable differences in the experimental and simulated energy resolution values were reported for SIMIND modelling a Siemens E Cam gamma camera using ^{99m}Tc (23). The authors found slightly better absolute and percentage difference values of 0.2% and 1.4% for the intrinsic energy resolution and 0.3% and 3.4% for the extrinsic values between the experimental and simulated data. These results are expected since the authors modelled ^{99m}Tc, and the specific version of SIMIND used in their study simulated the energy response with reference to ^{99m}Tc. The gamma camera's energy response was beyond the scope of this study and therefore was not investigated. To note, a constant energy resolution was used in the simulations, which may affect quantification when dual peak (112.9 keV and 208.4 keV) imaging is used.

ii. System Spatial Resolution

The FWHM and FWTM values of the system spatial resolution for the experimental and simulated line spread functions compared well (Table 2-3). The small difference may be attributed to the uncertainty in the thickness of the collimator cover (which includes a touch-pad) and the distance between the back of the collimator and the crystal. Better spatial resolution values were found for the simulated data compared to the experimental data. This finding is corroborated by Ejeh et al. (24) who validated SIMIND for modelling a Siemens Symbia T for ^{131}I. The results in this study correspond with findings by Rodrigues et al. (27) where the simulated spatial resolution was found to be better than the experimental spatial resolution for validation of GEANT4 MC program for a Siemens E Cam dual-head gamma camera using ^{99m}Tc with a LEHR collimator. Overall, the spatial resolution performance of the simulated model shows an acceptable level of agreement with the experimental values.

iii. System Sensitivity

The system sensitivity accounts for the number of photons recorded by the detector system for a given activity, and depends on factors such as crystal thickness, collimator type, radionuclide energy, pulse-height analyser window width settings and imaging geometry (40). Activity measurements play a vital role in the determination of the gamma camera sensitivity factor. Traceability to a secondary standard reduced the uncertainty in the accuracy with which the dose calibrator measured ^{177}Lu activity. This was demonstrated by the good agreement found between the experimental and simulated system sensitivity values (Table 2-4). The rather small difference observed may be attributed to the different measurement geometries, to ascertain the measured activity, used by NMISA compared to that used by our group for the purpose of this study. This is in addition to the relative uncertainty (1.8%) with which the activity accuracy was determined by NMISA. Higher simulated system sensitivity values, compared to the experimental values, have been reported in literature (27).

iv. SPECT Calibration Factors

The largest source of inaccuracy in the determination of the gamma camera calibration factor has been attributed to the dose calibrator (14). For this reason, the uncertainty in the dose calibrator was kept to a minimum through traceability to NIMSA. The experimental and simulated air calibration factors compared well, showing small absolute and percentage differences (Table 2-5), with slightly higher differences for the water calibration factor. The concentrations used for the air and water calibration factors were comparable. As mentioned in Section 1.3.1.2, the acquisitions followed a clinical protocol. Thus, the SPECT projection count density obtained for the water calibration factor was slightly lower due to attenuation. Although the count density of the simulated SPECT projections corresponded to the experimental projections, the uncertainty in the lower count density may propagate in the reconstruction process into a larger difference between the experimental and simulated water calibration factors. This may serve as a possible attribution to the larger difference observed for the water calibration factors. Overall, the results were comparable to the 7.82 cps/MBq and 7.28 cps/MBq for a sphere in air and water, respectively, inserted in a Jaszczack phantom, acquired with a 20% energy window over the 208.4 keV photopeak (14). Similarly, the authors found the air calibration to be slightly higher compared to the water calibration.

The transverse slices of the reconstructed SPECT images obtained for the sphere in air (Figure 2-3) displayed the Gibbs artefact for both the experimental and simulated images. The Gibbs artefact was observed due to the use of the collimator depth-dependent 3D resolution recovery incorporated in the reconstruction algorithm. An increased intensity was displayed around the edges of the images with a lower intensity in the centre. Literature has reported this effect to underestimate the counts recovered in larger spherical volumes of interest (38). The authors showed the effect of the

Gibbs artefact in a phantom study, which investigated collimator correction artefacts using different sized hot spheres filled with ^{99m}Tc placed in a cylindrical phantom. One of their objectives was to investigate artefacts from the SPECT images of the hot spheres, reconstructed using the OSEM reconstruction algorithm with and without collimator response correction. Their findings included the display of a "hole" in the middle of the image, which was found to be more pronounced for their largest sphere with a diameter of 3.7 cm. This may be applicable to the current study since our sphere size (4 cm) was approximately equivalent to their largest sphere (3.7 cm). As mentioned in Section 1.3.1, $LuCl_3$ was produced using the indirect method, which excludes the production of significant long-lived contaminants such as ^{177m}Lu. This method has been described to provide ^{177}Lu in the highest possible radionuclide purity (25). This may exempt significant contaminants as a possible attribute to the difference found between the experimental and simulated images. Furthermore, metal radionuclide solutions have been shown to adhere to phantom walls, resulting in non-homogeneous activity distributions (41). This observation may apply to our study since the $^{177}LuCl_3$ adheres to the walls of the spheres causing a non-uniform activity distribution. The experimental image (Figure 2-3(a)) displayed a non-uniform intensity around the edges (indicated by the intensity difference between arrow 1 and 2) due to the possible inconsistent adherence of the $^{177}LuCl_3$. Therefore, the experimental non-uniformity at the edges is a combination of the inconsistent adherence of the $^{177}LuCl_3$ and the Gibbs artefact. The simulated image (Figure 2-3(b)), however, displayed a relatively uniform intensity around the edges, distinctly indicating the effects of the Gibbs artefact.

For SPECT quantification purposes, the use of a predetermined SPECT calibration factor would incorporate the limitations of the correction techniques, hence reducing the inaccuracies with which SPECT data may be quantified. Better SPECT quantification accuracies have been reported for a sphere filled with activity in a phantom containing background activity for ^{131}I compared to planar images (5). In the current study, background was not included in the determination of the calibration factor as $^{177}LuCl_3$ is expensive and could result in contamination of the cylindrical phantom for an extended period. However, a calibration factor determined from a radioactive sphere of ^{177}Lu placed inside a cylindrical phantom filled with non-radioactive water produced activity quantification accuracies of 1% in an anthropomorphic torso phantom. This was reported as being suitable for quantifying ^{177}Lu SPECT data using the 208.4 keV photopeak (14). Therefore, it was decided to validate the water calibration factor without background activity. The routine experimental use of $^{177}LuCl_3$ poses certain challenges. Firstly, $^{177}LuCl_3$ is expensive and secondly, due to its long physical half-life, it will contaminate phantoms that will exclude them from being used in other experiments for an extended period of time. It should be noted that the optimisation of the number of updates was not in the scope of this study, therefore, the manufacturer specified reconstruction parameters were used. This may serve as a limitation for quantification accuracy of SPECT data, and for that purpose, the reconstruction algorithm should be optimised for any future quantification studies.

2.6 Conclusion

To our knowledge, a model of the Siemens Symbia T16 SPECT/CT gamma camera with ^{177}Lu using the SIMIND MC program has not been reported. Therefore, this study aimed to model the Symbia dual-head T16 with ^{177}Lu using SIMIND. This was achieved by comparing the simulated results obtained with the modelled gamma camera with the experimental results of the clinical gamma camera. For most of the tests, the results from the simulation data and those of the experiments compared well. The general shape and alignment of the energy spectra indicated that the interactions in the detector were well modelled with minor differences observed at lower energies. The respective energy spectra over the 208.4 keV photopeak region, used for clinical imaging, showed good agreement. This suggested that the simulated images, at the 208.4 keV photopeak, were a true representation of the images obtained with the clinical gamma camera.

This validation proved the potential use of SIMIND for further investigation of quantitative planar and SPECT data is possible. From the above, it is evident that SIMIND is capable of emulating the clinical Symbia T16 successfully, and therefore can be used confidently to model planar and SPECT images for ^{177}Lu.

2.7 References

1. Cachovan M, Vija AH, Hornegger J, Kuwert T. Quantification of ^{99m}Tc-DPD concentration in the lumbar spine with SPECT/CT. EJNMMI Res. 2013 Jun 5;3:45. https://doi.org/10.1186/2191-219X-3-45

2. Gnesin S, Leite Ferreira P, Malterre J, Laub P, Prior JO, Verdun FR. Phantom Validation of Tc-99m Absolute Quantification in a SPECT/CT Commercial Device. Comput Math Methods Med. 2016. https://doi.org/10.1155/2016/4360371

3. Willowson K, Bailey DL, Baldock C. Quantitative SPECT reconstruction using CT-derived corrections. Phys Med Biol. 2008 Jun 21;53(12):3099–112. https://doi.org/10.1088/0031-9155/53/12/002

4. Pereira JM, Stabin MG, Lima FRA, Guimarães MICC, Forrester JW. Image quantification for radiation dose calculations--limitations and uncertainties. Health Phys. 2010 Nov;99(5):688–701. https://doi.org/10.1097/HP.0b013e3181e28cdb

5. Dewaraja YK, Ljungberg M, Koral KF. Characterization of Scatter and Penetration Using Monte Carlo Simulation in ^{131}I Imaging. J Nucl Med Off Publ Soc Nucl Med. 2000 Jan;41(1):123–30.

6. Sjögreen K, Ljungberg M, Strand S-E. An activity quantification method based on registration of CT and whole-body scintillation camera images, with application to ^{131}I. J Nucl Med Off Publ Soc Nucl Med. 2002 Jul;43(7):972–82.

7. Garkavij M, Nickel M, Sjögreen-Gleisner K, Ljungberg M, Ohlsson T, Wingårdh K, et al. ^{177}Lu-[DOTA0,Tyr3] octreotate therapy in patients with disseminated neuroendocrine tumors: Analysis of dosimetry with impact on future therapeutic strategy. Cancer. 2010 Feb 15;116(4 Suppl):1084–92.

8. Ljungberg M, Celler A, Konijnenberg MW, Eckerman KF, Dewaraja YK, Sjögreen-Gleisner K, et al. MIRD Pamphlet No. 26: Joint EANM/MIRD Guidelines for Quantitative ^{177}Lu SPECT Applied for Dosimetry of Radiopharmaceutical Therapy. J Nucl Med Off Publ Soc Nucl Med. 2016 Jan;57(1):151–62. https://doi.org/10.2967/jnumed.115.159012

9. Ljungberg M, Sjögreen-Gleisner K. The accuracy of absorbed dose estimates in tumours determined by quantitative SPECT: a Monte Carlo study. Acta Oncol Stockh Swed. 2011 Aug;50(6):981–9. https://doi.org/10.3109/0284186X.2011.584559

10. Zaknun JJ, Bodei L, Mueller-Brand J, Pavel ME, Baum RP, Hörsch D, et al. The joint IAEA, EANM, and SNMMI practical guidance on peptide receptor radionuclide therapy (PRRNT) in neuroendocrine tumours. Eur J Nucl Med Mol Imaging. 2013;40(5):800–16. https://doi.org/10.1007/s00259-012-2330-6

11. Browne, E., 1993. Table of isotope decay data. The Lund/LBNL Nuclear Data Search. Department of Physics, Lund University, Sweden. LBNL, Berkeley, USA. (http://nucleardata.nuclear.lu.se/toi/nuclide.asp?iZA=710177) [Accessed 15 November 2018].

12. Beauregard J-M, Hofman MS, Pereira JM, Eu P, Hicks RJ. Quantitative ^{177}Lu SPECT (QSPECT) imaging using a commercially available SPECT/CT system. Cancer Imaging Off Publ Int Cancer Imaging Soc. 2011 Jun 15;11:56–66. https://doi.org/10.1102/1470-7330.2011.0012

13. Uribe CF, Esquinas PL, Gonzalez M, Celler A. Characteristics of Bremsstrahlung emissions of ^{177}Lu, ^{188}Re, and ^{90}Y for SPECT/CT quantification in radionuclide therapy. Phys Medica PM Int J Devoted Appl Phys Med Biol Off J Ital Assoc Biomed Phys AIFB. 2016 May;32(5):691–700. https://doi.org/10.1016/j.ejmp.2016.04.014

14. D'Arienzo M, Cazzato M, Cozzella ML, Cox M, D'Andrea M, Fazio A, et al. Gamma camera calibration and validation for quantitative SPECT imaging with ^{177}Lu. Appl Radiat Isot Data Instrum Methods Use Agric Ind Med. 2016;112:156–64. https://doi.org/10.1016/j.apradiso.2016.03.007

15. de Nijs R, Lagerburg V, Klausen TL, Holm S. Improving quantitative dosimetry in ^{177}Lu-DOTATATE SPECT by energy window-based scatter corrections. Nucl Med Commun. 2014 May;35(5):522–33. https://doi.org/10.1097/MNM.0000000000000079

16. He B, Nikolopoulou A, Osborne J, Vallabhajosula S, Goldsmith S. Quantitative SPECT imaging with Lu-177: A physical phantom evaluation. J Nucl Med. 2012 Jan 5;53(supplement 1):2407–2407.

17. Shcherbinin S, Piwowarska-Bilska H, Celler A, Birkenfeld B. Quantitative SPECT/CT reconstruction for ^{177}Lu and ^{177}Lu/^{90}Y targeted radionuclide therapies. Phys Med Biol. 2012;57(18):5733. https://doi.org/10.1088/0031-9155/57/18/5733

18. Zaidi H. Relevance of accurate Monte Carlo modeling in nuclear medical imaging. Med Phys. 1999 Apr;26(4):574–608. https://doi.org/10.1118/1.598559

19. Staelens S, Strul D, Santin G, Vandenberghe S, Koole M, D'Asseler Y, et al. Monte Carlo simulations of a scintillation camera using GATE: validation and application modelling. Phys Med Biol. 2003;48(18):3021. https://doi.org/10.1088/0031-9155/48/18/305

20. He B, Du Y, Song X, Segars WP, Frey EC. A Monte Carlo and physical phantom evaluation of quantitative In-111 SPECT. Phys Med Biol. 2005 Sep 7;50(17):4169–85. https://doi.org/10.1088/0031-9155/50/17/018

21. Islamian JP, Bahreyni Toossi MT, Momennezhad M, Naseri S, Ljungberg M. Simulation of a Quality Control Jaszczak Phantom with SIMIND Monte Carlo and Adding the Phantom as an Accessory to the Program. Iran J Med Phys. 2012 Jun 1;9(2):135–40.

22. Ljungberg M, Strand S-E. A Monte Carlo program for the simulation of scintillation camera characteristics. Comput Methods Programs Biomed. 1989 Aug 1;29(4):257–72. https://doi.org/10.1016/0169-2607(89)90111-9

23. Bahreyni Toossi MT, Islamian JP, Momennezhad M, Ljungberg M, Naseri SH. SIMIND Monte Carlo simulation of a single photon emission CT. J Med Phys Assoc Med Phys India. 2010;35(1):42–7. https://doi.org/10.4103/0971-6203.55967

24. Ejeh JE, van Staden JA, du Raan H. Validation of SIMIND Monte Carlo Simulation Software for Modelling a Siemens Symbia T SPECT Scintillation Camera. In: Lhotska L, Sukupova L, Lacković I, Ibbott GS, editors. World Congress on Medical Physics and Biomedical Engineering 2018. Springer Singapore; 2019. p. 573–6. (IFMBE Proceedings).

25. Dash A, Pillai MRA, Knapp FF. Production of ^{177}Lu for Targeted Radionuclide Therapy: Available Options. Nucl Med Mol Imaging. 2015 Jun;49(2):85–107. https://doi.org/10.1007/s13139-014-0315-z

26. National Electrical Manufacturers Association. NEMA NU 1. Performance measurements of gamma cameras. Rosslyn, Virginia, USA: National Electrical Manufacturers Association; 2012. p. 2012.

27. Rodrigues S, Tome B, Abreu MC, Santos N, Mendes PR, Peralta L. Monte Carlo Simulation and Experimental Characterization of a Dual Head Gamma Camera. 2007 Nov 16. (https://arxiv.org/abs/0711.2577). [accessed 27 Sept 2019].

28. Schindelin J, Arganda-Carreras I, Frise E, Kaynig V, Longair M, Pietzsch T, et al. Fiji: an open-source platform for biological-image analysis. Nat Methods. 2012 Jun 28;9(7):676–82. https://doi.org/10.1038/nmeth.2019

29. de Wit TC, Xiao J, Nijsen JFW, van het Schip FD, Staelens SG, van Rijk PP, et al. Hybrid scatter correction applied to quantitative holmium-166 SPECT. Phys Med Biol. 2006 Oct 7;51(19):4773–87. https://doi.org/10.1088/0031-9155/51/19/004

30. Shcherbinin S, Celler A, Belhocine T, Vanderwerf R, Driedger A. Accuracy of quantitative reconstructions in SPECT/CT imaging. Phys Med Biol. 2008 Sep 7;53(17):4595–604. https://doi.org/10.1088/0031-9155/53/17/009

31. Dewaraja YK, Frey EC, Sgouros G, Brill AB, Roberson P, Zanzonico PB, et al. MIRD pamphlet No. 23: quantitative SPECT for patient-specific 3-dimensional dosimetry in internal radionuclide therapy. J Nucl Med Off Publ Soc Nucl Med. 2012 Aug;53(8):1310–25. https://doi.org/10.2967/jnumed.111.100123

32. International Atomic Energy Agency (IAEA). Chapter 5 - Quantitative SPECT OR SPECT/CT imaging. In: Quantitative nuclear medicine imaging: concepts, requirements and methods. IAEA Human Health Report No.9. Vienna, Austria: IAEA; 2014. p. 27–36.

33. Ogawa K, Harata Y, Ichihara T, Kubo A, Hashimoto S. A practical method for position-dependent Compton-scatter correction in single photon emission CT. IEEE Trans Med Imaging. 1991;10(3):408–12. https://doi.org/10.1109/42.97591

34. Loening AM, Gambhir SS. AMIDE: A Free Software Tool for Multimodality Medical Image Analysis. Mol Imaging. 2003 Jul 1;2(3):131–137. https://doi.org/10.1162/15353500200303133

35. Cherry SR, Sorenson JA, Phelps ME. Chapter 14 - The Gamma Camera: Performance Characteristics. In: Physics in Nuclear Medicine (Fourth Edition). Philadelphia: W.B. Saunders; 2012. p. 209–231. https://doi.org/10.1016/B978-1-4160-5198-5.00014-9

36. Rault E, Staelens S, Van Holen R, De Beenhouwer J, Vandenberghe S. Accurate Monte Carlo modelling of the back compartments of SPECT cameras. Phys Med Biol. 2011 Jan 7;56(1):87–104. https://doi:10.1088/0031-9155/56/1/006

37. Yushkevich PA, Piven J, Hazlett HC, Smith RG, Ho S, Gee JC, et al. User-guided 3D active contour segmentation of anatomical structures: significantly improved efficiency and reliability. NeuroImage. 2006 Jul 1;31(3):1116–28. https://doi.org/10.1016/j.neuroimage.2006.01.015

38. Kangasmaa T, Sohlberg A, Kuikka JT. Reduction of Collimator Correction Artefacts with Bayesian Reconstruction in Spect. Int J Mol Imaging. 2011. https://doi.org/10.1155/2011/630813

39. Cherry SR, Sorenson JA, Phelps ME. Chapter 10 - Pulse-Height Spectrometry. In: Physics in Nuclear Medicine (Fourth Edition). Philadelphia: W.B. Saunders; 2012. p. 141–154. https://doi.org/10.1016/B978-1-4160-5198-5.00010-1

40. King M, Farncombe T. An Overview of Attenuation and Scatter Correction of Planar and SPECT Data for Dosimetry Studies. Cancer Biother Radiopharm. 2003 Apr 1;18(2):181–90. https://doi.org/10.1089/108497803765036346

41. Park M-A, Mahmood A, Zimmerman RE, Limpa-Amara N, Makrigiorgos GM, Moore SC. Adsorption of metallic radionuclides on plastic phantom walls. Med Phys. 2008 Apr;35(4):1606–10. https://doi.org/10.1118/1.2871191.

3

Chapter 3:

Article II

The Effect of Calibration Factors and Recovery Coefficients on ^{177}Lu SPECT Activity Quantification Accuracy: A Monte Carlo study

This chapter includes the original work that has been published in the European Journal of Nuclear Medicine and Molecular Imaging.

The front page of the published article is shown in Appendix B

DOI: https://doi.org/10.1186/s40658-021-00365-8

TABLE OF CONTENTS

3.1 Abstract

Background: Different gamma camera calibration factor (CF) geometries have been proposed to convert SPECT data into units of activity concentration. However, no consensus has been reached on a standardised geometry. The CF is dependent on the selected geometry and is affected by partial volume effects. This study investigated the effect of two CF geometries and their corresponding recovery coefficients (RCs) on the quantification accuracy of ^{177}Lu SPECT images using Monte Carlo simulations.

Methods: The CF geometries investigated were (i) a radioactive-sphere surrounded by non-radioactive water (CF_{sphere}) and (ii) a cylindrical phantom uniformly filled with radioactive water (CF_{cyl}). Recovery coefficients were obtained using the CF_{sphere} and CF_{cyl}, yielding the RC_{sphere} and RC_{cyl} values, respectively, for partial volume correction (PVC). The quantification accuracy was evaluated using four different sized spheres (15.6 ml – 65.4 ml) and a kidney model with known activity concentrations inside a cylindrical, torso and patient phantom. Images were reconstructed with the OS-EM algorithm incorporating attenuation, scatter and detector-response corrections. Segmentation was performed using the physical size and a small cylindrical volume inside the cylinder for the CF_{sphere} and CF_{cyl}, respectively.

Results: The sphere quantification error (without PVC) was better for the CF_{sphere} (-5.5%) compared to the CF_{cyl} (-20.9%), attributed to the similar geometry of the quantified and CF_{sphere}. Partial volume correction yielded equivalent results (≤ 3.5%) for the CF_{sphere} and CF_{cyl}. The accuracy of the kidney quantification was poorer (≤ 22.3%) for the CF_{sphere} without PVC compared to the CF_{cyl} (≤ 2.4%). Similarly, with PVC, the kidney quantification results were equivalent for the CF_{sphere} and the CF_{cyl} (≤ 3.5%).

Conclusion: The study demonstrated that upon careful selection of CF-RC combinations, comparable quantification errors (≤ 3.5%) were obtained between the CF_{sphere} and CF_{cyl}, when all corrections were applied.

Keywords: ^{177}Lu, Quantification, Monte Carlo, SIMIND, Calibration factor, Recovery coefficients

3.2 Introduction

Lutetium-177 (^{177}Lu) has become widely used for targeted radionuclide therapy in nuclear medicine (1). This is owing to its favourable decay characteristics as both a therapeutic as well as an imaging agent (2). In addition, it is produced with high specific activity and exhibits reliable labelling of peptides used for tumour targeting (3,4). ^{177}Lu has gained favour in the clinical application of peptide receptor radionuclide therapy (PRRT) with ^{177}Lu-DOTATATE for the treatment of patients with late-stage metastatic neuroendocrine tumours (5–9). The kidneys have been identified as the dose-limiting organs for ^{177}Lu-DOTATATE PRRT (10). A significant correlation was found between the tumour-absorbed dose and tumour reduction (11). Therefore, dosimetry should be extended to include both the kidneys and tumour sites to provide a satisfactory understanding of PRRT treatment. There is a large variation in kidney and tumour response among patients following PRRT (12,13). This would facilitate the application of accurate patient-specific dosimetry for PRRT treatment planning, as is the norm in external beam radiotherapy.

Accurate dosimetry is strongly dependent on the accuracy with which activity quantification can be achieved. The imaging and quantification process is not ideal and therefore has been investigated and refined for many years (14–17). There are factors inherent in the imaging process that degrade the images from an ideal representation of the imaged object. These factors include photon attenuation and scattering, collimator blurring, partial volume effects (PVEs), and the reconstruction algorithms (18). SPECT/CT images have been included in many dosimetry protocols for ^{177}Lu activity quantification, and this is owing to their superior quantitative accuracy in comparison to planar images (19, 20). However, the effects of the above-mentioned degrading factors complicate SPECT imaging. Therefore, attempts to compensate for these factors have to be made to improve the accuracy of the quantified activity.

The 3D ordered subset expectation maximization (OS-EM) iterative reconstruction algorithm (21) can include modelling of the physical characteristics of the imaging process. These may include compensation for photon attenuation, photon scatter and collimator detector response (CDR). This algorithm results in reconstructed images with better image quality, improved quantitative accuracy, and less prone to artefacts than analytical methods such as filtered back projection (22–24). The 3D OS-EM reconstruction algorithm has become a standard algorithm with most clinical

SPECT processing units; it is highly recommended and commonly used to obtain improved quantitative SPECT data (25). An important consideration when using the above-mentioned 3D OS-EM reconstruction algorithm is the optimum number of updates which is defined as the product of the number of subsets and iterations. The choice for the number of iterations used in patient studies is a trade-off between the image noise level and improved activity quantitative accuracy, where the latter improves with an increasing number of iterations (26). For quantification purposes, the criteria for the optimum number of 3D OS-EM updates have been accepted as the convergence where 90% of the activity has been recovered (26). Complex reconstruction algorithms incorporating more corrections require a larger number of iterations to reach convergence, and larger objects have been shown to converge faster than smaller objects (27). The percentage root mean square (%RMS) has been used to assess the noise levels in volumes of interest (VOIs) (28–30). It is recommended that phantom or Monte Carlo (MC) simulation studies be used to investigate the optimum number of 3D OS-EM updates needed to provide adequate convergence for accurate activity quantification (16). The optimization is unique to a specific SPECT system and associated reconstruction algorithm as well as the imaging geometry.

The X-ray CT in hybrid SPECT/CT systems has provided an automated way to compensate for object attenuation. The availability of the co-registered SPECT and CT data has made routine attenuation compensation practical and easy to implement. Multiple window scatter compensation methods such as the Dual Energy Window (DEW) and the Triple Energy Window (TEW) methods are available with most gamma camera vendors, and these methods can be used to apply scatter correction during or post-reconstruction. However, model-based scatter correction methods, such as effective source scatter estimation (ESSE), model the scatter function more accurately and thus better resemble the true scatter distribution (31). The ESSE method estimates the degrading scatter effect from a point source at various depths behind a slab of material (mimicking tissue) using MC simulations to pre-calculate a set of scatter kernels. The MC simulation methods are also used to model the geometric response, septal penetration and septal scatter response functions of the gamma camera from a point source in air. For SPECT imaging purposes, these response functions are incorporated during reconstruction to improve spatial resolution. The VOI definition for object delineation is also an important consideration for quantification of SPECT images, and no standardised method has yet been identified. CT data has been used in a number of clinical and phantom studies for object delineation (17,32). The impact of errors due to misdefinition (variability in organ delineation) and misregistration (between emission and CT data) on SPECT and planar quantification accuracy has been investigated (33). The VOI definition is affected by PVEs, which has a larger impact on smaller objects with a size smaller than three times the system spatial resolution (3 × full width at half maximum (FWHM)) (34). The PVE is related to the gamma camera's limited spatial resolution and can be compensated for by including a CDR correction during the iterative reconstruction process. A consequence of the PVE is that the image counts from a photon originating from a point will contribute not only to a single voxel but also to neighbouring voxels. This is known as spill-out of counts and is widely seen in tumour imaging and reported to result in underestimation of the quantified activity distribution (35). Conversely, spill-in of counts from surrounding radioactive objects is also observed resulting in an overestimation of the quantified activity. If this spill-in and spill-out of counts at the edges of objects is not compensated for, it will result in biased quantification results (18). Recovery coefficients (RCs) for partial volume correction (PVC) can easily be determined in phantom studies where true activity and object size can be measured (36). CT-based RCs have been successfully used for PVC in ^{177}Lu SPECT activity quantification in a torso phantom (15) and extended to 3D printed kidney phantoms (32). Another important consideration of PVE is image sampling. Due to the limited voxel size, a combination of objects having different activity concentrations may contribute to a specific voxel count. Thus, a small shift in the delineated region can result in a significant variation in counts. The extent of the variation can be limited by using smaller voxel sizes (37).

SPECT was traditionally regarded as a non-quantitative imaging modality, unlike its counterpart PET. In both modalities, advances in hybrid systems include automation of compensation methods for photon attenuation, scatter and limited spatial resolution in a unified manner using iterative reconstruction algorithms. In general, SPECT images are obtained in units of image counts, unlike PET reconstructed images, which have units of tissue radioactive concentration (kBq.cm^{-3}). Thus, a calibration factor (CF) has to be applied to obtain SPECT reconstructed images in units of radioactive concentration. It is only recently, with modern SPECT/CT systems, that reconstructed SPECT images are routinely provided in units of radioactive concentration. An example of such a SPECT/CT system is the Siemens Symbia Intevo^{TM} scanner (Siemens Healthineers, Germany), which incorporates a point source traceable to a secondary standard laboratory for calibration purposes and conversion of the reconstructed SPECT images to activity concentration.

The system sensitivity, as defined by the National Electrical Manufacturers Association (NEMA) (38), is conventionally used as a CF in SPECT images to convert the quantified counts into units of activity (39–41). It is generally accepted that the CF, with a source geometry that incorporates photon attenuation and scatter properties in the acquisition reduces the effects of imperfect scatter and attenuation corrections (26). Different geometries have been reported for obtaining CFs for ^{177}Lu SPECT quantitative imaging (42). The authors investigated four geometries to obtain CFs which included: a point source in air, a sphere in air, a sphere in non-radioactive water and a 20 cm diameter cylinder uniformly filled with $^{177}LuCl_3$. The point source in air and the sphere in water yielded the worst and best results respectively for the activity quantification in an anthropomorphic torso phantom. The sphere in a non-radioactive background was reported as suitable for activity quantification of ^{177}Lu SPECT data using the 208.4 keV photopeak. Superior quantification accuracy has been reported for SPECT imaging with a CF obtained using a sphere in a radioactive background (sphere-to-background ratio of 6:1) compared to that obtained using a cylindrical phantom uniformly filled with ^{131}I (27). The authors also reported the sphere CF yielded more stable results compared to a point source in air which is highly sensitive to the selected VOI size. Due to down-scatter and septal penetration from high energy photons into the photopeak window for isotopes such as ^{131}I and ^{188}Re, Zhao et al. (43) suggested that a CF obtained from a planar point source must include scatter correction for these isotopes, and to a lesser extent for the ^{177}Lu 208.4 keV photopeak. In addition, the study showed that CFs obtained using spheres in a non-radioactive background may overestimate the CF by 10% attributed to the underestimation of the TEW scatter approximation and accentuated further by the attenuation correction during reconstruction.

The disparities between ^{177}Lu SPECT activity quantification accuracy reported by different authors for various phantoms, as well as their data acquisition and processing protocols, have been summarised in the MIRD pamphlet 26 (16). The MIRD pamphlet 26 also documents guidelines for ^{177}Lu SPECT quantitative imaging established using the SIMIND (Simulating Medical Imaging Nuclear Detectors) MC program (44). However, this document does not report the quantification accuracy or error obtained with the recommended methods. Each clinic should thus determine the quantification error relevant for their chosen setup and method. There is increasing evidence supporting the need for personalised dosimetry based on SPECT quantitative information. The attempt has been hindered by the lack of standardised methods, which include determining the gamma camera CF. As indicated in the above studies, there is no consensus with regard to the CF geometry. Wevrett et al. (45) demonstrated the feasibility of using simple phantom geometries to standardise gamma camera calibrations for activity quantification of ^{177}Lu and ^{131}I. These phantom geometries included a sphere placed centrally in air and in water as well as at an offset of 8.6 cm in water. The authors concluded that none of their geometries were sufficient to be used individually and recommended that a mean value obtained from the different geometries should be incorporated. They also suggested that the characterisation of the change in the CF with lesion volume was necessary due to the PVE and have proposed that the CF and RC should be combined in a mean calibration coefficient. This approach may require that a large range of CF values be determined from different geometries and tabulated. In addition, the CF would be affected by the VOI definition and further affected by the segmentation method used to determine the RC. In another publication, Wevrett et al. (46) assessed the feasibility of carrying out an international inter-comparison of European hospitals to determine the consistency of the CFs used at these sites. In the exercise dual compartment spherical sources of known activity concentration and volume, were sent to seven hospitals and acquired in a water-filled Jaszczak phantom. The hospitals acquired and processed the data using their own choice of methods. The authors reported that no single method reported by the different hospitals yielded a significantly improved accuracy. Further research has to be carried out to investigate the uncertainties associated with determining a suitable CF for ^{177}Lu SPECT quantitative imaging.

In this study, we aimed to investigate the effect of two CF geometries and their corresponding RCs on the quantification accuracy of ^{177}Lu SPECT images using MC simulations. The CFs were obtained from (i) a radioactive sphere surrounded by non-radioactive water, termed $\text{CF}_{\text{sphere}}$, and (ii) a cylindrical phantom uniformly filled with radioactive water, termed a CF_{cyl}. Two sets of RC curves were generated as a function of object size, using the two CFs. The first RC curve was constructed using the $\text{CF}_{\text{sphere}}$ and the second RC curve was created using the CF_{cyl}. The two curves were used to obtain the $\text{RC}_{\text{sphere}}$ and RC_{cyl} values, respectively. The effects of the CF-$\text{RC}_{\text{sphere}}$ and CF-RC_{cyl} combinations, on the quantification accuracy of ^{177}Lu activity derived from SPECT images, were evaluated using three phantom geometries.

3.3 Materials and Methods

The SIMIND MC program (SIMIND version 6.1.2) was used in this study. Its ability to successfully mimic ^{177}Lu SPECT images with a model of a Siemens Symbia T16 hybrid SPECT/CT (Symbia T16) (Siemens Medical Solutions, Inc. Hoffman Estates, IL., USA) dual-head gamma camera was validated in a previous study (47). The validation included planar tests stipulated for gamma camera performance criteria following the NEMA recommendations (38). The differences between the experimental and simulated values of three particular validation tests are significant to report herein. These three planar tests, namely, the intrinsic energy resolution (%), the system spatial resolution (FWHM), and the system sensitivity (cps/MBq) had percentage differences of -3.1%, 4.3%, and 0.3% between the experimental and simulated values, respectively. The last two parameters' data was obtained in a 20% energy window centred over the 208.4 keV photopeak. Details describing the validation tests and the gamma camera physical parameters are defined in the above-mentioned publication. Three voxelized phantoms, as shown in Figure 3-1, were used in this study. They were created by segmenting the CT images of these phantoms with the software ITK-snap (version 3.2.0) (48) as described in detail by Ramonaheng et al. (47). The three phantoms shown in Figure 3-1 were: (a) a cylindrical phantom with a segmented volume of 9 900 ml, (b) an RSD Alderson anthropomorphic torso phantom (Radiological Support Devices Inc, USA) which was segmented to separate the lung inserts (combined segmented volume of 2 090 ml), the liver insert (1 090 ml) and the remainder of the phantom (2 095 ml), and (c) a randomly selected SPECT/CT patient study anonymously obtained from the Symbia T16 patient database, approved by our institution's ethics committee. For the patient phantom, the liver (1 590 ml), lungs (2 270 ml), spleen (160 ml), left (159 ml) and right (169 ml) kidneys, as well as the remaining volume of the patient (14 100 ml), were segmented. Each of the voxelized phantoms was appropriately equipped with spherical inserts using ITK-snap to mimic tumours.

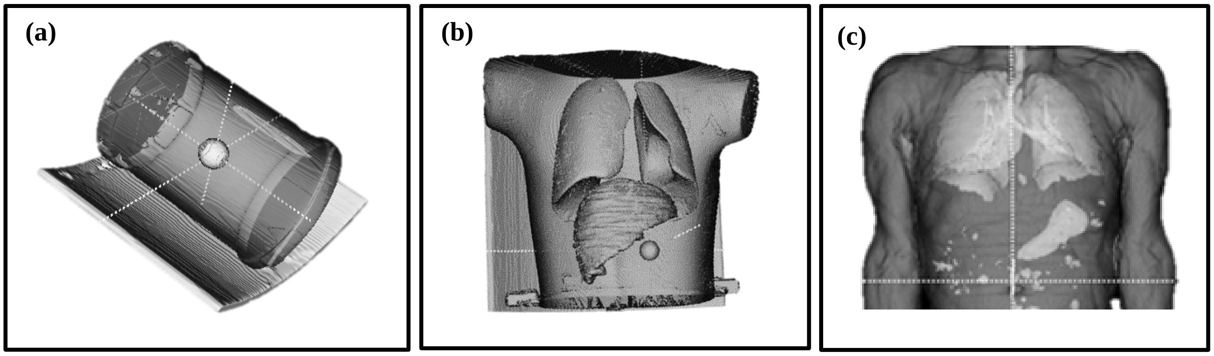

Figure 3-1: *Segmented images of the* ***(a)*** *cylindrical* ***(b)*** *torso and* ***(c)*** *patient phantoms.*

The simulations were set up for ^{177}Lu using a medium-energy (ME) collimator with a 20% energy window centred over the 208.4 keV photopeak (187.2 – 228.8 keV) (19, 49–51). For all SPECT simulations, the phantoms were placed in the centre of the field of view and projection data were simulated over 360° with equally spaced projections using a non-circular orbit. The phantom to detector distance was determined for each projection angle using a density map to mimic auto-contour detection of the phantom outline (47). All simulations were conducted with a high number of photon histories to ensure data sets with low simulation noise. Sixty (60) projections with an equivalent of 45 s acquisition time were simulated and the image data were stored in a 128 × 128 matrix with a pixel size of 4.8 × 4.8 mm (16, 52).

Our study comprised two phases. The *first phase* of the study focused on three essential steps required to optimize the reconstruction parameters and the quantification process. The steps consisted of (i) optimizing the 3D OS-EM reconstruction algorithm, (ii) establishing the CFs and (iii) determining the RCs. The *second phase* of the study evaluated the quantification accuracy, reported as the quantification error, achieved with the steps established in the initial phase by quantifying spherical inserts in the three above-mentioned phantoms. The kidney quantification in the patient phantom was also evaluated. The simulations of the phantoms comprised simulated projection images and result files describing the simulation protocol. A 3D OS-EM algorithm was used for image reconstruction and employed CT-based attenuation correction, ESSE scatter correction (31, 53), and CDR correction. The CDR correction included modelling of the intrinsic and geometric response as well as the septal penetration and septal scatter. All the reconstructed data were analysed using the public domain software Amide (54). Spherical volumes corresponding to the physical sizes of the spheres were used to delineate all the spheres. This method of delineation is analogous to the use of CT images for the segmentation of quantitative

SPECT images (15,55,56). The mean counts from the fractional voxels were used to calculate the total counts from these VOIs.

3.3.1 Quantification Steps

For the first phase of the study, each of the phantom geometries in the quantification steps was simulated with a uniform ^{177}Lu concentration of 3.04 MBq/ml. This is comparable to concentrations reported in the literature for similar investigations (57). Different sphere sizes were simulated individually in the centre of the phantom to avoid spill-in of nearby spheres.

3.3.1.1 3D OS-EM Optimization

To determine the optimal number of 3D OS-EM updates required for convergence (where 90% of the true activity is recovered), SPECT images of a cylindrical phantom equipped with radioactive spheres with volumes (and their corresponding diameters) of 4.2 ml (2.0 cm), 14.1 ml (3.0 cm) and 65.4 ml (5.0 cm) in a warm background were simulated. To further investigate the effect of the sphere-to-background ratio on the convergence, each sphere was simulated using sphere-to-background ratios of 6:1 and 13:1 (55,57,58). The reconstruction was performed as described above and multiple 3D OS-EM updates (ranging from 24 to 204) were used. As the quantified activity for the spheres is not yet known, the total counts for each sphere size were normalised to the maximum number of counts obtained at 204 updates for each particular VOI, and expressed as percentage recovery. The aforementioned percentage recovery for each sphere was plotted as a function of the number of updates. The optimization process was repeated with a clinical geometry by simulating the left and right kidneys of the patient. Similarly, the kidney-to-background ratios and concentrations were equivalent to those used for the spheres. The convergence, needed for high reconstruction accuracy for both the sphere and kidneys, was defined as the 90% recovery (26). The noise levels in the sphere and kidney volumes obtained for the different updates were calculated using Equation 3-1.

$$\% RMS = 100 \times \frac{SD}{mean} \tag{3-1}$$

Where *RMS, mean* and *SD* are the root mean square, the mean counts per voxel and the standard deviation of the counts per voxel obtained from the VOIs of the spheres and the kidneys. Although noise is typically evaluated by calculating the %RMS of the counts in a uniform area (29–30). In this study, it was however used to assess the noise level changes within the entire target VOIs as a function of the number of updates. In both cases of the spheres and kidneys, the VOIs were defined according to their physical dimensions described during the segmentation process ('Materials and methods' section). The sphere VOIs were defined as described previously, while the kidneys' physical volumes were delineated as described subsequently in the 'Evaluation of quantification accuracy' section. The noise was assessed using the target objects' physical volume, which provided a consistent delineation method that could be applied to evaluate the quantification accuracy.

3.3.1.2 Calibration Factors

The CF_{sphere} was calculated using a simulation of a 65.4 ml (5.0 cm) radioactive sphere placed in the cylindrical phantom (Figure 3-1(a)) with a non-radioactive background. The sphere diameter was selected to be more than three times the system spatial resolution to limit the influence of PVE on the accuracy of activity quantification. The planar system spatial resolution for the ^{177}Lu 208.4 keV photopeak using a ME collimator was determined in our previous study, resulting in a FWHM of 1.1 cm (47). The CF_{cyl} was calculated using a simulation of the above-mentioned cylindrical phantom filled with a uniform activity distribution. Both geometries offered simple scatter and attenuation properties that could be used to minimise the effect of imperfect corrections. Considering that ^{177}Lu is a costly therapeutic isotope, with a relatively long physical half-life of 6.7 days, the non-radioactive background of the CF_{sphere} offered a more practical alternative that could easily be implemented in clinical practice compared to the CF_{cyl}. The CFs were calculated using the general formula shown in Equation 3-2.

$$CF\ (cps/MBq) = \frac{CR(cps)/V(ml)}{TC(MBq/ml)} \times 100 \tag{3-2}$$

where *CF* is the calibration factor, *CR* is the count rate, *V* is the volume of the VOI, and *TC* is the true concentration obtained from the SIMIND result file. For the CF_{cyl} the cylindrical VOI was defined in a uniform area in the centre of the image to exclude edge effects, as recommended by D'Arienzo et al. (42). The VOI for the CF_{sphere} corresponded to the physical dimensions of the sphere. The CF_{cyl} was taken as the reference to calculate the percentage difference between the two CFs.

3.3.1.3 Recovery Coefficients

The RCs for partial volume compensation were obtained from simulated SPECT images of the cylindrical phantom uniformly filled with ^{177}Lu and radioactive spheres of eight varying sizes below and above the known system spatial resolution, with known concentration. The sphere volumes (and diameters) used were 2.4 ml (1.5 cm), 4.2 ml (2.0 cm), 8.2 ml (2.5 cm), 14.1 ml (3.0 cm), 22.4 ml (3.5 cm), 33.5 ml (4.0 cm), 47.7 ml (4.5 cm) and 65.4 ml (5.0 cm) with a sphere-to-background ratio of 6:1. The concentration was calculated using the CF_{sphere} and the CF_{cyl} and expressed as a fraction of the true concentration (Equation 3-3) to determine the RC of the sphere and cylinder respectively.

$$RC = \frac{C_{SPECT}}{C_{true}} \tag{3-3}$$

where *RC* is the recovery coefficient, C_{SPECT} and C_{true} are the SPECT estimated and true activity concentrations (MBq/ml) in the spheres, respectively. The values of the coefficients from the curve function shown in Equation 3-4 were determined by fitting a mono-exponential function to the above-mentioned sphere and cylinder RC data to generate the RC_{sphere} and RC_{cyl} values used for PVC.

$$y = a - b(e^{-cx}) \tag{3-4}$$

where *y* indicates the required RC value, *x* is the sphere diameter and *a*, *b*, and *c* are the fitting constants. The application of sphere-based RC curves (look-up tables) for PVC of the kidneys based solely on volume dependence has been reported to be non-optimal for ^{177}Lu SPECT/CT image quantification (32). This was due to the differences found between the renal RCs and RC_{sphere}. The authors suggested the replacement of sphere-based RCs with geometry specific RC look-up tables for the kidneys. Therefore, instead of applying a volume-dependent RC value based on the fitted functions of the spheres, we opted to calculate the RC values for the RC_{sphere} and RC_{cyl} using Equation 3-3 directly. The generation of geometry specific look-up tables using kidneys of different volumes was beyond the scope of this study and the calculation of the kidney RC values in the above-mentioned manner seemed to be the better choice. The RC_{sphere} and RC_{cyl} values, for the different size spheres and the kidneys used for PVC in the subsequent sections, were tabulated with their percentage differences.

3.3.1.4 Evaluation of Quantification Accuracy

The second phase of the study evaluated the ^{177}Lu SPECT quantification error in the three phantoms. The objective of the first phantom (cylindrical phantom) was to determine the ^{177}Lu quantitative error of the spherical inserts in a phantom that characterised a simple cylindrical geometry and a homogeneous attenuating medium. The second phantom (torso phantom) represented a more complex geometry as well as a non-homogeneous attenuating medium. The third phantom extended the quantification error to a clinically realistic patient phantom. All the phantoms were simulated four times with the inclusion of one of the spheres of volume: 15.6 ml (3.1 cm), 24.4 ml (3.6 cm), 33.5 ml (4.0 cm) and 65.4 ml (5.0 cm) for each simulation, respectively. The sphere concentrations were 2.2 MBq/ml with a sphere-to-background ratio of 13:1. The sphere-to-background ratios selected for the three phantom simulations were different from those simulated for the RC (6:1) to avoid biased results in the determination of the quantification error. Each sphere was simulated in the centre of the cylindrical phantom as well as in the abdomen next to the liver for the torso and patient phantoms. The relative concentration in the various structures found in these two phantoms was defined to reflect typical activity distribution of ^{177}Lu-DOTATATE (52, 59). The torso phantom had lung and liver concentrations of 0.34 MBq/ml and 0.51 MBq/ml, respectively (similar to the patient phantom), with a background concentration of 0.17 MBq/ml. For the patient phantom, the spleen concentration was 0.52 MB/ml, with corresponding kidney and background concentrations of 0.45 MBq/ml and 0.02 MBq/ml, respectively. It is important to note that all the segmented low-dose CT images were generated with a 5-mm slice thickness using a smooth reconstruction kernel (B08) to create the simulated phantoms. Therefore, the kidneys were segmented as whole left and right kidneys, encompassing the cortex, medulla, and to a lesser extent the renal pelvis. The 3D iso-contour feature of Amide was used to delineate the kidney volumes. All areas above and below the minimum and maximum threshold values were chosen to result in each kidney's equivalent volume as obtained from the simulation results. The VOI used for kidney delineation corresponded to the true (known) volumes established from the segmented kidneys, which included the whole left and right kidneys as described above. The kidney-to-background ratio of 23:1 for the patient phantom reflected a 24-hour uptake for a ^{177}Lu-DOTATATE pharmacokinetic study (52).

Two sets of quantification results were obtained for each of the phantoms. Firstly, the counts were converted to concentration using the CF_{sphere} without PVC to generate the CF_{sphere} quantification error, and subsequently corrected for partial volume using the corresponding RC_{sphere} to generate a CF-RC_{sphere} quantification error. Secondly, the counts were converted to concentration using the CF_{cyl} without PVC to obtain the CF_{cyl} results and the RC_{cyl} applied for PVC, resulting in the CF-RC_{cyl} data. The quantification error was calculated as the percentage difference between the true concentration (true (MBq/ml)) used as input into SIMIND and the quantitative SPECT estimated concentration (SPECT (MBq/ml))calculated from the images (Equation 3-5).

$$Quantification\ Error\ (\%) = \frac{SPECT(MBq/ml) - True(MBq/ml)}{True(MBq/ml)} \qquad (3\text{-}5)$$

3.4 Results

3.4.1 Quantification Steps

3.4.1.1 3D OS-EM Optimization

The effect of the number of 3D OS-EM updates on the percentage recovery and the %RMS is illustrated in Figure 3-2. The values in Figure 3-2 were calculated from the reconstructed ^{177}Lu SPECT images of three different sized spheres simulated in a cylindrical phantom, as well as the left and right kidneys of the patient phantom. The images used to calculate these values were derived from simulations when the object-to-background ratios of 13:1 (Figure 3-2 (a) and (b)) and 6:1 (Figure 3-2 (c) and (d)) were used. The total counts obtained for each VOI were normalised to the maximum counts of the 3D OS-EM updates, obtained at 204 updates, and expressed as a percentage recovery. Similarly, the %RMS was normalised to the maximum percentage obtained at 204 updates.

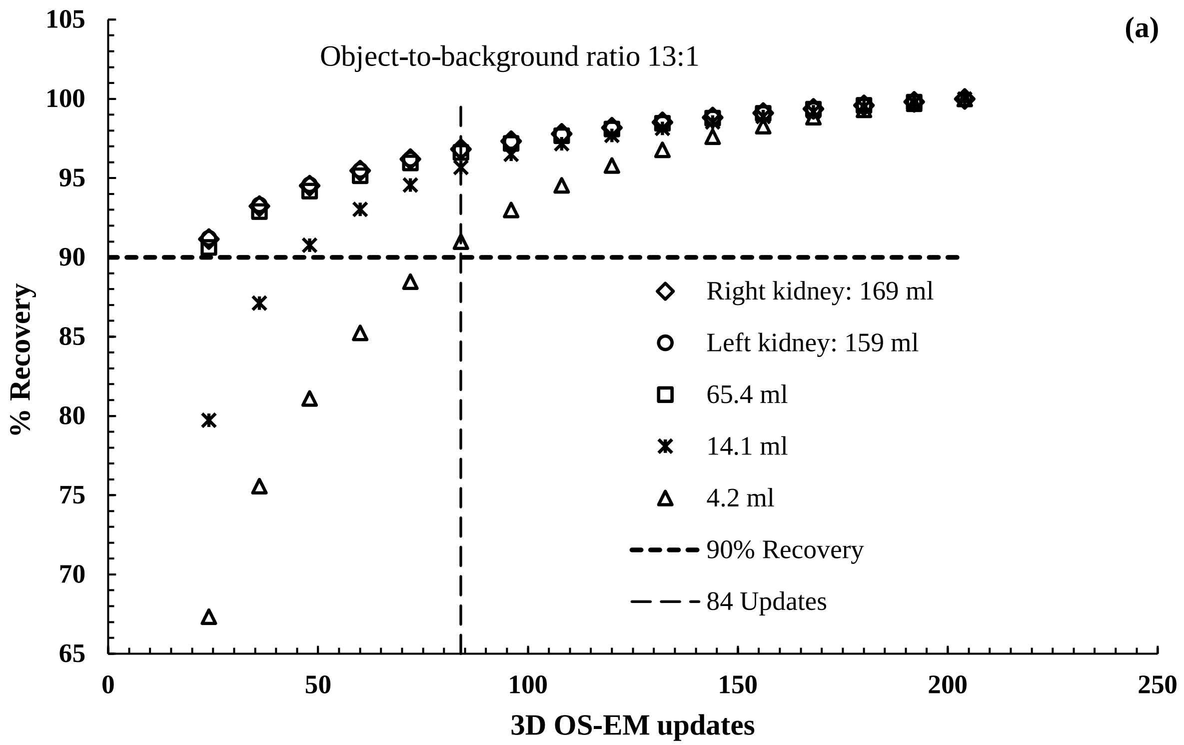
(a)
Object-to-background ratio 13:1
% Recovery
105
100
95
90
85
80
75
70
65
0
50
100
150
200
250
3D OS-EM updates
◇ Right kidney: 169 ml
○ Left kidney: 159 ml
□ 65.4 ml
✱ 14.1 ml
△ 4.2 ml
90% Recovery
84 Updates

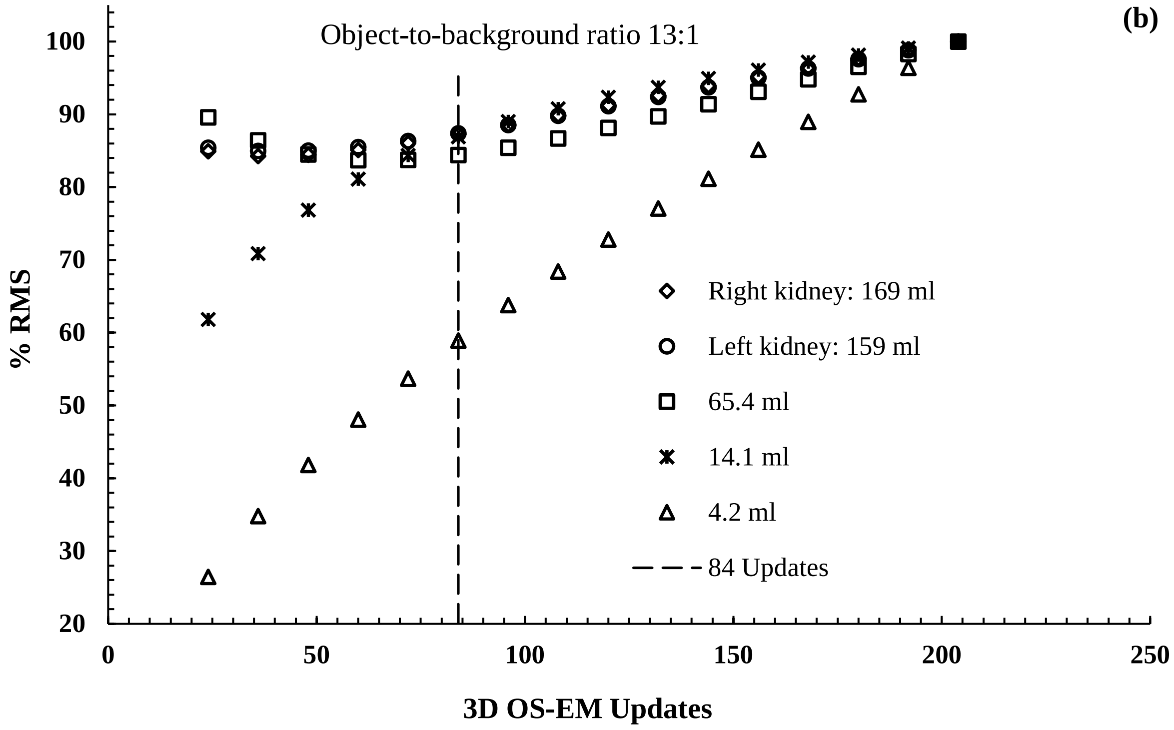
(b)
Object-to-background ratio 13:1
% RMS
100
90
80
70
60
50
40
30
20
0
50
100
150
200
250
3D OS-EM Updates
◇ Right kidney: 169 ml
○ Left kidney: 159 ml
□ 65.4 ml
✱ 14.1 ml
△ 4.2 ml
84 Updates

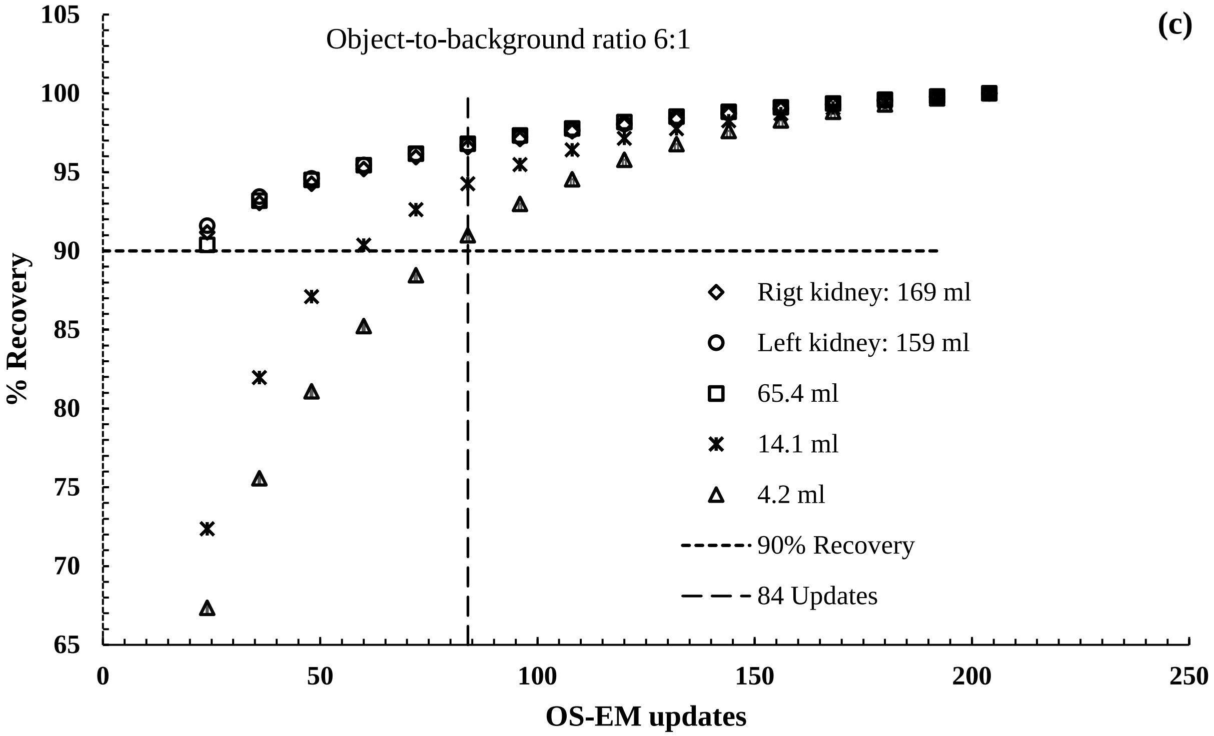
(c)
Object-to-background ratio 6:1
% Recovery
105
100
95
90
85
80
75
70
65
0
50
100
150
200
250
OS-EM updates
◇ Rigt kidney: 169 ml
○ Left kidney: 159 ml
□ 65.4 ml
✱ 14.1 ml
△ 4.2 ml
------ 90% Recovery
— — 84 Updates

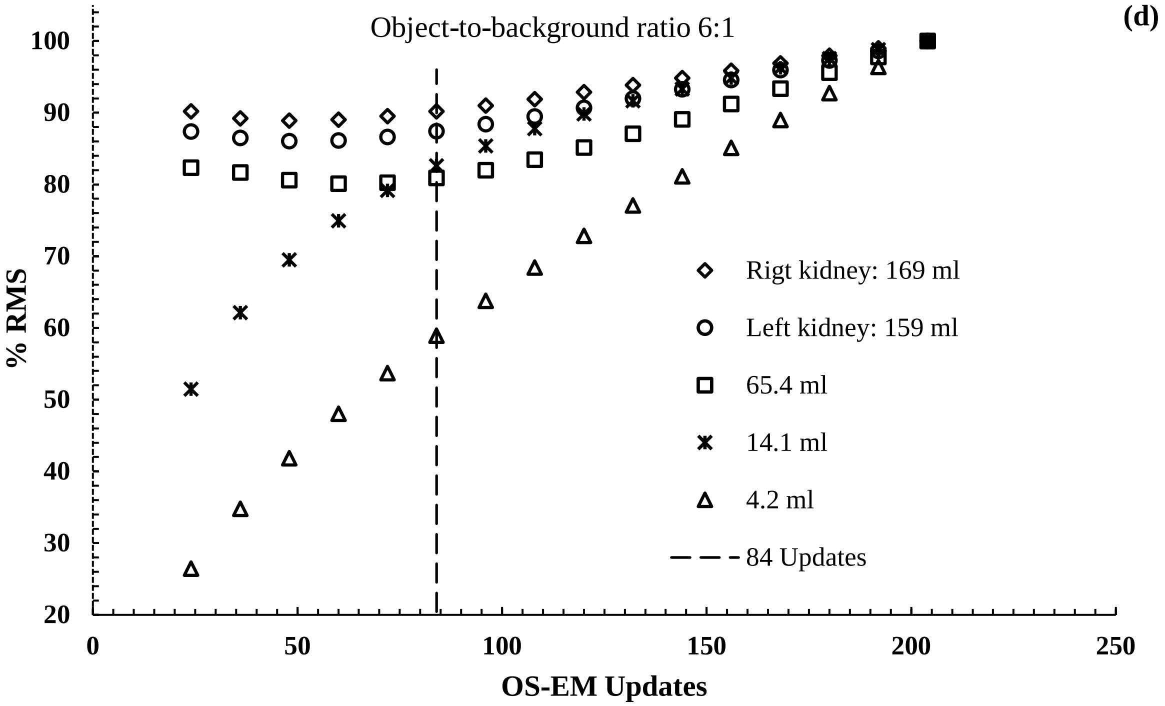
(d)
Object-to-background ratio 6:1
% RMS
100
90
80
70
60
50
40
30
20
0
50
100
150
200
250
OS-EM Updates
◇ Rigt kidney: 169 ml
○ Left kidney: 159 ml
□ 65.4 ml
✱ 14.1 ml
△ 4.2 ml
— — 84 Updates

Figure 3-2: ***(a)*** *Percentage counts recovered and* ***(b)*** *percentage root mean square (%RMS) obtained from reconstructed images as a function of 3D OS-EM updates for different size spheres simulated inside a cylindrical phantom, as well as for the right and left kidney of a patient phantom with an object-to-background ratio of 13:1.* ***(c)*** *Percentage counts recovered and* ***(d)*** *%RMS calculations were repeated for simulations with an object-to-background ratio of 6:1. Reconstruction included CT-based attenuation correction, effective source scatter estimation (ESSE) scatter correction and collimator detector response (CDR) compensation.*

As seen from Figure 3-2 (a) and (c), fewer updates were required for the larger objects to reach convergence (count recovery > 90%). Convergence was reached for the right and the left kidney as well as the 65.4 ml sphere after only 24 updates. In contrast, the 14.1 ml and the 4.2 ml spheres achieved 90% recovery only after 48 and 84 updates, respectively. These observations applied to both concentration ratios. Figures 3-2 (b) and (d) show similar trends for the two concentration ratios where the %RMS increased rapidly by 32.5% for the 4.2 ml sphere from 24 updates to 84 updates. The 14.1 ml sphere had a %RMS increase of ≤ 31.1% from 24 updates to 84 updates. A smaller variation in the %RMS was observed for the larger objects, with a variation of ≤ 5.2% for the 65.4 ml sphere and ≤ 2.3% for the left and right kidneys.

3.4.1.2 Calibration Factors

The results for the CF_{sphere} and the CF_{cyl} were 13.9 cps/MBq and 16.6 cps/MBq, respectively, where the CF_{sphere} was less than the CF_{cyl} by 16.3%. The results demonstrated that the VOI drawn based on the physical dimensions of the sphere excluded some of the counts for the CF_{sphere} due to spill-out. As a result, a lower CF value was obtained for the CF_{sphere} in comparison to that of the CF_{cyl}.

3.4.1.3 Recovery Coefficients

Figure 3-3 shows the characteristic non-linear curves fitted with R^2 values of 0.99 (Equation 3-4), generated using the CF_{sphere} and CF_{cyl}, when RC values were plotted for the eight different sphere sizes, allowing for interpolation between the sphere sizes. The curves provided the fraction of ^{177}Lu activity concentration recovered from the reconstructed images for the given sphere sizes, and in so doing allowed for the true concentration to be calculated, thus compensating for PVE. Although the simulated concentrations (C_{true}) were the same for all VOIs, the smaller spheres had a lower SPECT estimated concentration (C_{SPECT}) values, demonstrating the PVE. It is evident from these curves that RC is strongly dependent on the size of the spheres. The fit of the curves in Figure 3-3 was used to determine the RC values of the four spheres, shown in Table 3-1, which were quantified in the three phantoms.

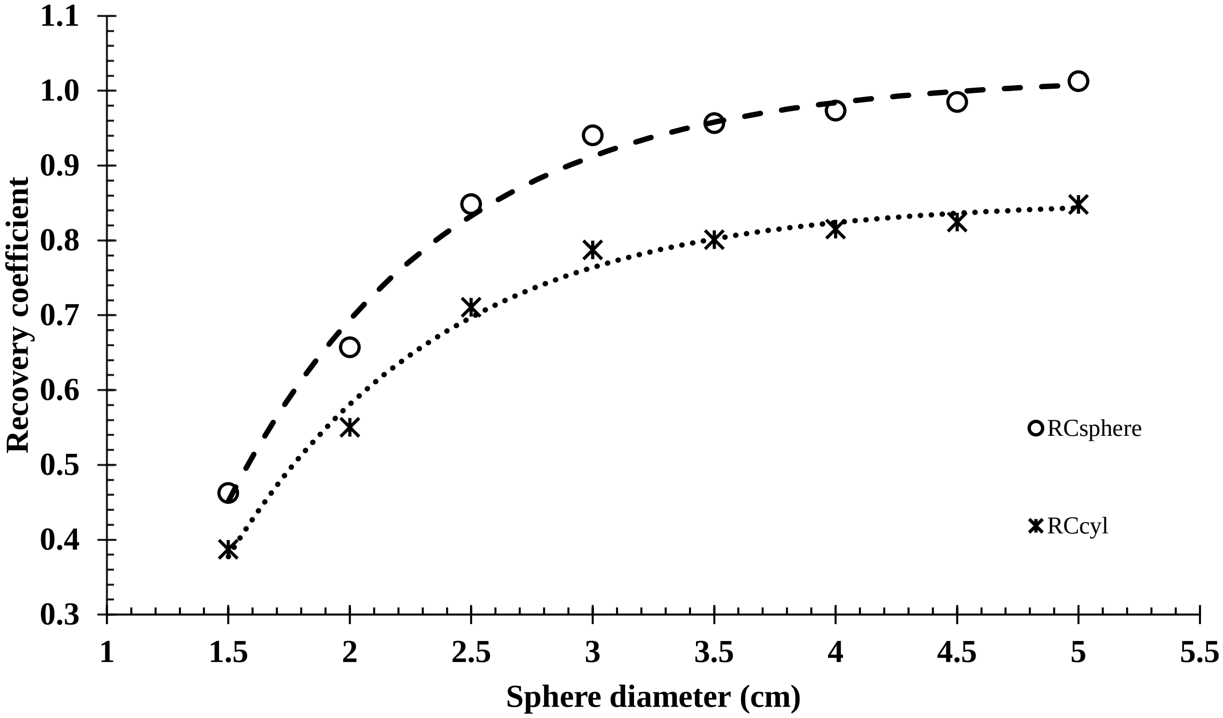

Figure 3-3: *Recovery coefficient (RC) curves generated using a sphere calibration factor (CF) and a cylinder calibration factor (CF) plotted for different sphere sizes.*

The RC_{sphere} and RC_{cyl} for the spheres and kidneys are summarised in Table 3-1. The RC values ranged from 0.77 to 1.00 as the size of the sphere increased from 15.6 ml to 65.4 ml. The kidney RC values were 1.18 and 0.99 for the RC_{sphere} and RC_{cyl}, respectively. Table 3-1 demonstrates a difference between the RC_{sphere} and the RC_{cyl} values for all the simulated objects. The average RC_{sphere} value overestimated the average RC_{cyl} value by 16.1±0.26%, which may be attributed to the CF difference reported in Section 1.4.1.2.

Table 3-1: *The recovery coefficient (RC) values for the sphere and kidney volumes generated for the sphere and cylinder calibration factors (CFs).*

Objects	**RC$_{sphere}$**	**RC$_{cyl}$**	**% difference**
Kidneys			
L-K: 159 ml	1.18	0.99	16.1
R-K: 169 ml	1.18	0.99	16.1
Spheres			
15.6 ml	0.92	0.77	16.3
24.4 ml	0.96	0.81	15.6.
33.5 ml	0.98	0.82	16.3
65.4 ml	1.00	0.84	16.0
		Average	**16.1±0.26**

L-K, left kidney; *R-K*, right kidney; *RC*, recovery coefficient; *Cyl*, cylinder

3.4.1.4 Evaluation of Quantification Accuracy

i. Cylindrical Phantom

Table 3-2 shows the quantification error results for the spheres simulated in the cylindrical phantom with and without PVC. The results were calculated using the CF$_{sphere}$ and CF$_{cyl}$ without PVC, while the combinations of CF-RC$_{sphere}$ and CF-RC$_{cyl}$ were applied to compensate for the PVE.

Table 3-2: *Quantification error results for spheres simulated in a cylindrical phantom with and without partial volume corrections (PVCs).*

	Quantification error (%)			
Object	**Without PVC**	**With PVC**	**Without PVC**	**With PVC**
Sphere	CF$_{sphere}$	CF-RC$_{sphere}$	CF$_{cyl}$	CF-RC$_{cyl}$
15.6 ml	-4.6	3.3	-20.1	3.3
24.4 ml	-3.4	0.2	-19.1	0.2
33.5 ml	-2.1	-0.4	-18.0	-0.4
65.4 ml	1.6	0.8	-15.0	0.9
Average	**-2.1±2.7**	**1.0±1.6**	**-18.1±2.2**	**1.0±1.6**

CF, calibration factor; *PVC*, partial volume correction; *RC*, recovery coefficient; *Cyl*, cylinder

As seen in Table 3-2, the trend for the quantification error without PVC was as expected. The smallest sphere showed the largest quantification error, demonstrating the influence of PVEs, which was less important with increasing sphere size. The average quantification error obtained with the CF_{sphere} without PVC was -2.1±2.7% in comparison to -18.1±2.2% obtained with the CF_{cyl}. The use of the CF_{cyl} without PVC underestimated the true activity evidently for all the sphere sizes. PVC improved the average quantification error dramatically from -18.1±2.2% to 1.0±1.6% for the cylinder results. The precision (standard deviation) of the average quantification error improved slightly with PVC for both the sphere and cylinder data. A slight overestimation (≤ 3.3%) of the activity values was observed for both phantoms for the smallest spheres when PVC was applied. The use of the $CF\text{-}RC_{sphere}$ and $CF\text{-}RC_{cyl}$ both resulted in average quantification errors of 1.0±1.6%.

ii. Torso Phantom

The quantitative error results obtained for the spheres simulated in the torso phantom are demonstrated in Table 3-3. Similar to the cylindrical phantom, the results were analysed using the CF_{sphere} and CF_{cyl} without PVC, and the corresponding RC_{sphere} and RC_{cyl} applied to correct for PVE.

Table 3-3: *Quantification error results for spheres simulated in the torso phantom with and without partial volume corrections (PVCs).*

	Quantification error (%)			
Object	**Without PVC**	**With PVC**	**Without PVC**	**With PVC**
Sphere	CF_{sphere}	$CF\text{-}RC_{sphere}$	CF_{cyl}	$CF\text{-}RC_{cyl}$
15.6 ml	-4.9	2.9	-20.4	3.0
24.4 ml	-5.5	-2.0	-20.9	-2.0
33.5 ml	-4.8	-3.3	-20.3	-3.3
65.4 ml	-2.7	-3.4	-18.5	-3.4
Average	**-4.5±1.2**	**-1.5±3.0**	**-20.0±1.1**	**-1.4±3.0**

CF, calibration factor; *PVC*, partial volume correction; *RC*, recovery coefficient; *Cyl*, cylinder

Without PVC, the quantification error showed an average underestimation of 4.5±1.2% for the CF_{sphere} (Table 3-3). Similar to the sphere quantification results in the cylindrical phantom, the CF_{cyl} considerably underestimated the quantified concentration, with an absolute average of 20.0±1.1% for all sphere sizes.

It can be seen from the results in Table 3-2 and Table 3-3 that the calculated concentration underestimated the true concentration to the same extent between the two phantoms, with the worst quantification results obtained when applying the CF_{cyl} with no PVC. Partial volume correction for both the sphere and cylinder slightly overestimated the concentration of the two smallest spheres ($\leq$ 3.0%). Analogous to the sphere quantification in the cylindrical phantom, the application of the $CF\text{-}RC_{sphere}$ and $CF\text{-}RC_{cyl}$ resulted in comparable average quantification errors of -1.5±3.0% and -1.4±3.0%, respectively.

iii. Patient Phantom

Figure 3-4 shows the patient phantom's reconstructed SPECT data with its associated CT data illustrating the sphere and the kidney objects (indicated by the arrows) used for quantification analysis. Table 3-4 compares the quantification errors obtained for the spherical and kidney objects simulated in the patient phantom calculated using the sphere and the cylinder data.

Figure 3-4: *Reconstructed coronal slices of the patient phantom illustrating the* ***(a)*** *sphere and* ***(b)*** *kidneys used to determine the quantification error.*

As seen from Table 3-4, the sphere quantification errors showed similar trends to those obtained in the cylindrical and torso phantoms. A small average quantification error of -0.9±3.0% was obtained when applying the CF_{sphere} without PVC in the patient phantom. Partial volume correction using the $CF\text{-}RC_{sphere}$ altered the average quantification error to 2.2±0.9%. These results were comparable to those obtained in the torso (-1.5±3.0%) and the cylindrical phantom (1.0±1.6%). The CF_{cyl} underestimated the absolute average quantified concentration of the spheres (17.1±2.5%) similar to the torso (20.0±1.1%) and the cylindrical phantom (18.1±2.2%). Partial volume correction improved the $CF\text{-}RC_{cyl}$ to an average of 2.2±0.9% similar to the torso (-1.4±3.0%) and cylindrical phantom (1.0±1.6%). When all corrections were applied, the quantification accuracy using the $CF\text{-}RC_{sphere}$ (2.2±0.9%) was equivalent to that of the $CF\text{-}RC_{cyl}$ data, validating the quantification accuracy findings of the cylindrical and torso phantoms.

Table 3-4: *Quantification error results for the spherical and kidney objects simulated in the patient phantom calculated with and without partial volume corrections (PVCs).*

	Quantification error (%)			
Objects	**Without PVC**	**With PVC**	**Without PVC**	**With PVC**
Spheres	CF_{sphere}	$CF\text{-}RC_{sphere}$	CF_{cyl}	$CF\text{-}RC_{cyl}$
15.6 ml	-4.4	3.5	-20.0	3.5
24.4 ml	-1.7	2.0	-17.7	1.9
33.5 ml	-0.3	1.3	-16.7	1.3
65.4 ml	2.7	2.0	-14.0	2.0
Average	**-0.9±3.0**	**2.2±0.9**	**-17.1±2.5**	**2.2±0.9**
Kidneys				
L-K: 159 ml	19.0	1.0	-0.4	0.9
R-K: 169 ml	22.3	3.5	2.4	3.5
Average	**20.7±2.3**	**2.3±1.8**	**1.0±2.0**	**2.2±1.8**

CF, calibration factor; *L-K*, left kidney; *PVC*, partial volume correction; *R-K*, right kidney; *RC*, recovery coefficient *Cyl*, cylinder

The kidney quantification showed an average overestimation of 20.7±2.3% for the CF_{sphere} without PVC, in comparison to the better results (1.0±2.0%**)** obtained for the RC_{cyl}. This was contrary to the sphere quantification results where a considerable underestimation of the quantification error was obtained using the CF_{cyl} without PVC. The kidney quantification error improved to 2.3±1.8%

with the CF-RC$_{sphere}$ corrections. With PVC, both the CF-RC$_{sphere}$ and CF-RC$_{cyl}$ yielded average quantification results of 2.3±1.8%, similar to the findings of the sphere quantification results. The results suggest that PVC did not play a major role in the kidney quantification error using the cylinder data. This may be attributed to the fact that the RC$_{cyl}$ value applied to the kidneys was close to 1.0.

3.5 Discussion

3.5.1 Quantification Steps

3.5.1.1 3D OS-EM Optimization

The trends observed in Figure 3-2 (a) and (c) were similar, and convergence (recovery ≥ 90%) was observed at 84 updates for all the objects indicated by the 90% dashed line. Although better reconstruction accuracy, beyond the 90% recovery, could be reached at higher updates, the following was taken into consideration. A higher number of updates increased the number of recovered counts, but has also been shown in the literature to increase image noise levels(27, 60). This was also confirmed in our study when considering the graphs shown in Figure 3-2 (b) and (d). In addition, the use of CDR compensation in the reconstruction process has been shown to result in pronounced edge ringing artefacts with an increased number of iterations, particularly for larger objects (61, 62). The larger increase (32.5%) in the %RMS for the 4.2 ml sphere (Figure 3-2 (b) and (d)) in comparison to the smaller variation (≤ 5.2%) for the largest objects (65.4 ml sphere, the left and right kidneys) was expected due to the lower mean value obtained for the smaller sphere owing to the PVEs. Leong et al. (29) reported similar trends in comparative investigations. Furthermore, the reconstruction computational times are longer with increased updates, which is an important consideration for practical implementation. The data presented in Figure 3-2 (a) and (c) shows that the number of updates used was governed by the smallest sphere (4.2 ml), which only reached the 90% recovery at 84 updates. Although there is a larger increase in the %RMS for the smallest sphere from 24 updates to 84 updates, choosing updates less than 84 updates would compromise the recovered counts and the recovered activity. It was stated by Dewaraja et al. (27) that a large number of iterations is justified for the purpose of obtaining accurate quantitative information in post-therapy administrations where noise is not a significant problem. The findings in our study were in par with Brolin et al. (52) and Ljungberg et al. (16) who used a total of 80 OS-EM updates for quantification of ^{177}Lu-DOTATATE distribution.

Therefore, 84 updates were considered sufficient to attain a 90% recovery for all investigated object sizes used in our study and were further used for reconstruction of the SPECT data.

3.5.1.2 Calibration Factors

The underestimation of the CF_{sphere} in comparison to the CF_{cyl} value was attributed to PVE due to spill-out of counts. Some authors have suggested the simple use of an additional 3 cm margin to the physical dimensions of the sphere to include spilled-out counts (42). Other authors have defined VOIs according to the physical dimensions of the CF sphere (63) or bottles (15) for quantification of ^{177}Lu SPECT studies. We found purpose in defining the CF_{sphere} VOI as the physical dimensions of the sphere in order to have a consistent delineation method for the quantified spheres. The 65.4 ml sphere was chosen to limit PVEs, however, the comparative assessment between the CF_{cyl} and the CF_{sphere} indicated that the effect of spill-out counts from the sphere were not completely eliminated but were reduced. The cylinder VOI was selected centrally on the cylinder image where the effects of spill-in and spill-out of counts were presumed to cancel. Several ^{177}Lu SPECT CFs, obtained for the Siemens Symbia series (Siemens, Healthineers, Germany) gamma cameras, similar to that simulated in the current study, have been reported in the literature. The reported CFs were all obtained for a 0.95-cm-thick NaI (Tl) detector crystal equipped with a ME collimator using a 20% energy window centred over the 208.4 keV photopeak. The reconstructed images were all corrected for attenuation, scatter and CDR, however, the correction methodologies varied. Although the CFs were acquired with similar gamma camera settings, the values differ vastly depending on the phantom configurations, VOI definition, the gamma camera used, and the types of corrections applied to the data. A value of 20.2 cps/MBq for a cylindrical phantom with a VOI containing the entire phantom is reported for a Siemens Symbia Intevo Bold SPECT/CT system (Siemens Healthineers, Germany) (32). The same authors reported values of 18.86 cps/MBq and 20.36 cps/MBq for VOIs drawn centrally in the cylindrical phantom and that encompassing the entire phantom (64). While other authors have reported values of 10.1 cps/MBq and 10.3 cps/MBq for the Symbia T16 (Siemens Healthineers, Germany) obtained using a cylindrical phantom and by applying a 50% threshold of the maximum voxel value to define the VOI for the CF (65). Mean CF values (simulated for different gamma cameras) of 10.5 cps/MBq, 9.5 cps/MBq and 10.1 cps/MBq, for phantom geometries, which included a sphere in a non-radioactive background, a sphere in a radioactive background and a uniform cylindrical phantom, respectively, have been reported (43). The above variations illustrate the variability obtained with the different gamma cameras, processing software, phantom geometries and VOI definitions, emphasising the need to establish a CF suitable for a specific SPECT quantification study.

3.5.1.3 Recovery Coefficients

Creating RC_{sphere} and RC_{cyl} curves aimed to obtain approximate RC values for spherical objects of different sizes where spill-out of counts were present and when PVC is required. In order to use RC_{sphere} and RC_{cyl} curves from Figure 3-3 for PVC, the physical size of the sphere is needed and may be obtained from the CT image of the study. The difference between the RC_{sphere} and the RC_{cyl} was demonstrated by the average difference of 16.1±0.26%. The results were consistent for both the spheres and the kidneys. The discrepancy was attributed to the differences between the two CFs used to calculate the RCs. The overestimation of the RC_{sphere} served as compensation for underestimating the CF_{sphere} and vice versa for the RC_{cyl} and CF_{cyl}. The RC_{cyl} value of 0.81 for the 24.4 ml sphere was comparable to the 0.85 RC value reported by Hippeläinen et al. (15) for a 26 ml sphere. Similarly, Sanders et al. (63) reported a RC value of 0.80 for a 16 ml sphere compared to our 0.77 value for the same size sphere. Our study contained spherical objects mimicking tumours, and therefore PVC using curves from Figure 3-3 may be applicable if the object in the phantom has a similar configuration. The RCs may differ if the object's shape has an irregular form, or a non-uniform activity distribution (32). For this reason, the kidney RC values were calculated directly using Equation 3-3 and not from the fitted RC curves. This method is applicable when the size and activity concentration of the object is known. The size of the objects may be obtained from high resolution images such as CT or MRI.

3.5.1.4 Evaluation of Quantification Accuracy

The sphere quantification error results (Table 3-2 to Table 3-4) obtained with the sphere and cylinder CF and RC data showed similar trends for all three phantoms. The slight overestimation of the activity values observed for the smallest sphere (15.6 ml) when PVC was applied for both the sphere and cylinder data may be attributed to the discrepancy between the calculated RC value and that obtained from the fitted function shown in Figure 3-3. It can be seen from Figure 3-3 that the function slightly underestimated the calculated RC_{sphere} and RC_{cyl} values at a sphere diameter of 3 cm, comparable to the diameter of the smallest quantified sphere (3.1 cm). Another source for this discrepancy may be found in the different object-to-background ratios used for the RCs compared to those used to assess the quantification error. A different object-to-background ratio was selected to avoid bias in the quantification evaluation of the phantoms. The CF_{sphere} without PVC showed a general tendency of a small quantification error for the quantified spheres compared to the large underestimation by the CF_{cyl}. This may be expected due to the similar geometry between the quantified spheres and the sphere used for the CF_{sphere}. These results illustrated the dependence of the quantified error on the geometry of the CF. Whole-organ specific CFs, obtained using 3D printed phantom inserts in the shape of the spleen, kidney, pancreas and liver, have been shown to improve the accuracy of organ dosimetry for ^{99m}Tc and ^{177}Lu SPECT studies (55). This type of dependence was verified in our study by extending the quantification error evaluation to a clinical kidney geometry. Without PVC, a large overestimation of the quantified kidney concentration for the CF_{sphere} was obtained vs. the small kidney quantification error obtained with the CF_{cyl}. The total counts used to determine the kidney quantification error were equivalent when using the CF-RC_{sphere} or the CF-RC_{cyl}. Therefore, the large overestimation may be explained, at least in part, by the VOI selection for the CF_{sphere} and CF_{cyl}, which resulted in differences in the contribution of spill-in and spill-out of counts due to the PVE. The lower value of the CF_{sphere}, compared to the CF_{cyl}, demonstrated this effect. This CF discrepancy may also offer a possible explanation for the difference in the kidney quantification trend found between the current study and other literature studies, that reported underestimations of kidney activity without PVC (16, 32). These studies applied a “nearly partial-volume-free CF” determined from a cylinder that was less susceptible to spill-out effects (32). Another important consideration is that the kidneys used in our study were segmented and delineated as whole kidneys without separate compartments for the cortex, medulla, and renal pelvis areas. This will affect the shape of the kidneys and, as a result, the corresponding PVEs. The discrepancy may presumably be exacerbated by the fact that the kidney RCs were calculated directly from Equation 3-3 instead of using a look-up curve or table. This may lead to some bias in the quantification results. Therefore, it is important to note both the geometry and the delineation method used for the CF, RCs, and object of interest. The different effects of the two CFs, used in our study, were balanced by their corresponding RC values. This was shown by the comparable average quantification error results obtained for the different sized spheres in all three phantoms as well as the kidneys in the patient phantom.

The quantification errors obtained in this study compared well with literature investigations of similar phantom and patient geometries, which employed OS-EM-based reconstruction algorithms with compensation for scatter, attenuation using CT data, and CDR. De Nijs et al. (58) investigated the ^{177}Lu SPECT activity quantification of radioactive spherical inserts placed in a cylindrical phantom with a radioactive background. The authors applied the ESSE scatter correction method and compensated for PVEs by drawing VOIs larger than the spherical inserts and reported errors of 10% for their largest sphere of 37 ml. Sanders et al. (63) reported larger errors of up to 20% for smaller sphere inserts (16 ml) in the same geometry, using the TEW scatter correction and VOIs defined according to CT data without PVC. An average percentage error of 6.6±3.5% for quantification of 175 ml cylindrical inserts placed in a larger cylinder was reported by Beauregard et al. (49). The authors used the DEW scatter correction and manually adjusted the VOIs using a percentage threshold of maximum activity to compensate for spill-out due to PVEs. Therefore, the quantification errors (≤ 1.0±1.6%) found for the cylindrical phantom used in our study were satisfactory when all corrections were applied.

Hippeläinen et al. (15) investigated the ^{177}Lu SPECT activity quantification of spheres measured in the same torso RSD phantom, as simulated in our study, and reported errors of 15% for their largest spherical insert (104 ml). They used an accelerated MC simulation method for scatter correction and CT-based VOIs without PVC. The quantification errors found in our study (≤ 1.4±3.0%) were comparable to that of D'Arienzo et al. (66) who quantified a cylindrical insert (19.13 ml) in an anthropomorphic torso phantom (Data Spectrum Corporation, USA) with an accuracy of 2.0%. D'Arienzo et al. (66) applied a transmission-depended convolution subtraction scatter compensation method and RCs, as defined in the current study, for PVC. Uribe et al. (57) used a thorax phantom (Data Spectrum Corporation, USA) and reported accuracies of better than 5.0%, for their largest insert (34 ml) using the analytical photon distribution interpolated for scatter correction. The accuracy was achieved for their iterative adaptive dual threshold segmentation method, which recovered the activity better than the CT-based and 40% fixed threshold segmentation methods. Both these methods underestimated the activity due to PVEs, grossly.

Beauregard et al. (49) reported quantification error results of 2.6±1.8% for ^{177}Lu SPECT activity data of five patients acquired with the Symbia TruePoint T6 SPECT/CT gamma camera (Siemens, Healthineers, Germany). The authors evaluated their quantification error by comparing the calibrated activity injected into the patients with the quantified activity obtained by drawing a VOI surrounding the patient using a −400 Hounsfield unit threshold for the CT images. Although their quantification method was different to ours, their results were comparable to our patient phantom findings when all corrections were applied with sphere and kidney quantification errors of ≤ 2.2 ±0.9% and ≤ 2.3±1.8%, respectively. Sanders et al. (63) compared ^{177}Lu bladder activity concentrations obtained from SPECT/CT patient images with urine sample measurements from calibrated well counters. Their segmentation method for the bladder included placing a smaller ellipsoid VOI in the bladder's interior to avoid edge roll-off that causes variations in the iso-contour measurements. The total mean counts in the VOI were normalised to the volume of the bladder. The method yielded mean quantification errors of 10±8.3%. Bailey et al. (14) reported an accuracy of ±10% for ^{177}Lu activity quantification of whole body planar scans and cardiac blood pool SPECT images. Hippeläinen et al. (15) reported errors of up to 25% for kidney quantification of patients who underwent ^{177}Lu-DOTATATE treatment using SPECT images. The systematically higher activity quantification errors were attributed to CT-based VOIs that were sensitive to PVEs and estimates obtained at different time points. Willowson et al. (56) investigated the accuracy of using a single time point for renal dosimetry and showed improvement in the quantification accuracy to 13% and 2% when using the 4-hour and 24-hour data only. Similarly, the kidney volumes were defined on the co-registered CT data, however, no information on PVC was available. Optimization of kidney quantification for ^{177}Lu SPECT/CT using geometry specific RCs for PVC was investigated using a 3D printed two-compartment kidney phantom (32). The best quantification accuracies of 1.5% and 10.3% were reported using the commercially available reconstruction algorithms xSPECT and Flash-3D (Siemens, Healthineers, Germany), respectively, when model-based RCs were applied to compensate for PVE. These studies demonstrate the disparity in quantitative accuracy found for the different imaging geometries processing protocols and methods evaluating the quantitative error. The overall improved quantitative results obtained in our study when all corrections are applied may be indicative of the accuracy of the correction methods used in the reconstruction process. The ESSE model-based scatter correction used in this study has been reported to be more accurate for scatter correction of ^{177}Lu data compared to window-based methods (58).

3.6 Conclusion

In this study, we used the SIMIND MC program to model a Siemens Symbia T16 gamma camera for ^{177}Lu SPECT imaging of voxelized phantoms as validated by Ramonaheng et al. (47). Emanating from the fact that there is currently no consensus on the ideal SPECT CF geometry for quantitative data, we presented two CFs and their corresponding RCs. The quantification errors obtained with the two-combination CF-RC$_{sphere}$ and CF-RC$_{cyl}$ were evaluated by quantifying different size spheres in three different phantom geometries as well as the kidneys in the patient phantom. Our study showed the effect on the quantification error, by using the CF$_{sphere}$ or the CF$_{cyl}$, without PVC, depends on the quantified geometry. The quantification results emphasised the importance of applying a PVC with an RC obtained with the same CF used to convert the quantified data into units of concentration. We demonstrated that when all corrections were applied (attenuation, scatter, CDR and partial volume), the ^{177}Lu SPECT quantification errors in the three phantoms were comparable for the CF-RC$_{sphere}$ and CF-RC$_{cyl}$ combinations. Our absolute quantification errors of smaller than and equal to 3.5% for the three phantoms, compared well to literature findings and complied with the ±5% absorbed dose accuracy required for molecular radiotherapy (67). Although our findings suggest the feasibility of obtaining accurate ^{177}Lu SPECT activity quantification upon the careful selection of a CF-RC combination, certain considerations may be limiting. These include firstly, that the application of patient-specific RCs in the clinic entails the use of CT or MRI data in combination with MC simulations. This would require modelling of CF-RC combinations for every patient geometry and activity distribution, which may be cumbersome to implement routinely. Secondly, the presence of non-uniform activity distributions may further complicate activity quantification. Thirdly, the segmented kidney volumes used in this study were obtained from low-dose, low-resolution, non-contrast-enhanced CT data, which was inadequate to differentiate between the different kidney compartments, such as the medulla, cortex, and renal pelvis, reliably. For this reason, each whole left and right kidney was assigned a uniform activity concentration. High-resolution image data such as contrast-enhanced CT images or MRI would facilitate segmentation and VOI delineation that is more reliable with a better representation of a clinical kidney model. Another limitation of this study is the methodology used to calculate the kidney RCs directly from Equation 3-3, which requires prior knowledge of the kidneys' activity concentration, and is not clinically available. This study reinforces the need to standardise segmentation methods for CF, RCs and tumour and organ delineation.

3.7 References

1. Bodei L, Mueller-Brand J, Baum RP, Pavel ME, Hörsch D, O'Dorisio MS, et al. The joint IAEA, EANM, and SNMMI practical guidance on peptide receptor radionuclide therapy (PRRNT) in neuroendocrine tumours (published correction appears in Eur J Nucl Med Mol Imaging. 2014 Mar;41(3):584. O'Dorisiol, TM (corrected to O'Dorisio, TM)). Eur J Nucl Med Mol Imaging. 2013;40(5):800–16. https://doi.org/10.1007/s00259-012-2330-6

2. Volkert WA, Goeckeler WF, Ehrhardt GJ, Ketring AR. Therapeutic radionuclides: production and decay property considerations. J Nucl Med. 1991;32(1):174–85.

3. Banerjee S, Pillai MR, Knapp FF. Lutetium-177 therapeutic radiopharmaceuticals: linking chemistry, radiochemistry, and practical applications. Chem Rev. 2015;115(8):2934–74. https://doi.org/10.1021/cr500171e

4. Dash A, Pillai MR, Knapp FF Jr. Production of ^{177}Lu for Targeted Radionuclide Therapy: Available Options. Nucl Med Mol Imaging. 2015;49(2):85–107. https://doi.org/10.1007/s13139-014-0315-z

5. Bodei L, Cremonesi M, Ferrari M, Pacifici M, Grana CM, Bartolomei M, et al. Long-term evaluation of renal toxicity after peptide receptor radionuclide therapy with ^{90}Y-DOTATOC and ^{177}Lu-DOTATATE: the role of associated risk factors (published correction appears in Eur J Nucl Med Mol Imaging. 2008 Oct;35(10):1928). Eur J Nucl Med Mol Imaging. 2008;35(10):1847–56. https://doi.org/10.1007/s00259-008-0778-1

6. Bodei L, Cremonesi M, Grana CM, Fazio N, Iodice S, Baio SM, et al. Peptide receptor radionuclide therapy with ^{177}Lu-DOTATATE: the IEO phase I-II study. Eur J Nucl Med Mol Imaging. 2011;38(12):2125–35. https://doi.org/10.1007/s00259-011-1902-1

7. Bodei L, Kidd M, Paganelli G, Grana CM, Drozdov I, Cremonesi M, et al. Long-term tolerability of PRRT in 807 patients with neuroendocrine tumours: the value and limitations of clinical factors. Eur J Nucl Med Mol Imaging. 2015;42(1):5–19. https://doi.org/10.1007/s00259-014-2893-5

8. Kam BL, Teunissen JJ, Krenning EP, de Herder WW, Khan S, van Vliet EI, et al. Lutetium-labelled peptides for therapy of neuroendocrine tumours. Eur J Nucl Med Mol Imaging. 2012;39(Suppl 1):S103–12. https://doi.org/10.1007/s00259-011-2039-y

9. Van Vliet EI, Teunissen JJ, Kam BL, de Jong M, Krenning EP, Kwekkeboom DJ. Treatment of gastroenteropancreatic neuroendocrine tumors with peptide receptor radionuclide therapy. Neuroendocrinology. 2013;97(1):74–85. https://doi.org/10.1159/000335018

10. Oyen WJ, Bodei L, Giammarile F, Maecke HR, Tennvall J, Luster M, et al. Targeted therapy in nuclear medicine--current status and future prospects. Ann Oncol. 2007;18(11):1782-1792. https://doi.org/10.1093/annonc/mdm111

11. Ilan E, Sandström M, Wassberg C, Sundin A, Garske-Román U, Eriksson B, et al. Dose response of pancreatic neuroendocrine tumors treated with peptide receptor radionuclide therapy using ^{177}Lu-DOTATATE. J Nucl Med. 2015;56(2):177–82. https://doi.org/10.2967/jnumed.114.148437

12. Kwekkeboom DJ, Bakker WH, Kooij PP, et al. (^{177}Lu-DOTA0,Tyr^{3})octreotate: comparison with (^{111}In-DTPA^{0})octreotide in patients. Eur J Nucl Med. 2001;28(9):1319–25. https://doi.org/10.1007/s002590100574

13. Sandström M, Garske-Román U, Granberg D, Johansson S, Widström C, Eriksson B, et al. Individualized dosimetry of kidney and bone marrow in patients undergoing ^{177}Lu-DOTA-octreotate treatment. J Nucl Med. 2013;54(1):33–41. https://doi.org/10.2967/jnumed.112.107524

14. Bailey DL, Hennessy TM, Willowson KP, Henry EC, Chan DL, Aslani A, et al. In vivo quantification of ^{177}Lu with planar whole-body and SPECT/CT gamma camera imaging. EJNMMI Phys. 2015;2(1):20. https://doi.org/10.1186/s40658-015-0123-2

15. Hippeläinen E, Tenhunen M, Mäenpää H, Sohlberg A. Quantitative accuracy of ^{177}Lu SPECT reconstruction using different compensation methods: phantom and patient studies. EJNMMI Res. 2016;6(1):16. https://doi.org/10.1186/s13550-016-0172-0

16. Ljungberg M, Celler A, Konijnenberg MW, Eckerman KF, Dewaraja YK, Sjögreen-Gleisner K, et al. MIRD Pamphlet No. 26: Joint EANM/MIRD Guidelines for Quantitative ^{177}Lu SPECT applied for dosimetry of radiopharmaceutical therapy. J Nucl Med. 2016;57(1):151–62. https://doi.org/10.2967/jnumed.115.159012

17. Ljungberg M, Sjögreen Gleisner K. Personalized dosimetry for radionuclide therapy using molecular imaging tools. Biomedicines. 2016;4(4):25. https://doi.org/10.3390/biomedicines4040025

18. Frey EC, Humm JL, Ljungberg M. Accuracy and precision of radioactivity quantification in nuclear medicine images. Semin Nucl Med. 2012;42(3):208–18. https://doi.org/10.1053/j.semnuclmed.2011.11.003

19. Garkavij M, Nickel M, Sjögreen-Gleisner K, Ljungberg M, Ohlsson T, Wingårdh K, et al. ^{177}Lu-(DOTA0,Tyr3) octreotate therapy in patients with disseminated neuroendocrine tumors: Analysis of dosimetry with impact on future therapeutic strategy. Cancer. 2010;116(4 Suppl):1084–92. https://doi.org/10.1002/cncr.24796

20. Guerriero F, Ferrari ME, Botta F, Fioroni F, Grassi E, Versari A, et al. Kidney dosimetry in ^{177}Lu and ^{90}Y peptide receptor radionuclide therapy: influence of image timing, time-activity integration method, and risk factors. Biomed Res Int. 2013;2013:935351. https://doi.org/10.1155/2013/935351

21. Hudson HM, Larkin RS. Accelerated image reconstruction using ordered subsets of projection data. IEEE Trans Med Imaging. 1994;13(4):601–9. https://doi.org/10.1109/42.363108

22. Alzimami KS, Sassi SA, Spyrou NM. A comparison between 3D OSEM and FBP image reconstruction algorithms in SPECT. In: Ao SI, Gelman L, editors. Advances in electrical engineering and computational science. Lecture Notes in Electrical Engineering, vol 39. Dordrecht: Springer; 2009. pp 195–206. https://doi.org/10.1007/978-90-481-2311-7_17

23. Sowa-Staszczak A, Lenda-Tracz W, Tomaszuk M, Głowa B, Hubalewska-Dydejczyk A. Optimization of image reconstruction method for SPECT studies performed using (^{99m}Tc-EDDA/HYNIC) octreotate in patients with neuroendocrine tumors. Nucl Med Rev Cent East Eur. 2013;16(1):9–16. https://doi.org/10.5603/NMR.2013.0003

24. Yokoi T, Shinohara H, Onishi H. Performance evaluation of OSEM reconstruction algorithm incorporating three-dimensional distance-dependent resolution compensation for brain SPECT: a simulation study. Ann Nucl Med. 2002;16(1):11–8. https://doi.org/10.1007/BF02995286

25. Kemin H. Impact of different reconstruction algorithms and OSEM reconstruction parameters on quantitative results in SPECT/CT. J Nucl Med. 2018;59(Suppl 1):1800.

26. Dewaraja YK, Frey EC, Sgouros G, Brill AB, Roberson P, Zanzonico PB, et al. MIRD pamphlet No. 23: quantitative SPECT for patient-specific 3-dimensional dosimetry in internal radionuclide therapy. J Nucl Med. 2012;53(8):1310–25. https://doi.org/10.2967/jnumed.111.100123

27. Dewaraja YK, Wilderman SJ, Ljungberg M, Koral KF, Zasadny K, Kaminiski MS. Accurate dosimetry in ^{131}I radionuclide therapy using patient-specific, 3-dimensional methods for SPECT reconstruction and absorbed dose calculation. J Nucl Med. 2005;46(5):840–9.

28. Usman F, Zainon R, Saidu A, Bala A. Evaluation of image reconstruction techniques in Single Photon Emission Computed Tomography (SPECT/CT) Imaging. Res Rev J Physics. 2016: 5(2), 13–22.

29. Leong LK, Kruger RL, O’Connor MK. A comparison of the uniformity requirements for SPECT image reconstruction using FBP and OSEM techniques. J Nucl Med Technol. 2001: 29(2), 79–83.

30. Brambilla M, Cannillo B, Dominietto M, Leva L, Secco C, Inglese E. Characterization of ordered-subsets expectation maximization with 3D post-reconstruction gauss filtering and comparison with filtered backprojection in ^{99m}Tc SPECT. Ann Nucl Med. 2005. 19(2), 75–82. https://doi.org/10.1007/BF03027384

31. Frey EC, Tsui BM. A new method for modeling the spatially-variant, object-dependent scatter response function in SPECT. 1996 IEEE Nuclear Science Symposium. Conference Record, Anaheim, CA, USA; 1996, pp. 1082-1086 vol. 2. https://doi.org/10.1109/NSSMIC.1996.591559

32. Tran-Gia J, Lassmann M. Optimizing image quantification for ^{177}Lu SPECT/CT based on a 3D printed 2-compartment kidney phantom. J Nucl Med. 2018;59(4):616–24. https://doi.org/10.2967/jnumed.117.200170

33. He B, Frey EC. The impact of 3D volume of interest definition on accuracy and precision of activity estimation in quantitative SPECT and planar processing methods. Phys Med Biol. 2010;55(12):3535–44. https://doi.org/10.1088/0031-9155/55/12/017

34. International Atomic Energy Agency (IAEA). Quantitative SPECT OR SPECT/CT imaging. In: Quantitative nuclear medicine imaging: Concepts, requirements and methods. IAEA Human Health Report No.9. IAEA, Vienna, Austria; 2014. pp. 27–36.

35. Erlandsson K, Thomas B, Dickson J, Hutton BF. Partial volume correction in SPECT reconstruction with OSEM. Nucl Instrum Meth A. 2011;648(Suppl 1):S85–8. https://doi.org//10.1016/j.nima.2010.12.106

36. Willowson K, Bailey DL, Baldock C. Quantitative SPECT reconstruction using CT-derived corrections. Phys Med Biol. 2008;53(12):3099–112. https://doi.org/10.1088/0031-9155/53/12/002

37. Adams MC, Turkington TG, Wilson JM, Wong TZ. A systematic review of the factors affecting accuracy of SUV measurements (published correction appears in AJR Am J Roentgenol. 2010 Oct;195(4):1043). AJR Am J Roentgenol. 2010;195(2):310–20. https://doi.org/10.2214/AJR.10.4923

38. National Electrical Manufacturers Association. NEMA NU 1: 2012. Performance measurements of gamma cameras. Rosslyn, Virginia, USA: National Electrical Manufacturers Association; 2012.

39. de Wit TC, Xiao J, Nijsen JF, van het Schip FD, Staelens SG, van Rijk PP, et al. Hybrid scatter correction applied to quantitative holmium-166 SPECT. Phys Med Biol. 2006;51(19):4773–87. https://doi.org/10.1088/0031-9155/51/19/004

40. He B, Du Y, Song X, Segars WP, Frey EC. A Monte Carlo and physical phantom evaluation of quantitative In-111 SPECT. Phys Med Biol. 2005;50(17):4169–85. https://doi.org/10.1088/0031-9155/50/17/018

41. Shcherbinin S, Celler A, Belhocine T, Vanderwerf R, Driedger A. Accuracy of quantitative reconstructions in SPECT/CT imaging. Phys Med Biol. 2008;53(17):4595–4604. https://doi.org/10.1088/0031-9155/53/17/009

42. D'Arienzo M, Cazzato M, Cozzella ML, Cox M, D'Andrea M, Fazio A, et al. Gamma camera calibration and validation for quantitative SPECT imaging with ^{177}Lu. Appl Radiat Isot. 2016;112:156–64. https://doi.org/10.1016/j.apradiso.2016.03.007

43. Zhao W, Esquinas PL, Hou X, Uribe CF, Gonzalez M, Beauregard J-M, et al. Determination of gamma camera calibration factors for quantitation of therapeutic radioisotopes. EJNMMI Phys. 2018;5(1):8. https://doi.org/10.1186/s40658-018-0208-9

44. Ljungberg M, Strand SE. A Monte Carlo program for the simulation of scintillation camera characteristics. Comput Methods Programs Biomed. 1989;29(4):257–72. https://doi.org/10.1016/0169-2607(89)90111-9

45. Wevrett J, Fenwick A, Scuffham J, Nisbet A. Development of a calibration protocol for quantitative imaging for molecular radiotherapy dosimetry. Radiat Phys Chem. 2017;140:355–60. https://doi.org/10.1016/j.radphyschem.2017.02.053

46. Wevrett J, Fenwick A, Scuffham J, Johansson L, Gear J, Schlögl S, et al. Inter-comparison of quantitative imaging of lutetium-177 (^{177}Lu) in European hospitals. EJNMMI Phys. 2018;5(1):17. https://doi.org/10.1186/s40658-018-0213-z

47. Ramonaheng K, van Staden JA, du Raan H. Validation of a Monte Carlo modelled gamma camera for Lutetium-177 imaging. Appl Radiat Isot. 2020;163:109200. https://doi.org/10.1016/j.apradiso.2020.109200

48. Yushkevich PA, Piven J, Hazlett HC, Smith RG, Ho S, Gee JC, et al. User-guided 3D active contour segmentation of anatomical structures: significantly improved efficiency and reliability. Neuroimage. 2006;31(3):1116–28. https://doi.org/10.1016/j.neuroimage.2006.01.015

49. Beauregard JM, Hofman MS, Pereira JM, Eu P, Hicks RJ. Quantitative ^{177}Lu SPECT (QSPECT) imaging using a commercially available SPECT/CT system. Cancer Imaging. 2011;11(1):56–66. https://doi.org/10.1102/1470-7330.2011.0012

50. He B, Nikolopoulou A, Osborne J, Vallabhajosula S, Goldsmith S. Quantitative SPECT imaging with Lu-177: A physical phantom evaluation. J Nucl Med. 2012;53(Suppl 1):2407.

51. Shcherbinin S, Piwowarska-Bilska H, Celler A, Birkenfeld B. Quantitative SPECT/CT reconstruction for ^{177}Lu and ^{177}Lu/^{90}Y targeted radionuclide therapies. Phys Med Biol. 2012;57(18):5733–47. https://doi.org/10.1088/0031-9155/57/18/5733

52. Brolin G, Gustafsson J, Ljungberg M, Gleisner KS. Pharmacokinetic digital phantoms for accuracy assessment of image-based dosimetry in ^{177}Lu-DOTATATE peptide receptor radionuclide therapy. Phys Med Biol. 2015;60(15):6131–49. https://doi.org/10.1088/0031-9155/60/15/6131

53. Frey EC, Tsui BM. A practical method for incorporating scatter in a projector-backprojector for accurate scatter compensation in SPECT. IEEE Trans Nucl Sci 1993;40(4):1107–16. https://doi.org/10.1109/23.256720

54. Loening AM, Gambhir SS. AMIDE: a free software tool for multimodality medical image analysis. Mol Imaging. 2003;2(3):131–7. https://doi.org/10.1162/15353500200303133

55. Robinson AP, Tipping J, Cullen DM, Hamilton D, Brown R, Flynn A, et al. Organ-specific SPECT activity calibration using 3D printed phantoms for molecular radiotherapy dosimetry. EJNMMI Phys. 2016;3(1):12.

56. Willowson KP, Eslick E, Ryu H, Poon A, Bernard EJ, Bailey DL. Feasibility and accuracy of single time point imaging for renal dosimetry following ^{177}Lu-DOTATATE (‘Lutate’) therapy. EJNMMI Phys. 2018;5(1):33. https://doi.org/10.1186/s40658-018-0232-9

57. Uribe CF, Esquinas PL, Tanguay J, Gonzalez M, Gaudin E, Beauregard J-M, et al. Accuracy of ^{177}Lu activity quantification in SPECT imaging: a phantom study. EJNMMI Phys. 2017;4(1):2. https://doi.org/10.1186/s40658-016-0170-3

58. de Nijs R, Lagerburg V, Klausen TL, Holm S. Improving quantitative dosimetry in ^{177}Lu-DOTATATE SPECT by energy window-based scatter corrections. Nucl Med Commun. 2014;35(5):522–33. https://doi.org/10.1097/MNM.0000000000000079

59. Mezzenga E, D’Errico V, D’Arienzo M, Strigari L, Panagiota K, Matteucci F, et al. Quantitative accuracy of ^{177}Lu SPECT imaging for molecular radiotherapy. PLoS One. 2017;12(8):e0182888. https://doi.org/10.1371/journal.pone.0182888

60. Dewaraja YK, Ljungberg M, Green AJ, Zanzonico PB, Frey EC, SNMMI MIRD Committee, et al. MIRD pamphlet No. 24: Guidelines for quantitative ^{131}I SPECT in dosimetry applications. J Nucl Med. 2013;54(12):2182–8. https://doi.org/10.2967/jnumed.113.122390

61. Dewaraja YK, Koral KF, Fessler JA. Regularized reconstruction in quantitative SPECT using CT side information from hybrid imaging. Phys Med Biol. 2010;55(9):2523–39. https://doi.org/10.1088/0031-9155/55/9/007

62. Tsui BM, Frey EC, Zhao X, Lalush DS, Johnston RE, McCartney WH. The importance and implementation of accurate 3D compensation methods for quantitative SPECT. Phys Med Biol. 1994;39(3):509–30. https://doi.org/10.1088/0031-9155/39/3/015

63. Sanders JC, Kuwert T, Hornegger J, Ritt P. Quantitative SPECT/CT imaging of ^{177}Lu with in vivo validation in patients undergoing peptide receptor radionuclide therapy. Mol Imaging Biol. 2014;17(4):585–93. https://doi.org/10.1007/s11307-014-0806-4

64. Tran-Gia J, Lassmann M. Characterization of noise and resolution for quantitative ^{177}Lu SPECT/CT with xSPECT Quant. J Nucl Med. 2019;60(1):50–9. https://doi.org/10.2967/jnumed.118.211094

65. Peters SM, Meyer Viol SL, van der Werf NR, de Jong N, van Velden FH, Meeuwis A, et al. Variability in lutetium-177 SPECT quantification between different state-of-the-art SPECT/CT systems. EJNMMI Phys. 2020;7(1):9. https://doi.org/10.1186/s40658-020-0278-3

66. D'Arienzo M, Cozzella ML, Fazio A, De Felice P, Iaccarino G, D'Andrea M, et al. Quantitative ^{177}Lu SPECT imaging using advanced correction algorithms in non-reference geometry. Phys Med. 2016;32(12):1745–52. https://doi.org/10.1016/j.ejmp.2016.09.014

67. International Commission on Radiation Units and Measurements. ICRU Report 67: Absorbed-dose specification in nuclear medicine. J ICRU. 2002;2(1):3–110.

4

Chapter 4:

Article III

Accuracy of two dosimetry software programs for ^{177}Lu radiopharmaceutical therapy using voxel-based patient-specific phantoms.

This chapter includes the original work that has been published in the Journal of Applied Radiation and Isotopes.

The front page of the published article is shown in Appendix C

DOI: http://dx.doi.org/10.2139/ssrn.3958626

TABLE OF CONTENTS

4.1 Abstract

Purpose: Virtual dosimetry using voxel-based patient-specific phantoms and Monte Carlo (MC) simulations offer the advantage of having a gold standard against which absorbed doses may be benchmarked to establish the dosimetry accuracy. Furthermore, these reference values assist in investigating the accuracy of the absorbed dose methodologies from different software programs. Therefore, this study aimed to compare the accuracy of the absorbed doses computed using LundADose and OLINDA/EXM 1.0.

Methods: The accuracy was based on ^{177}Lu-DOTATATE distributions of three voxel-based phantoms. SPECT projection images were simulated for 1, 24, 96, and 168 hours post-administration and reconstructed with LundADose using 3D OS-EM reconstruction. Mono-exponential curves were fitted to the bio-kinetic data for the kidneys, liver, spleen, and tumours resulting in SPECT time-integrated activity (SPECT-TIA). The SPECT-TIA were used to compute mean absorbed doses using LundADose (LND-D_{SPECT}) and OLINDA (OLINDA-D_{SPECT}) for the organs. Pre-defined true activity images, were used to obtain TRUE-TIA and, together with full MC simulations, computed the true doses (MC-D_{True}). The dosimetry accuracy was assessed by comparing LND-D_{SPECT} and OLINDA-D_{SPECT} to MC-D_{True}.

Results: Overall, the results presented an overestimation of the mean absorbed dose by LND-D_{SPECT} compared to the MC-D_{True} with a dosimetry accuracy ≤ 6.6%. This was attributed to spill-out activity from the reconstructed LND-D_{SPECT}, resulting in a higher dose contribution than the MC-D_{True}. There was a general underestimation (< 8.1%) of OLINDA-D_{SPECT} compared to MC-D_{True} attributed to the geometrical difference in shape between the voxel-based phantoms and the OLINDA models. Furthermore, OLINDA-D_{SPECT} considers self-doses while MC-D_{True} reflects self-doses plus cross-doses.

Conclusion: The better than 10% accuracy suggests that the mean dose values obtained with LND-D_{SPECT} and OLINDA-D_{SPECT} approximate the true values. The mean absorbed doses of the two software programs, and the gold standard were comparable. This work shall be of use for optimising ^{177}Lu dosimetry for clinical applications.

Keywords: SPECT, Dosimetry, accuracy, Monte Carlo, ^{177}Lu-DOTATATE, OLINDA, LundADose, radiopharmaceutical therapy, patient-specific phantom, voxel-based phantom.

4.2 Introduction

The recent development of novel radiopharmaceutical agents in the field of Nuclear Medicine (NM) has resulted in renewed interest in radiopharmaceutical therapy (RPT) and internal radiation dosimetry to evaluate the efficacy and toxicity of RPT. Different terminologies such as targeted radionuclide therapy, theranostics (theragnostics), targeted radiopharmaceutical therapy, and molecular-targeted radionuclide therapy have been used to describe patient therapy using radioactive pharmaceuticals. However, the Society of Nuclear Medicine Molecular Imaging therapy task force survey has recently suggested the use of a consistent nomenclature for the field and recommends the term RPT to describe such a treatment (1). The authors argue that the name offers differentiation from external beam radiation therapy (EBRT) by clarifying that the therapeutic agent is a pharmaceutical and not another form of radiation therapy. For this reason, the term RPT will be adopted herein to further describe therapy using radioactive pharmaceuticals.

Lutetium-177 (^{177}Lu) has gained widespread interest and importance in the field of RPT due to its decay properties. The radionuclide emits both gamma rays (predominantly with the energy of 208.4 keV and 112.9 keV) and beta particles with maximum energy of 498.3 keV (mean range in soft tissue of 0.7 mm) and has a physical half-life of 6.7 days (2). Therefore, it can be used for therapeutic and imaging purposes since it has ideal properties for post-administration imaging, which allows for patient-specific dosimetry. Neuroendocrine tumours (NETs) have been treated successfully using RPT, specifically peptide receptor radionuclide therapy (PRRT) with ^{177}Lu-DOTATATE (3–6). PRRT aims to irradiate tumour cells by coupling radionuclides such as ^{177}Lu to peptide molecules that bind to cell receptors. In some tumours these receptors may be over-expressed in abundance, allowing a high radiation dose to be delivered to the tumour cells. However, some non-tumour physiological uptake also occurs in organs such as the kidneys, liver, spleen, and bone marrow. Thus, the radiation dose administered to the patient during PRRT (and RPT in general) is limited by the dose of the healthy tissue (also referred to as organs at risk (OAR)). The effectiveness of RPT lies in the ability to deliver a lethal dose to the tumour cells while sparing the healthy tissue. PRRT with ^{177}Lu-DOTATATE has been well established in treating patients with late-stage NETs that overexpress somatostatin receptors. Trials have shown ^{177}Lu-DOTATATE to be an effective and well-tolerated form of treatment for NETs (7–10). Even though RPT (which includes ^{177}Lu-DOTATATE and ^{131}I-MIBG (metaiodobenzylguanidine)) has been used for many years to treat NETs there is still much room for optimising its patient-specific treatment efficacy.

Patient individualised therapy is a standard in treatment planning with EBRT, aiming to achieve better tumour control and less normal tissue toxicity. The same principle of individualised dosimetry-driven treatment planning is sought for RPT. According to Haug, (11) the NM community must work towards harmonizing dosimetry methods. Further on, the author emphasizes the clinical need to establish a dose-response relation for RPT and not only adapt the EBRT dosimetry threshold values. The usefulness of adapting EBRT threshold values to RPT is not substantiated. To establish RPT dose-response relations, large clinical trials will be necessary (12). Without a well-established harmonized dosimetry protocol, these trials will not result in reliable threshold values that can be applied across all patients.

Patient-specific treatment would require patient-specific factors to maximize its effectiveness. The principal OAR for ^{177}Lu-DOTATATE treatment of NETs are identified as the kidneys and bone marrow (13). The kidneys are recognised as the most critical dose-limiting OAR for ^{177}Lu-DOTATATE PRRT because of the additional re-absorption by proximal tubules. As a result, potential damage from deterministic effects may manifest itself one or several years after completion of treatment (14). Therefore the radiation dose to critical organs such as the kidneys must be determined as accurately as possible. Internal radiation dosimetry facilitates calculating the absorbed dose to these OAR. Ilan et al. (15) have shown a significant correlation between tumour absorbed dose, tumour size, and tumour control for pancreatic NETs. It is thus valid, where possible, to extent dosimetry to the tumours. Similar to EBRT treatment planning, accurate knowledge of absorbed doses to both the tumour and normal tissue is advantageous in RPT treatment planning.

Since internal radiation dosimetry determines the amount of absorbed dose in tissue, the terms absorbed dose calculation and dosimetry shall be used interchangeably. For accurate patient-specific dosimetry, the bio-distribution and bio-kinetic data of the radiopharmaceutical is required to calculate the time-integrated activity (TIA) for each organ of interest. The total amount of radiation energy emitted by the radioactivity in each source organ is further required and known for the specific radionuclide used. The final parameter to include in the absorbed dose calculation is the fraction of energy emitted by each source organ and absorbed by the relevant target organs. Since this is dependent on the relative organ positions and sizes, patient-specific anatomical information is required.

Bio-kinetic data is patient-specific therefore, it emphasizes the validity of personalised dosimetry. The bio-kinetic data may be monitored with a gamma camera through patient-specific image-based quantification. The challenge for clinics and institutions is determining the best data collection method to quantify bio-kinetic data for different tissue regions. Clinics have adopted different image acquisition and data processing protocols. Quantification can be obtained using planar whole-body (14, 16–19), SPECT/CT (15, 20, 21) or hybrid planar whole-body SPECT/CT images (further referred to as hybrid WB/SPECT images) (13,22–25). There seems to be a consensus that planar whole-body imaging may not be the accurate approach of image quantification for dosimetry purposes mainly due to overlap of activity uptake regions (organs and background tissue). Several researchers promote the use of SPECT/CT images to obtain quantitative dosimetric data for RPT (26–34). In some studies, planar images have been reported to overestimate absorbed dose measurements attributed to organ overlap, compared to more accurate measurements obtained with SPECT data (13,35). This overestimation of absorbed dose to the relevant target organs can result in the under-treatment of a patient. The compromise between planar imaging advocated to speed up multiple image data acquisitions for dosimetry versus the improved accuracy by SPECT/CT images may be overcome by the hybrid WB/SPECT imaging method.

SPECT/CT is promoted as part of a clinical workflow, however, using SPECT data to determine absorbed dose estimates is protocol-dependent and has method-specific limitations. According to Bardiès and Gear (36), dosimetry is a component of a clinical workflow chain that includes the following steps: gamma camera acquisition calibration, patient data acquisition, activity quantification, image registration and segmentation, time-activity curve (TAC) fits and absorbed dose calculations. Although commercial software applications are available to perform dosimetry, not all aspects of the chain are always included on par with one another. Thus, there is always a need to optimize these applications (37). The image acquisition and processing methods for dosimetry are predominately dependant on a clinic's accessibility and acquaintance with dosimetry software.

The demand for patient-specific image-based dosimetry treatment planning necessitates developing clinically feasible dosimetry protocols. Mora-Ramirez et al. (37) published a list of recommended operations that should be included in such a protocol. Patient-specific dosimetry entails using patient bio-kinetic data and the patient anatomy to perform the dose calculations. Although more accurate, it is also laborious (38). Currently, the approach to clinical dosimetry is two-fold: One, it may be patient-specific, or two, model-based, where the former is known to be more accurate and the latter easier and faster to implement routinely. There is a trend to move from model-based to patient-specific dosimetry to improve the accuracy of absorbed dose calculations (19,30,39). The use of patient-specific phantoms has demonstrated that determining patient organ sizes versus model-based estimates may result in a two-fold difference in dose estimation (40). Heikkonen et al. (41) reported an average kidney absorbed dose of 0.44 mGy/MBq when CT-based delineation was used instead of the 0.74 mGy/MBq when using a small sub-volume.

The standard method used for absorbed dose calculations, which has gained wide acceptance in NM, is the Medical Internal Radiation Dose (MIRD) formalism (42,43). The MIRD method calculates the mean absorbed dose $\overline{D}(r_T, T_D)$ delivered to the target organ r_T over a defined dose-integration time T_D (from 0 to ∞) after administering a radionuclide, expressed as Equation 4-1:

$$\overline{D}(r_T, \quad T_D) = \sum_{r_S} \tilde{A}(r_S, T_D) \, . \, S(r_T \leftarrow r_S) \tag{4-1}$$

where $\tilde{A}(r_S)$ is the time-integrated activity (TIA) (also referred to as the cumulated activity, i.e., the total number of nuclear decays) in the source organ r_S, $\sum_{r_S}$ denotes the contribution of several source organs, $S(r_T \leftarrow r_S)$ is the mean absorbed dose delivered to the target organ r_T per unit cumulated activity in the source organ- also known as the S value. The S value is radionuclide specific since it depends on the energy and yield of each nuclear transition. The fraction of radiation energy emitted from the source region and absorbed in the target region is also incorporated in the S value. Monte Carlo (MC) radiation energy transport simulations are used to calculate the S values. Multiple target and source region S values have been published in MIRD pamphlet 11 for a range of radionuclides and patient phantoms (44). In essence, the absorbed dose calculations are the product of TIA with the S values, and the universal accuracy relies on these two terms. Improving the dosimetry accuracy requires improving the accuracy of these two variables. The simplified formulation (Equation 4-1) hides the previously mentioned series of operations that are part of the clinical dosimetry workflow chain. The TIA encompasses steps in the chain from the gamma camera acquisition calibration to determining and fitting the TIA. From calibration to image quantification, the initial steps are generally referred to as image activity quantification, whereas the TIA and S values calculations are referred to as absorbed dose calculations and are the subject of this paper. Noteworthy, the TIA depends mainly on the image quantification methods and their accuracy. Therefore, our image activity quantification method is presented in our preceding work (45). We demonstrated that comparable quantification accuracies are obtained when corrections for scatter, attenuation, collimator-detector response (CDR), and partial volume effects (PVEs) are applied to ^{177}Lu SPECT data for calibration factors (CFs) obtained either using a sphere or a large cylindrical phantom geometry. Our findings were based on the principle that partial volume correction (PVC) should be applied using recovery coefficients (RCs) obtained with the same CF geometry, which converted the reconstructed SPECT data into units of activity.

Apart from the activity quantification accuracy, the accuracy of TIA depends on the number of consecutive imaging time-points post-administration, the frequency of the imaging time-point, the appropriate imaging time-span after administration (integration period), and the integration of these time-points, i.e., the model used to fit the TAC before integration (46–48). The results used to calculate the absorbed doses are usually presented either as TIA (MBq.s) or the residence time (s) defined as TIA normalised to the activity (MBq) administered to the patient.

The S values may be determined from computed pre-calculations based on reference models (49–51) and radiation transport algorithms. These algorithms are subdivided into local energy depositions (LEDs) (52,53), convolution with dose-voxel kernels (54,55), and full MC-based radiation transport calculations (56–60). Although the LED method is the simplest, it may be limited in accuracy and valid only for non-penetrating radiation particles such as alpha's, beta's, and Auger electrons (61). The LED method assumes that all the radiation energy is deposited within the respective voxel. Since most radiation-charged particles used in RPT have a path length less than the voxel dimensions of the reconstructed SPECT activity image, the assumption is valid

(59). It falls short when the gamma radiation is emitted with a high yield and an increased cross-dose contribution (62,63). The convolution with the dose-voxel kernels method assumes each voxel to have a uniform source distribution (54,64) and computes voxel S values for a specific radionuclide, tissue density, and voxel dimension using MC transport (55,65). On the other hand, MC-based radiation calculations are known to be accurate but also time-consuming. They not only account for cross-doses but also consider bremsstrahlung photons, energy loss, and tissue penetration depth. The distinct advantage of MC-based calculations is the ability to take non-homogeneous activity distribution into account. This is in addition to accounting for patient-specific geometry, the transition between tissue types, and the induction of secondary particles (55,66).

These subdivisions may result in differences in the mean absorbed doses and, although not explicitly considered in this study, dose-volume histograms and biological effective doses. The approach to choosing the radiation transport algorithm depends on the range of the radiation particles, the imaged geometry, and the gamma camera's spatial resolution assuming that the activity is quantified accurately for the given spatial resolution. As a rule of thumb, LED may be used for non-penetrating radiation, while convolution-based and full MC transport algorithms may be intended for penetrating radiation in homogeneous and non-homogeneous geometries, respectively (36). In the last few years, many dosimetry software programs were created either by gamma camera manufacturers or independent companies using the algorithms mentioned above. The accessibility of the dosimetry software programs is determined by whether they are commercial or academic, have Food and Drug Administration (FDA) approval, are available in the public domain, and are well maintained and documented. Commercial dosimetry software programs available for clinical use, including the European CE marking, are summarised in Table 4-1.

Table 4-1: *Commercial dosimetry software programs with CE marking available for clinical use.*

Dosimetry software	Imaging methods	Dosimetry method	Manufacturer	Reference
QDOSE ®	Planar, SPECT/CT, hybrid WB/SPECT	Convolution	ABX-CRO advanced pharmaceutical services Forschungsgesellschaft Germany	https://www.quantitativedose.com/ (67)
PLANET® Onco Dose (PDOSE)	SPECT/CT, hybrid WB/SPECT	LED convolution	DOSIsoft SA, Cachan, France	https://www.dosisoft.com/products/planet-dose/
MIM SurePlan ™ MRT	SPECT/CT, hybrid WB/SPECT	Convolution	MIM Software Inc. Cleveland. OH, USA	https://www.mimsoftware.com/nuclear _medicine/sureplan_mrt
Dosimetry Toolkit®	Planar, SPECT/CT, hybrid WB/SPECT	OLINDA/EXM 1.0 and 2.0	GE healthcare, Waukesha, WI, USA	https://www.gehealthcare.com/products/ molecular-imaging/nuclear-medicine/xeleris-4-dr
Hybrid Dosimetry Module™ (HDM)	Planar, SPECT/CT, hybrid WB/SPECT	OLINDA/EXM 2.0 and MC method	HERMES medical solutions, Stockholm, Sweden	https://www.hermesmedicalsolutions.cm/dosimetry/ OLINDA/EXM 2.0: (49)

LED, Local energy deposition; *MC*, Monte Carlo; *hybrid WB/SPECT images*, hybrid planar whole-body SPECT/CT images

Various dosimetry methods, such as the *Voxel-Based Internal Dosimetry Application* (68), use MC simulations to generate voxel-level dose rate maps using patient anatomic and physiological data. A whole-body voxel-based dosimetry method using a Deep Neural Network has also been proposed (69). The validity of voxel-based dosimetry is under debate due to the gamma camera's limited spatial resolution resulting in large uncertainty associated with voxel activity. In addition, voxel registration and performing TIA at a voxel level pose a challenge (70). Bearing in mind that the dose distribution has been convolved with the SPECT reconstruction resolution, what one sees on a voxel level may not be the true absorbed dose distribution (71).

The dosimetry software programs mentioned above are of limited access to some clinics due to a lack of affordability. Research institutions and clinics become resourceful in obtaining in-house developed dosimetry software, which strives to encompass most, if not all aspects, of the clinical dosimetry workflow. Two dosimetry software programs, *LundADose* and *OLINDA/EXM 1.0,* will be used in this work. OLINDA/EXM 1.0 (51), which shall further be termed OLINDA, is available to the public domain to automate and standardise absorbed dose calculations for NM applications. It has also served well as a teaching tool and has practically facilitated comparisons between clinics. LundADose is an institution-specific software accessible to our group through research collaboration.

4.2.1 LundADose

LundADose was developed in-house by the Department of Medical Radiation Physics, University of Lund, Lund, Sweden (63,72). The software includes all the steps needed in a clinical dosimetry workflow (59,73). The software program was initially written using the EGS4 code system (74) for MC particle simulation of the electron and photon transport and, for the most part, has since been replaced by the updated version EGSnrc program (57). The MC particle transport methods use the physics of particle interaction to model the individual particle tracks of radiation, such as charged particles and photons, and their energy depositions (75). The energy depositions in the different tissue sites are used to estimate the absorbed doses. The MC-based absorbed dose calculations, together with the patient CT and SPECT data, can be used for patient-specific dosimetry. The reconstructed SPECT image is used to estimate the activity distribution during the transport modelling (also known as particle tracking). Assuming that each voxel value reflects the activity distribution corresponding to the voxel location within the patient, the program can sample the decay of the particles through the radionuclide-specific decay scheme. The particle tracking and energy deposition (from appropriate interactions) is done through a density map derived from the patient CT data. The result is a 3-D dose map of absorbed dose rate with the same dimensions as the reconstructed SPECT image (25). Apart from the absorbed dose calculations, LundADose also incorporates all other steps in the clinical dosimetry chain. The interface is written and developed in Interactive Data Language and calculates image-based absorbed doses using either planar whole-body, SPECT/CT, or hybrid WB/SPECT images. It incorporates methods for SPECT reconstruction with complete corrections, including image registration. The method used in this software program has been successfully validated in clinical studies (76,77). The software program follows the photons by full MC transport to include the cross-doses between organs.

4.2.2 OLINDA/EXM 1.0

OLINDA/EXM 1.0 is an extension of MIRDOSE 1 – 3 (50) and uses the same technical fundamentals as the Radiation Dose Assessment Resource, RADAR website (78–81). OLINDA is the most established and the first software program to receive FDA clearance in 2004 and has been adopted by many institutions to perform clinical dose calculations. This version of OLINDA/EXM was available through Vanderbilt University (Nashville, TN, USA) at a lower cost than OLINDA/EXM 2.0, which is available through HERMES. OLINDA provides S values, which are termed dose conversion factors (DFs), calculated using MC radiation transport (simulations) for a series of radionuclides using standard OLINDA models (51,81). The greater utility of the software program is that it allows the user to combine these DFs with the bio-kinetic model results to compute dose estimates for different organs of interest. The first generation of phantom models from Oak Ridge used geometrical shapes to define the body and its organs (82). The phantom models have been replaced with a more realistic phantom series of NURBS models based on standardised masses (83) published in the ICRP publication 89 (84,85). The software program has ten whole-body OLINDA models, including the adult male and female, the same as those used in MIRDOSE 3. In addition, Olinda has incorporated tumours excluded from the whole-body phantoms as sub-nodules that include unit density spheres to represent these tumours (81). OLINDA allows customisation through adjusting the reported doses by organ mass scaling of the S values.

There has been extensive work on absorbed dose calculations for ^{177}Lu-DOTATATE in the last decade (15,16,34,41,86–91). These reports demonstrate variations in absorbed dose estimates for critical organs such as the kidneys. This variation is caused by the differences in methods used in the clinics. As a result, dosimetry with ^{177}Lu-DOTATATE remains an ongoing investigation for many clinics with a scope for optimising the methods. This is even more so in developing country clinics where access to ^{177}Lu-DOTATATE is limited due to its high cost. Individualised dosimetry may allow for dose escalation in terms of the number of planned cycles, at 7.4 GBq per cycle of up to four cycles, while maintaining the tolerance of the critical structures such as the kidneys (92). This is an important consideration since the residual tolerance of the critical organs after the first cycle is divided amongst the remaining cycles. Due to the reported variations in the absorbed dose estimates, an investigation into the accuracy of the dosimetry calculations becomes an important factor to consider. *Therefore, we aimed to quantitatively compare the accuracy of two patient-specific dosimetry software programs based on the analysis of three SPECT voxel-based patient-specific phantoms with ^{177}Lu-DOTATATE distribution.*

Many literature studies have reported absorbed doses of patients undergoing clinical ^{177}Lu-DOTATATE RPT using different dosimetry formulations and methods (34,37,70,88,92–95). However, a limited number of studies have performed virtual absorbed dose calculations based on MC simulated gamma camera images of clinically realistic voxel-based patient-specific phantoms. The result of such a study has the advantage of having a reference value (gold standard) to which the absorbed doses could be compared, which may be cumbersome to establish in a clinical context.

4.3 Materials and Methods

4.3.1 Monte Carlo Simulations

The MC simulation software program SIMIND (SIMIND version 6.1.2 (96), validated in our previous work (97), was used in this study. We created a model of the Siemens Symbia T16 hybrid SPECT/CT gamma camera (Symbia T16) (Siemens Medical Solutions, Inc. Hoffman Estates, IL., USA), which was used to mimic ^{177}Lu gamma camera performance characteristics successfully. In the current work, we created three individual voxel-based clinically realistic phantoms, shown in Figure 4-1, identified as two females and a male. Due to the unavailability of ^{177}Lu-DOTATATE patient data in our clinic, the phantoms were created from anonymised liver-spleen SPECT/CT patient datasets obtained from the Symbia T16 database at Universitas Academic Hospital in Bloemfontein, South Africa. This study was approved by our institution's ethics committee in accordance with the Declaration of Helsinki and the radiation control committee. The voxel-based patients were created by segmenting the CT images of the patients using ITK-snap (98). Each segmented region was assigned a unique value to represent the different organs, generating a source map. The method followed to create the voxel-based patient phantoms, and the details of the simulation protocol are discussed in our preceding publications (45,97). The patient phantom simulations were performed as described by Ramonaheng et al. (45).

This work represents the third contribution from our group concerning the accuracy of ^{177}Lu SPECT activity quantification and patient-specific dosimetry using MC simulations. The current study was designed to investigate the dosimetry accuracy, i.e., the last step in the absorbed dose calculation chain, for the two software programs mentioned above. For this reason, the data acquisition, processing protocols, and the SPECT image activity quantification method extends from our previous work and has been documented (45). The same methodology was followed to determine the CF and SPECT activity quantification of the voxel-based patient phantom mentioned in our previous publication. The reader is referred to Ramonaheng et al. (45) for more information. Our previous work further demonstrated that comparable SPECT quantification accuracies were obtained between sphere and cylinder CFs when their corresponding RCs were used for PVC. We opted for the sphere CF in this study due to its potential practical implementation in the clinic.

The patient-specific bio-kinetic data was based on aspects of ^{177}Lu-DOTATATE bio-kinetic distribution from Brolin et al. (23), who used three pharmacokinetic digital phantoms from the XCAT generation to assess the dosimetry accuracy of ^{177}Lu-DOTATATE RPT. Similarly, we used the three voxel-based phantoms to investigate the dosimetry accuracy of the kidneys, liver, spleen, and tumours pertinent to ^{177}Lu-DOTATATE. The organ and tumour, (segmented as described above) activity concentrations were kept the same for the three phantoms. Spheres are well established to mimic tumours (99). Therefore, two spheres of volume 33.5 ml (with a corresponding diameter 4.0 cm) were positioned adjacent to the liver (tumour-LV) and between the lungs (tumour-LNG). The organ and tumour concentrations of the three phantoms were based on the administered activity of 5533±1850 MBq (19,100) during the simulation. Simulations were performed for the ^{177}Lu 208.4 keV photopeak and 20% centred energy window, using a medium-energy (ME) collimator. The SPECT projections were simulated with an equivalent acquisition time of 45 s per projection in a 128 × 128 image matrix with a pixel size of 4.8×4.8 mm^2. SPECT projections were simulated for imaging time-points 1, 24, 96, and 168 hours post-administration. A large number (> 1 billion) of photon histories were used for all simulations to ensure low simulation noise in the datasets (101).

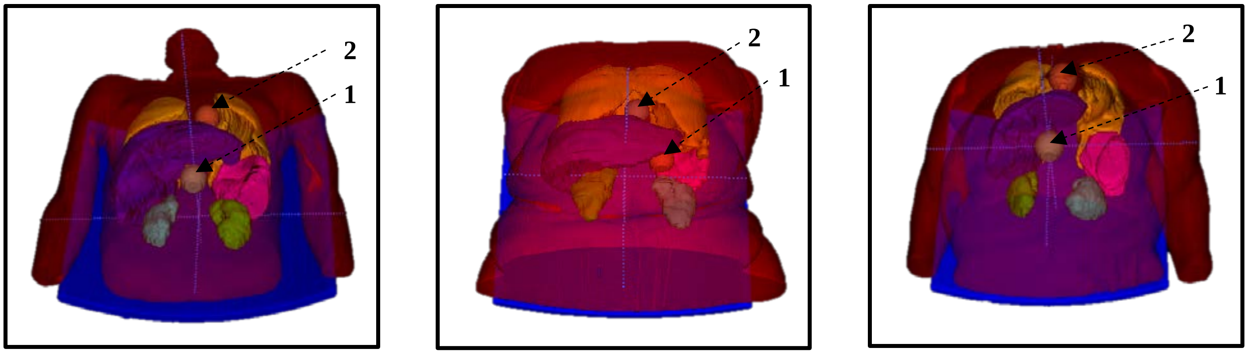

Figure 4-1: *Three voxel-based patient-specific phantoms segmented using CT data fitted with spheres representing tumours. The arrows indicate sphere positions 1 and 2, representing tumours adjacent to the liver (tumour-LV) and between the lungs (tumour-LNG).*

The challenge for a comparative study such as ours, as indicated by Mora-Ramirez et al. (37), who compared five commercial dosimetry software programs in patients treated with ^{177}Lu-DOTATATE, is that the software programs do not all address the same steps in the clinical dosimetry workflow chain. In addition, the data handling in each part of the chain may be different for each software program, which complicates the comparative exercise and entails evaluating the uncertainties in each step. To reduce these uncertainties and allow for a fair comparison of the dosimetry section, we found it reasonable to have a checkpoint for the accuracy only at the absorbed dose calculation step. Of the two software platforms under investigation, LundADose included all steps in the dosimetry workflow chain and allowed for standard criteria to be used for input data prior to the absorbed dose calculations. Therefore, the TIA was computed using LundADose, as explained below, and thereafter the absorbed dose estimates were computed using LundADose and OLINDA.

4.3.2 LundADose

4.3.2.1 Reconstructed SPECT Dose Image

The simulated SPECT projections of the voxel-based patient phantoms obtained with SIMIND were reconstructed in LundADose using the 3D ordered subset expectation maximisation (OS-EM) algorithm with pre-determined optimal OS-EM updates (80 updates) (45). The 3D OS-EM algorithm incorporated a CT-based attenuation correction, effective source scatter estimation scatter correction, and a CDR correction (102,103). Appropriate PVC was applied using previously determined RCs for the tumours, and partial volume was corrected for the kidneys and spleen as described in Ramonaheng et al. (45). Using Image J, the reconstructed activity images were compensated for partial volume by numerically correcting each segmented region with an appropriate RC.

The organ delineation part of the software program allowed the user to define volumes of interest (VOIs) from the segmented images based on the CT data. The VOIs for the kidneys, liver, spleen, and tumours were delineated according to the physical borders of the CT data, and each organ VOI file was saved. The reconstructed SPECT images of the four time-points were fed into LundADose and analysed using the saved VOI files. The program sums the activity concentration within each segmented volume of the different organs. The VOIs were superimposed on each organ's four time-points, generating a TAC (MBq vs. hr). A mono-exponential curve (3,23,88,104) appropriate to the data for each organ was fitted to the data generating a result file with SPECT-TIA (MBq. hr) for each organ. The mean absorbed dose estimates were computed utilising full MC transport by incorporating phantom-specific density map information generated from CT data and the phantom reconstructed SPECT data.

The absorbed dose calculations for *full MC transport* incorporated in LundADose (72) used the EGS4 and EGSnrc program to calculate the S values for all source-to-target combinations of the three phantoms. The program used "all" particles' interaction of matter with photons, electrons, and beta particles, which includes spatial energy deposition scoring and sampling of decay positions (105). The MC transport incorporated patient-specific anatomical information from the density map and the activity distribution obtained from the reconstructed SPECT data. The code generates cross-sections for lung, soft tissue, and bone normalised to a unit density. The voxel mass density is multiplied with the appropriate normalised cross-section to obtain the voxel cross-sections during the simulation. The transport simulation cut-off energies for which each history was terminated and the energy deposited were 0.01 MeV and 0.1 MeV for the photons and electrons, respectively. Subsequently, the energy deposition in all structures was scored and divided by the respective region mass. All simulations were performed with an adequate number of histories (100 million histories) to ensure low statistical uncertainty. The cut-off energy and number of histories were selected to ensure reasonable simulation time while maintaining low statistical uncertainty. The mean absorbed doses computed with LundADose using full MC transport from reconstructed SPECT images shall be termed LND-D_{SPECT}.

4.3.2.2 True Dose Image

i. Full Monte Carlo Transport

The accuracy of the mean absorbed doses from the reconstructed SPECT images of the patient phantoms was benchmarked against the true MC absorbed doses determined from a true dose image and MC transport. This image was created directly from the pre-defined activity source map and the aligned density map of the voxelized patient phantoms. The source map contained unique values of the segmented organs (97) for the kidneys, liver, spleen, lungs, tumour, and the body's remainder. Using Image J (Fiji) (106) the source map was scaled to a 128 × 128 image matrix, and the organ indexes were assigned the radioactive concentrations defined in the simulation. These images represented the true activity maps as they exclude the degradation induced by the imaging and reconstruction processes, including poor resolution, attenuation, and scatter. The true activity images were used to calculate the True-TIA. Similar to the reconstructed SPECT images, the true activity images were fed into LundADose to compute the absorbed doses using full MC transport as described above, resulting in an MC-D_{True}. MC transport modelling is considered the gold standard for calculating absorbed doses (72), and for this reason, MC-D_{True} shall be used as the reference standard to evaluate the dosimetry accuracy.

ii. Local Energy Deposition

Ljungberg and Sjögreen Gleisner (58) have reported LundADose to accurately calculate absorbed doses for voxel dimensions used in clinical SPECT images, assuming the kinetic energy from charged particles (electrons) is locally absorbed. The assumption holds true, based on the poor spatial resolution of the SPECT images used as input for dosimetry which is comparable to or larger than the projected maximum range of the electrons. ^{177}Lu emits gamma radiation (208.4 keV) with low yield (10.4%) and thus has negligible cross-dose contribution (107). Because the LED assumption within a voxel for the energy delivering electrons simplifies SPECT/CT dosimetry and holds true for most radionuclides used for RPT, it was fitting to calculate the true doses using the same assumption. Even though MC is the gold standard, it is justified when the range of the particle under investigation is larger than the voxel size of the SPECT/CT image (63), which is not the case for ^{177}Lu.

Furthermore, full MC dosimetry calculations can be computationally intensive and therefore have not been entirely adopted in routine clinical applications where the amount of time taken to perform the dosimetry is an important consideration. Therefore, for this study, the true doses were additionally computed assuming LED, self-dose from electrons.

Similar to the MC-D_{True}, the phantom-specific density map and true activity images were incorporated, and the LED was computed as follows. The ^{177}Lu decay emission data was obtained from the Nudat2 database of the National Nuclear Data Center at Brookhaven National Laboratory, New York, USA (108). LundADose was used to compute the average absorbed dose, assuming the LED from electrons is absorbed in the respective voxel. The emitted electron energy was weighted by the yield and summed over all electron energies resulting in the total energy emitted per decay. This assumption serves as reasonable since for ^{177}Lu the electron dose is completely dominant due to the low photon yield. The aligned density map for each patient was converted to a mass image. The absorbed dose was calculated by curve fitting and numerical integration, multiplying the TIA by the emitted energy per decay. Further on, the mean absorbed dose rate was computed by dividing the rate of absorbed energy with the corresponding mass taking into account the voxel dimensions, resulting in the absorbed dose rate per voxel. The dose computed from the LED of electrons using the true activity images shall be termed e-D_{True}

4.3.3 OLINDA

OLINDA (version 1) was used in this work due to its availability in our institution. OLINDA allows the user to input TIA per administered activity to obtain the mean absorbed organ doses. The adult male or female OLINDA models were appropriately selected for ^{177}Lu. The results obtained using LundADose, up until and including the fitting of TIA data, were transcribed to OLINDA to represent the kinetic input data. The TIA obtained from LundADose was normalised to the total activity used in the simulation, and target organ doses were calculated using OLINDA. Instead of using specific S values calculated using full MC transport for the voxel-based patient phantoms (LND-D_{SPECT}), each simulated patient organs' total doses were computed using the pre-computed S values from the OLINDA models (51). The target organ S values (Vanderbilt University, Nashville, Tennessee, USA) (for self-irradiation) were scaled appropriately to the respective masses of the voxelized patient phantoms' organs as defined by the VOIs obtained from the CT data. The sphere sub-nodule was used to calculate the tumour absorbed doses, modelled as unit-density spheres of mass 33.6 g, estimating the absorbed dose to this volume. The main objective of this work was to investigate the accuracy of the mean absorbed dose estimates from OLINDA-D_{SPECT} and LND-D_{SPECT} to the MC-$D_{True.}$ Although it is possible to calculate self-dose plus cross-dose contribution to the target organ using OLINDA, it is in most cases generally used and accepted to calculate only self-dose from the target organ for RPT. Furthermore, OLINDA does not account for cross-dose to and from the tumours. For this reason, it seemed meaningful to explore the e-$D_{True,}$ which accounted only for self-dose in the true dose images.

4.3.4 Evaluation of Dosimetry Accuracy

The main aim of this work was to calculate the dosimetry accuracy of three voxel-based patient-specific phantoms for ^{177}Lu-DOTATATE distribution in the kidneys, spleen, liver, and tumours. The measure of error, termed the accuracy, was represented as a percentage difference between the mean SPECT estimates $(SPECT)$ and the true estimates $(TRUE)$, as shown in Equation 4-2.

$$Accuracy\ (\%) = \frac{SPECT - TRUE}{TRUE} \times 100 \tag{4-2}$$

The accuracy was essentially evaluated four-fold for:

i) SPECT-TIA versus True-TIA
ii) LND-D_{SPECT} versus MC-D_{True} (self-dose and cross-dose)
iii) OLINDA-D_{SPECT} versus MC-D_{True} (self-dose and cross-dose)
iv) OLINDA-D_{SPECT} versus e-D_{True} (self-dose)

It should be noted that $SPECT$ (Equation 4-2) appropriately represented the SPECT-TIA, LND-D_{SPECT} or OLINDA-D_{SPECT} while $TRUE$ represented True-TIA, MC-D_{True} or e-D_{True} depending on the comparison (i-iv), which shall be stipulated accordingly. Where appropriate, the absolute differences between the average values shall be reported. The evaluation of the dosimetry accuracy is illustrated in Figure 4-2.

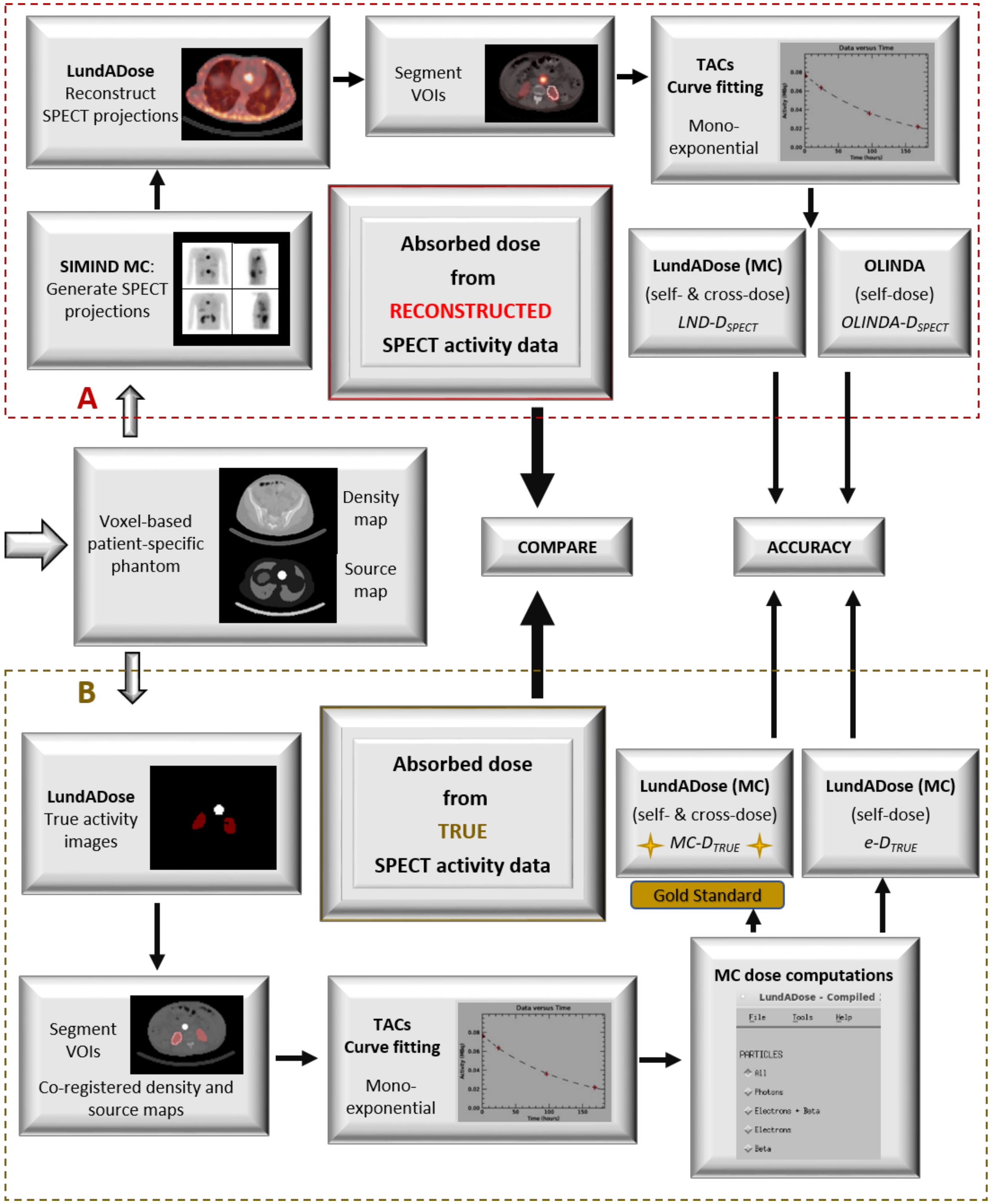

Figure 4-2: *Schematic flow chart showing the steps followed to determine the dosimetry accuracy between the reconstructed SPECT data **(A)** and the true activity data **(B)**.*

4.4 Results

4.4.1 Time-Integrated Activity Accuracy

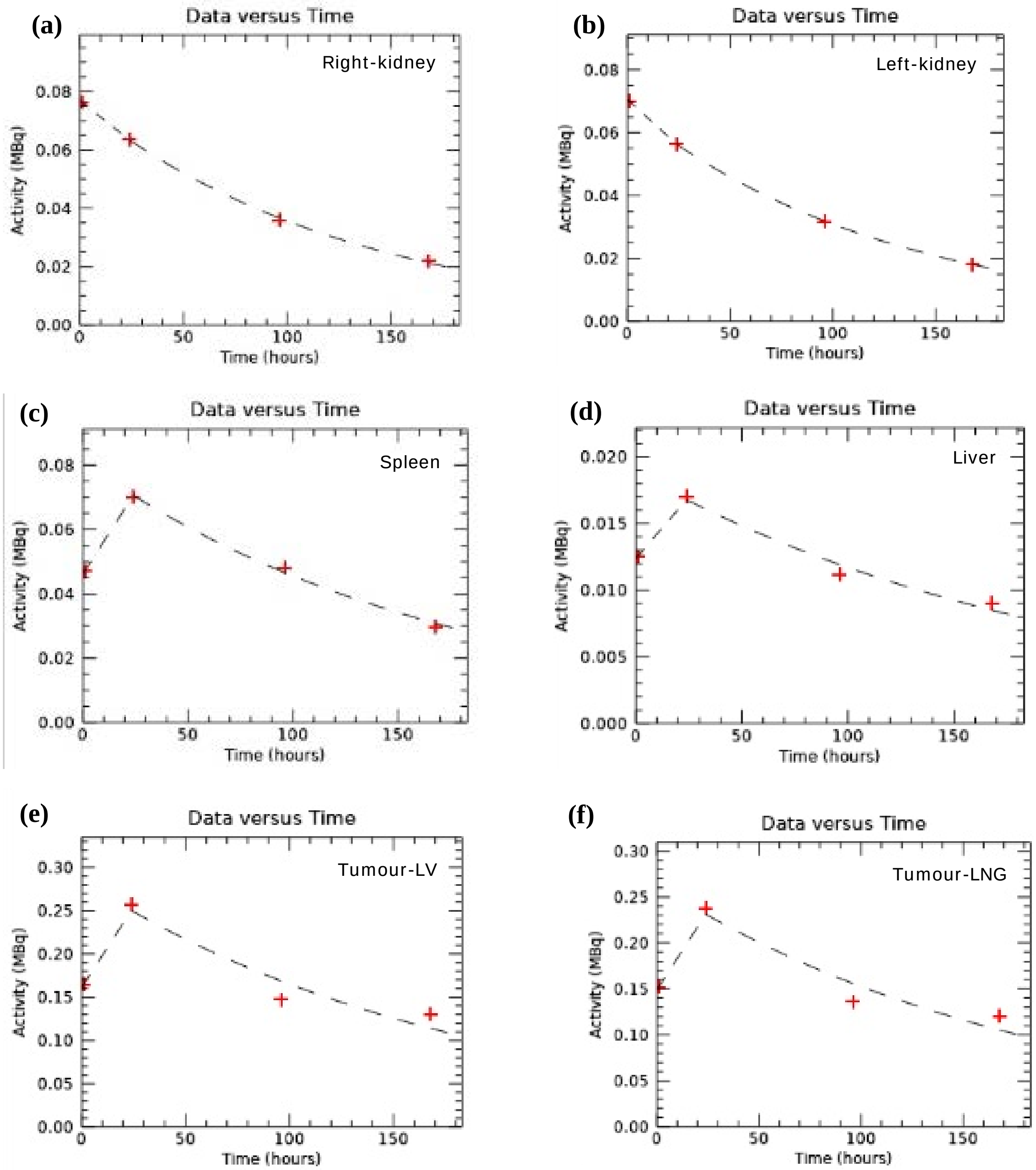

Figure 4-3: *Examples of time activity fits obtained from the reconstructed SPECT images, used to calculate time-integrated activity for the* ***(a)*** *right-kidney,* ***(b)*** *left-kidney,* ***(c)*** *spleen,* ***(d)*** *liver,* ***(e)*** *tumour-LV (tumour adjacent to the liver) and* ***(f)*** *tumour-LNG (tumour between the lungs).*

Using data obtained for voxel-based patient phantom 2, an example of the typical TACs obtained from the three patient phantoms for the four time-points at 1, 24, 96, and 168 hours of the reconstructed SPECT images are shown in Figure 4-3. The best-fitting function available with LundADose for the curves was evaluated by visual inspection, a method previously adopted by other authors (109). Mono-exponential fits were the best model to describe the progression of the activity in the source VOIs for the organs of interest, including the tumours. A slight deviation from the fitting function was observed for the tumour data at 96 and 168 hours. Except for the kidneys, all the organs of interest exhibited a two-phase TAC characterised by a rapid activity uptake followed by a slower washout phase. The kidneys exhibited a single-phase curve with a more rapid washout phase in comparison to the other organs. In addition, co-registered true activity images and reconstructed SPECT images indicating VOIs for the kidneys, spleen and tumour-LNG are shown in Figure 4-4.

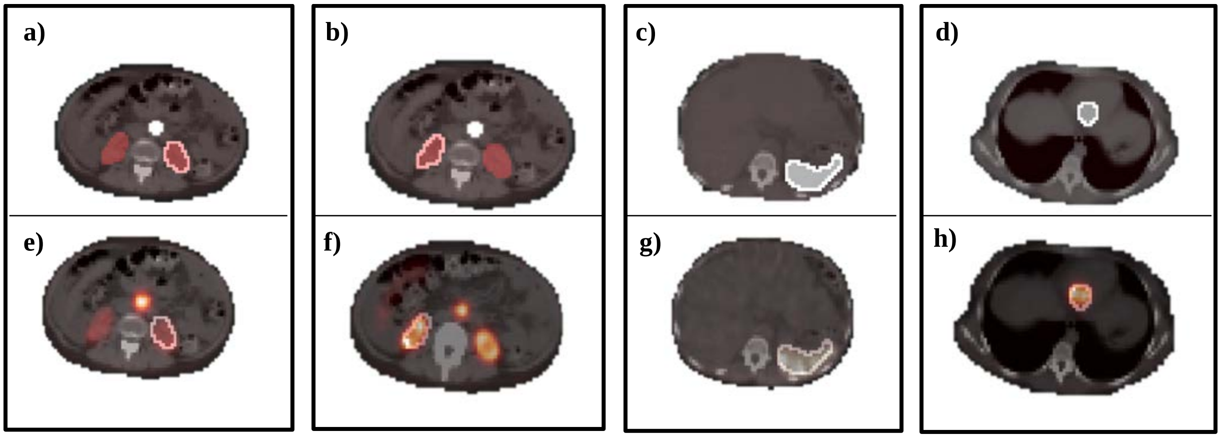

Figure 4-4: *Example of coronal slices of the right-kidney, left-kidney, spleen, and the tumour placed between the lungs for the true activity images (**(a)-(d)**) and the corresponding reconstructed SPECT slices (**(e)-(h)**).*

The TIA was calculated using the true activity images (True-TIA) and the reconstructed SPECT (SPECT-TIA) images and computed in LundADose by fitting the mono-exponential model to the data obtained for the four time-points (Figure 4-3). The average TIA data and associated standard deviation of the three phantoms for the kidneys, spleen, liver, and tumours are summarised in Table 4-2 and presented in Figure 4-5. To note, Table 4-2 includes the absolute difference between the average values of the TRUE-TIA and SPECT-TIA data.

Table 4-2: *The average time-integrated activity (TIA) data of the three phantoms for the kidneys, spleen, liver, tumour-LV (tumour adjacent to the liver), and tumour-LNG (tumour between the lungs) computed from the true activity (TRUE-TIA) and reconstructed SPECT (SPECT-TIA) images.*

	Time-integrated activity (MBq.hr)		
Organ	**TRUE-TIA**	**SPECT-TIA**	**Abs difference**
Right-kidney	5.27±0.72	5.44±0.75	0.17
Left-kidney	4.61±0.51	4.72±0.59	0.11
Spleen	6.48±0.92	6.79±1.10	0.31
Liver	2.46±0.48	2.54±0.48	0.09
Tumour-LV	42.29±10.02	43.73±10.21	1.44
Tumour-LNG	53.49±10.34	55.27±11.09	1.78

Abs, absolute

The largest cumulated activity concentration was found in the tumours, followed by the spleen, kidneys, and liver. Overall, the standard deviation obtained between the phantoms for both the TRUE-TIA and SPECT-TIA was relatively small except for the tumour data. The spleen exhibited the largest source of activity variation amongst the critical organs with an average of 6.48±0.92 MBq.hr and 6.79±1.10 MBq.hr for the TRUE-TIA and SPECT-TIA, respectively. The tumour's uptake was on average 10-fold that of the dose-limiting kidneys. The reconstructed SPECT data showed slightly higher TIA versus the true activity images. On average, comparable TIA values were obtained between the TRUE-TIA and SPECT-TIA for the respective organs with less than 5% percentage differences.

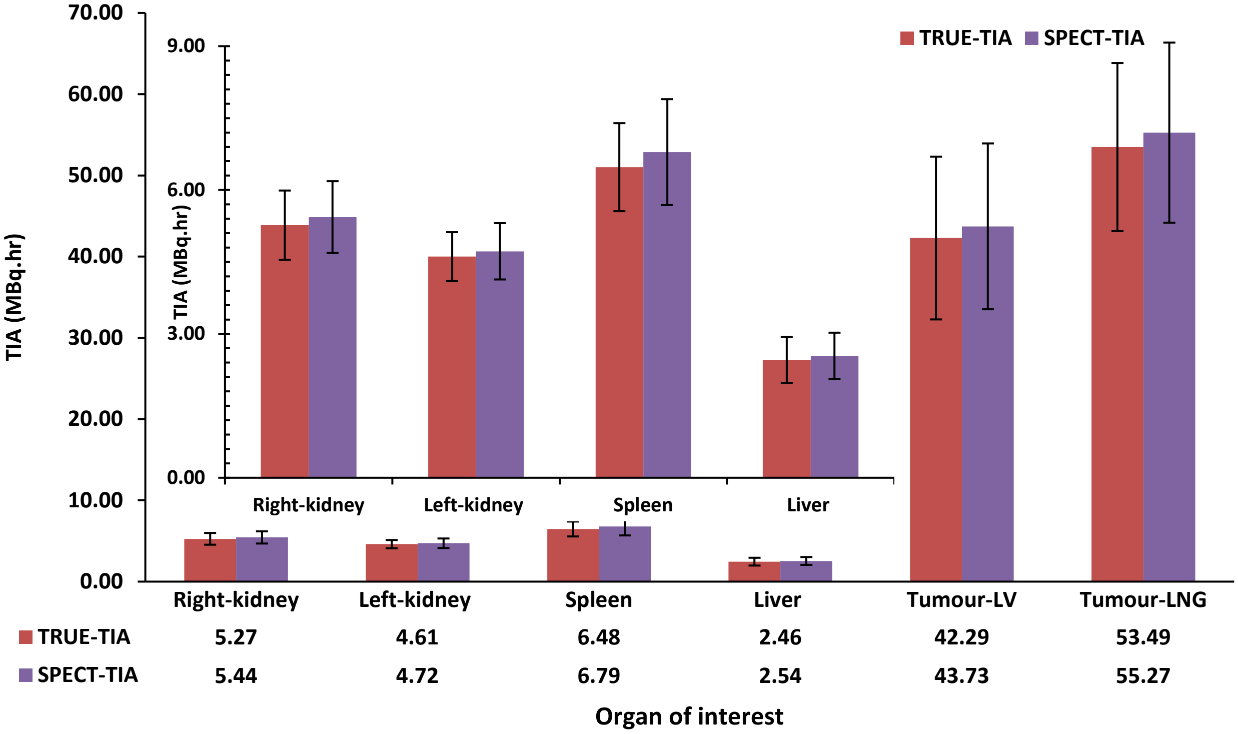

Figure 4-5: *The average time-integrated activity (TIA) for the right-kidney, left-kidney, spleen, liver, tumour-LV (tumour adjacent to the liver), and tumour-LNG (tumour between the lungs), with a zoom-in of the data shown in the upper left section and the average of the values shown at the bottom. The TIA was computed from the true activity images (TRUE-TIA) and reconstructed SPECT images (SPECT-TIA).*

The mean absorbed doses for LundADose and OLINDA were calculated using SPECT-TIA data. As a result, it was worthwhile to compare the accuracy between the TRUE-TIA and the SPECT-TIA for the three patients, which is summarised in Table 4-3.

Table 4-3: *The accuracy of the time-integrated activity (TIA) from the reconstructed SPECT images (SPECT-TIA) versus the TIA from the true images (TRUE-TIA) of the three phantoms for the kidneys, spleen, liver, tumour-LV (tumour adjacent to the liver) and tumour-LNG (tumour between the lungs).*

	SPECT-TIA versus TRUE-TIA			
	Accuracy (%)			
Organ	**Phantom 1**	**Phantom 2**	**Phantom 3**	**Average**
Right-kidney	1.7	3.3	4.6	3.2±1.5
Left-kidney	1.3	3.9	1.9	2.4±1.4
Spleen	3.5	7.2	3.2	4.6±2.2
Liver	2.5	3.0	5.3	3.6±1.5
Tumour-LV	3.4	2.3	4.8	3.5±1.3
Tumour-LNG	4.3	2.8	2.6	3.2±0.9
Average	2.8±1.2	3.8±1.8	3.7±1.4	

The accuracy of the SPECT-TIA for all organs considered was in the range 1.3 – 7.2%, with the largest percentage difference obtained for the spleen of phantom 2 (Table 4-3). The average accuracy was calculated for the respective organs between the phantoms (inter-phantom) and between the organs for a particular phantom (intra-organ) to show variability. A slightly higher inter-phantom variability (≤ 4.6±2.2%) was observed compared to the intra-organ variability (≤ 3.8±1.8%). Overall the accuracy between the TRUE-TIA and SPECT-TIA was less than 7.2%.

4.4.2 Mean Absorbed Dose Accuracy

The mean absorbed doses computed in LundADose by full MC transport using the true activity images (MC-D_{True}) and fitting mono-exponential functions (gold standard), were compared to the mean absorbed doses from the reconstructed SPECT images fitted to the same function calculated in LundADose (LND-D_{SPECT}) and OLINDA (OLINDA-D_{SPECT}), and presented demographically in Figure 4-6. As mentioned above, the e-D_{True} estimates are presented because they carry a similar assumption to OLINDA (self-dose from target) and at the same time offer the opportunity to assess the contribution of the MC cross-dose. The overall trend of the mean absorbed doses, with the largest doses in the tumours, followed by the spleen, kidneys, and liver, was observed by other authors (22,37,110) assessing dosimetric comparisons of ^{177}Lu-DOTATATE distributions.

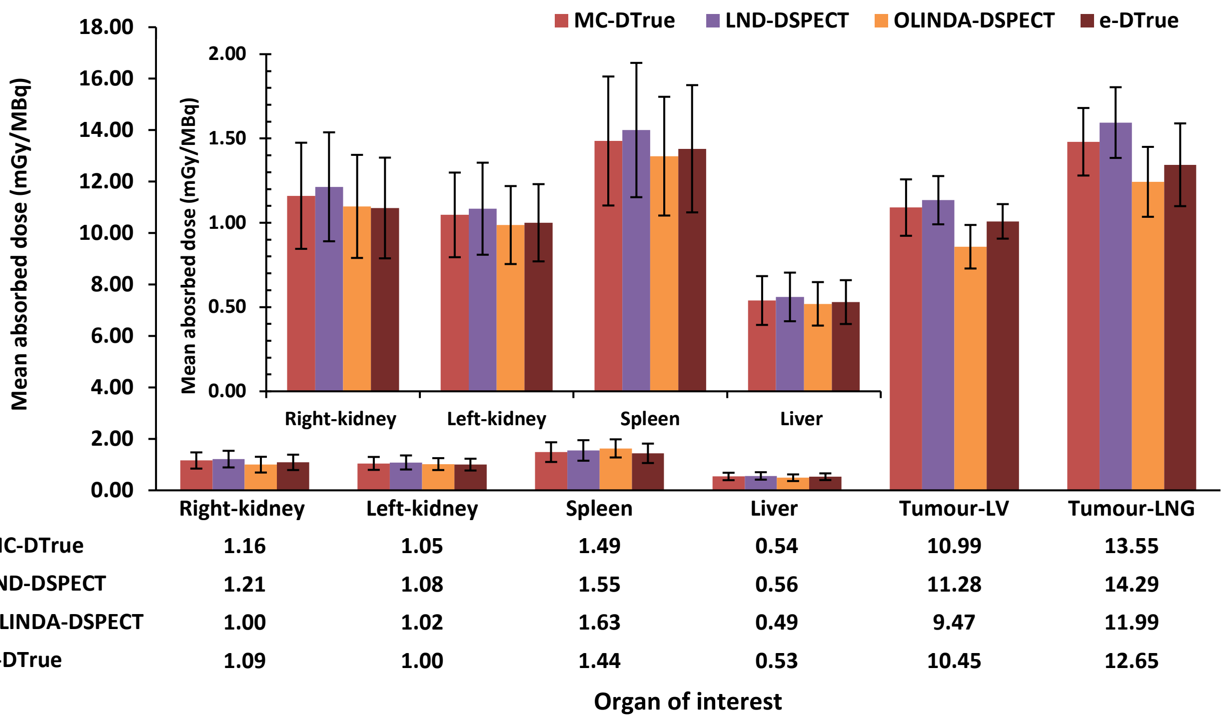

	Right-kidney	Left-kidney	Spleen	Liver	Tumour-LV	Tumour-LNG
MC-DTrue	1.16	1.05	1.49	0.54	10.99	13.55
LND-DSPECT	1.21	1.08	1.55	0.56	11.28	14.29
OLINDA-DSPECT	1.00	1.02	1.63	0.49	9.47	11.99
e-DTrue	1.09	1.00	1.44	0.53	10.45	12.65

Figure 4-6: *The mean absorbed doses for the right-kidney, left-kidney, spleen, liver and tumour-LV (tumour adjacent to the liver) and tumour-LNG (tumour between the lungs) with a zoom-in of the data shown in the upper left section and the average values shown at the bottom. Doses were computed from the true activity images using full Monte Carlo (MC) transport (MC-D$_{True}$) and assuming electron self-dose (e-D$_{True}$), as well as from reconstructed SPECT images using LundADose (LND-D$_{SPECT}$) and OLINDA/EXM 1.0 (OLINDA-D$_{SPECT}$).*

4.4.2.1 LND-D$_{\text{SPECT}}$ versus MC-D$_{\text{True}}$

The MC-D$_{\text{True}}$ values were generally marginally lower than those obtained from LND-DSPECT, following the same trend of the highest and lowest absorbed doses seen in the tumours and liver. The absolute difference between the MC-D$_{\text{True}}$ and the LND-D$_{\text{SPECT}}$ for the average values showed an overestimation by the LND-D$_{\text{SPECT}}$ of $\geq$ 0.75 mGy/MBq. The dosimetry accuracy (Equation 4-2) of the mean absorbed doses for the LND-D$_{\text{SPECT}}$ versus MC-D$_{\text{True}}$ are summarised in Table 4-4 for the three patient phantoms. In general, the results present an overestimation of the mean absorbed dose by LND-D$_{\text{SPECT}}$ compared to the MC-D$_{\text{True}}$ with an accuracy better than 6.6%. The observed differences followed those seen with the TIA, with the highest accuracy observed for the spleen of phantom 2 with an inter-phantom variability of ≤ 4.4±2.2%, which was of the same order magnitude as the intra-organ variability of ≤ 4.4±1.8%.

Table 4-4: *The accuracy of the mean absorbed doses computed in LundADose with full Monte Carlo (MC) transport using the reconstructed SPECT images (LND-D_{SPECT}) versus the true activity images (MC-D_{True}) of the three phantoms for the kidneys, spleen, liver, tumour-LV (tumour adjacent to the liver) and tumour-LNG (tumour between the lungs).*

	LND-D_{SPECT} versus MC-D_{True}			
	Accuracy (%)			
Organ	**Phantom 1**	**Phantom 2**	**Phantom 3**	**Average**
Right-kidney	4.4	4.0	5.6	4.7±0.8
Left-kidney	2.6	5.6	1.8	3.3±2.0
Spleen	4.3	6.6	2.3	4.4±2.2
Liver	4.8	2.9	4.8	4.2±1.1
Tumour-LV	1.5	1.8	4.8	2.7±1.8
Tumour-LNG	5.6	5.4	5.5	5.5±0.1
Average	3.9±1.5	4.4±1.8	4.1±1.7	

4.4.2.2 OLINDA-D_{SPECT} versus MC-D_{True}

The MC-D_{True} values were generally slightly higher than OLINDA-D_{SPECT} values with absolute differences ≤ 0.66 mGy/MBq. Similarly, the accuracies between the MC-D_{True} and OLINDA-D_{SPECT} values are presented in Table 4-5. The results showed a general underestimation of OLINDA-D_{SPECT} in comparison to MC-D_{True}. The highest accuracy was observed for the right (≤ 6.7%) and left kidneys (≤ 8.1%) of phantom 3 where the inter-phantom and intra-organ variability were of the same order magnitude, ≤ 5.6±2.2%, and ≤ 5.2±2.8%, respectively.

Table 4-5: *The accuracy of the mean absorbed doses computed in OLINDA using the reconstructed SPECT images (LND-D_{SPECT}) versus the mean absorbed doses computed in LundADose with full Monte Carlo (MC) transport using the true activity images (MC-D_{True}) of the three phantoms for the kidneys, spleen, liver, tumour-LV (tumour adjacent to the liver) and tumour-LNG (tumour between the lungs).*

		OLINDA-D_{SPECT} versus MC-D_{True}		
		Accuracy (%)		
Organ	**Phantom 1**	**Phantom 2**	**Phantom 3**	**Average**
Right-kidney	-5.2	-4.6	-6.7	-5.5±1.1
Left-kidney	-3.9	-4.8	-8.1	-5.6±2.2
Spleen	-5.3	-6.3	-6.3	-6.0±0.6
Liver	-3.1	-5.7	-1.2	-3.3±2.3
Tumour-LV	-6.6	-5.4	-2.9	-5.0±1.9
Tumour-LNG	-4.5	-4.1	-6.2	-4.9±1.1
Average	-4.8±1.2	-5.2±0.8	-5.2±2.6	

4.4.2.3 OLINDA-D_{SPECT} versus e-D_{True}

To show the effect of comparing true dose with MC electron self-dose versus true dose with full MC cross-dose plus self-dose, OLINDA-D_{SPECT} was compared to e-D_{True} with the percentage differences summarised in Table 4-6 for the three patient phantoms. The inter-phantom and intra-organ accuracy variability of ≤ 2.9±2.0% and ≤ 2.9±2.1%, compared marginally better than those obtained from Table 5 with corresponding values of ≤ 5.6±2.2%, and ≤ 5.2±2.6%. The absolute differences between the average values obtained in Table 5 and Table 6 presented an overall improved accuracy for e-D_{True} (up to 4.7% when considering the tumour next to the liver). These results suggest that the difference in the accuracy obtained by considering only self-dose by electrons was less than 5% across all the phantoms. Table 4-6 showed an overall improvement in the underestimations reported in Table 4-5.

Table 4-6: *The accuracy of the mean absorbed doses computed in OLINDA using the reconstructed SPECT images (LND-D_{SPECT}) versus the mean absorbed doses computed in LundADose assuming self-dose from electrons using the true activity images (e-D_{True}), of the three phantoms for the kidneys, spleen, liver, tumour-LV (tumour adjacent to the liver) and tumour-LNG (tumour between the lungs).*

	OLINDA-D_{SPECT} versus e-D_{True}			
	Accuracy (%)			
Organ	**Phantom 1**	**Phantom 2**	**Phantom 3**	**Average**
Right-kidney	0.4	1.2	0.8	0.8±0.4
Left-kidney	-1.3	-0.1	-2.9	-1.4±1.4
Spleen	-2.0	-1.4	-5.2	-2.9±2.0
Liver	-0.7	-1.2	-3.9	-1.9±1.7
Tumour-LV	2.3	-0.9	-2.2	-0.3±2.3
Tumour-LNG	2.7	-0.3	-3.7	-0.4±3.2
Average	0.2±1.9	-0.5±1.0	-2.9±2.1	

Globally, the higher mean absorbed dose by the spleen was indicative of the increased ^{177}Lu-DOTATATE uptake compared to the other OAR. The kidney-to-tumour mean absorbed dose ratio was, on average 1:11. The absolute differences between the average values obtained amongst the three phantoms for the two tumour locations were, 2.56 mGy/MBq, 3.02 mGy/MBq, 2.45 mGy/MBq and 2.20 mGy/MBq for the MC-D_{True}, LND-D_{SPECT}, OLINDA-D_{SPECT} and e-D_{True}, respectively. Altogether, the better than 10% dose accuracy for all the data (Table 4-6) suggests that the mean dose values obtained with LND-D_{SPECT} and OLINDA-D_{SPECT} approximate the true values. The mean absorbed dose values between the two software programs and the gold standard were comparable.

4.5 Discussion

4.5.1 Time-Integrated Activity

Different fitting models have been used to describe the evolution of activity distribution over time in organs of interest for ^{177}Lu-DOTATATE. These include: mono-exponential (3,7,19,88,104,111), bi-exponential (112) and trapezoidal integration. A mono-exponential or a bi-exponential fit is often used to integrate the TAC for ^{177}Lu-DOTATATE RPT (37). Various fitting functions, available with LundADose, were appropriate to fit the data presented in Figure 4-3, including a mono-exponential, bi-exponential and quadratic exponential. In addition, there is an automatic option available in LundADose to assess the best fitting model. Although not explicitly investigated in this work, both options for automatic fit and mono-exponential fits were explored for the tumour data and resulted in equivalent values for the cumulated activity. A high target to non-target ratio characterised these curves with the highest accumulation of activity in the tumours, followed by the spleen, kidneys, and liver, respectively. The bio-kinetic profile was in agreement with ^{177}Lu-DOTATATE accumulation observed by other authors (95,110). The shape of the kidney curves was in agreement with the shape shown by Sandström et al. (34), who investigated aspects of extrapolations and measurement time-point for kidney dosimetry in 777 patients who underwent ^{177}Lu-DOTATATE RPT.

LundADose included all steps required in the clinical dosimetry chain and was our reference software program in this comparison. Since our objective was to evaluate the dosimetry accuracy focussing on the absorbed dose calculation step, the same SPECT-TIAs computed from LundADose were used to compute absorbed doses in OLINDA. We followed this approach to reduce the software's variations and discrepancies in pre-preliminary steps regarding CFs, reconstruction, registration, segmentation, organs' volume determination, TACs, and the curve fitting to obtain TIA. In this way, we could independently evaluate the accuracy of the dose computation step solely. However, this may be different when considering other clinical software that may incorporate most of the steps. In this case, a method would be needed to assess the methodology's performance applied in each step up until this point. Furthermore, each step's uncertainty and propagation to calculate the absorbed doses would have to be evaluated.

Considering only the OAR, the average cumulated activity concentrations were the highest for the spleen, followed by the kidneys and the liver, as observed by Grimes, (107) and Mora Ramirez et al. (113) who compared the absorbed dose computed by different dosimetry software programs. The largest variation in the TIA was found in the tumours, in agreement with Grimes, (107) who mainly compared dose estimates from OLINDA, the voxel S value technique, and MC simulations for ^{177}Lu, ^{131}I and ^{90}Y. The average percentage difference of 4.6±2.2% (Table 4-3) amongst the phantoms was acceptable. Overall, the comparable results obtained by the TRUE-TIA and SPECT-TIA indicated that the SPECT-TIA was reliable in estimating true absorbed dose values.

4.5.2 Mean Absorbed Dose Estimates

Patient-specific dosimetry offers the potential for improved RPT efficacy, however, it entails significant time and effort. Several authors have reported on the dosimetry of ^{177}Lu-DOTATATE distribution (13,22,23,23,30,34,34,37,38,63,89–91,95,110,112,114–119). Most of these reports were based on patients who have undergone clinical ^{177}Lu-DOTATATE RPT, tailoring the dosimetry to be personalised by using patient-specific bio-kinetic data. However, only a limited amount of studies investigated dosimetry based on phantom studies. A comparison of the estimated absorbed doses for dosimetry from ^{177}Lu-DOTATATE by a number of authors is shown in Table 4-7. It can be noted from Table 4-7 that most of the authors applied the SPECT/CT or the hybrid WB/SPECT imaging method to perform the dosimetry. The number of subjects mainly was based on patients who underwent ^{177}Lu-DOTATATE treatment in the respective clinics and varied between the authors.

In this article, we evaluated the accuracy of patient-specific virtual dosimetry using three voxel-based patient phantoms. The accuracy was assessed by comparing the mean absorbed dose estimates from reconstructed SPECT data (LND-D_{SPECT} and OLINDA-D_{SPECT}) to those assessed from the true activity images (MC-D_{True} and e-D_{True}). Since the study is phantom-based, our reduced subject number seemed reasonably in line with digital phantoms' investigations and comparative studies on dosimetry software programs. Brolin et al. (23) used three pharmacokinetic digital phantoms from the XCAT generation to assess the dosimetry accuracy of ^{177}Lu-DOTATATE. Also, Mora-Ramirez et al. (37) compared commercial dosimetry software programs using two patients during two cycles of ^{177}Lu-DOTATATE RPT. This study would, in fact, be a preliminary investigation for clinical dosimetry, taking into account a larger number of subjects and clinical data that might become available to our institution in the future.

The similarity in the trend observed between the TIA and the mean absorbed doses was in agreement with findings by Mora-Ramirez et al. (37). Most of our mean absorbed dose estimates agreed with those reported by other authors (Table 4-7). For example, in the case of the kidneys, our dose estimates equal to 1.16±0.31 mGy/MBq, 1.21±0.32 mGy/MBq, 1.10±0.31 mGy/MBq and 1.09±0.30 mGy/MBq computed for MC-D_{True}, LND-D_{SPECT}, OLINDA-D_{SPECT} and e-D_{True} respectively, were comparable to those indicated in Table 4-7 (13,112,116). The large range of the kidney mean absorbed dose estimates by Sandström et al. (34), who used 777 patients in their study, indicates the dose range that may be found when considering an extensive range of patients. Kidney dosimetry has been comprehensively researched in the last decade (22,38,90,91,120), and still, there is no final consensus on how to conduct dosimetry for the kidneys. The highlight from the different methods was that planar images overestimate the quantified activity due to organ overlap, which artificially increases the kidney absorbed dose. This may be overcome by using SPECT images for activity quantification adjustment in the hybrid WB/SPECT method. Ex-vivo radiography studies of the kidneys have confirmed that the limited spatial resolution of SPECT/CT or PET/CT data does not support the segmentation of the kidney sub-regions (121). For this reason, CT data has been well adopted as a standard method used to segment the kidney as a single structure.

Our spleen doses of equal to 1.49±0.38 mGy/MBq, 1.55±0.40 mGy/MBq, 1.40±0.35 mGy/MBq, and 1.44±0.38 mGy/MBq obtained with MC-D_{True}, LND-D_{SPECT}, OLINDA-D_{SPECT} and e-D_{True}, respectively, were comparable to previous reports listed in Table 4-7. The spleen doses were often higher than those by the other organs (Figure 4-6), which corresponded to their higher increased uptake indicated in the TIA. In the case of the liver, our corresponding computations of 0.54±0.14 mGy/MBq, 0.56±0.14 mGy/MBq, 0.52±0.13 mGy/MBq, and 0.53±0.13 mGy/MBq were similar to those published in literature (37,117). The tumour doses of 13.55±1.31 mGy/MBq, 14.29±1.37 mGy/MBq, 12.89±1.36 mGy/MBq, and 12.65±1.61 mGy/MBq, obtained with MC-D_{True}, LND-D_{SPECT}, OLINDA-D_{SPECT} and e-$D_{True,}$ agreed with those listed in the existing publications (Table 4-7). The reported wide tumour dose range is not surprising as clinical tumour activity uptake, and as a result tumour dose, is related to several factors: necrosis, hypoxia, receptors density, viability, and binding affinity (94). Our tumour uptake of eleven-fold that of the dose-limiting kidneys implied the potential of delivering ideal high therapeutic doses to the tumours with less doses to the critical organs.

We considered relatively large organs i.e., the kidneys, spleen, liver, and tumours of volume 33.5 ml, to decrease any residual PVEs due to spill out. The tumour volume we used was in the same range as Grimes (107), who used three tumours ranging in size from 23 ml to 95 ml to compare internal dosimetry estimates using OLINDA, a voxel S value technique, and MC simulations.

Table 4-7: *A comparison of published mean absorbed doses for dosimetric analysis of* ^{177}*Lu-DOTATATE distribution.*

Organ	Image method	Dosimetry method	Number of subjects	Mean Dose range (mGy/MBq)	Reference
Kidneys					
	SPECT/CT	MC transport	21	0.90±0.21	(13)
	SPECT/CT	Olinda/EXM 1.0	47	0.55 – 1.15	(112)
	SPECT/CT	MIRD-dosimetry	20	0.34±1.16	(116)
	Hybrid-WB/SPECT	Olinda/EXM 1.0 and MC transport	3 – XCAT phantom population	2.98 – 4.34	(23)
	SPECT/CT	Olinda/EXM 1.0	777	0.5 – 13.1	(34)
Liver					
	SPECT/CT	Olinda/EXM 1.0	12	0.54±0.58	(95)
	SPECT/CT	DTK, HDM, Stratos, PDOSE, MIM	2	1.28±1.25	(37)
	Hybrid-WB/SPECT	Olinda/EXM 1.0 and MC transport	3 – XCAT phantom population	1.66 – 1.69	(23)
Spleen					
	SPECT/CT	DTK, HDM, Stratos, PDOSE, MIM	2	0.7±0.92	(37)
	SPECT/CT	Olinda/EXM 1.0	61	1.17±0.14	(86)
	Hybrid-WB/SPECT	MIRD-scheme	41	1.5 – 10.6	(118)
Tumour					
	SPECT/CT	Full MC-transport	5	5.20 – 42.60	(30)
	SPECT/CT	LED from SPECT	7	0.10 – 20.00	(13)
	Hybrid-WB/SPECT	MC transport	180	2 – 77	(122)

MC, Monre Carlo*; DTK*, Dosimetry Toolkit® from GE-Olinda/EXM 1.0; *HDM*, Hybrid dosimetry module™ from HERMES (v1)-Olinda/EXM 2.0; *Stratos*, from Phillips-convolution; *PDOSE*, PLANET® Onco Dose from DOSIsoft (v 3.1.1)-local energy deposition convolution

We followed a modular approach to have the input of the reconstructed SPECT data up until the fitting of the TIA curves to be the same for both LundADose and OLINDA. Our dosimetry accuracy was assessed by comparing these results with those computed from the true activity images. Overall, the two software programs produced dosimetry accuracy results that were comparable (Table 4-4 – 4-6) between the MC-D_{True} and LND-D_{SPECT} ($\leq$ 4.4±2.2%) and MC-D_{True} and OLINDA-D_{SPECT} ($\leq$ 5.6±2.2%) for the three phantoms. The comparable dose estimates between LND-D_{SPECT} and OLINDA-D_{SPECT} suggest that the preliminary steps' variability and compounding uncertainty between the two software programs might have been reduced. Mora-Ramirez et al. (37) presented a comparison of dosimetry results from five commercial software programs using the same TIA data and found that the dose computation step did not have a major impact on the mean absorbed doses at an organs tissue level (123). Our findings might have to be revised when considering voxel-based dosimetry and dose-volume histograms, which offer better discrimination for the radiation transport. OLINDA assumes a uniform organ activity distribution i.e. it does not account for non-homogeneous activity uptake, and therefore our reporting of organ-level dosimetry does not reflect the impact of this non-uniform dose distribution.

The underestimation of the absorbed doses by OLINDA compared to the true doses may be attributed to the differences in the geometry between the voxel-based phantoms used in this study and the geometric reference phantoms used in OLINDA. Although the differences in the organs' masses between our phantoms and models by OLINDA are accounted for by normalising the OLINDA organs masses to ours, this does not account for the geometric differences in shape. In comparing dose calculations between OLINDA and patient-specific MC dose calculations, Grimes (2013) found that even with considerable anatomy differences between patients, mean dose estimates reported on an organ level were in good agreement between OLINDA and MC doses. Bearing in mind that the VOI delineation was in accordance with the CT data, the overestimations by LND-D_{SPECT} compared to MC-D_{True} may be attributed to the PVE. Even though PVC was applied to the quantified activity by numerical compensation using RCs in the LND-D_{SPECT} computation. This did not account for the spill-out activity outside the VOI border delineation by the CT images. This spill-out activity from the reconstructed SPECT images (LND-D_{True}) can result in dose contribution to tissue inside the VOI and offers a possible explanation for the higher dose estimates (LND-D_{True}) compared to the true doses (MC-D_{True}).

Cross-organ dose contributions are higher for more penetrating gamma rays emitted at higher intensities, such as those for ^{131}I with an energy of 364.5 keV and a yield of 83.0%, compared to the ^{177}Lu 208.4 keV gamma-ray with a yield of 10.4%. ^{177}Lu thus exhibits a lower probability of depositing energy in target organs further away from the source organ. Furthermore, due to the limited electron maximum energy of 177 keV (11.6%), 385 (9.1%), 498 keV (79.3%), the pathway for the ^{177}Lu energy depositing electrons is short in soft tissue, and thus the mean absorbed dose would be primarily due to self-dose. On average, the accuracy calculated using e-D_{True} instead of MC-D_{True} resulted in a ~ 5% improvement.

Our findings were on par with those of Santoro et al. (115), who compared mean absorbed doses obtained with the PDOSE dosimetry toolkit with mean absorbed doses calculated by OLINDA for OAR in 21 patients who underwent ^{177}Lu-DOTATATE RPT. The authors found a 5% relative difference between the two software programs for all OAR except for the kidneys showing a 6.5% difference. The authors attributed the different kidney estimates between PDOSE and OLINDA to the fact that the right and left kidneys were considered separately for PDOSE. In contrast, OLINDA considers the kidneys as a single organ, which affects the bio-kinetic data. Our study showed a dosimetry accuracy smaller than and equal to 6.6% using the LundADose software (Table 4-4: LND-D_{SPECT} with the highest difference obtained in the spleen of phantom 2) and is thus comparable to the results reported by Santoro et al. (117). In the current study, LundADose considered the kidneys separately thus, the reason mentioned above for the higher accuracy found for the kidneys may be extended to our study with the largest absorbed dose underestimation of 8.1% (Table 4-5) seen for the left kidney of phantom 3 using OLINDA-D_{SPECT}. Grimes, (107) compared dose estimates by OLINDA with MC techniques using six patients and concluded that although the anatomy may vary between the six patients and the models used in OLINDA, the mean organ dose estimates between OLINDA and MC were in good agreement (-6.2%). The overall accuracy between the two software programs of less than 10% deemed acceptable by other authors conducting similar investigations (107,123).

4.6 Conclusion

We presented a comparative study on the accuracy of dosimetry results generated by two dosimetry software programs: LundADose and OLINDA. LundADose was accessible to our group through a research collaboration, while OLINDA was available in our institution. The dosimetry results were computed using the same TIA data from reconstructed SPECT images of three voxel-based phantoms, which served as input to absorbed dose calculation procedures in LundADose and OLINDA. The accuracy of mean absorbed dose estimates from the kidneys, spleen, liver, and tumours for ^{177}Lu-DOTATATE distribution was assessed by comparing the mean absorbed doses from the two software programs to the true doses. The accuracy of the dose estimates showed overestimations by LundADose ($\leq 6.6\%$) and underestimations by OLINDA ($\leq 8.1\%$) compared to the true doses. Our accuracy results of better than 10% were satisfactory, and our mean absorbed doses to the OAR and tumours for both software programs were concordant with literature findings. This work suggests that standardising the crucial preliminary steps in the dosimetry chain, from the gamma camera calibration process up to and including the determination of the TIA data, offers the potential to obtain comparable dose estimates between LundADose, and OLINDA for ^{177}Lu voxel-based patient-specific phantoms.

This work was based on voxel-based phantoms and not actual patients, however, the study is useful for further investigations and offers the potential for optimising clinical dosimetry for ^{177}Lu RPT. Indeed, several favourable aspects in our study may contribute to the satisfactory accuracy, and the favourable comparison obtained between LundADose and OLINDA. These approximations and limitations would need to be addressed in the application to patient data, which were not available at the time of the study. Since the study is based on virtual dosimetry using MC and voxel-based phantoms, quantities such as the true activity and the segmented volumes were known. These quantities would be unknown in real patients. The number of patient phantoms was relatively small and sufficient for a phantom study, however, the number would need to be increased when applied to patient data to reduce the probability of missing any small effect on the results. We opted to use the same TIA estimates computed in LundADose, which comprised all the clinical dosimetry chain steps. However, this may not always be feasible, especially when conducting multi-centre trials with different methods for the different steps. In this case, an uncertainty analysis by each step in the chain would have to be determined. The study may also be extended to other isotopes used for RPT, such as ^{131}I and ^{90}Y, and possibly, to voxel-based dosimetry and DVH, which are still under development and have not been clinically validated. As the use of dosimetry in RPT expands, attention to the compounding effect by all the steps involved in the absorbed dose estimate computations should become relevant. Standardising these steps should be attempted, and the approach to personalised clinical dosimetry should be as simple as possible yet as personalised as necessary. The growing development and availability of user-friendly software programs encompassing all steps in the clinical dosimetry workflow are promising to this idea.

4.7 References

1. Wahl RL, Ahuja S, Clarke B. Current Landscape of Radiopharmaceutical Therapies: SNMMI Therapy Task Force Survey. J Nucl Med Off Publ Soc Nucl Med. 2021 May 10;62(5):11N-16N.

2. Dash A, Pillai MRA, Knapp FF. Production of ^{177}Lu for Targeted Radionuclide Therapy: Available Options. Nucl Med Mol Imaging. 2015 Jun;49(2):85–107. https://doi.org/10.1007/s13139-014-0315-z

3. Bodei L, Cremonesi M, Ferrari M, Pacifici M, Grana CM, Bartolomei M, et al. Long-term evaluation of renal toxicity after peptide receptor radionuclide therapy with ^{90}Y-DOTATOC and ^{177}Lu-DOTATATE: the role of associated risk factors. Eur J Nucl Med Mol Imaging. 2008 Oct;35(10):1847–56. https://doi.org/10.1007/s00259-008-0778-1

4. Kendi AT, Halfdanarson TR, Packard A, Dundar A, Subramaniam RM. Therapy With ^{177}Lu-DOTATATE: Clinical Implementation and Impact on Care of Patients With Neuroendocrine Tumors. Am J Roentgenol. 2019 Aug 1;213(2):309–17. https://doi: 10.2214/AJR.19.21123

5. Kwekkeboom DJ, de Herder WW, Kam BL, van Eijck CH, van Essen M, Kooij PP, et al. Treatment with the radiolabeled somatostatin analog [^{177} Lu-DOTA 0,Tyr3]octreotate: toxicity, efficacy, and survival. J Clin Oncol Off J Am Soc Clin Oncol. 2008 May 1;26(13):2124–30. https://doi.org/10.1200/JCO.2007.15.2553

6. Smith-Palmer J, Leeuwenkamp OR, Virk J, Reed N. Lutetium oxodotreotide (^{177}Lu-Dotatate) for the treatment of unresectable or metastatic progressive gastroenteropancreatic neuroendocrine tumors: a cost-effectiveness analysis for Scotland. BMC Cancer. 2021 Jan 5;21(1):10. https://doi:10.1186/s12885-020-07710-7

7. Bodei L, Cremonesi M, Grana CM, Fazio N, Iodice S, Baio SM, et al. Peptide receptor radionuclide therapy with ^{177}Lu-DOTATATE: the IEO phase I-II study. Eur J Nucl Med Mol Imaging. 2011 Dec;38(12):2125–35. https://doi.org/10.1007/s00259-011-1902-1

8. Kunikowska J, Królicki L, Hubalewska-Dydejczyk A, Mikołajczak R, Sowa-Staszczak A, Pawlak D. Clinical results of radionuclide therapy of neuroendocrine tumours with ^{90}Y-DOTATATE and tandem ^{90}Y/^{177}Lu-DOTATATE: which is a better therapy option? Eur J Nucl Med Mol Imaging. 2011 Oct;38(10):1788–97. https://doi: 10.1007/s00259-011-1833-x

9. Strosberg J, El-Haddad G, Wolin E, Hendifar A, Yao J, Chasen B, et al. Phase 3 Trial of ^{177}Lu-Dotatate for Midgut Neuroendocrine Tumors. N Engl J Med. 2017 12;376(2):125–35. https://doi.org/10.1056/NEJMoa1607427

10. Villard L, Romer A, Marincek N, Brunner P, Koller MT, Schindler C, et al. Cohort study of somatostatin-based radiopeptide therapy with [^{90}Y-DOTA]-TOC versus [^{90}Y-DOTA]-

TOC plus [^{177}Lu-DOTA]-TOC in neuroendocrine cancers. J Clin Oncol Off J Am Soc Clin Oncol. 2012 Apr 1;30(10):1100–6. https://doi:10.1200/JCO.2011.37.2151

11. Haug AR. PRRT of neuroendocrine tumors: individualized dosimetry or fixed dose scheme? EJNMMI Res. 2020 Apr 15;10:35. https://doi:10.1186/s13550-020-00623-3

12. Eberlein U, Cremonesi M, Lassmann M. Individualized Dosimetry for Theranostics: Necessary, Nice to Have, or Counterproductive? J Nucl Med. 2017 Sep 1;58(Supplement 2):97S-103S.

13. Garkavij M, Nickel M, Sjögreen-Gleisner K, Ljungberg M, Ohlsson T, Wingårdh K, et al. ^{177}Lu-[DOTA0,Tyr3] octreotate therapy in patients with disseminated neuroendocrine tumors: Analysis of dosimetry with impact on future therapeutic strategy. Cancer. 2010 Feb 15;116(4 Suppl):1084–92. https://doi.org/10.1002/cncr.24796

14. Valkema R, Pauwels SA, Kvols LK, Kwekkeboom DJ, Jamar F, de Jong M, et al. Long-term follow-up of renal function after peptide receptor radiation therapy with ^{90}Y-DOTA(0),Tyr(3)-octreotide and ^{177}Lu-DOTA(0), Tyr(3)-octreotate. J Nucl Med Off Publ Soc Nucl Med. 2005 Jan;46 Suppl 1:83S-91S.

15. Ilan E, Sandström M, Wassberg C, Sundin A, Garske-Román U, Eriksson B, et al. Dose response of pancreatic neuroendocrine tumors treated with peptide receptor radionuclide therapy using ^{177}Lu-DOTATATE. J Nucl Med Off Publ Soc Nucl Med. 2015 Feb;56(2):177–82.

16. Bergsma H, Konijnenberg MW, Kam BLR, Teunissen JJM, Kooij PP, de Herder WW, et al. Subacute haematotoxicity after PRRT with ^{177}Lu-DOTA-octreotate: prognostic factors, incidence and course. Eur J Nucl Med Mol Imaging. 2016 Mar;43(3):453–63. https://doi.org/10.1007/s00259-015-3193-4

17. Garske-Román U, Sandström M, Fröss Baron K, Lundin L, Hellman P, Welin S, et al. Prospective observational study of ^{177}Lu-DOTA-octreotate therapy in 200 patients with advanced metastasized neuroendocrine tumours (NETs): feasibility and impact of a dosimetry-guided study protocol on outcome and toxicity. Eur J Nucl Med Mol Imaging. 2018;45(6):970–88. https://doi:10.1007/s00259-018-3945-z

18. Gosewisch A, Delker A, Tattenberg S, Ilhan H, Todica A, Brosch J, et al. Patient-specific image-based bone marrow dosimetry in Lu-177-[DOTA0,Tyr3]-Octreotate and Lu-177-DKFZ-PSMA-617 therapy: investigation of a new hybrid image approach. EJNMMI Res. 2018 Aug 3;8(1):76. https://doi:10.1186/s13550-018-0427-z

19. Sundlöv A, Sjögreen-Gleisner K, Svensson J, Ljungberg M, Olsson T, Bernhardt P, et al. Individualised ^{177}Lu-DOTATATE treatment of neuroendocrine tumours based on kidney dosimetry. Eur J Nucl Med Mol Imaging. 2017 Aug;44(9):1480–9. https://doi:10.1007/s00259-017-3678-4

20. Beauregard J-M, Hofman MS, Pereira JM, Eu P, Hicks RJ. Quantitative ^{177}Lu SPECT (QSPECT) imaging using a commercially available SPECT/CT system. Cancer Imaging

Off Publ Int Cancer Imaging Soc. 2011 Jun 15;11:56–66. https://doi:10.1102/1470-7330.2011.0012

21. Sanders JC, Kuwert T, Hornegger J, Ritt P. Quantitative SPECT/CT Imaging of ^{177}Lu with In Vivo Validation in Patients Undergoing Peptide Receptor Radionuclide Therapy. Mol Imaging Biol MIB Off Publ Acad Mol Imaging. 2015 Aug;17(4):585–93. doi: https://doi:10.1007/s11307-014-0806-4

22. Bailey DL, Hennessy TM, Willowson KP, Henry EC, Chan DLH, Aslani A, et al. In vivo quantification of ^{177}Lu with planar whole-body and SPECT/CT gamma camera imaging. EJNMMI Phys. 2015 Sep;2(1):20. https://doi.org/10.1186/s40658-015-0123-2

23. Brolin G, Gustafsson J, Ljungberg M, Gleisner KS. Pharmacokinetic digital phantoms for accuracy assessment of image-based dosimetry in^{177}Lu-DOTATATE peptide receptor radionuclide therapy. Phys Med Biol. 2015 Jul;60(15):6131–49. https://doi.org/10.1088/0031-9155/60/15/6131

24. Guerriero F, Ferrari ME, Botta F, Fioroni F, Grassi E, Versari A, et al. Kidney Dosimetry in ^{177}Lu and ^{90}Y Peptide Receptor Radionuclide Therapy: Influence of Image Timing, Time-Activity Integration Method, and Risk Factors. BioMed Res Int. 2013 Jun; 935351. https://doi.org/10.1155/2013/935351

25. Ljungberg M, Sjögreen Gleisner K. Hybrid Imaging for Patient-Specific Dosimetry in Radionuclide Therapy. Diagnostics. 2015 Jul 10;5(3):296–317. https://doi.org/10.3390/diagnostics5030296

26. Bin Said MA, Bin Abdul Razak HR, Musarudin M. The comparison of serial SPECT-CT imaging to estimate absorbed dose to the organ at risk from peptide receptor radionuclide therapy dosimetry. Iran J Nucl Med. 2021 Jan 1;29(1):2–7.

27. Chicheportiche A, Ben-Haim S, Grozinsky-Glasberg S, Oleinikov K, Meirovitz A, Gross DJ, et al. Dosimetry after peptide receptor radionuclide therapy: impact of reduced number of post-treatment studies on absorbed dose calculation and on patient management. EJNMMI Phys. 2020 Jan 23;7(1):5. https://doi:10.1186/s40658-020-0273-8

28. Chicheportiche A, Ben-Haim S, Godefroy J. SPECT/CT studies for dosimetry after PRRT: impact of reduced number of studies on organ dose calculation and patient management. J Nucl Med. 2019 May 1;60(supplement 1):264–264.

29. Couch P, Webb C, Botkin C, Frye S, Muzaffar R, Osman M. Added Value of SPECT/CT in Post Lu-177 Dotatate Treatment for Neuroendocrine Tumors. J Nucl Med. 2019 May 1;60(supplement 1):2044–2044.

30. Dewaraja Y, Wilderman S, Niedbala J, Frey K, Wong KK. Multi SPECT/CT-based patient specific lesion and kidney dosimetry for verification of simpler approaches for treatment planning in Lu-177 DOTATATE PRRT. J Nucl Med. 2019 May 1;60(supplement 1):1626–1626.

31. Dewaraja YK, Wilderman SJ, Koral KF, Kaminski MS, Avram AM. Use of Integrated SPECT/CT Imaging for Tumor Dosimetry in I-131 Radioimmunotherapy: A Pilot Patient Study. Cancer Biother Radiopharm. 2009 Aug;24(4):417–26. https://doi:10.1089/cbr.2008.0568

32. Gregory RA, Murray I, Gear J, Leek F, Chittenden S, Fenwick A, et al. Standardised quantitative radioiodine SPECT/CT Imaging for multicentre dosimetry trials in molecular radiotherapy. Phys Med Biol. 2019 Dec;64(24):245013. https://doi:10.1088/1361-6560/ab5b6c

33. Potrebko PS, Shridhar R, Biagioli MC, Sensakovic WF, Andl G, Poleszczuk J, et al. SPECT/CT image-based dosimetry for Yttrium-90 radionuclide therapy: Application to treatment response. J Appl Clin Med Phys. 2018;19(5):435–43. https://doi:10.1002/acm2.12400

34. Sandström M, Freedman N, Fröss-Baron K, Kahn T, Sundin A. Kidney dosimetry in 777 patients during ^{177}Lu-DOTATATE therapy: aspects on extrapolations and measurement time points. EJNMMI Phys. 2020 Dec 9;7(1):73. https://doi.org/10.1186/s40658-020-00339-2

35. Sandström M, Garske U, Granberg D, Sundin A, Lundqvist H. Individualized dosimetry in patients undergoing therapy with ^{177}Lu-DOTA-D-Phe (1)-Tyr (3)-octreotate. Eur J Nucl Med Mol Imaging. 2010 Feb;37(2):212–25. https://doi.org/10.1007/s00259-009-1216-8

36. Bardiès M, Gear JI. Scientific Developments in Imaging and Dosimetry for Molecular Radiotherapy. Clin Oncol R Coll Radiol G B. 2021 Feb;33(2):117–24. https://doi.org/10.1016/j.clon.2020.11.005

37. Mora-Ramirez E, Santoro L, Cassol E, Ocampo-Ramos JC, Clayton N, Kayal G, et al. Comparison of commercial dosimetric software platforms in patients treated with ^{177}Lu-DOTATATE for peptide receptor radionuclide therapy. Med Phys. 2020 Sep;47(9):4602–15.

38. Larsson M, Bernhardt P, Svensson JB, Wängberg B, Ahlman H, Forssell-Aronsson E. Estimation of absorbed dose to the kidneys in patients after treatment with ^{177}Lu-octreotate: comparison between methods based on planar scintigraphy. EJNMMI Res. 2012 Sep 24;2(1):49. https://doi:10.1186/2191-219X-2-49

39. Zanzonico PB. Internal radionuclide radiation dosimetry: a review of basic concepts and recent developments. J Nucl Med Off Publ Soc Nucl Med. 2000 Feb;41(2):297–308.

40. Pauwels S, Barone R, Walrand S, Borson-Chazot F, Valkema R, Kvols LK, et al. Practical dosimetry of peptide receptor radionuclide therapy with ^{90}Y-labeled somatostatin analogs. J Nucl Med Off Publ Soc Nucl Med. 2005 Jan;46 Suppl 1:92S-8S.

41. Heikkonen J, Mäenpää H, Hippeläinen E, Reijonen V, Tenhunen M. Effect of calculation method on kidney dosimetry in ^{177}Lu-octreotate treatment. Acta Oncol. 2016 Oct 2;55(9–10):1069–76. https://doi:10.1080/0284186X.2016.1182642

42. Bolch WE, Eckerman KF, Sgouros G, Thomas SR. MIRD pamphlet No. 21: a generalized schema for radiopharmaceutical dosimetry--standardization of nomenclature. J Nucl Med Off Publ Soc Nucl Med. 2009 Mar;50(3):477–84.

43. Loevinger R, Budinger TF, Watson EE. MIRD Primer for Absorbed Dose Calculations. Revised, Subsequent edition. New York, NY: Society of Nuclear Medicine; 1991.

44. Snyder WS, Ford MR, Warner GG, Watson SB. MIRD Pamphlet no 11: S, Absorbed Dose per Unit Cumulated Activity for Selected Radionuclides and Organs. 1975.

45. Ramonaheng K, van Staden JA, du Raan H. The effect of calibration factors and recovery coefficients on ^{177}Lu SPECT activity quantification accuracy: a Monte Carlo study. EJNMMI Phys. 2021 Mar 18;8(1):27. https://doi: 10.1186/s40658-021-00365-8

46. Glatting G, Kletting P, Reske SN, Hohl K, Ring C. Choosing the optimal fit function: comparison of the Akaike information criterion and the F-test. Med Phys. 2007 Nov;34(11):4285–92. https://doi.org/10.1118/1.2794176

47. Kletting P, Schimmel S, Hänscheid H, Luster M, Fernández M, Nosske D, et al. The NUKDOS software for treatment planning in molecular radiotherapy. Z Med Phys. 2015 Sep;25(3):264–74. https://doi.org/10.1016/j.zemedi.2015.01.001

48. Kletting P, Kull T, Reske SN, Glatting G. Comparing time activity curves using the Akaike information criterion. Phys Med Biol. 2009 Nov 7;54(21):N501-507. https://doi: 10.1088/0031-9155/54/21/N01

49. Stabin M, Farmer A. OLINDA/EXM 2.0: The new generation dosimetry modeling code. J Nucl Med. 2012 May 1;53(supplement 1):585–585.

50. Stabin MG. MIRDOSE: personal computer software for internal dose assessment in nuclear medicine. J Nucl Med Off Publ Soc Nucl Med. 1996 Mar;37(3):538–46.

51. Stabin MG, Sparks RB, Crowe E. OLINDA/EXM: the second-generation personal computer software for internal dose assessment in nuclear medicine. J Nucl Med Off Publ Soc Nucl Med. 2005 Jun;46(6):1023–7.

52. Pasciak AS, Bourgeois AC, Bradley YC. A Comparison of Techniques for ^{90}Y PET/CT Image-Based Dosimetry Following Radioembolization with Resin Microspheres. Front Oncol. 2014 May 22;4:121. https://doi:10.3389/fonc.2014.00121

53. Traino AC, Piccinno M, Avigo C. Dosimetry of non-uniform activity distribution: possibility to use the local energy deposition approach at the voxel level in radionuclide therapy. Biomed Phys Eng Express. 2016 Nov;2(6):065001.

54. Dieudonné A, Hobbs RF, Lebtahi R, Maurel F, Baechler S, Wahl RL, et al. Study of the impact of tissue density heterogeneities on 3-dimensional abdominal dosimetry: comparison between dose kernel convolution and direct Monte Carlo methods. J Nucl Med Off Publ Soc Nucl Med. 2013 Feb;54(2):236–43.

55. Dieudonné A, Hobbs RF, Bolch WE, Sgouros G, Gardin I. Fine-resolution voxel S values for constructing absorbed dose distributions at variable voxel size. J Nucl Med Off Publ Soc Nucl Med. 2010 Oct;51(10):1600–7.

56. Agostinelli S, Allison J, Amako K, Apostolakis J, Araujo H, Arce P, et al. Geant4—a simulation toolkit. Nucl Instrum Methods Phys Res Sect Accel Spectrometers Detect Assoc Equip. 2003 Jul 1;506(3):250–303.

57. Kawrakow I, Mainegra-Hing E, Tessier F, et al. The EGSnrc Code System: Monte Carlo Simulation of Electron and Photon Transport. National Research Council Canada. Ottawa, ON, Canada 2016.

58. Larsson E, Ljungberg M, Strand S-E, Jönsson B-A. Monte Carlo calculations of absorbed doses in tumours using a modified MOBY mouse phantom for pre-clinical dosimetry studies. Acta Oncol Stockh Swed. 2011 Aug;50(6):973–80. https://doi.org/10.3109/0284186X.2011.582517

59. Ljungberg M, Sjögreen Gleisner K. Personalized Dosimetry for Radionuclide Therapy Using Molecular Imaging Tools. Biomedicines. 2016 Nov 15;4(4):25. https://doi.org/10.3390/biomedicines4040025

60. Waters L, Mckinney G, Durkee J, Fensin M, Hendricks J, James M, et al. The MCNPX Monte Carlo radiation transport code. AIP Conf Proc. 2007 Mar 19;896:81–90. https://doi.org/10.1063/1.2720459

61. Huizing DMV, de Wit-van der Veen BJ, Verheij M, Stokkel MPM. Dosimetry methods and clinical applications in peptide receptor radionuclide therapy for neuroendocrine tumours: a literature review. EJNMMI Res. 2018 Aug 29;8:89. https://doi.org/10.1186/s13550-018-0443-z

62. Hippeläinen E, Tenhunen M, Sohlberg A. Fast voxel-level dosimetry for ^{177}Lu labelled peptide treatments. Phys Med Biol. 2015 Sep 7;60(17):6685–700. https://doi.org/10.1088/0031-9155/60/17/6685

63. Ljungberg M, Sjögreen-Gleisner K. The accuracy of absorbed dose estimates in tumours determined by quantitative SPECT: a Monte Carlo study. Acta Oncol Stockh Swed. 2011 Aug;50(6):981–9. https://doi.org/10.3109/0284186X.2011.584559

64. Bolch WE, Bouchet LG, Robertson JS, Wessels BW, Siegel JA, Howell RW, et al. MIRD pamphlet No. 17: the dosimetry of nonuniform activity distributions--radionuclide S values at the voxel level. Medical Internal Radiation Dose Committee. J Nucl Med Off Publ Soc Nucl Med. 1999 Jan;40(1):11S-36S.

65. Loudos G, Tsougos I, Boukis S, Karakatsanis N, Georgoulias P, Theodorou K, et al. A radionuclide dosimetry toolkit based on material-specific Monte Carlo dose kernels. Nucl Med Commun. 2009 Jul;30(7):504–12. https://doi:10.1097/MNM.0b013e3283299a11

66. Lanconelli N, Pacilio M, Lo Meo S, Botta F, Di Dia A, Aroche AT, et al. A free database of radionuclide voxel S values for the dosimetry of nonuniform activity distributions. Phys Med Biol. 2012 Jan 21;57(2):517–33. https://doi:10.1088/0031-9155/57/2/517

67. Denis-Bacelar A, Chittenden S, Divoli A, Gear J, Flux G. qDose, a 3D Treatment Planning System for Molecular Radiotherapy. In: EANM conference. Conference record, Milan, Italy; 2012:39(2)S351.

68. Kost SD, Dewaraja YK, Abramson RG, Stabin MG. VIDA: A Voxel-Based Dosimetry Method for Targeted Radionuclide Therapy Using Geant4. Cancer Biother Radiopharm. 2015 Feb 1;30(1):16–26. https://doi:10.1089/cbr.2014.1713

69. Akhavanallaf A, Shiri I, Arabi H, Zaidi H. Whole-body voxel-based internal dosimetry using deep learning. Eur J Nucl Med Mol Imaging. 2021 Mar 1;48(3):670–82. https://doi:10.1007/s00259-020-05013-4

70. Chiesa C, Bardiès M, Zaidi H. Voxel-based dosimetry is superior to mean absorbed dose approach for establishing dose-effect relationship in targeted radionuclide therapy. Med Phys. 2019;46(12):5403–6. https://doi:10.1002/mp.13851

71. Tran-Gia J, Salas-Ramirez M, Lassmann M. What You See Is Not What You Get: On the Accuracy of Voxel-Based Dosimetry in Molecular Radiotherapy. J Nucl Med Off Publ Soc Nucl Med. 2020 Aug;61(8):1178–86. https://doi:10.2967/jnumed.119.231480

72. Ljungberg M, Sjögreen K, Liu X, Frey E, Dewaraja Y, Strand S-E. A 3-Dimensional Absorbed Dose Calculation Method Based on Quantitative SPECT for Radionuclide Therapy: Evaluation for ^{131}I Using Monte Carlo Simulation. J Nucl Med Off Publ Soc Nucl Med. 2002 Aug;43(8):1101–9.

73. Sjögreen K, Ljungberg M, Wingårdh K, Minarik D, Strand S-E. The LundADose method for planar image activity quantification and absorbed-dose assessment in radionuclide therapy. Cancer Biother Radiopharm. 2005 Feb;20(1):92–7. https://doi:10.1089/cbr.2005.20.92

74. Nelson WR, Hirayama H, Rogers DWO. EGS4 code system. Stanford Linear Accelerator Center, Menlo Park, CA (USA). 1985 Dec; Report No.: SLAC-265.

75. Andreo P. Monte Carlo techniques in medical radiation physics. Phys Med Biol. 1991 Jul;36(7):861–920. https://doi:10.1088/0031-9155/36/7/001

76. Chiesa C, Mira M, Maccauro M, Spreafico C, Romito R, Morosi C, et al. Radioembolization of hepatocarcinoma with ^{90}Y glass microspheres: development of an individualized treatment planning strategy based on dosimetry and radiobiology. Eur J Nucl Med Mol Imaging. 2015 Oct;42(11):1718–38. https://doi:10.1007/s00259-015-3068-8

77. Knoll P, Kotalova D, Köchle G, Kuzelka I, Minear G, Mirzaei S, et al. Comparison of advanced iterative reconstruction methods for SPECT/CT. Z Med Phys. 2012 Feb;22(1):58–69. https://doi:10.1016/j.zemedi.2011.04.007

78. Budinger TF. Physical attributes of single-photon tomography. J Nucl Med Off Publ Soc Nucl Med. 1980 Jun;21(6):579–92.

79. RADAR: dose information on the desktop. J Nucl Med Off Publ Soc Nucl Med. 2002 May;43(5):28N,31N.

80. Stabin MG, Siegel JA. RADAR Dose Estimate Report: A Compendium of Radiopharmaceutical Dose Estimates Based on OLINDA/EXM Version 2.0. J Nucl Med. 2018 Jan 1;59(1):154–60. https://doi:10.2967/jnumed.117.196261

81. Stabin MG, Siegel JA. Physical models and dose factors for use in internal dose assessment. Health Phys. 2003 Sep;85(3):294–310. https://doi:10.1097/00004032-200309000-00006

82. Cristy M, Eckerman KF. Specific absorbed fractions of energy at various ages from internal photon sources. Oak Ridge National Lab. 1987. Report No.: ORNL/TM--8381/V7.

83. Stabin M, Brill A, Segars W, Emmons M, Gesner J, Milam R. Realistic phantom series for OLINDA/EXM 2.0. J Nucl Med. 2006 May 1;47(suppl 1):156P-156P.

84. Stabin M, Emmons MA, Segars WP, Fernald M, Brill AB. ICRP-89 based adult and pediatric phantom series. J Nucl Med. 2008 May 1;49(supplement 1):14P-14P.

85. Valentin J. Basic anatomical and physiological data for use in radiological protection: reference values: ICRP Publication 89. Ann ICRP. 2002 Sep 1;32(3):1–277.

86. Gupta S, Singla S, Bal C. Patient specific dosimetry in peptide receptor radionuclide therapy of neuroendocrine tumors with ^{177}Lu-DOTATATE. J Nucl Med. 2013 May 1;54(supplement 2):583–583.

87. Kupitz D, Wetz C, Wissel H, Wedel F, Apostolova I, Wallbaum T, et al. Software-assisted dosimetry in peptide receptor radionuclide therapy with ^{177}Lutetium-DOTATATE for various imaging scenarios. PloS One. 2017;12(11):e0187570. https://doi.org/10.1371/journal.pone.0187570

88. Sandström M, Garske-Román U, Granberg D, Johansson S, Widström C, Eriksson B, et al. Individualized dosimetry of kidney and bone marrow in patients undergoing ^{177}Lu-DOTA-octreotate treatment. J Nucl Med Off Publ Soc Nucl Med. 2013 Jan;54(1):33–41. https://doi:10.2967/jnumed.112.107524

89. Svensson J, Berg G, Wängberg B, Larsson M, Forssell-Aronsson E, Bernhardt P. Renal function affects absorbed dose to the kidneys and haematological toxicity during ^{177}Lu-

DOTATATE treatment. Eur J Nucl Med Mol Imaging. 2015;42(6):947–55. https://doi: 10.1007/s00259-015-3001-1

90. Willowson K, Ryu H, Jackson P, Singh A, Eslick E, Bailey D. A Comparison of 2D and 3D Kidney Absorbed Dose Measures in Patients Receiving ^{177}Lu-DOTATATE. Asia Ocean J Nucl Med Biol. 2018;6(2):113-119. https://doi:10.22038/aojnmb.2018.26105.1182

91. Willowson KP, Eslick E, Ryu H, Poon A, Bernard EJ, Bailey DL. Feasibility and accuracy of single time point imaging for renal dosimetry following ^{177}Lu-DOTATATE ('Lutate') therapy. EJNMMI Phys. 2018;5(1):33. https://doi:10.1186/s40658-018-0232-9

92. Driscoll B, Shessel A, Laidley D, Breen S, Yeung I, Farcombe T, et al. Individualized dosimetry for Lu-177 DOTATATE therapy - What difference does it make? J Nucl Med. 2019 May 1;60(supplement 1):630–630.

93. Cremonesi M, Botta F, Di Dia A, Ferrari M, Bodei L, De Cicco C, et al. Dosimetry for treatment with radiolabelled somatostatin analogues. A review. Q J Nucl Med Mol Imaging Off Publ Ital Assoc Nucl Med AIMN Int Assoc Radiopharmacol IAR Sect Soc Of. 2010 Feb;54(1):37–51.

94. Kwekkeboom DJ, Bakker WH, Kooij PP, Konijnenberg MW, Srinivasan A, Erion JL, et al. [^{177}Lu-DOTAOTyr3]octreotate: comparison with [^{111}In-DTPAo]octreotide in patients. Eur J Nucl Med. 2001 Sep;28(9):1319–25. https://doi:10.1007/s002590100574

95. Santoro L, Mora-Ramirez E, Trauchessec D, Chouaf S, Eustache P, Pouget J-P, et al. Implementation of patient dosimetry in the clinical practice after targeted radiotherapy using [^{177}Lu-[DOTA0, Tyr3]-octreotate. EJNMMI Res. 2018 Nov 29;8(1):103. https://doi:10.1186/s13550-018-0459-4

96. Ljungberg M, Strand S-E. A Monte Carlo program for the simulation of scintillation camera characteristics. Comput Methods Programs Biomed. 1989 Aug 1;29(4):257–72. https://doi.org/10.1016/0169-2607(89)90111-9

97. Ramonaheng K, van Staden JA, du Raan H. Validation of a Monte Carlo modelled gamma camera for Lutetium-177 imaging. Appl Radiat Isot. 2020 Apr 27;109200. https://doi.org/10.1016/j.apradiso.2020.109200

98. Yushkevich PA, Gao Y, Gerig G. ITK-SNAP: an interactive tool for semi-automatic segmentation of multi-modality biomedical images. Conf Proc Annu Int Conf IEEE Eng Med Biol Soc IEEE Eng Med Biol Soc Annu Conf. 2016 Aug;2016:3342–5. https://doi: 10.1109/EMBC.2016.7591443

99. Siegel JA, Stabin MG. Absorbed fractions for electrons and beta particles in spheres of various sizes. J Nucl Med Off Publ Soc Nucl Med. 1994 Jan;35(1):152–6.

100. Sabet A, Ezziddin K, Pape U-F, Reichman K, Haslerud T, Ahmadzadehfar H, et al. Accurate assessment of long-term nephrotoxicity after peptide receptor radionuclide

therapy with ^{177}Lu-octreotate. Eur J Nucl Med Mol Imaging. 2014 Mar;41(3):505–10. https://doi: 10.1007/s00259-013-2601-x

101. Dewaraja YK, Wilderman SJ, Ljungberg M, Koral KF, Zasadny K, Kaminiski MS. Accurate dosimetry in ^{131}I radionuclide therapy using patient-specific, 3-dimensional methods for SPECT reconstruction and absorbed dose calculation. J Nucl Med Off Publ Soc Nucl Med. 2005 May;46(5):840–9.

102. Frey EC, Tsui BMW. A New method for modeling the spatially-variant, object-dependent scatter response function in SPECT. In: IEEE Nuclear Science Symposium & Medical Imaging Conference. Conference record, Anaheim, CA, USA; 1996;(2)1082-1086. https://doi:10.1109/NSSMIC.1996.591559

103. Frey EC, Tsui BMW. A practical method for incorporating scatter in a projector-backprojector for accurate scatter compensation in SPECT. IEEE Trans Nucl Sci. 1993 Aug;40(4):1107–16. https://doi:10.1109/23.256720

104. Wehrmann C, Senftleben S, Zachert C, Müller D, Baum RP. Results of individual patient dosimetry in peptide receptor radionuclide therapy with ^{177}Lu DOTA-TATE and ^{177}Lu DOTA-NOC. Cancer Biother Radiopharm. 2007 Jun;22(3):406–16. https://doi:10.1089/cbr.2006.325

105. Ljungberg M, Frey E, Sjögreen K, Liu X, Dewaraja Y, Strand S-E. 3D Absorbed Dose Calculations Based on SPECT: Evaluation for ^{111}In/^{90}Y Therapy using Monte Carlo Simulations. Cancer Biother Radiopharm. 2003 Feb 1;18(1):99–107. https://doi.org/10.1089/108497803321269377

106. Schindelin J, Arganda-Carreras I, Frise E, Kaynig V, Longair M, Pietzsch T, et al. Fiji: an open-source platform for biological-image analysis. Nat Methods. 2012 Jun 28;9(7):676–82. https://doi:10.1038/nmeth.2019

107. Grimes J. Patient-specific internal dose calculation techniques for clinical use in targeted radionuclide therapy. University of British Columbia; 2013.

108. National Nuclear Database Center 2014. Information extracted from Nudat 2 interface. (https://www.nndc.bnl.gov/nudat2/). [Accessed 2021 Sep 13]

109. Begum NJ, Thieme A, Eberhardt N, Tauber R, D’Alessandria C, Beer AJ, et al. The Effect of Total Tumor Volume on the Biologically Effective Dose to Tumor and Kidneys for ^{177}Lu-Labeled PSMA Peptides. J Nucl Med. 2018 Jun 1;59(6):929–33. https://doi: 10.2967/jnumed.117.203505

110. Kim Y, Oh J, Yoo C, Ryoo B-Y, Ryu J-S. Prediction of absorbed dose by tumors and critical organs after Lu-177-DOTATATE therapy using pretherapeutic Ga-68-DOTATOC PET/CT. J Nucl Med. 2021 May 1;62(supplement 1):76–76.

111. Zhao W, Esquinas PL, Frezza A, Hou X, Beauregard J-M, Celler A. Accuracy of kidney dosimetry performed using simplified time activity curve modelling methods: a ^{177}Lu-

DOTATATE patient study. Phys Med Biol. 2019 Aug;64(17):175006. https://doi:10.1088/1361-6560/ab3039

112. Marin G, Vanderlinden B, Karfis I, Guiot T, Wimana Z, Reynaert N, et al. A dosimetry procedure for organs-at-risk in ^{177}Lu peptide receptor radionuclide therapy of patients with neuroendocrine tumours. Phys Med. 2018 Dec 1;56:41–9. https://doi:10.1016/j.ejmp.2018.11.001

113. Mora Ramirez E, Santoro L, Cassol E, Ocampo Ramos J, Clayton N, Kayal G, et al. Comparison of commercial dosimetric software platforms in patients treated with ^{177}Lu-DOTATATE for peptide receptor radionuclide therapy. Med Phys. 2020 Jul 6;47. https://doi.org/10.1002/mp.14375

114. Gleisner KS, Brolin G, Sundlöv A, Mjekiqi E, Östlund K, Tennvall J, et al. Long-Term Retention of ^{177}Lu/^{177m}Lu-DOTATATE in Patients Investigated by γ-Spectrometry and γ-Camera Imaging. J Nucl Med Off Publ Soc Nucl Med. 2015 Jul;56(7):976–84. https://doi: 10.2967/jnumed.115.155390

115. Kesner A, Chicheportiche A, Freedman N. Automated batch dosimetry data processing software for improved clinical applications and workflow. J Nucl Med. 2018 May 1;59(supplement 1):1744–1744.

116. Nickel M, Ljungberg M, Sjogreen-Gleisner K. A comparison of different image-based methods for kidney dosimetry in patients treated with ^{177}Lu-DOTATATE. J Nucl Med. 2009 May 1;50(supplement 2):501–501.

117. Santoro L, Pitalot L, Trauchessec D, Mora-Ramirez E, Kotzki PO, Bardiès M, et al. Clinical implementation of PLANET® Dose for dosimetric assessment after [^{177}Lu]Lu-DOTA-TATE: comparison with Dosimetry Toolkit® and OLINDA/EXM® V1.0. EJNMMI Res. 2021 Jan 4;11(1):1. https://doi:10.1186/s13550-020-00737-8

118. Svensson J, Hagmarker L, Magnander T, Wängberg B, Bernhardt P. Radiation exposure of the spleen during ^{177}Lu-DOTATATE treatment and its correlation with haematological toxicity and spleen volume. EJNMMI Phys. 2016 Aug 5;3:15. https://doi:10.1186/s40658-016-0153-4

119. Yeyin N, Tanyildizi H, Demirci E, Akyel R, Aygun A, Toklu T, et al. Radiation absorbed dose calculation of Lu-177-DOTA-TATE therapy in patients with somatostatin receptor expressing tumors. J Nucl Med. 2013 May 1;54(supplement 2):1027–1027.

120. Tran-Gia J, Lassmann M. Optimizing Image Quantification for Lu-177 SPECT/CT Based on a 3D Printed 2-Compartment Kidney Phantom. J Nucl Med. 2017 Nov 2;jnumed.117.200170. https://doi:10.2967/jnumed.117.200170

121. Helisch A, Förster GJ, Reber H, Buchholz H-G, Arnold R, Göke B, et al. Pre-therapeutic dosimetry and biodistribution of ^{86}Y-DOTA-Phe1-Tyr3-octreotide versus ^{111}In-pentetreotide in patients with advanced neuroendocrine tumours. Eur J Nucl Med Mol Imaging. 2004 Oct;31(10):1386–92. https://doi:10.1007/s00259-004-1561-6

122. Roth D, Gustafsson JR, Warfvinge CF, Sundlöv A, Åkesson A, Tennvall J, et al. Dosimetric quantities of neuroendocrine tumors over treatment cycles with ^{177}Lu-DOTA-TATE. J Nucl Med Off Publ Soc Nucl Med. 2021 Jul 16;jnumed.121.262069. https://doi: 10.2967/jnumed.121.262069

123. Mora-Ramirez E, Santoro L, Trauchessec D, Chouaf S. Dosimetric estimations using commercial workstations for peptide receptor radionuclide therapy (PRRT) patients treated with ^{177}Lu-DOTATATE. Eur J Nucl Med Mol Imaging. 2017;44S810. https://doi: 10.1002/mp.14375

5

Chapter 5:

Concluding Remarks and Future Aspects

TABLE OF CONTENTS

5.1 Concluding Remarks

There has been a rapid proliferation in the development of novel targeting agents for RPT. However, compared to other therapeutic modalities such as EBRT, RPT has been the slowest to develop into a patient-specific individualised dose regime using dosimetry-guided treatment planning. The first technical stumbling block was quantitative SPECT image data unavailability as part of the clinical gamma camera workflow. The introduction of hybrid SPECT/CT systems, combined with automatic CT-based attenuation correction, scatter correction, and CDR correction in the reconstruction methods, has eliminated most of the obstacles previously encountered when attempting to obtain quantitative SPECT information from SPECT images. These corrections have become relatively standard from the gamma cameras vendors' and may be optimised for radionuclides used in RPT. Further development has been the introduction of SPECT/CT systems presenting SPECT images in units of activity concentration for application in the dosimetry calculations. The progression to the actual dose calculations has seen several vendors offering dosimetry packages as part of the gamma camera workflow at an additional cost. The different dose calculation algorithms and the criteria for choosing the optimal algorithm for a specific application have been presented in Chapter 1.

Even with the above-mentioned developments, there are still logistical challenges involved in the clinical dosimetry workflow. The images used for dosimetry need to be obtained at several time-points and involve more steps compared to a conventional imaging examination. The imaging at specific times for dosimetry would have to be incorporated into the daily patient imaging throughput. Another important consideration is the reproducibility of the patient position during imaging at different time-point. Ideally, the patient should be imaged in a reproducible manner guided by positional lasers and patient couch markings. Post-acquisition steps for dosimetry, such as the registration of the successive images and automatic methods for VOI determination, should be done with care and precision to reduce error propagation in the dosimetry results.

Therefore, dosimetry requires a multidisciplinary effort from technologists, medical physicists, and physicians. The additional steps needed for dosimetry should be part of the routine clinical load and introduced as part of the non-negotiable workload. A clinically inspired dosimetry workflow that engages the professionals mentioned above will assist in the mind shift to this concept. While dosimetry is the responsibility of the medical physicist, without an organised teamwork and engagement of all stakeholders, performing dosimetry as part of the non-negotiable patient workload becomes challenging. A modular workflow approach, designed to be a team effort, must be established to allow a step-wise flow through the dosimetric chain. The medical physicist is responsible for the dosimetry protocol, including the SPECT image acquisition protocol, optimisation of SPECT/CT image reconstruction for quantification, optimisation of calibration measurements, and dose computations. However, the medical physicist should engage the technologist and physician to play a vital role in the VOI definitions. The final RPT planning discussion regarding the optimal dose to be delivered to the target and critical organs should include the physician. Inspired by the fact that a linear accelerator will not be purchased without a treatment planning system for EBRT, a dosimetry-based treatment planning system could be a mandatory part of the clinical workflows upon purchasing the gamma camera. The personalised medicine approach could be fully adopted with a directorate available to prevent the use of RPT without considering patient-specific absorbed doses.

Even with all the attempts for patient-specific dosimetry to tailor RPT for each patient, there is still an ongoing debate of the benefits of individualised activity dosing versus the one dose fits all approach. However, as with any treatment regime, the goal is to deliver the highest dose to the tumours while sparing the healthy tissue. Patient-specific dosimetry is the gateway to achieving the “as high as safely achievable” use of RPT and rendering its full potential as a high-precision treatment. Yet, considering all perspectives to individualised RPT, there should be no doubt to the value of the additional information that NM could benefit from using image-based patient-specific dosimetry as a guide for treatment planning of RPT.

This thesis aimed to determine the accuracy of ^{177}Lu SPECT activity quantification and patient-specific dosimetry using MC simulations. The dosimetry accuracy was investigated for tumours and OAR pertinent to ^{177}Lu-DOTATATE distribution in the RPT of patients with late-stage NETs. The investigations used voxel-based phantoms derived from CT data and virtual image activity quantification and dosimetry with MC simulations. The results of the original articles, included in this thesis, are discussed in detail in the preceding chapters (Chapters 2 to 4) and their corresponding articles (Articles I to III).

There are several advantages to the use of MC simulations in NM. One such advantage is the generation of virtual gamma camera models for emission imaging investigations and virtual dosimetry using voxel-based phantoms. Therefore it becomes imperative to ascertain the integrity of the modelled gamma camera to mimic the clinical gamma camera of interest. For this reason, the first objective (**Objective I**) of this thesis was to validate the ability of the SIMIND MC program to model the Siemens Symbia T16 gamma camera available in our clinic at Universitas Academic Hospital (UAH). The validation was achieved by comparing the experimental and simulated results of planar and SPECT gamma camera performance criteria tests. CT images of the experimental setup used for the experimental acquisitions on the clinical gamma camera aided to mimic the exact setup on the modelled gamma camera. The results showed that all prominent energy spectrum features in the shape, alignment and peak energies for ^{177}Lu were modelled well. The satisfactory matching of the energy spectrum features, including the height of the ^{177}Lu 208 keV photopeak of interest between the experimental and simulation data, emphasised the importance of incorporating the measured energy resolution value into the SIMIND as part of the input parameters instead of applying the energy resolution from a Gaussian function varying $\frac{1}{\sqrt{Energy}}$ with ^{99m}Tc (140 keV) as the reference energy. Overall the results of the experiments and simulations compared well and confirmed that SIMIND could be used confidently for further investigations of ^{177}Lu SPECT activity quantification and patient-specific dosimetry.

The clinical dosimetry workflow for SPECT image-based dosimetry essentially consists of five crucial steps: (i) SPECT image acquisition protocol, (ii) SPECT/CT activity image quantification and reconstruction, (iii) TAC analysis and integration, (iv) absorbed dose calculations, as well as (v) dosimetry software used to analyse and present the results. Each step was incorporated in the thesis as part of the investigated objectives. The first two steps were combined and dealt with under the thesis's **Objective II**, focussing on quantification accuracy for ^{177}Lu SPECT images. The last three steps were streamlined under the SPECT/CT dosimetry accuracy for ^{177}Lu RPT as **Objective III**.

Objective II of the thesis investigated the effect of sphere and cylinder CF geometries and their corresponding RCs on the quantification accuracy of ^{177}Lu SPECT images using MC simulations. The quantification accuracy depends on the SPECT/CT imaging acquisition protocol and whether the confounding image degrading factors have been corrected as part of the reconstruction process. Furthermore, for dosimetry, the quantified activity SPECT/CT images are required in activity concentration units, which are achieved by applying a CF. The CF is a direct source of potential inaccuracy in determining the absolute activity values. The findings of the second objective showed that the segmentation or VOI selection criteria to define the CF, should be consistent with the VOI definition of the quantified data. Furthermore, the same CF used to convert the quantified image counts into units of activity concentration or activity values should be applied consistently in determining the RC curve for PVC. In this manner, the quantification accuracy becomes comparable, irrespective of whether a sphere or cylinder geometry was used to determine the CF. This was attributed to the fact that the differences due to the spill-in and spill-out effects encountered from the two CF geometries were balanced by the corresponding RC values. It is, however, imperative that all SPECT corrections for attenuation, scatter, CDR and PVC were applied. As a result, the accuracy of the sphere-CF-RC and the cylinder-CF-RC for quantifying ^{177}Lu SPECT activity were found to be comparable.

Objective III was dedicated to the last steps of the dosimetry workflow, investigating the accuracy of two dosimetry software programs, namely LundADose and OLINDA. This objective's findings showed merit in optimising and standardising the first steps in the dosimetry workflow. These initial steps defined the accuracy of activity quantification (Objective II), and their methodology was directly applied to dose calculations, having an effect on the dosimetry results. Because LundADose included all of the steps required for a clinical dosimetry workflow, it was used for SPECT/CT activity quantification and reconstruction (Objective II), as well as for TAC analysis and integration (part of Objective III). From here, the dosimetry values were computed using either (i) LundADose, or (ii) OLINDA. In light of the fact that OLINDA did not include the first steps in the dosimetry workflow for activity quantification, using the same TIA data from LundADose reduced the uncertainty that could be introduced from different software programs in the first steps. In addition, the simulated data eliminated errors that could have been caused by image misregistration at different time-points during the acquisitions. This allows for a true comparison of the dose calculation obtained with the two software programs. Since the dosimetry was performed virtually using MC simulations, the OAR and tumour volumes were obtained accurately from the segmented CT data, and the OLINDA results were scaled in accordance with the mass of the OAR. Comparable accuracies were obtained between average doses calculated with OLINDA and LundADose, both of which compared well to the true doses. These findings encourage the idea of patient-specific dosimetry being a dependable guide for planning treatment of RPT.

5.2 Future Aspects

The work presented in this thesis could expand to several possibilities. Concurrent research projects have validated SIMIND to model the Siemens Symbia T16 SPECT/CT, modelled in this thesis, for ^{123}I and ^{131}I. The work could be extended to ^{90}Y for bremsstrahlung imaging. SIMIND may be validated for other gamma cameras such as the GE discovery NM/CT 670 SPECT/CT system available in the Department of NM at our associate National Annex Hospital (NAH).

Future plans for the Department of NM at UAH include obtaining a PET/CT system, therefore, validation of other MC programs such as GATE for PET imaging could be of interest. An apparent expansion of the dosimetry methodology implemented in this thesis would be for ^{177}Lu-PSMA treatments, which have recently been implemented in our clinic. The patients for this treatment are diagnostically selected using ^{99m}Tc-PSMA SPECT/CT imaging. Since quantification is performed for standard uptake values in ^{68}Ga-PSMA imaging, the same could be explored with ^{99m}Tc-PSMA. Of interest would be investigating the quantitative difference between imaging with ^{99m}Tc-PSMA and ^{68}Ga-PSMA using MC simulations.

Currently, quantification for dosimetry at UAH employs planar whole-body imaging using the geometric mean with background correction. The methodology presented in this thesis could be implemented in the clinic. Most corrections for quantification of SPECT/CT data in terms of attenuation, scatter, and CDR have been fairly standardised on the gamma camera workflow. However, PVC does not come standard with the SPECT/CT corrections on the gamma camera workflow. The PVE, owing to the limited SPECT system spatial resolution on ^{177}Lu data acquired with a medium-energy collimator, places major limitations on dosimetry objects of less than three times the reconstructed spatial resolution. The effect is that objects near the SPECT resolution limit will be underestimated. The correlation of the sphere-based and cylinder-based CFs and their corresponding RCs can be implemented. The conventional sphere-based RCs were used in this thesis for PVC, however, the effect of object shape on the RC would be of interest. The absorbed dose calculations from SPECT/CT images could be extended to ^{131}I. Other research work by our group included the accuracy of patient-specific dosimetry using hybrid WB/SPECT imaging for ^{131}I applications using LundADose. This work may be extended to ^{177}Lu and implemented clinically. More dosimetry software programs could be used in a comparative study using actual clinical data as they become available.

Lastly, OLINDA/EXM program (version 1) was used to compare dose estimates from the LundADose program with OLINDA. OLINDA (version 1) uses S values generated for computational phantoms using stylized models. It would be interesting to compare dose estimates obtained from the new reference phantom S values based on more realistic image-based models available in the current version of OLINDA/EXM (version 2) to dose estimates obtained from patient-specific S values estimated using LundADose.

Appendices:

TABLE OF CONTENTS

Appendix A-1:

Front page of the published article I.

https://doi.org/10.1016/j.apradiso.2020.109200

Applied Radiation and Isotopes 163 (2020) 109200

Contents lists available at ScienceDirect

Applied Radiation and Isotopes

journal homepage: http://www.elsevier.com/locate/apradiso

Validation of a Monte Carlo modelled gamma camera for Lutetium-177 imaging

K. Ramonaheng *, J.A. van Staden, H. du Raan

Department of Medical Physics, University of the Free State, PO Box 339, Bloemfontein, 9300, South Africa

ARTICLE INFO

Keywords:
Validation
Modelling
^{177}Lu
Monte Carlo
SIMIND
Simulations
Experiments
Planar
SPECT

ABSTRACT

This study validated a model of the Siemens Symbia T16 dual-head SPECT/CT gamma camera created using the Monte Carlo program SIMIND for ^{177}Lu. The validation was done by comparing experimental and simulated gamma camera performance criteria tests for the ^{177}Lu 208 keV photopeak with a medium-energy collimator. Results showed good agreement between the experimental and simulated values. These results illustrated that SIMIND could emulate the Symbia T16 successfully and therefore, can be used with confidence to model ^{177}Lu images.

1. Introduction

Gamma camera imaging with ^{99m}Tc using a low-energy high-resolution (LEHR) collimator has fulfilled the role of ideal imaging in nuclear medicine for both planar and single-photon emission computed tomography (SPECT) images. SPECT imaging has been proven, in phantom and clinical studies, to demonstrate superior images and better quantitative accuracy in comparison to planar images (Cachovan et al., 2013; Gnesin et al., 2016; Willowson et al., 2008). This is attributed to the fact that problems such as organ overlap and superimposed background activity are overcome in SPECT imaging. However, factors complicating quantitative SPECT imaging are photon attenuation, photon scatter, collimator detector response and partial volume effect. Furthermore, it is necessary to establish a calibration factor to convert image counts into absolute units of activity (Pereira et al., 2010).

^{131}I has been used as a common therapeutic isotope for decades. Its imaging and quantification capabilities with a high-energy collimator have been investigated extensively in the literature (Dewaraja et al., 2000; Sjögreen et al., 2002). However, with the development of new peptides, ^{177}Lu has gained popularity as one of the isotopes of choice for peptide receptor radionuclide therapy (PRRNT) using the theranostic approach. This is owing to its favourable physical characteristics that make it an ideal imaging and therapeutic radionuclide (Garkavij et al., 2010; Ljungberg et al., 2016; Ljungberg and Sjögreen-Gleisner, 2011). It has also been proven to reduce patient bone marrow toxicity in comparison to ^{131}I (Zaknun et al., 2013). ^{177}Lu has a physical half-life of 6.7 days and emits gamma rays, beta particles, characteristic x-rays and bremsstrahlung radiation (Browne, 1993). Of these gamma rays, two with an energy of 113 keV (6.2%) and 208 keV (10.4%) have been used successfully for imaging purposes (Beauregard et al., 2011). The beta particles have a maximum and mean kinetic energy of 498 keV (78.6%) and 134 keV, respectively, and are used in radionuclide therapy. Characteristic x-rays from ^{177}Lu are prominent at energies of 54.6 keV (1.6%) and 55.8 keV (2.8%) (Browne, 1993). The bremsstrahlung yield, due to the interaction of the beta particles with tissue, has been observed to be very low (<0.2%), with most (~ 85%) of the created photons having energies below 50 keV (Uribe et al., 2016).

The ideal choice of which; collimator, gamma-ray imaging energy and energy window settings for ^{177}Lu are needed, have been well investigated using Monte Carlo (MC) simulations (Ljungberg et al., 2016). Literature suggests the use of the 208 keV photopeak with a medium-energy (ME) collimator and a 20% energy window setting (Beauregard et al., 2011; D'Arienzo et al., 2016; de Nijs et al., 2014; Garkavij et al., 2010; He et al., 2012; Ljungberg et al., 2016; Shcherbinin et al., 2012). This is owing to the higher yield of the 208 keV gamma-ray emission compared to the 113 keV photon, the avoidance of down

---

* Corresponding author. Department of Medical Physics (G68), Faculty of Health Sciences, University of the Free State, PO Box 339, Bloemfontein, 9300, South Africa.

E-mail address: BoomK@ufs.ac.za (K. Ramonaheng).

https://doi.org/10.1016/j.apradiso.2020.109200
Received 15 October 2019; Received in revised form 11 February 2020; Accepted 8 April 2020

Appendix A-2:

NMISA certificate of calibration.

nmisa
National Metrology Institute of South Africa

Certificate of Calibration

15 Lower Hope Road, Rosebank, Cape Town, 7700
Tel: +27 21 685 2065/7776
Fax: +27 21 686 2759
E-mail enquiries: info@nmisa.org
www.nmisa.org

Calibration of:	One Lu-177 solution
Type:	Lu-177 solution in a 10 ml glass vial
Sample Identification:	Lu-177 UFS
Calibrated for:	Johan van Staden Faculty of Health Sciences, Medical Physics University of the Free State Bloemfontein
Location of calibration:	Radioactivity Standards Laboratory 15 Lower Hope Road Rosebank, Cape Town
Balance used:	Mettler B6 (NML-RS-005)
Measuring instrument:	NAC 03540
Calibration procedures:	RS-TEC-0001 RS-TEC-0003
Period of calibration:	25 July 2018
Half-life: (information from Table of Radionuclides, Monographie BIPM-5, Volume 2)	Lu-177 $T_{½}$ = (6,647 ± 0,004) days
Impurity content:	Certified by manufacturer $\leq$ 0,01 %

Calibrated by **M.J. van Staden** **Metrologist (Technical Signatory)**	Checked by **M.W. van Rooy** **Metrologist**	For Chief Executive Officer
Date of Issue **03 August 2018**	**Page 1 of 3**	Certificate number **RS\18-52**

1 PROCEDURE

The Lu-177 vial was measured, as received, in current mode (pA), using a radionuclide factor of 0300 in the NMISA secondary standard calibrated ionization chamber (NAC 03540). A total of 3,5 g of the Lu-177 solution was transferred (accurately weighed) to a 5 ml glass ampoule and measured in current mode (pA) in the ionization chamber. A previously-determined calibration figure of (0,3179 ± 0,0028) pA/MBq was used to determine the activity of Lu-177 in the ampoule. This calibration figure was also used to determine the activity in the vial with an added uncertainty of 1,3 % to account for the difference in geometry of the vial.

The remaining content of the vial was removed and the initial mass of the Lu-177 solution in the vial was determined.

The activity concentration in the vial, as received, was determined and compared with the activity concentration in the ampoule, where a large discrepancy was found. The empty vial was measured in the ionization chamber, indicating that approximately 20 % of the Lu-177 activity received, remained in the empty vial. The vial was rinsed three times with de-ionised water and re-measured. This confirmed that approximately 18 % of the original Lu-177 activity remained as adsorption in the empty vial.

Therefore, the activity concentration of the Lu-177 solution transferred to the ampoule was not comparable to the original activity concentration transferred to the vial. Therefore, the activity concentration of the solution in the ampoule could not be used to determine the total activity in the vial, instead the current measurements made on the vial were used.

The results of the measurements are traceable to the relevant national measurement standards for radioactivity.

2 RESULTS

The decay corrected activity, uncertainty of measurement and reference date for the original solution transferred to the vial is shown in Table 1 below.

Table 1.

Activity (MBq)	Uncertainty at 1σ (MBq)	Relative Uncertainty at 1σ (%)	Reference Date & Time
55,92	± 1,02	± 1,8	25 July 2018, 12h00 SAST

For your interest, the amount of the solution received in the vial is indicated in Table 2 below.

Table 2.

Sample ID	Mass (g)
Lu-177 UFS	4,455 (0,003)

3 REMARKS

3.1 The reported uncertainties of measurement were calculated and expressed in accordance with the BIPM, IEC, ISO, IUPAP, OIML document entitled "A Guide to the Expression of Uncertainty in Measurement" (International Organisation for Standardisation, Geneva, Switzerland, 2008).

3.2 The reported uncertainty of measurement is stated as the standard uncertainty of measurement multiplied by a coverage factor of k = 1, which for a normal distribution approximates a level of confidence of 68,27%.

3.3 Certain of the NMISA certificates are consistent with the capabilities that are included in appendix C of the MRA (Mutual Recognition Arrangement) drawn up by the CIPM. Under the MRA, all participating institutes recognise the validity of each other's calibration and measurement certificates for the quantities and ranges and measurement uncertainties specified in Appendix C. For details see http://www.bipm.org.

3.4 The calibration was carried out at an ambient temperature of 18 °C ± 3 °C and a relative humidity of 65 %RH ± 15 %RH.

------------------ *end of certificate* ------------------

Appendix B:

Front page of the published article II.

https://doi.org/10.1186/s40658-021-00365-8

Ramonaheng *et al. EJNMMI Physics* (2021) 8:27
https://doi.org/10.1186/s40658-021-00365-8

EJNMMI Physics

ORIGINAL RESEARCH **Open Access**

The effect of calibration factors and recovery coefficients on ^{177}Lu SPECT activity quantification accuracy: a Monte Carlo study

Keamogetswe Ramonaheng*, Johannes A. van Staden and Hanlie du Raan

* Correspondence: BoomK@ufs.ac.za
Department of Medical Physics, Faculty of Health Sciences, University of the Free State, PO Box 339, Bloemfontein 9300, South Africa

Abstract

Background: Different gamma camera calibration factor (CF) geometries have been proposed to convert SPECT data into units of activity concentration. However, no consensus has been reached on a standardised geometry. The CF is dependent on the selected geometry and is further affected by partial volume effects. This study investigated the effect of two CF geometries and their corresponding recovery coefficients (RCs) on the quantification accuracy of ^{177}Lu SPECT images using Monte Carlo simulations.

Methods: The CF geometries investigated were (i) a radioactive-sphere surrounded by non-radioactive water (sphere-CF) and (ii) a cylindrical phantom uniformly filled with radioactive water (cylinder-CF). Recovery coefficients were obtained using the sphere-CF and cylinder-CF, yielding the sphere-RC and cylinder-RC values, respectively, for partial volume correction (PVC). The quantification accuracy was evaluated using four different-sized spheres (15.6–65.4 ml) and a kidney model with known activity concentrations inside a cylindrical, torso and patient phantom. Images were reconstructed with the 3D OS-EM algorithm incorporating attenuation, scatter and detector-response corrections. Segmentation was performed using the physical size and a small cylindrical volume inside the cylinder for the sphere-CF and cylinder-CF, respectively.

Results: The sphere quantification error (without PVC) was better for the sphere-CF (≤ − 5.54%) compared to the cylinder-CF (≤ − 20.90%), attributed to the similar geometry of the quantified and CF spheres. Partial volume correction yielded comparable results for the sphere-CF-RC (≤ 3.47%) and cylinder-CF-RC (≤ 3.53%). The accuracy of the kidney quantification was poorer (≤ 22.34%) for the sphere-CF without PVC compared to the cylinder-CF (≤ 2.44%). With PVC, the kidney quantification results improved and compared well for the sphere-CF-RC (≤ 3.50%) and the cylinder-CF-RC (≤ 3.45%).

Conclusion: The study demonstrated that upon careful selection of CF-RC combinations, comparable quantification errors (≤ 3.53%) were obtained between the sphere-CF-RC and cylinder-CF-RC, when all corrections were applied.

Keywords: ^{177}Lu, Quantification, Monte Carlo, SIMIND, Calibration factor, Recovery coefficients

Appendix C:

Front page of article III under review.

http://dx.doi.org/10.2139/ssrn.3958626

Heliyon First Look
Heliyon

Accuracy of Two Dosimetry Software Programs for ^{177}Lu Radiopharmaceutical Therapy Using Voxel-Based Patient-Specific Phantoms

Heliyon

53 Pages
Posted: 8 Nov 2021
Publication Status: **Under Review**

Keamogetswe Ramonaheng
University of the Free State

Johan A. van Staden
University of the Free State

Hanlie du Raan
University of the Free State

Abstract

PurposeVirtual dosimetry using voxel-based patient-specific phantoms and Monte Carlo (MC) simulations offer the advantage of having a gold standard against which absorbed doses may be benchmarked to establish the dosimetry accuracy. Furthermore, these reference values assist in investigating the accuracy of the absorbed dose methodologies from different software programs. Therefore, this study aimed to compare the accuracy of the absorbed doses computed using LundADose and OLINDA/EXM 1.0.MethodsThe accuracy was based on ^{177}Lu-DOTATATE distributions of three voxel-based phantoms. SPECT projection images were simulated for 1, 24, 96, and 168 hours post-administration and reconstructed with LundADose using 3D OS-EM reconstruction. Mono-exponential curves were fitted to the bio-kinetic data for the kidneys, liver, spleen, and tumours resulting in SPECT time-integrated activity (SPECT-TIA). The SPECT-TIA were used to compute mean absorbed doses using LundADose (LND-D SPECT) and OLINDA (OLINDA-D SPECT) for the organs. Pre-defined true activity images, were used to obtain TRUE-TIA and, together with full MC simulations, computed the true doses (MC-D True). The dosimetry accuracy was assessed by comparing LND-D SPECT and OLINDA-D SPECT to MC-D True .ResultsOverall, the results presented an overestimation of the mean absorbed dose by LND-D SPECT compared to the MC-D True with a dosimetry accuracy ≤ 6.59%. This was attributed to spill-out activity from the reconstructed LND-D SPECT , resulting in a higher dose contribution than the MC-D True . There was a general underestimation (< 8.11%) of OLINDA-D SPECT compared to MC-D True attributed to the geometrical difference in shape between the voxel-based phantoms and the OLINDA models. Furthermore, OLINDA-D SPECT considers self-doses while MC-D True reflects self-doses plus cross-doses.ConclusionThe better than 10% accuracy suggests that the mean dose values obtained with LND-D SPECT and OLINDA-D SPECT approximate the true values. The mean absorbed doses of the two software programs, and the gold standard were comparable. This work shall be of use for optimising ^{177}Lu dosimetry for clinical applications.

Keywords: SPECT, Dosimetry, accuracy, Monte Carlo, ^{177}Lu-DOTATATE, OLINDA, LundADose, radiopharmaceutical therapy, patient-specific phantom, voxel-based phantom.

Appendix D-1 to D-3:

Meetings and presentations.

Appendix D-1:

International meeting	Society of Nuclear Medicine and Molecular Imaging 2019 annual meeting, Anaheim, California, USA.
Date	22-25 June 2019
Presentation	Poster
Abstract title	*SIMIND Monte Carlo validation for Lutetium-177 imaging.*

English▼

JNM
The Journal of Nuclear Medicine

Meeting Report | Physics, Instrumentation & Data Sciences

SIMIND Monte Carlo validation for Lutetium-177 imaging

Keamogetswe Ramonaheng

Journal of Nuclear Medicine May 2019, 60 (supplement 1) 1349;

Article Info & Metrics

Abstract

1349

Objectives: Due to the development of new peptides Lu-177 has gained popularity as one of the isotopes of choice for peptide receptor radionuclide therapy using the theranostics approach. The choice of; collimator, gamma ray energy to image and energy window settings for Lu-177 is well investigated using Monte Carlo (MC) simulations. MC offers the advantage of evaluating phenomena involved in nuclear medicine imaging which may be cumbersome to measure physically. Gamma cameras are subject to a variety of detector and electronic challenges therefore it is deemed useful to validate the capability of MC programs to model physical gamma cameras. The MC program SIMIND has been validated for modelling various gamma cameras for a number of different radionuclides. Validation of SIMIND for a Siemens Symbia T16 dual head SPECT/CT gamma camera with Lu-177 has not been reported. The aim of this study was to validate the MC simulation setup of the Siemens Symbia T16 dual head SPECT/CT gamma camera for Lu-177 using SIMIND.

Methods: The validation was done by comparing experimental and simulated gamma camera performance criteria tests for the Lu-177208 keV photopeak with a medium-energy low-penetration collimator. These tests included four planar NEMA stipulated tests namely; intrinsic and extrinsic energy resolution, extrinsic spatial resolution and extrinsic sensitivity. In addition, two SPECT tests termed air and water calibration factor (CF) were validated. The SPECT tests used an activity-filled sphere suspended in air and in awater-filled cylindrical phantom to generate the air and water CF respectively. Sequential SPECT and CT images were acquired following a clinical imaging protocol. These images were reconstructed using FLASH 3D with CT-based attenuation correction, TEW scatter correction and full 3D collimator-detector response. Experimental measurements were repeated three times, while simulations were only performed once for each test. The data was processed and the results compared.

Results: The intrinsic experimental and simulated energy resolution values were 9.6 ± 0.06 % and 9.9 % respectively. The % and absolute difference of -3.1 % and 0.3 % between these values indicated good agreement. The corresponding extrinsic energy resolution values were 9.4 ± 0.09 % and 9.9 % for the experimental and simulated data, with a % and absolute difference of -5.3 % and 0.5 %. The calculated FWHM and FWTM for the extrinsic spatial resolution were 11.5 ± 0.35 mm and 20.8 ± 0.82 mm for the experimental and 11.0 mm and 20.1 mm for the simulated data. The system sensitivity values of 10.0 ± 0.03 cps/MBq vs. 10.3 cps/MBq showed good agreement between the experimental and simulated values. The SPECT experimental and simulated air CF values were 8.4 ± 1.04 cps/MBq and 8.3 cps/MBq with % and absolute differences of 1.2 % and 0.1 cps/MBq. The water CF values of 7.8 ± 0.94 cps/MBq vs. 7.2 cps/MBq showed slightly higher % and absolute differences of 7.7 % and 1.6 cps/MBq between the experimental and simulated studies. These larger differences may be attributed to the introduction of attenuation and scatter by the water-filled phantom in both the experimental and simulated setup. **Conclusion:** The results obtained in this study were found to be in good agreement for both the planar and SPECT tests. From this study, it is evident that SIMIND can emulate the Symbia T16 successfully and therefore can be used with confidence in future studies to model planar and SPECT Lu-177 images.

Appendix D-2:

Local meeting	The 18th Annual Free State Provincial Health Research Day
Date	07-08 November 2019
Presentation	Oral presentation
Abstract title	*SIMIND Monte Carlo validation for Lutetium-177 imaging.*

SIMIND Monte Carlo Validation for Lutetium-177 Imaging.

K Ramonaheng[1], JA van Staden[1], H du Raan[1].

Department of Medical Physics, University of the Free State[1].

Introduction: Lu-177 is one of the ideal radionuclides used in Nuclear Medicine (NM) for cancer imaging and treatment. Computer Monte Carlo (MC) programs offers the advantage of evaluating phenomena involved in NM imaging and treatment, which may be cumbersome to measure clinically. Gamma cameras used to acquire NM images can be modelled using MC programs such as SIMIND. In order to ascertain the integrity of the modelled gamma camera to mimic the clinical gamma camera, it is necessary to validate the MC program.

Aim: The aim of this study was to model the Siemens Symbia SPECT/CT gamma camera with 177Lu using the SIMIND MC program.

Design and Methods: The validation was done by comparing experimental and simulated tests of Lu-177 obtained with the clinical and simulated gamma cameras respectively. These tests included; four planar gamma camera performance criteria tests stipulated by NEMA and two SPECT tests. SPECT data were reconstructed using a 3-D OS-EM algorithm. The planar and SPECT data were processed and the results compared.

Results: The planar experimental and simulated test data showed absolute and percentage differences not exceeding 0.5 and -5.3 % respectively. These minor differences indicated good agreement between the experimental and simulated tests. The experimental and simulated SPECT data showed maximum absolute and percentage differences of 0.6 and 7.7 % respectively. These slightly larger differences may be attributed to the combination of the 3-D reconstruction artefacts and chemical properties of the Lu-177 observed in the experimental tests.

Conclusion: All the results obtained were found to be in good agreement (< 10 %). From the results of this study, it is evident that SIMIND can model the Siemens Symbia SPECT/CT gamma camera successfully and therefore can be used with confidence in future studies to mimic Lu-177 clinical images.

Appendix D-3:

Local meeting	The 19th Biennal South African Society of Nuclear Medicine
Date	26-28 February 2021
Presentation	Oral presentation
Abstract title	*The Effect of Calibration Factors and Recovery Coefficients on* ^{177}*Lu SPECT Activity Quantification Accuracy: A Monte Carlo study*.

THE EFFECT OF CALIBRATION FACTORS AND RECOVERY COEFFICIENTS ON LU-177 SPECT ACTIVITY QUANTIFICATION ACCURACY: A MONTE CARLO STUDY.

K Ramonaheng[1], J.A. van Staden[1], H. du Raan[1].

Department of Medical Physics, University of the Free State[1].

Background: There is increasing evidence supporting the need for personalized dosimetry based on Lu-177 SPECT quantitative information. The lack of standardized methods, which include determining the gamma camera calibration factor (CF), has hindered the process. The CF is dependent on the selected geometry and affected by partial volume effects. This study investigated the effect of two CF geometries and their corresponding recovery coefficients (RCs) on the quantification accuracy of Lu-177 SPECT images using Monte Carlo simulations.

Methods: The CF geometries investigated were (i) a radioactive-sphere surrounded by non-radioactive water (sphere-CF) and (ii) a cylindrical phantom uniformly filled with radioactive water, (cylinder-CF). Recovery coefficients were obtained using the sphere-CF and cylinder-CF, yielding the sphere-RC and cylinder-RC values, respectively, for partial volume correction (PVC). The quantification accuracy was evaluated using four different sized spheres (15.6 ml – 65.4 ml) and a kidney model with known activity concentrations inside a cylindrical, torso and patient phantom. Images were reconstructed with the OS-EM algorithm incorporating attenuation, scatter and detector-response corrections. Segmentation was performed using the physical size and a small cylindrical volume inside the cylinder for the sphere-CF and cylinder-CF, respectively.

Results: Sphere quantification error (with no PVC) was better for the sphere-CF (≤ -5.54%) compared to the cylinder-CF (≤ -20.90%), attributed to the similar geometry of the quantified and CF spheres. Partial volume correction yielded comparable results for the sphere-CF (≤ 3.47%) and cylinder-CF (≤ 3.53%). The accuracy of the kidney quantification was poorer (≤ 22.34%) for the sphere-CF without PVC compared to the cylinder-CF (≤ 2.44%). With PVC, the kidney quantification results improved and compared well for the sphere-CF (≤ 3.50%) and the cylinder-CF (≤ 3.45%).

Conclusion: The study demonstrated that upon careful selection of CF-RC combinations, comparable quantification errors (≤ 3.53%) were obtained between the sphere-CF and cylinder-CF, with all corrections applied.

Appendix E:

Ethical approval.

UNIVERSITY OF THE
FREE STATE
UNIVERSITEIT VAN DIE
VRYSTAAT
YUNIVESITHI YA
FREISTATA

UFS·UV
HEALTH SCIENCES
GESONDHEIDSWETENSKAPPE

Health Sciences Research Ethics Committee

21-Sep-2021

Dear **Mrs Keamogetswe Ramonaheng**

Ethics Number: UFS-HSD2019/1506/0110-0001

Ethics Clearance: **Accuracy of Lutetium-177 SPECT Activity Quantification and Patient-Specific Dosimetry: A Monte Carlo Study.**

Principal Investigator: **Mrs Keamogetswe Ramonaheng**

Department: **Medical Physics Department (Bloemfontein Campus)**

Submission Page

SUBSEQUENT SUBMISSION APPROVED

With reference to your recent submission for ethical clearance from the Health Sciences Research Ethics Committee. I am pleased to inform you on behalf of the HSREC that you have been granted ethical clearance for your request as stipulated below:

Continuation Report: The project's ethics clearance is extended until 20 September 2022.

The HSREC functions in compliance with, but not limited to, the following documents and guidelines: The SA National Health Act. No. 61 of 2003; Ethics in Health Research: Principles, Structures and Processes (2015); SA GCP(2006); Declaration of Helsinki; The Belmont Report; The US Office of Human Research Protections 45 CFR 461 (for non-exempt research with human participants conducted or supported by the US Department of Health and Human Services- (HHS), 21 CFR 50, 21 CFR 56; CIOMS; ICH-GCP-E6 Sections 1-4; International Council for Harmonisation (ICH) Harmonised Guideline, Integrated Addendum to ICH E6(R1), Guideline for Good Clinical Practice (GCP) E6(R2), 2016, SAHPRA Guidelines as well as Laws and Regulations with regard to the Control of Medicines, Constitution of the HSREC of the Faculty of Health Sciences.

For any questions or concerns, please feel free to contact HSREC Administration: 051-4017794/5 or email EthicsFHS@ufs.ac.za.

Thank you for submitting this request for ethical clearance and we wish you continued success with your research.

Yours Sincerely

Prof. A. Sherriff
Chairperson : Health Sciences Research Ethics Committee

Appendix F:

Turnitin report.

PhD Thesis

ORIGINALITY REPORT

9%	8%	2%	1%
SIMILARITY INDEX	INTERNET SOURCES	PUBLICATIONS	STUDENT PAPERS

PRIMARY SOURCES

1	link.springer.com Internet Source	1%
2	scholar.ufs.ac.za:8080 Internet Source	1%
3	assets.researchsquare.com Internet Source	1%
4	open.library.ubc.ca Internet Source	<1%
5	jnm.snmjournals.org Internet Source	<1%
6	iopscience.iop.org Internet Source	<1%
7	www.mdpi.com Internet Source	<1%
8	ejnmmiphys.springeropen.com Internet Source	<1%
9	ir.canterbury.ac.nz Internet Source	<1%

10	www.ncbi.nlm.nih.gov Internet Source	<1 %
11	Erick Mora - Ramirez, Lore Santoro, Emmanuelle Cassol, Juan C. Ocampo - Ramos et al. " Comparison of commercial dosimetric software platforms in patients treated with Lu - DOTATATE for peptide receptor radionuclide therapy ", Medical Physics, 2020 Publication	<1 %
12	thesesups.ups-tlse.fr Internet Source	<1 %
13	Submitted to King's College Student Paper	<1 %
14	preview-ejnmmires.springeropen.com Internet Source	<1 %
15	edoc.ub.uni-muenchen.de Internet Source	<1 %
16	repub.eur.nl Internet Source	<1 %
17	doku.pub Internet Source	<1 %
18	journals.plos.org Internet Source	<1 %
19	www.encyclopedias.biz Internet Source	<1 %

20	aapm.onlinelibrary.wiley.com Internet Source	<1 %
21	epubs.surrey.ac.uk Internet Source	<1 %
22	Michael Ljungberg, Katarina Sjögreen Gleisner. "Personalized Dosimetry for Radionuclide Therapy Using Molecular Imaging Tools", Biomedicines, 2016 Publication	<1 %
23	www.sciencegate.app Internet Source	<1 %
24	worldwidescience.org Internet Source	<1 %
25	Submitted to Higher Education Commission Pakistan Student Paper	<1 %
26	ejnmmires.springeropen.com Internet Source	<1 %
27	tel.archives-ouvertes.fr Internet Source	<1 %
28	"Clinical Applications of Nuclear Medicine Targeted Therapy", Springer Science and Business Media LLC, 2018 Publication	<1 %
29	silo.tips Internet Source	<1 %

30	Michaella Morphis, Johan A. van Staden, Hanlie du Raan, Michael Ljungberg. "Evaluation of Iodine-123 and Iodine-131 SPECT activity quantification: a Monte Carlo study", EJNMMI Physics, 2021 Publication	<1 %
31	digitalcommons.library.tmc.edu Internet Source	<1 %
32	archive.org Internet Source	<1 %
33	pinlab.hcuge.ch Internet Source	<1 %
34	preview-ejnmmiphys.springeropen.com Internet Source	<1 %
35	tech.snmjournals.org Internet Source	<1 %
36	www.jmp.org.in Internet Source	<1 %
37	www.science.gov Internet Source	<1 %
38	www.scribd.com Internet Source	<1 %
39	etd.library.vanderbilt.edu Internet Source	<1 %

40	Lore Santoro, L. Pitalot, D. Trauchessec, E. Mora-Ramirez, P. O. Kotzki, M. Bardiès, E. Deshayes. "Clinical implementation of PLANET® Dose for dosimetric assessment after [177Lu]Lu-DOTA-TATE: comparison with Dosimetry Toolkit® and OLINDA/EXM® V1.0", EJNMMI Research, 2021 Publication	<1 %
41	Mendonça, Catarina Ramos de(Cullum, Ian and Pires, Rui Jorge Correia Mendes Alves). "Radionuclide therapy in nuclear medicine : applying Monte Carlo simulation to investigate Bremsstrahlung imaging with a gamma camera", Veritati - Repositório Institucional da Universidade Católica Portuguesa, 2013. Publication	<1 %
42	Submitted to University of Liverpool Student Paper	<1 %
43	onlinelibrary.wiley.com Internet Source	<1 %
44	ufdc.ufl.edu Internet Source	<1 %
45	jacmp.org Internet Source	<1 %
46	research.library.mun.ca Internet Source	<1 %

47	Targeted Radionuclide Tumor Therapy, 2008. Publication	<1 %
48	thesis.library.caltech.edu Internet Source	<1 %
49	www.medimaging.gr Internet Source	<1 %
50	ampi.org.in Internet Source	<1 %
51	brain.oxfordjournals.org Internet Source	<1 %
52	dipot.ulb.ac.be Internet Source	<1 %
53	thno.org Internet Source	<1 %
54	www.guillemet.org Internet Source	<1 %
55	Basic Sciences of Nuclear Medicine, 2011. Publication	<1 %
56	Clinical Applications of SPECT-CT, 2014. Publication	<1 %
57	digital.library.unt.edu Internet Source	<1 %
58	dspace.lib.cranfield.ac.uk Internet Source	<1 %

59	epub.uni-regensburg.de Internet Source	<1 %
60	interactive.snm.org Internet Source	<1 %
61	www.cmej.org.za Internet Source	<1 %
62	"Theranostics, Gallium-68, and Other Radionuclides", Springer Science and Business Media LLC, 2013 Publication	<1 %
63	www.sprmn.pt Internet Source	<1 %
64	Submitted to Medizinischen Universität Wien Student Paper	<1 %
65	Submitted to Mahidol University Student Paper	<1 %
66	Submitted to University of Auckland Student Paper	<1 %
67	www.sydneyvital.org.au Internet Source	<1 %
68	www.vizijavarnosti.com Internet Source	<1 %
69	"Basic Sciences of Nuclear Medicine", Springer Science and Business Media LLC, 2021 Publication	<1 %

70	Arun Gupta, Min Sun Lee, Joong Hyun Kim, Dong Soo Lee, Jae Sung Lee. "Preclinical Voxel-Based Dosimetry in Theranostics: a Review", Nuclear Medicine and Molecular Imaging, 2020 Publication	<1 %
71	Daphne Merel Valerie Huizing, Berlinda Jantina de Wit-van der Veen, Marcel Verheij, Marcellus Petrus Maria Stokkel. "Dosimetry methods and clinical applications in peptide receptor radionuclide therapy for neuroendocrine tumours: a literature review", EJNMMI Research, 2018 Publication	<1 %
72	Submitted to University of Malaya Student Paper	<1 %
73	ndl.ethernet.edu.et Internet Source	<1 %
74	users.ugent.be Internet Source	<1 %
75	ecancer.org Internet Source	<1 %
76	etheses.dur.ac.uk Internet Source	<1 %
77	www.eanm.org Internet Source	<1 %

78	www.pubmedcentral.nih.gov Internet Source	<1 %
79	www.recentmedicalfindings.com Internet Source	<1 %
80	Submitted to University of Pretoria Student Paper	<1 %
81	abstracts.ncri.org.uk Internet Source	<1 %
82	gupea.ub.gu.se Internet Source	<1 %
83	ssrpm.ch Internet Source	<1 %
84	storage.googleapis.com Internet Source	<1 %
85	www.rahd.com Internet Source	<1 %
86	"Molecular Imaging in Oncology", Springer Science and Business Media LLC, 2020 Publication	<1 %
87	Alexandre Chicheportiche, Elinor Goshen, Jeremy Godefroy, Simona Grozinsky-Glasberg et al. "Can a penalized-likelihood estimation algorithm be used to reduce the injected dose or the acquisition time in 68Ga-DOTATATE PET/CT studies?", Research Square, 2020	<1 %

Publication

88	Eero T. Hippeläinen, Mikko J. Tenhunen, Hanna O. Mäenpää, Jorma J. Heikkonen, Antti O. Sohlberg. "Dosimetry software Hermes Internal Radiation Dosimetry", Nuclear Medicine Communications, 2017 Publication	<1 %
89	aojnmb.mums.ac.ir Internet Source	<1 %
90	apps.dtic.mil Internet Source	<1 %
91	archive-ouverte.unige.ch Internet Source	<1 %
92	ascopubs.org Internet Source	<1 %
93	bioone.org Internet Source	<1 %
94	bmccancer.biomedcentral.com Internet Source	<1 %
95	e-notabene.ru Internet Source	<1 %
96	eanm13.eanm.org Internet Source	<1 %
97	jsnm.org Internet Source	<1 %

98	lup.lub.lu.se Internet Source	<1 %
99	upcommons.upc.edu Internet Source	<1 %
100	www.mayoclinic.org Internet Source	<1 %
101	www.nucleide.org Internet Source	<1 %
102	www.thieme-connect.de Internet Source	<1 %
103	Anastassia Löser, Sarah M. Schwarzenböck, Martin Heuschkel, Holger S. Willenberg, Bernd J. Krause, Jens Kurth. "Peptide receptor radionuclide therapy with 177Lu-DOTA-octreotate", Nuclear Medicine Communications, 2018 Publication	<1 %
104	Gustav Brolin, Johan Gustafsson, Michael Ljungberg, Katarina Sjögreen Gleisner. " Pharmacokinetic digital phantoms for accuracy assessment of image-based dosimetry in Lu-DOTATATE peptide receptor radionuclide therapy ", Physics in Medicine and Biology, 2015 Publication	<1 %
105	core.ac.uk	

	Internet Source	<1 %
106	d-nb.info Internet Source	<1 %
107	digital.lib.washington.edu Internet Source	<1 %
108	docplayer.net Internet Source	<1 %
109	ejnmmipharmchem.springeropen.com Internet Source	<1 %
110	epdf.pub Internet Source	<1 %
111	inis.iaea.org Internet Source	<1 %
112	mafiadoc.com Internet Source	<1 %
113	mts.intechopen.com Internet Source	<1 %
114	orca.cf.ac.uk Internet Source	<1 %
115	portal.research.lu.se Internet Source	<1 %
116	scholar.sun.ac.za Internet Source	<1 %

117	scholarcommons.usf.edu Internet Source	<1 %
118	slidelegend.com Internet Source	<1 %
119	spotidoc.com Internet Source	<1 %
120	umexpert.um.edu.my Internet Source	<1 %
121	www.aifm2013.org Internet Source	<1 %
122	www.esp.org Internet Source	<1 %
123	www.karger.com Internet Source	<1 %
124	www.medrxiv.org Internet Source	<1 %
125	www.revistas.usp.br Internet Source	<1 %
126	www.tandfonline.com Internet Source	<1 %
127	www.yumpu.com Internet Source	<1 %

Exclude quotes	On	Exclude matches	< 8 words
Exclude bibliography	On		

Promoter: Dr. Johannes A. van Staden